Scaling-up the Tweezer Platform - Trapping Arrays of Single Atoms in a Cryogenic Environment

Kai-Niklas Schymik

université
PARIS-SACLAY

Scaling-up the Tweezer Platform - Trapping Arrays of Single Atoms in a Cryogenic Environment

Passage à l'échelle de matrices d'atomes dans des pinces optiques – Piégeage d'atomes individuels en environnement cryogénique

Thèse de doctorat de l'université Paris-Saclay

École doctorale n° 572, Ondes et Matières (EDOM)
Spécialité de doctorat : Physique
Graduate School : Physique. Référent : Institut d'Optique

Thèse préparée au **Laboratoire Charles Fabry (Université Paris-Saclay, Institut d'Optique Graduate School, CNRS)**, sous la direction de **Thierry Lahaye,** Chargé de recherche.

Thèse soutenue à Paris-Saclay, le 24 mars 2022, par

Kai-Niklas Schymik

Composition du Jury

François Marquier Professeur, ENS Paris-Saclay	Président
Sebastian Hofferberth Professeur, Université de Bonn	Rapporteur
Fred Jendrzejewski Professeur, Université de Heidelberg	Examinateur
Michel Brune Directeur de recherche, CNRS – LKB	Rapporteur
Hélène Perrin Directrice de recherche, CNRS – LPL	Examinatrice
Thierry Lahaye Chargé de recherche, CNRS – LCF	Directeur de thèse
Antoine Browaeys Directeur de recherche, CNRS – LCF	Invité

THESE DE DOCTORAT

NNT : 2022UPASP031

université PARIS-SACLAY

ÉCOLE DOCTORALE
Ondes et matière (EDOM)

Titre : Piégeage d'atomes individuels en environnement cryogénique

Mots clés : pinces optiques, simulation quantique, cryogénie

Résumé : Des atomes individuels piégés dans des matrices de pinces optiques forment une des meilleures plateformes expérimentales pour la simulation quantique de modèles de spins. Comme pour la plupart des plateformes de simulation quantique, l'augmentation du nombre d'objets quantiques contrôlés individuellement est un défi majeur. Dans cette thèse, je présente notre travail sur la levée des principales limitations à la réalisation de grandes matrices d'atomes sans défaut avec des fidélités élevées. Ces limitations des fidélités de préparation incluent la durée de vie limitée par le vide d'un seul atome dans la pince, et le temps nécessaire pour préparer de grandes matrices, atome par atome, avec une pince optique mobile. Nous avons d'abord amélioré l'assemblage de grands réseaux d'atomes sans défaut en développant des nouveaux algorithmes plus efficaces. En utilisant ces derniers, nous avons augmenté le nombre d'atomes d'une quarantaine à deux cents sur notre expérience à température ambiante. Nous avons ensuite construit une nouvelle plateforme cryogénique de pinces à atomes dans laquelle la durée de vie d'un seul atome est supérieure à 6000 secondes, soit une amélioration d'environ 300 fois par rapport à notre expérience à température ambiante. Nous décrivons la conception et la construction de la nouvelle configuration cryogénique et évaluons ses performances dans une série de tests. Enfin, nous démontrons le piégeage d'atomes uniques dans des réseaux de pinces optiques à des températures cryogéniques et analysons les différents mécanismes de perte présents pendant la mesure de la durée de vie. Ces résultats ouvrent la voie à des simulations quantiques à grande échelle sur notre plateforme.

Title : Scaling-up the Tweezer Platform - Trapping Arrays of Single Atoms in a Cryogenic Environment

Keywords : optical tweezers, quantum simulation, cryogenics

Abstract : Arrays of single atoms trapped in optical tweezers are a prominent platform for the quantum simulation of spin models. As for most quantum simulation platforms, scaling up the number of individually controlled quantum objects is a major challenge. In this thesis, I present our work on lifting principal limitations to achieving large defect-free atom arrays with high fidelities. These limitations of the preparation fidelities include the vacuum-limited lifetime of a single atom in the tweezer, and the time needed to prepare large arrays atom-by-atom with a moveable optical tweezer. We first improved the assembly of large defect-free atom arrays by developing a new algorithmic framework. Using the new framework, we increased the number of atoms from around forty to two hundred on our room-temperature setup. We then built a novel cryogenic atom tweezer platform in which the single-atom lifetime is over 6000 seconds, an approximately 300-fold improvement over our room-temperature experiment. We describe the design and construction of the new cryogenic setup and evaluate its performance in a series of tests. Finally, we demonstrate the trapping of single atoms in tweezer arrays at cryogenic temperatures and analyze different loss mechanisms present during the lifetime measurement. These results open the way to large-scale quantum simulations on our platform.

Contents

Acknowledgements

This manuscript summarizes my doctoral studies between November 2018 and March 2022. I have spent these three and a half years at the Laboratoire Charles-Fabry in the group of Antoine Browaeys, under direction of Thierry Lahaye. As you can read in detail in this thesis, after months of planning and testing, we have finally constructed a new cryogenic tweezer experiment, trapped single atoms at 4 K and demonstrated the scalability of this platform. But not every story has found its way into this document, so let me take this space to give a bit of context with a few personal notes and thank everyone that made these results possible.

First, I want to express my gratidude towards the members of my Jury, Hélène Perrin, Michel Brune, Sebastian Hofferberth, François Marquier and Fred Jendrzejewski. Thank you for carefully reading my manuscript and the questions at my defense. It was an honor to defend in front of you.

I had the privilege to work at the Laboratoire Charles Fabry which is directed by Patrick Georges. This privilege became especially apparent to me throughout the pandemic. After the first lock-down, we were able to return to working in the lab relatively quickly. I am very grateful to Patrick for ensuring that; a new experiment cannot be built from home after all!

When I first arrived on the plateau in July 2018 for my interview, I received a warm welcome by Antoine Browaeys and Thierry Lahaye. I remember Thierry picking me up from the hotel and driving me to the institute in the morning, followed by a labtour during which the new project was presented to me. From our discussions, both their immense knowledge and passion for physics became evident, and even though building a new setup is never without risks, I knew I would be in good hands in this group. Three and a half years later I am happy that I trusted my first instinct. I thank Antoine for the enriching discussions we had, about physics and life, and for ensuring these excellent working conditions in the group. Further, I thank Thierry for his guidance throughout the project and for sharing his immense knowledge with me. I am especially grateful for your pragmatism and your ability to take the right decision(s) at the right time, even if it means readjusting one's goals. Without it, I am certain that we would not have had all these results in the time of my PhD.

Even if I was the only PhD student on this project, the work described in this thesis is not the work of a single person but the work of an amazing team.

I am grateful to Florence, for her dedicated work on the design and construction of the experiment, and for her joyfully singing and kind personality. You and Thierry taught me a lot of French, although I am not sure if I will be able to replicate all the puns that I have heard during my time here.

I thank Eric, for starting the cryogenic endeavor in his last PhD year and for constructing the room temperature setup on which I trapped my first single atoms. Further, I thank Sam for taking the RER A to Fontenay-sous-Bois with me to test the design of our optical assembly in a cryostat at the facilities of MyCryoFirm. I thank Julien, Franck, Mohammed for working on the cryogenic side of this experiment, and I thank Sara for her patient work during assembling and trapping of our first atoms.

At the beginning of my second year, I worked with Pascal and Hannah on CHADOQ. Despite competition from overseas and malfunctioning lasers, we managed to make it work and I think the results speak for themselves. Thank you for your hard work and dedication!

Then, in the middle of my second year, the Covid pandemic started, which changed everything for everyone. I am grateful to my parents for welcoming me home with open arms during the first lock-down, thank you for your constant emotional support! I am also happy to have my brother Jan and sister Hanna by my side, who are always a call or train away.

During the time of the first lock-down, my work shifted towards programming and algorithms. Even though this project started mainly because we did not have access to our experiment, I am extremely happy about the outcome of this project. Also, because I had the opportunity to work closely with Daniel and Vincent. It was a pleasure to work with Vincent, who is an endless source of new, smart ideas. And Daniel, with his impressive stamina, that never runs out of motivation and dedication. After the first lock-down I had many more occasions to work together with Daniel in the lab, thank you for spending many evenings with me, not all of them were successful, but we always had some fun!

I would also like to thank the other people of our group for discussions and good moments. Thank you to Igor, Toni, Giovanni, Sylvain, Tom, Guillaume, Gabriel, Cheng, Damien!

In the weeks before my defense, I was working together with people from the start-up PASQAL. Bruno, Etienne, Davide, this beautiful experiment is in your hands now, treat it with care!

This thesis was also made possible through funding from the Studienstiftung des deutschen Volkes, which I would like to thank not only for its financial support, but

also for the rich programming that connects us to other doctoral students and allows us to learn from other disciplines.

Next to my work in the lab, I had the pleasure to destress with some amazing people, enjoying life, with good food or coffee in Paris, learning about art and music, or cycling in the Vallée de Chevreuse. Thank you, Jan, Franck, Alysha, Pablo, Jez, Ali and Béatrice!

Chapter 1

Introduction

In recent decades, the ability to manipulate individual quantum systems [Wineland, 2013; Haroche, 2013] has improved at a rapid pace, leading many researchers to believe that we are on the verge of a second quantum revolution. Several new quantum technologies, which utilize unique quantum properties to gain an advantage over their classical counterparts, have been developed in recent years and their industrialization leads to breakthroughs in various fields. While some of these technologies rely on the precise control of a single quantum object, other entangle multiple quantum systems. This unique property of quantum systems led to a long-standing debate in the physics community that started with Einstein, Podolsky and Rosen in 1935 [Einstein, Podolsky, and Rosen, 1935], and was experimentally settled nearly fifty years later by [Aspect, Grangier, and Roger, 1982]. Today's quantum technologies are implemented in a variety of physical systems, from single particles to solid-state devices. They find applications in different fields which can be categorized broadly in quantum sensing and metrology, quantum communication, quantum computing and quantum simulation.

Quantum systems are very sensitive to disturbances from their environment, a characteristic which is exploited to build quantum sensors. As an example, Nitrogen-vacancy (NV) centers are solid-state systems, whose electron spin is sensitive to external perturbations like strain or electric and magnetic fields. Their use as a magnetometer was first demonstrated in 2008 [Balasubramanian *et al.*, 2008; Maze *et al.*, 2008]. Together with their small size, allowing for the resolution of structures on the nanometer scale, having a sensitivity on the order of $\mathrm{pT}/\sqrt{\mathrm{Hz}}$ makes NV centers particularly interesting for future sensing applications in many fields.

The sensitivity of quantum systems can further be used for secure communication. By making use of the quantum property of photons, data can be transferred in a secure way. This secure protocol was suggested first in 1984 [Bennett and Brassard, 1984], and quantum-key-distribution was shown a few years later on a laboratory table [Bennett *et al.*, 1992]. Today, researchers strive to extend the distance of quantum communication, by decreasing decoherence effects and building quantum

repeaters. In 2017, a satellite-to-ground quantum key distribution over 1200 km was first demonstrated [Liao *et al.*, 2017].

To study quantum mechanical systems encountered, e.g. in condensed matter physics or high-energy physics, it is convenient to use another quantum system, as Feynman suggested in 1982 [Feynman, 1982]. The amount of data needed to store the full wavefunction of a quantum system on a classical computer grows exponentially with the number of particles N, leading to an unfeasible amount of storage space even for moderate N. As an example, to represent a system of N spin-1/2 particle, one needs to store 2^N complex amplitudes. With $N = 40$, this implies about $2^{40} \simeq 10^{12}$ numbers which — for double-precision — is a storage space of about $\sim 6.4 \times 10^{13}$ bits, or 8 TB of data. This scaling problem could be solved by using a universal quantum computer. Through the excellent control of isolated two-level systems, so-called qubits, such a device only needs N qubits to store the full wavefunction of a N-particle system. Furthermore, through the application of single- and two-qubit gates, any many-qubit unitary transformation could be implemented, and for instance the time-evolution of any quantum system could be studied [Lloyd, 1996]. A very high fidelity of these gates is of utmost importance, as many of them have to be sequentially applied to the system.

Apart from the simulation of quantum systems, such a universal quantum computer has the potential to solve many computational problems considerably faster than a classical computer, most notably the factorization of large integers into prime factors [Shor, 1994], which would have far-reaching consequences for cryptography. The potential advantage of a quantum device over its classical counterpart coined the term quantum advantage: a demonstration that a quantum device can solve a (not necessarily useful) problem, that no classical computer can solve in a feasible amount of time. Even though Google claimed a quantum advantage with a 53 qubit superconducting chip [Arute, Arya, and Babbush, 2019], realizing a scalable universal quantum computer is still a long way off.

A scalable quantum computer requires that arbitrarily large computational tasks can be implemented with small output errors. This requires very high gate fidelities. However, even with finite error probabilities per gate, one can construct fault-tolerant architectures with quantum error correction codes, when the error per gate is under a certain threshold [Preskill, 1998; Kitaev, 1997; Aharonov and Ben-Or, 1999; Knill, Laflamme, and Zurek, 1998; Steane, 2003; Gottesman, 1997; Knill, 2005]. This threshold depends on the error model and the device capability and ranges widely in the literature, e.g. 10^{-6} [Preskill, 1998; Kitaev, 1997; Aharonov and Ben-Or, 1999; Knill, Laflamme,

and Zurek, 1998], 10^{-4} [Gottesman, 1997], 3×10^{-3} [Steane, 2003]. Even 3×10^{-2} is possible in principle, although the needed fault-tolerant architecture is impractical because of its large resource requirements [Knill, 2005]: quantum error-correction codes combine many physical qubits with finite gate error to obtain one logical qubit. This resource requirement is difficult to fulfil, highlighting the need for a many-qubit platform with low gate errors. Currently, platforms operate in the noisy intermediate-scale quantum (NISQ) regime [Preskill, 2018], where fidelities and system sizes are too small to achieve fault-tolerance with many qubits.

Analog Quantum simulation

Another, more short-term approach to quantum simulation, is analog quantum simulation with NISQ devices. If the Hamiltonian of a (toy) model of a quantum mechanical system can be mapped onto a simulator system, the simulator can be used to produce properties of interest, like correlation functions or the ground state. Even though the simulator may be restricted to a class of Hamiltonians, it can be far more fault-tolerant than a universal quantum simulator.

Today, (analog) quantum simulations are possible on different platforms (see e.g. the review [Georgescu, Ashhab, and Nori, 2014]), which the most prominent are ultracold gases [Bloch, Dalibard, and Nascimbène, 2012], ions [Blatt and Roos, 2012], superconducting qubits [Houck, Türeci, and Koch, 2012] and Rydberg atoms in optical tweezers [Browaeys and Lahaye, 2020]. These platforms differ not only in their physical realization, but also with respect to the models that they can simulate. The models can be from a variety of fields, e.g., cosmology [Nation *et al.*, 2009], high-energy physics [Ott *et al.*, 2021], or condensed-matter physics, where phenomena such as superfluidity [Guo *et al.*, 2020; Eckel *et al.*, 2014; Madison *et al.*, 2000] are investigated and models such as the Hubbard model [Jaksch *et al.*, 1998] or spin models [Porras and Cirac, 2004] are implemented on simulators. Furthermore, two different approaches are taken: the *top-down* and the *bottom-up* approach. Ultracold gases in optical lattices start initially with many atoms — the *top-down* approach — which makes them a great prospect for scalability. On the other hand, ions, superconducting qubits and Rydberg tweezer platforms start by controlling single qubits and then try to scale up the number of interacting elements — therefore called *bottom-up* approach — while maintaining high fidelities and coherences. Even though scalability seems to be harder in these setups, they profit from excellent single-qubit and interaction control.

Neutral atoms in optical lattices is the platform with the largest number of particles so far. The lattice sites are loaded from a degenerate gas, achieving a typical

filling of approximately 90% of the lattice sites [Greiner *et al.*, 2012; Bloch, Dalibard, and Zwerger, 2008]. The system naturally implements the Fermi- or Bose-Hubbard model, as atoms can tunnel between lattice sites with a hopping amplitude t and experience an on-site interaction energy U. In the limit of $t \ll U$, only the spin-degree of freedom remains, and the system can simulate spin Hamiltonians. So-called quantum gas microscopes [Bakr *et al.*, 2009] are able to achieve single-site resolution, to probe single-site occupancy, or to address individual sites with light using digital mirror devices.

Trapped ions have demonstrated an extremely high level of control, with two-qubit gate errors of $8(4) \times 10^{-4}$ [Gaebler *et al.*, 2016], which is in the regime for fault-tolerant architectures. Recently, several groups demonstrated the encoding of one logical qubit with several physical qubits using fault-tolerant codes [Ryan-Anderson *et al.*, 2021; Egan *et al.*, 2021]. Therefore, trapped ions are candidates for both universal and analog quantum simulation. The ions are generally trapped in linear Paul traps, and can be cooled and manipulated by lasers. In contrast to neutral atoms, they have strong long-range interactions due to the Coulomb repulsion. Control of the quantum state is facilitated by changing the internal state of an ion with a laser, and coupling the internal state to the vibrational state in the trap potential. So far, quantum simulations have been done in 1-D chains of a few tens of qubits. Implementing 2-D trapping potentials and scaling up the number of ions remains a very challenging task.

Superconducting qubit chips are the most promising solid-state platform to date, showing excellent control with entangling gate errors of 6×10^{-3} [Jurcevic *et al.*, 2021]. Similarly to ions, this makes them an excellent candidate for universal quantum computing and simulation, as well as analog quantum simulation with hopping Hamiltonians. Major technology companies such as Google and IBM are investing in this platform because of its potential chip integrability. Again, scalability is challenging, largely due to the fact that each qubit needs wiring and connections with minimal cross-talk [Tabuchi, Tamate, and Yorozu, 2021]. IBM announced a new 127-qubit processor this year, the largest superconducting qubit chip to date [Ball, 2021].

Rydberg atoms are interesting for quantum technologies in various ways, such as sensing [Dietsche *et al.*, 2019; Schmidt *et al.*, 2018] or single-photon control [Ripka *et al.*, 2018; Stiesdal *et al.*, 2021]. As potential platform for quantum simulation, they were first identified in 2010 [Weimer *et al.*, 2010]. In that same year entangling gates between Rydberg atoms were also demonstrated for the first time [Isenhower *et al.*, 2010; Wilk *et al.*, 2010]. Recently, quantum gates with fidelities approaching those of

the best quantum computation platforms have been shown [Levine *et al.*, 2018, 2019; Graham *et al.*, 2019; Madjarov *et al.*, 2020] — e.g. exceeding 0.97 [Levine *et al.*, 2018] — and first Rydberg quantum processors have been demonstrated [Bluvstein *et al.*, 2021; Graham *et al.*, 2021].

Our platform is based on the trapping of neutral atoms in tightly confined optical dipole traps — also called tweezers — which was pioneered at the Institut d'Optique in the group of Philippe Grangier [Schlosser *et al.*, 2001]. Through the use of a spatial light modulator, any geometrical configuration of traps can be chosen [Nogrette *et al.*, 2014], with distances down to a few micrometers. It is possible to obtain fully loaded structures in arbitrary geometries through atom-by-atom assembling techniques that will be explained in detail in Chapters 2 and 3 of this thesis. Compared to the other platforms, this versatility is a major advantage, as condensed matter models can be simulated on any lattice or even non-regular geometries.

Furthermore, Rydberg platforms can simulate a variety of Hamiltonians, as they can work in different regimes depending on the way the qubit is encoded. If the qubit is encoded in ground- ($|g\rangle = |\downarrow\rangle$) and Rydberg ($|r\rangle = |\uparrow\rangle$) states of the atom, the van der Waals interaction leads to an Ising-like Hamiltonian. As the ground and Rydberg states are coupled by a laser field, the whole system can be described by an Ising model with transverse and longitudinal magnetic field. In recent years, many groups have demonstrated quantum simulations of the Ising model [Labuhn *et al.*, 2016; Lienhard *et al.*, 2018; Scholl *et al.*, 2021a; Bernien *et al.*, 2017; Kim *et al.*, 2020].

Two different Rydberg states, $|nS\rangle = |\downarrow\rangle$ and $|nP\rangle = |\uparrow\rangle$, that can be coupled by a microwave field, can also be used as a qubit basis. These Rydberg atoms can then interact via a spin-exchange process [Barredo *et al.*, 2015], and evolve back- and forth between $|\downarrow\uparrow\rangle$ and $|\uparrow\downarrow\rangle$ states. This interaction can be written as an XY-Hamiltonian, with the microwave playing the role of a magnetic field, but also as a hardcore-boson Hamiltonian, where a particle hops from site to site. As an example, the harcore-boson Hamiltonian of the Su-Schrieffer-Heeger model was investigated experimentally [de Léséleuc *et al.*, 2019]. Lately, it has also been shown, that the XXZ-Hamiltonian can be engineered by combining microwave drive and spin-exchange [Scholl *et al.*, 2021b].

Scalability

As increasing the number of individually-controlled quantum objects is a necessary condition for practical use [Alexeev *et al.*, 2021], all *bottom-up* quantum simulation platforms face the challenge of scalability. To reach a quantum advantage over classical

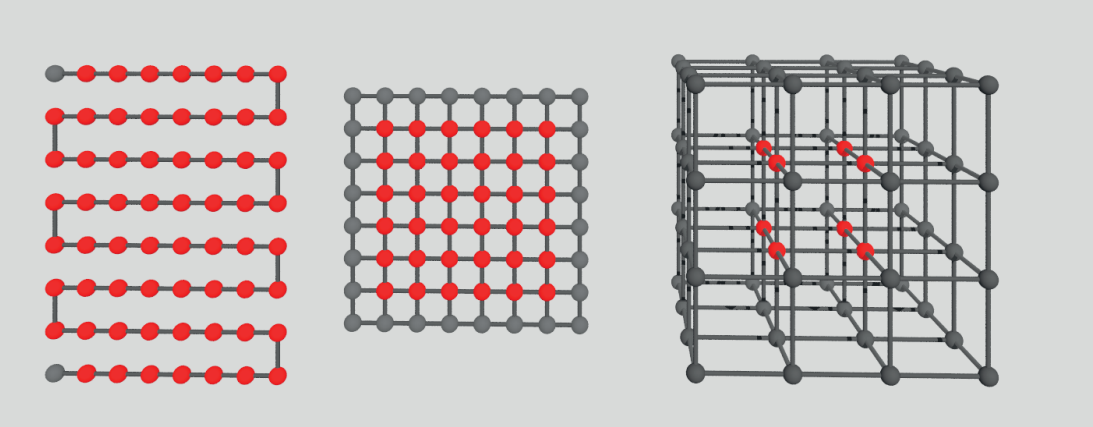

Figure 1.1: Comparison of number of bulk and border atoms. In multiple dimensions, the ratio between bulk (red) and border atoms (grey) gets smaller. A 64-atom chain has 62 bulk atoms, a 8×8 rectangle has 36 bulk atoms and a 4×4×4 cube has only 8 bulk atoms. To simulate quasi-infinite crystal structures in multiple dimensions, a large number of atoms are needed, as only bulk atoms capture the full dynamics.

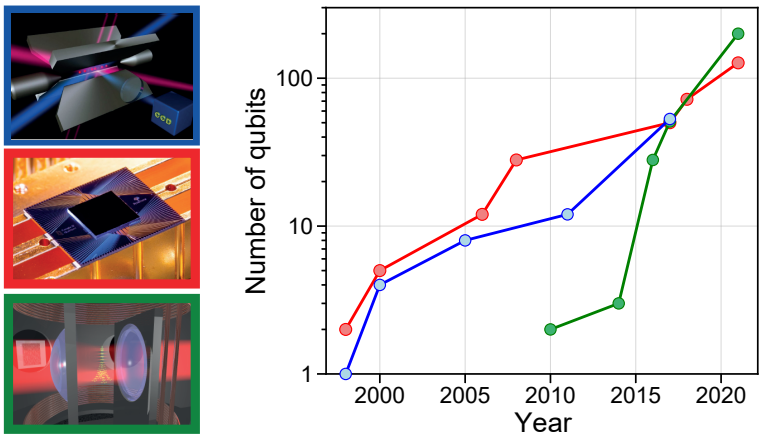

Figure 1.2: Comparison of bottom-up platforms in terms of scaling in the recent decades. Left: Images of the following platforms. In blue: sketch of a linear Paul traps for ions [Blatt], In red: A superconducting qubits chip [Gibney, 2019], In green: A Rydberg tweezer array. **Right:** The first entanglement of two ions was shown in [Turchette *et al.*, 1998]. The same year, researchers at IBM, Oxford, Berkeley, Stanford, and MIT demonstrated superconducting two-qubit systems. Although the first gate using Rydberg atoms was not shown until 2010 [Isenhower *et al.*, 2010; Wilk *et al.*, 2010], the platform grew at a rapid pace and is comparable in atom numbers compared to the other two platforms. Data taken from: Superconducting qubits [Feldman, 2019], Rydberg atoms [Barredo *et al.*, 2014],[Labuhn *et al.*, 2016],[Bernien *et al.*, 2017],[Ebadi *et al.*, 2021; Scholl *et al.*, 2021a], and ions [Sackett *et al.*, 2000],[Häffner *et al.*, 2005],[Monz *et al.*, 2011],[Zhang *et al.*, 2017] .

computers, the platforms ideally need to work in the regime of many qubits, where simulations unfeasible on a classical computer. Furthermore, as periodic boundary conditions are challenging to implement on a physical system, the large qubit limit is needed for an accurate understanding of quasi-infinite condensed matter systems.

This is illustrated in Figure 1.1. Only bulk atoms are useful for the understanding of quasi-infinite condensed matter models, as border atoms have fewer neighbors, leading to a different interaction. Whereas in one dimension, there are naturally only two border atoms, in two- or three dimensions the ratio of bulk versus border atoms is reduced. As an example, a $4 \times 4 \times 4$ cube with 64 atoms only has eight atoms in the bulk. We therefore need to produce a large atom number to be able to simulate these models in multiple dimensions while neglecting border effects.

To date, the bottom-up approaches have been restricted to a few tens of qubits [Arute, Arya, and Babbush, 2019; Zhang *et al.*, 2017; Bernien *et al.*, 2017] and upscaling has been a challenge. The Rydberg platform has made the fastest progress in recent years, as can be seen in Figure 1.2, compared to superconducting qubits or ion chains, which have existed for nearly twice as long.

The efforts of my thesis are directed towards further scaling up the number of qubits on the Rydberg platforms, from a few tens to a few hundreds of qubits, bringing the platform in the regime of the top-down approach of optical lattices. For this purpose, we built a second-generation experiment, that traps arrays of atoms in a cryogenic environment.

Cryogenic platforms

Cryogenic platforms cool down a macroscopic part of the experimental apparatus to cryogenic temperatures, depending on the used cryogenic liquid, e.g., below 77 K (liquid Nitrogen), or ~ 4 K (Helium 4). Even though the experiment described in this thesis trapped single atoms in tweezers at 4 K for the first time, cryogenic platforms have existed for a while in the atomic physics community for various reasons. The motivation might differ from setup to setup, but broadly two main advantages can be seen.

First, the number of phonons in materials decreases with temperature, and their contribution 'freezes-out' below a certain temperature. Systems that rely on chips or electrodes to trap particles are therefore less limited by phonon-noise. Ions trapped on the surface of cryogenic chips experience less radio-frequency loss and heating rates are reduced by orders of magnitude [Niedermayr *et al.*, 2014], leading to an increase of the coherence of the system. Similarly, atoms magnetically trapped close to the surface of

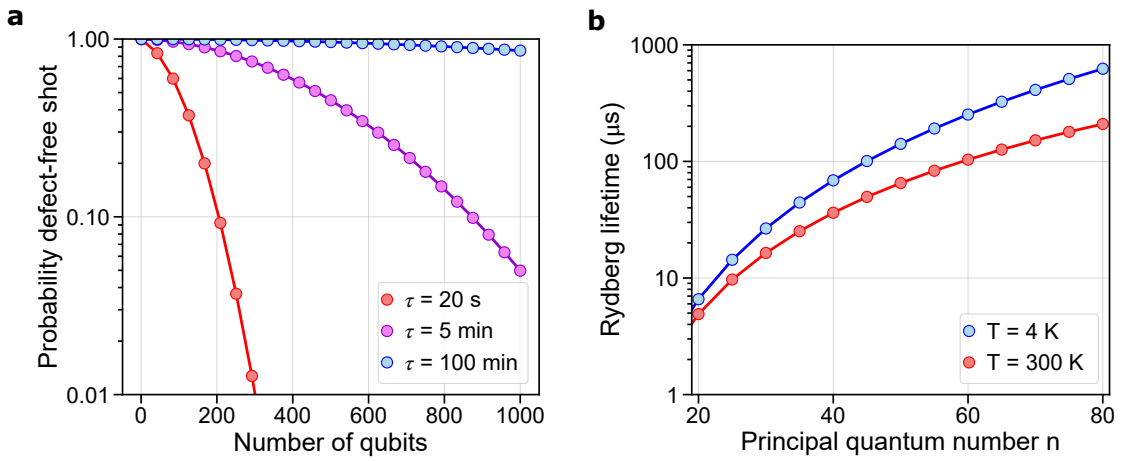

Figure 1.3: Advantages of a cryogenic tweezer platform. a: Probability of obtaining a defect-free shot $p(N) = \exp(-t_{\mathrm{assembly}}/\tau_{\mathrm{array}})$ as a function of the number N of atoms, solely considering experimental timescales and the vacuum-limited lifetime of the atoms (no experimental imperfections). Due to the small lifetime in our room-temperature setup, the probability for a perfect shot is small for $N > 100$ qubits and a lot of repetitions of the experiment are needed to acquire enough statistics. In the new cryogenic environment with lifetimes of 100 minutes however, the lifetime no longer is a limiting factor. **b:** Rydberg lifetime of a nS-state of $^{87}\mathrm{Rb}$ at 300K and 4K. The Rydberg lifetime is reduced at room-temperature due to black-body radiation induced transitions to neighboring Rydberg states. In a cryogenic environment at 4 K, the black-body radiation is surpressed which leads to longer Rydberg lifetimes (data from [Beterov *et al.*, 2009]). This increases the coherence of quantum simulations.

a chip [Nirrengarten *et al.*, 2006; Roux *et al.*, 2008; Bernon *et al.*, 2013] profit from the reduction of thermal current noise at low temperatures and have reported increased coherence and trapping lifetimes.

Second, in a cryogenic environment, experiments profit from a drastically reduced total vapor pressure. Residual gas 'freezes-out' when it comes in contact with a surface at cryogenic temperatures — an effect called cryo-pumping — and does not desorb. At liquid nitrogen temperatures (< 77 K), only neon, helium and hydrogen isotopes are still in the gas phase and at temperatures of 4 K all gases are condensed or frozen-out. In cryostats at 4 K, pressures below 10^{-14} mbar are routinely achieved [Benvenuti, 1974], and in sealed cryogenic ion traps, pressures as low as 10^{-17} mbar have been reported [Diederich *et al.*, 1998; Gabrielse *et al.*, 1990].

The main advantage of a low background gas pressure is long trapping lifetimes of particles due to a reduction of collisions with particles from the background gas. In

ion traps, these losses are induced by charge-exchange reactions with background gas particles and closed-cycle cryogenic ion traps have lately been reported in [Pagano *et al.*, 2018; Micke *et al.*, 2019; Leopold *et al.*, 2019]. In neutral atom experiments, the momentum transfer due to a background gas collision is usually large enough to expel the atom from its trap.

In Rydberg tweezer platforms, long trapping lifetimes are essential for simulations with high number of qubits. While one atom has a lifetime of $\tau = 20\,\mathrm{s}$ in our room-temperature setup, an array of N atoms has then a lifetime of $\tau_{\mathrm{array}} = \tau/N$. To benefit from fully loaded arrays, we have to work in a regime where the experimental timescale t_{exp} is much smaller than the lifetime of the array ($t_{\mathrm{exp}} \ll \tau_{\mathrm{array}}$), as otherwise atom losses reduce the probability to obtain a fully-loaded array. Unfortunately, the experimental time increases linearly with the number of atoms, as the assembly process takes more and more time as N increases. In [Barredo *et al.*, 2016], the assembly time for staggered arrays is found to be $t_{\mathrm{assembly}} = 50(\mathrm{ms}) + 0.85N(\mathrm{ms})$. As can be seen in Fig. 1.3a, a major limitation for scaling up the atom number in our room-temperature is the relatively short lifetime. The probability to prepare a defect-free array of N atoms scales as $p(N) = \exp(-t_{\mathrm{assembly}}/\tau_{\mathrm{array}})$. On our room-temperature experiment, the resulting probability to prepare arrays over 200 atoms is below 10%. In contrast, in a cryogenic environment with a lifetime of $\tau_{\mathrm{cryo}} = 100\,\mathrm{min}$, large atom arrays of up to a thousand atoms should be possible with a high fidelity.

A final advantage for Rydberg platforms comes from reduced black-body radiation at cryogenic temperatures. The Rydberg lifetime for low orbital angular momentum states, usually a few 100 µs for principal quantum numbers of $n \geq 50$, is limited by black-body induced transitions to neighboring Rydberg states. In a cryostat environment, these transition to neighboring states are negligible and the effective lifetime for Rydberg atoms is purely determined by the spontaneous decay to the ground state. This increases the effective lifetime, e.g. by a factor of approximately 3 for $n = 80$ (see Fig. 1.3b). In a quantum simulation experiment, this would lead to an increased coherence.

Compared to low orbital angular momentum Rydberg states, *circular* Rydberg states $|nC\rangle$ [Hulet and Kleppner, 1983] with maximal angular momentum $|m| = \ell = n - 1$ can have significantly longer natural lifetimes — e.g. approximately 25 ms for $n = 48$ — because they have only a single radiative decay channel to the next-lowest circular state. This motivates their use for quantum computing and simulation [Xia, Zhang, and Saffman, 2013; Nguyen *et al.*, 2018; Cohen and Thompson, 2021]. As recently proposed [Nguyen *et al.*, 2018], lifetimes in the minute range can be achieved when

spontaneous emission is inhibited by capacitor plates with a spacing smaller than half the radiated wavelength — e.g. $\lambda = 4.9\,\mathrm{mm}$ for the $|48\mathrm{C}\rangle \rightarrow |47\mathrm{C}\rangle$ transition — and black-body radiation induced transitions are limited when using a cryogenic platform.

Thesis outline

This thesis describes our efforts to scale up the number of atoms in Rydberg quantum simulators. For this purpose, we designed and built a new experimental platform that creates atom arrays in a cryogenic environment with unprecedented trapping lifetimes in excess of 100 minutes. Together with improved assembly techniques and algorithms, the thesis demonstrates the assembly of large atom arrays and therefore the scaling capabilities of this platform. The manuscript is arranged as follows:

Chapter 2 describes a state-of-the-art platform, namely the current room-temperature Rydberg platform in our group. I give an overview over single-atom trapping and the creation of fully-assembled structures in two dimensions. Then, I explain the excitation to the Rydberg states with a short overview of the new scheme that we implemented during my PhD. Lastly, I discuss the limitations of the current room-temperature setup in terms of scaling-up to higher atom numbers.

Chapter 3 presents improvements of the atom assembly techniques that have been pioneered in this group. I start by describing the problem at hand, highlighting the importance of different parameters in the optimization process. Then, I show in which ways the current algorithms are non-ideal and demonstrate new improved algorithms that can run on fully-arbitrary geometries that are not bound on a Bravais-lattice. Finally, I demonstrate their application on a project involving quantum simulations of the Ising model, where we assembled triangular and square arrays of up to 200 atoms.

Chapter 4 is dedicated to the design and construction of a new cryogenic tweezer platform and forms the core of this work. I begin by giving an overview of the new setup, after which I describe the different parts of the platform in detail. Finally, I evaluate the performance of the cryostat in a series of tests.

Chapter 5 shows the trapping of single atoms in tweezers in a cryogenic environment for the first time. I start by describing the laser system and the magneto-optical trap. Then, atom arrays with lifetimes of over 100 minutes are demonstrated and I characterize different effects limiting the measured lifetime.

Finally, Chapter 6 presents first steps towards scaling the platform to atom arrays with several hundreds of atoms. Different challenges are highlighted and I present work on how to improve current techniques of trap equalization.

Chapter 2

A State-of-the-Art Rydberg Quantum Simulator

This chapter will present a state-of-the-art Rydberg platform for the quantum simulation of spin models. The described experiment is the room-temperature platform of our group at Institut d'Optique, built by Lucas Béguin [Béguin, 2013] and Alice Vernier and upgraded by the following PhD students and postdocs. The working principles, capabilities, as well as the short-comings of this machine are described, as it serves as reference against which the novel setup, that was constructed during my PhD, can be compared.

The quantum simulations of the platform are typically based on two ingredients, which are explained in the first two sections. First, the microscopic structure of a condensed matter model, e.g., the specific lattice type, is mimicked, which will be presented in Section 2.1. This involves the trapping of single atoms in optical tweezers, the creation of holographic trap arrays using a spatial light modulator, and the creation of defect-free arrays of atoms.

Then, the interactions of the condensed matter model have to be emulated on our setup, utilizing the characteristics of Rydberg states. Section 2.2 describes the atoms' excitation to the Rydberg state. A novel scheme, that we implemented during my PhD, is presented briefly and a short overview of possible experiments is given.

Lastly, in Section 2.3, limitations of the current state-of-the-art setup are described. Focusing mainly on its ability to scale to larger number of atoms, the details of this section will motivate the efforts in the design and construction of the new cryogenic machine.

2.1 Creating atomic structures atom-by-atom

The experiment is based on trapping single atoms in tightly focused optical dipole traps, so-called optical tweezers. Historically, optical tweezers have first been used to trap micron-sized particles with a combination of radiation-pressure and dipole force [Ashkin, 1970]. Ashkin's work on optical trapping was recognized with the Nobel prize in 2018. Next to manipulating micron-sized particles, optical dipole traps became a tool to trap and manipulate atomic clouds in cold-atom experiments [Grimm, Weidemüller, and Ovchinnikov, 2000]. In red-detuned focused laser beams, atoms are attracted to the intensity maximum with a dipole force that is proportional to $F_{\text{dipole}} \propto \nabla I/\Delta$, with ∇I being the intensity gradient and Δ the detuning of the laser beam. Trap depths are usually on the order of 1 mK and therefore require the atoms to be pre-cooled, e.g. by an optical molasses.

Pioneering experiments with micron-sized dipole traps at the Institut d'Optique showed that single atoms can be isolated with help of light-assisted-collision processes [Schlosser *et al.*, 2001]. When the trapping volume is small enough, atom pairs are rapidly expelled from the traps. This effect, also called collisional blockade, leads to either one or zero atoms being in the trap at any time.

For many years, the probabilistic single atom occupation in a dipole trap was a strong limitation for using the platform for the quantum simulation of ordered condensed matter systems. In 2016 however, our group demonstrated a deterministic scheme to produce defect-free atom arrays, paving the way for the quantum simulation of spin Hamiltonians.

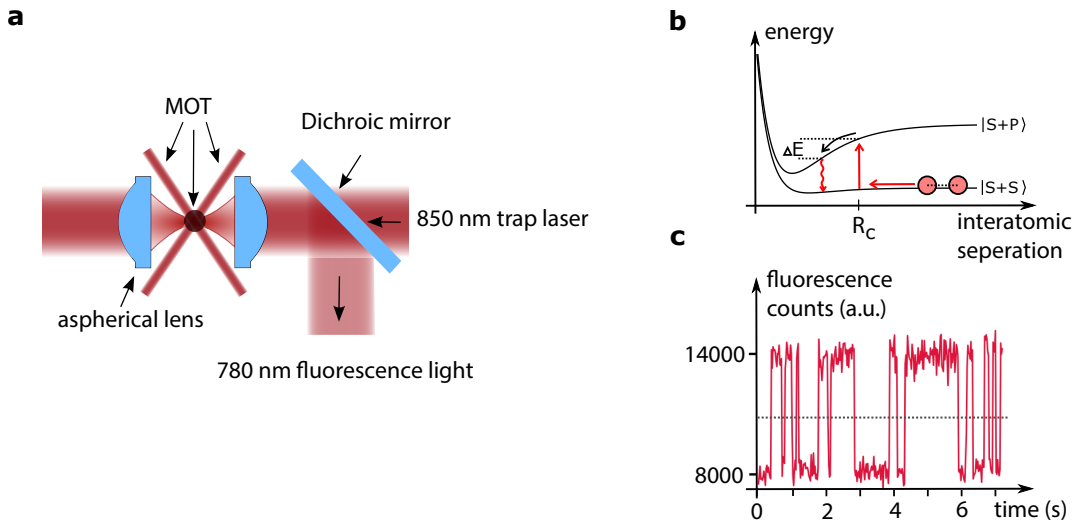

Figure 2.1: Principle of single atom loading. a: A 850 nm laser is focused by a high-numerical-aperture lens. The waist of approximately $1\,\mu\mathrm{m}$ in the focus is overlapping with an atomic cloud from a magneto-optical trap (MOT). The 780 nm fluorescence can be collected via the same lens, and separated from the trap laser light by a dichroic mirror. **b**: Light-assisted collision mechanism. In the presence of red-detuned light, atoms can associate to an attractive molecular potential at interatomic distance R_c. The gain in kinetic energy ΔE is usually much higher than the trap depth which leads to both atoms being expelled from the trap. **c**: The fluorescence signal shows the characteristic step-function for single-atom loading in the collisional-blockade regime. Two fluorescence levels can be separated, indicated by the dotted line, corresponding to one or no atom in the trap.

2.1.1 Single atoms in optical tweezers

The first single-atom experiment at Institut d'Optique (MIGOU) featured a home-made microscope objective under vacuum [Vigneron, 1998] to create the optical tweezers. In a second-generation experiment (ASPHERIX), this setup was later simplified by replacing the microscope objective with a large numerical-aperture aspheric lens [Sortais *et al.*, 2007]. On our room-temperature setup (CHADOQ), an improved lens design by Lucas Béguin [Béguin, 2013], was implemented. This lens is coated with a thin metallic layer of ITO to avoid the accumulation of charges, a crucial element for electric field-sensitive Rydberg atoms, and an advantage over the previous designs.

The room-temperature setup of our group is described in detail in the thesis of Lucas Béguin [Béguin, 2013]. It features two aspheric high-numerical-aperture lenses (NA = 0.5, focal length f = 10 mm, working distance of 7 mm), focusing a 850 nm

laser beam to a waist of approximately 1 µm at the center of a vacuum chamber (see Fig. 2.1a). The focus overlaps with a ^{87}Rb atom cloud. The Rubidium atoms originate from an oven at approximately 100 °C, are slowed down by a spin-flip Zeeman-slower before being trapped by a magneto-optical trap (MOT) in the science chamber. The far-red-detuned optical dipole trap has a power of about 3.5 mW, leading to a trap depth of approximately 1 mK, therefore it is much deeper than the usual MOT temperature of about 100 µK.

Atoms are loaded into the optical tweezer due to the cooling light of the magneto-optical trap. They can then be expelled from the trap by one- or two-body losses, as described e.g. in [Fuhrmanek *et al.*, 2012]. One-body losses are usually associated with either collisions with the background gas or heating due to cycles of absorption and emission of photons, whereas two-body losses are induced by light-assisted collisions. Due to the small trapping volume, the collisional blockade regime applies. In presence of the red-detuned light of the MOT, two atoms can form a loosely-bound pair, being attracted to each other due to the dipole potential ($V(r) \propto -C_3/r^3$, see Fig. 2.1b). If the gain in kinetic energy exceeds the trap depth, the atom-pair escapes the trap. When the two-body losses dominate over the loading rate of the magneto-optical trap, either one or no atom is in the trap at any time.

Part of the 780 nm fluorescence light that the atom scatters in all directions is collimated by the same aspheric lens (see Fig. 2.1a), separated from the trap light by a dichroic mirror, and then imaged onto an EMCCD camera (Andor iXon Ultra 897). To increase the signal-to-noise ratio, the imaging system is designed such that the light from a single tweezer is collected on one pixel of the camera. The characteristic fluorescence signal, extracted from of the photo-counts of this pixel (see Fig. 2.1c), reminds of a random telegraph noise signal. It is a sign of the light-assisted collisions, as two distinct fluorescence levels can be detected, corresponding to one or no atom in the tweezer.

A clear fluorescence signal such as in Figure 2.1c — with a clear separation of two levels corresponding to zero or one atom and a loading probability of approximately 50% — is only obtained in a small regime of laser powers corresponding to trap depths of approximately 1–1.5 mK. For smaller trap depths, the loading probability is reduced and atoms are lost easily during imaging due to heating. For higher laser powers, the increased light shift leads to a substantial loss in fluorescence light, as the atoms are detuned further from the imaging light and scatter less photons. As a result, the two levels are not clearly separated any more and detection errors increase. Furthermore the loading of multiple atoms in the deep tweezer traps has been observed as an

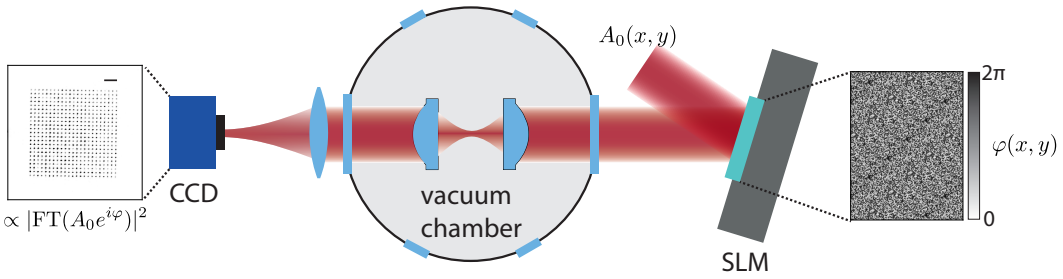

Figure 2.2: Generation of trap arrays. A phase $\varphi(x, y)$ is imprinted onto an incoming gaussian laser beam of amplitude $A_0(x, y)$, with help of a spatial-light modulator. Arrays of dipole traps can be created in the focal plane of the aspheric lens, by choosing the right phase pattern on the SLM. We image the intensity distribution in the focal plane of the aspheric lens, using the second asphere, a lens and a CCD camera. The scale bar depicts a distance of 20 µm.

increased loading rate competes with the rate of light-assisted collisions.

2.1.2 Creation of atom arrays using a spatial light modulator

Our experimental setup has the ability to create reconfigurable arrays of microtraps in the focal plane of the aspheric lens, using a spatial light modulator (SLM). This was first implemented in our group in [Nogrette *et al.*, 2014] and is described in the thesis of Henning Labuhn [Labuhn, 2016]. Later, the technique was extended to three-dimensional structures [Barredo *et al.*, 2018], which is reported in detail in the thesis of Sylvain de Leseleuc [de Léséleuc, 2018] and Vincent Lienhard [Lienhard, 2019].

The working principle is illustrated in Figure 2.2a. We imprint a phase $\varphi(x, y)$ onto an incoming gaussian beam of amplitude $A_0(x, y)$. The intensity distribution in the focal plane of the lenses is then given by the square modulus of the 2D-Fourier transform of $A_0 e^{i\varphi}$. With our spatial light modulator — a Hamamatsu X10468-02 SLM with 792×600 pixels and an active area of 12×15.8 mm^2 — we can control the phase of the light, but not its amplitude. Solving the inverse problem of finding the right SLM phase pattern for a given intensity distribution in the focal plane is not trivial, but there are several established iterative algorithms such as the Gerchberg-Saxton (GS) algorithm [Di Leonardo, Ianni, and Ruocco, 2007] that we use on the experiment.

Compared to an amplitude-only modulator, e.g. a digital mirror device (DMD), phase-only modulators have the advantage of using most of the intensity of the

incoming light to generate the arrays of microtraps. Whereas DMDs utilize only around 50% of the light, phase modulators with the GS algorithm are reported to use over 94% of the incoming light to create 100 traps in the focal plane of a lens [Di Leonardo, Ianni, and Ruocco, 2007].

Additional Phases The phase pattern on the SLM includes several contributions beyond the trap pattern calculated by the GS algorithm. First, Hamamatsu supplies a correction pattern that cancels the residual non-flatness of the SLM-chip. Second, we are able to translate the traps in the plane by adding a linear evolution of the phase modulo 2π (blazed grating), or in axial direction by adding a quadratic phase evolution modulo 2π (Fresnel lens). Lastly, the SLM provides us with the opportunity to correct aberrations from optical elements in the path, namely the mirrors, lenses, viewports and aspheric lenses. By measuring and decomposing the aberrations into Zernike-polynomials, we can add an aberration-correcting phase mask on the SLM. It is however non-trivial to measure the aberrations in the focal plane of the aspheric lens, as we only have access to the signal before and after the chamber. In the past, the aberrations were measured after the chamber using a Shack-Hartmann wavefront sensor. When the opposite of the measured phase distortion was added as a phase mask onto the SLM, an increase in trapping frequencies was observed, indicating a reduction in aberrations [Labuhn, 2016]. Similar results can be achieved by manually adjusting the coefficients of the various, low-degree Zernike polynomials using the trap images on the CCD camera.

Intensity Equalization When calculating the phase pattern with the GS algorithm, choosing all target intensities I_t to be equal, the peak intensities of the traps are usually not homogenous, as can be seen in Figure 2.3a. As an example, on our experiment the 23×23 trap array with a spacing of 5 µm, calculated with around 20 iterations of the GS algorithm, has a measured dispersion of trap intensities with a standard deviation of 45%. As previously explained, it is important for all trap depths to be similar to obtain a telegraphic-like trace (see Figure 2.1c) for each trap.

We therefore equalize the trap depths — assuming the same waist for all traps — in a feed-back loop, as illustrated in Figure 2.3b. We start by running the GS algorithm, choosing all target intensities $I_{t,0}$ to be equal. The obtained intensity of each trap I_i is then measured with a CCD camera (see Fig. 2.2a). We can then adjust the target intensities of the GS-algorithm in the next iteration of the feed-back loop. We choose the target intensities of the $k+1$-iteration to be $I_{t,k+1} = w_{k,i} I_{t,k}$ using the weights $w_{i,k} = w_{i,k-1}[\,1 - G(1 - I_i/\overline{I})]^{-1}$, with a gain factor $0 < G \leq 1$, $\overline{I}$ being the average trap intensity.

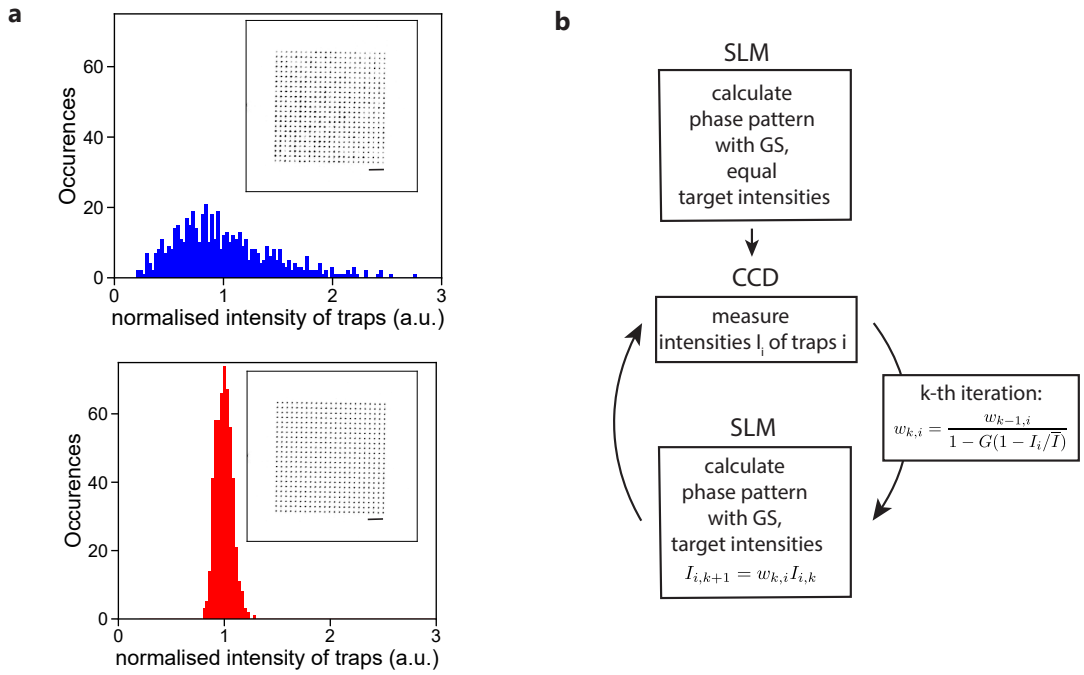

Figure 2.3: Intensity equalization of trap arrays. a: The exemplary intensity distribution of a 23x23 trap array, before and after 15 iterations of intensity equalization. Before, the distribution has a standard deviation of approximately 45%. With more than 400 traps, we typically reach a standard deviation of the mean of approximately 5% after 10-15 iterations. The scale bar depicts a distance of $20\,\mu\mathrm{m}$. **b**: Block diagram of the feedback-algorithm. We measure the intensity I_i of each trap i. This determines the weights w_i which are used for the calculation of the phase pattern in the next iteration.

The procedure is repeated, until a satisfying level of trap uniformity is reached. With 100 traps, we typically reach a standard deviation of the trap intensities of approximately 2% after 5-10 iterations [Labuhn, 2016]. Unfortunately, the intensities of the traps on the CCD-camera differ from the actual intensities in the focal plane of the lenses. This can be caused by aberrations, and will be explained in more detail in Section 2.3.

2.1.3 Defect-free atom arrays

To simulate large-scale condensed matter models on our tweezer platform, defect-free arrays of single atoms are essential. We are able to create arrays of micron-sized tweezers with a spatial light modulator. However, since we isolate single atoms with

light-assisted collisions, each tweezer has only a loading probability of 50% and therefore only half of our microtrap array is filled on average with atoms.

Several groups have shown that with careful engineering of the collision processes, loading probabilities of up to 90% can be achieved [Grünzweig *et al.*, 2010; Lester *et al.*, 2015; Brown *et al.*, 2019; Jenkins *et al.*, 2021]. By using a blue-detuned laser beam, only one atom is on average lost during a collision. However, this depends on the careful adjustment of detuning and trap depth, which is difficult on large-scale arrays, and we found the technique not to be robust on a day-to-day basis.

Furthermore, even with a loading probability of 90%, a defect-free 50-atom array would only be prepared with a probability of less than one percent. This highlights the need of an active sorting method to create large defect-free arrays with a high probability.

In our group, this was first implemented in [Barredo *et al.*, 2016] and is described in detail in the thesis of Vincent Lienhard [Lienhard, 2019] and Sylvain de Léséleuc [de Léséleuc, 2018]. At the same time, similar efforts have been reported in [Endres *et al.*, 2016; Kim *et al.*, 2016]. Later the technique in our group was extended to three dimensions in [Barredo *et al.*, 2018].

The creation of a user-defined N-atom structure, denoted *target array*, with high repetition rate is based on a fast programmable control system, as illustrated in Figure 2.4. Due to the stochastic loading, we usually start with at least $2N$ traps, containing the user-defined *target array* and additional *reservoir atoms*. After an initial fluorescence image of 20 ms, the control system determines the trap occupation, computes the necessary moves of reservoir atoms to target traps, and moves the atoms sequentially with a single moving tweezer. A final fluorescence image then determines the success of the assembly process. The assembly process usually takes less than 100 ms for structures with less than 100 atoms.

Moving Tweezer The fundamental concept of our assembly techniques relies on the transport of atoms between reservoir and target traps in a single moving tweezer. A schematic of the procedure is shown in Figure 2.5. We overlap the moving tweezer with a stationary SLM trap holding an atom, and ramp up the power in the moving tweezer to approximately 10 mK in 400 µs. The atom follows the deep potential of the moving tweezer, that is moved to the position of another empty stationary SLM trap with a velocity of $100\,\mu\mathrm{m\,ms^{-1}}$. Here, the trap power is ramped down to zero in 400 µs.

In [Barredo *et al.*, 2016], two types of moves are presented (see Fig. 2.5 c,d). We consider one move to be one atom being picked up from a reservoir trap by the moving

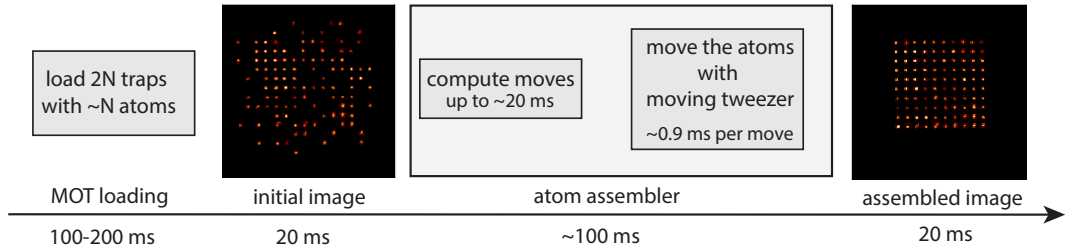

Figure 2.4: Schema of atom assembly. After we load $2N$ traps with on average N atoms, we take an initial fluorescence imaging, to determine the initial occupation of the traps. The assembly algorithm then computes the necessary moves from initial to target traps. Then, the atoms are moved with a moving tweezer. Finally, another fluorescence image is taken to determine the final occupation and success of the assembly process.

tweezer and transferred to an empty target trap. The moving tweezer can either "slalom" between the SLM traps (Fig. 2.5 c), or move along the Bravais lattice defined by the traps (Fig. 2.5 d). Today, only the latter is used, as its efficiency was in general found to be higher. The "slalom" moves lead to non-negligible atom loss, especially when the SLM traps are close.

The moving tweezer is controlled with a 2D-acousto-optical deflector (2D-AOD, DTSXY-400-850 from AA Opto Electronics), as illustrated in Figure 2.5a. A change of radio frequency applied to the AOD, changes the deflection angle which moves the tweezer in the focal plane of the aspheric lens with $5\,\mu\mathrm{m\,MHz}^{-1}$. By changing the RF-power of one of the AODs, we are able to control the amplitude of the moving tweezer. In the design of the optical system, we consider the following points [de Léséleuc, 2018]: First, we conjugate the approximate plane of the AODs with the plane of the aspheric lenses, such that the beam will not clip on the lens for any deflection angle. Second, we choose a slightly bigger waist of $1.3\,\mu\mathrm{m}$ for the moving tweezer, to help with the overlap of stationary traps and moving tweezer. Finally, the moving tweezer covers a range of $180\times180\,\mu\mathrm{m}^2$ in the focal plane of the asphere.

The radiofrequency applied to the 2D-AODs is supplied from voltage controlled oscillators (VCO, Mini circuits POS-150+). The frequency of the VCOs can be tuned with an analog voltage with a bandwidth of 100 kHz, setting an upper limit for the velocity of the moving tweezer. We tune the radiofrequency amplitude using a fast (500 MHz bandwidth) mixer after the VCO (see explanation below). The analog voltage to control both amplitude and frequency is supplied via two computer-controlled Arduino Due. The time resolution of the Arduino is $4\,\mu\mathrm{s}$.

Another possibility to control the 2D-AODs is driving them with an arbitrary wave-

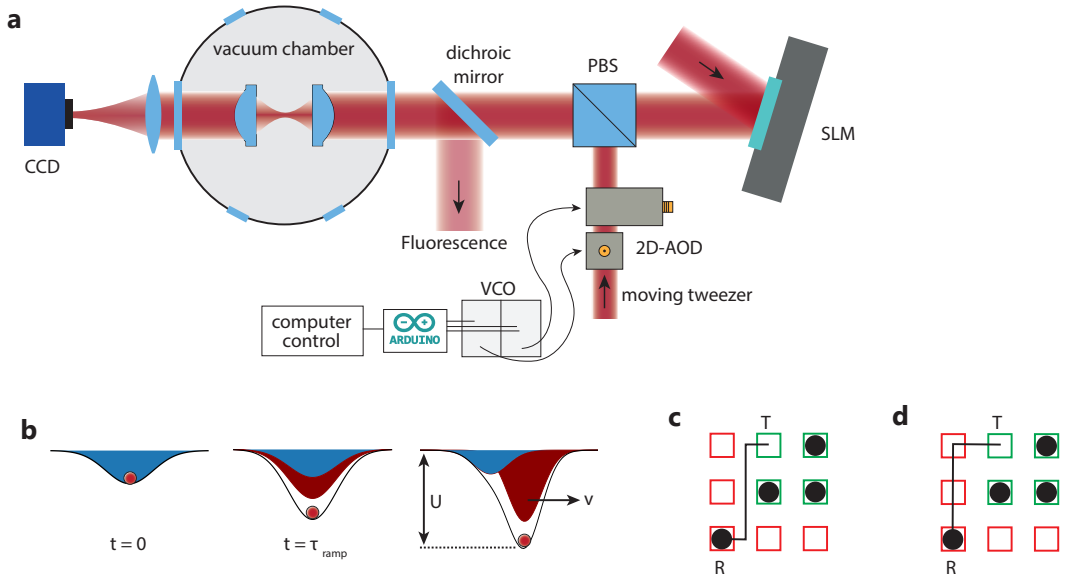

Figure 2.5: Assembly of defect-free arrays of atoms a: A stationary trap pattern is produced with the SLM. With a polarized beam splitter (PBS), we combine the trap beam with a moving tweezer that is deflected by a 2D-acousto-optical deflector. The positions of the moving tweezer with respect to the SLM traps is controlled with the 2D-AODs after being calibrated using a CCD-camera after the chamber. **b**: Illustration of the moving tweezer. At the position of a reservoir trap (blue), the power of the moving tweezer (red) is ramped up to approximately $U = 10\,\mathrm{mK}$ in $\tau_{\mathrm{ramp}} = 400\,\mu\mathrm{s}$, before the tweezer beam is moved with a speed $v = 100\,\mu\mathrm{m\,ms^{-1}}$. At the position of the target trap, the power in the moving tweezer is reduced to zero in another $400\,\mu\mathrm{s}$. **c,d**: Illustration of the two different types of moves.

form generator (AWG). However, since single moves are relatively long (approximately 1 ms) compared to the period of the RF signal at the center frequency of the AODs (approximately 10 ns), sampling the waveforms for the moves poses experimental challenges in terms of data memory and transfer speed. Using VCOs and Arduino Dues therefore is a much simpler and cheaper solution, as it allows to send comparably low-frequency signals that have been calculated on-the-fly.

For the assembly to work with high efficiency, it is crucial to ensure the perfect overlap of moving tweezer and stationary SLM traps. For the calibration of this overlap, we utilize a CCD camera after the vacuum chamber (see Fig. 2.5a). First, we record the positions of the SLM traps on the camera. Then, we scan the moving tweezer across the camera, recording its position for a set of RF frequencies, or analog voltages supplied by the Arduinos. Using interpolating functions, we can then map

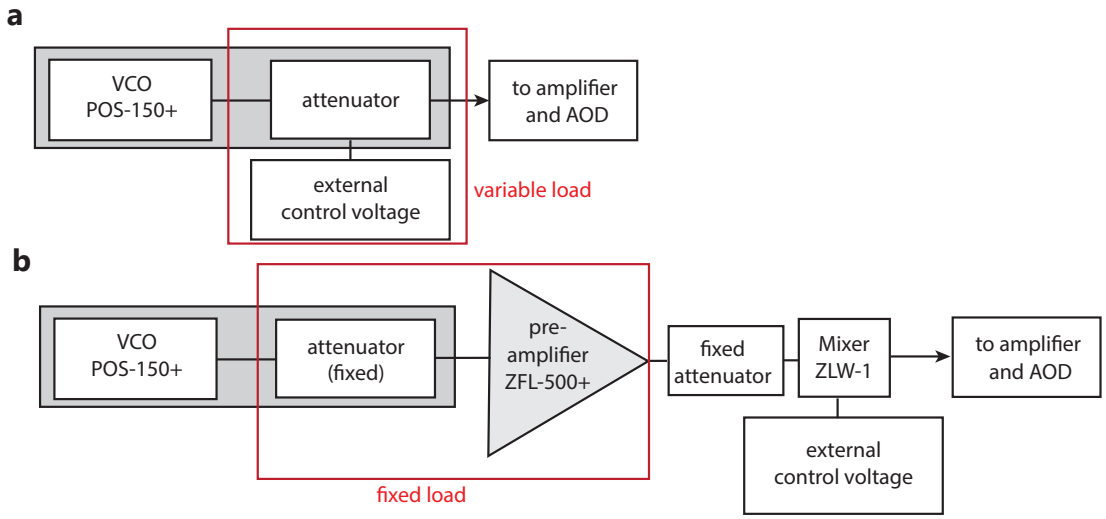

Figure 2.6: Change of RF control. a: Before, a RF-driver (grey box), built at the institute, consisting of a voltage controlled oscillator and a variable attenuator, was directly connected to an amplifier driving the AOD. When changing the RF power with the attenuator, back reflections due to a change in the load changed the VCO frequency by approximately $100\,\mathrm{kHz}$ (corresponding to $0.5\,\mu\mathrm{m}$ in the plane of the atoms). **b:** With the addition of a preamplifier with sufficient isolation (ZFL-500+ has an isolation of approximately 13 dB), load changes on the attenuator/mixer do not lead to significant back reflections into the VCO. The frequency pulling is now lower than $1\,\mathrm{kHz}$.

any position in the plane of the aspheric lens to an analog voltage of the Arduinos controlling the AODs.

During my PhD, I changed the radio frequency control of the AODs, as illustrated in Figure 2.6, leading to a better calibration and overlap of moving tweezer beam with the stationary SLM traps. The position and trap depth of the moving tweezer is controlled via VCOs which suffer from *frequency pulling* when their load changes. Because an impedance mismatch leads to back reflections into the device, its frequency changes when the load or attenuation after the VCO changes. In our experiment, this manifested in a change of RF frequency of approximately $100\,\mathrm{kHz}$, when the RF amplitude was changed from minimum to maximum power. For the moving tweezer, this corresponded to a change in position of $0.5\,\mu\mathrm{m}$ while the trap depth was ramped from zero to $10\,\mathrm{mK}$.

A solution to the problem is illustrated in Figure 2.6b. By fixing the attenuation inside the VCO driver box, and attaching a fixed-gain pre-amplifier (Mini Circuits

ZFL-500+, gain 25 dB, directivity 38 dB), the VCO is sufficiently isolated from the load changes of the attenuator/mixer (Mini Circuits ZLW-1). As a result, the frequency pulling effect is negligible and the overlap of moving tweezer and SLM trap is independent of the amplitude of the moving tweezer.

Shortest-move-first algorithm As illustrated in Figure 2.4, the atom assembly occurs on a relatively short time scale of up to 100 ms, ensuring high repetition rates of the experiment. This requires an algorithm which computes the moves from reservoir atoms to target traps in up to a few tens of milliseconds, while finding a minimal number of moves. As we will see in Chapter 3, finding the optimal set of moves, e.g. the set of moves that minimizes the assembly time, is an intractable problem as soon as we need to move more than a few tens of atoms, and therefore cannot be computed on experimental time scales.

The algorithm described in [Barredo *et al.*, 2016] is a heuristic method aiming to minimize the travelled distance of the moving tweezer. While not finding the minimal distance, its computation time is relatively short and scales as $O(N^2)$ with the number of atoms. In a first step, we compute a matrix of distances $D = d_{i,j}$ between each reservoir atom s_i and empty target trap t_j. On average there are $N/2$ reservoir and empty target traps. The entries of this matrix are ordered by increasing length after which the first $N/2$ elements are chosen, with the condition that it is only one element per row or column (meaning each atom or target trap is only assigned once). This first assignment is however not collision-free: Since we move along the lattice given by the SLM traps, it is possible that filled target traps lie in between the reservoir atom s_i and the target trap t_i. To avoid collisions, the assignment has therefore to be post-processed for these obstacle atoms O, by splitting these paths $[S \to T]$ into $[O \to T]$ and $[S \to O]$. While the post-processing does not change the travelled distance, it increases the number of total moves. The short-comings of this algorithm, mainly the large overhead of moves in certain geometries, are described in Section 2.3.

2.2 Quantum simulation with Rydberg atoms

To study large-scale spin-Hamiltonians on our setup, our group leverages the unique properties of Rydberg states to engineer spin-spin interactions. After we create defect-free atom arrays with a typical inter-atomic distance of a few micrometers, sizeable interactions are made possible by exciting the atoms to Rydberg states with a principal quantum number of above approximately 50. In a classical picture, these

Rydberg atoms have a strong dipole moment, that interact over large distances via the dipole-dipole interaction:

$$V_{\mathrm{dd}} = \frac{1}{4\pi\epsilon_0} \frac{\boldsymbol{d_1} \cdot \boldsymbol{d_2} - 3(\boldsymbol{d_1} \cdot \hat{\boldsymbol{r}})(\boldsymbol{d_2} \cdot \hat{\boldsymbol{r}})}{R^3}, \tag{2.1}$$

with $\boldsymbol{d}$ being the dipole operator, and R the distance between the two atoms.

The interaction between two Rydberg-atoms can be as large as tens of MHz for distances of 10 µm, whereas their lifetime is on the order of several hundreds of µs. Even though the Rydberg lifetime is finite, quantum simulation experiments are possible as the observed dynamics is on much shorter timescales than decoherence effects because of the finite lifetime of the states.

In the following section, the encoding of spin qubits with our Rydberg simulator is demonstrated with two examples. A detailed analysis of experiments can be found in the thesis of Sylvain de Léséleuc [de Léséleuc, 2018] and Vincent Lienhard [Lienhard, 2019], and furthermore in the review [Browaeys and Lahaye, 2020]. Then, the experimental realization of the Rydberg excitation is briefly described with emphasis on the new setup that we constructed during the time of my PhD. A detailed description of the new setup, including a quantitative comparison with the old excitation scheme, is found in the thesis of Pascal Scholl [Scholl, 2021].

2.2.1 Implementation of different spin-Hamiltonians

Spin-Hamiltonians are primarily used as a microscopic description of magnetic materials. The simplest models consider spin-1/2 particles localized on lattice sites, with observables being represented by the Pauli-matrices $(\sigma_x, \sigma_y, \sigma_z)$. The fully isotropic Heisenberg model can be written as $H = \sum_{i,j} J_{ij} \boldsymbol{\sigma}_i \cdot \boldsymbol{\sigma}_j$ and is used to describe (anti-)ferromagnets. However, most real-life materials are anisotropic and can be described by the generalized XXZ-Hamiltonian: $H = \sum_{i,j} J_{ij}(\sigma_i^x \sigma_j^x + \sigma_i^y \sigma_j^y) + J_{ij}^z \sigma_i^z \sigma_j^z$, where the coupling constant in two directions is equal ($J^x = J^y = J$) and differs in the third direction ($J^z \neq J$). Rydberg simulators naturally implement the two extremes of the XXZ-Hamiltonian, where spins interact in a plane, described by the planar XY-Hamiltonian $H = \sum_{i,j} J_{ij}(\sigma_i^x \sigma_j^x + \sigma_i^y \sigma_j^y)$, or out of plane, described by the uni-axial Ising-Hamiltonian $H = \sum_{i,j} J_{i,j}^z \sigma_i^z \sigma_j^z$.

Ising-Hamiltonian Our Rydberg simulator naturally implements an Ising-like Hamiltonian with effective transverse and longitudinal fields, if the spin-qubit is

encoded in ground- ($|g\rangle = |\downarrow\rangle$) and Rybderg state ($|r\rangle = |\uparrow\rangle$). Two Rydberg states in the *same* state ($|rr\rangle$) experience an energy shift due to the dipole interaction V_{dd}. Because of the odd parity of the interactions, there is no first-order perturbation term. However, to second-order, the pair-state is shifted by an energy scaling with $V_{ij} \propto 1/R_{ij}^6$, also called van der Waals interaction. Finally, as the two spin states are coupled via a coherent laser-field with Rabi-frequency Ω and detuning δ, we can write:

$$H = \frac{\hbar\Omega}{2}\sum_i \sigma_i^x - \hbar\delta\sum_i n_i + \sum_{i<j} V_{ij} n_i n_j, \text{ with } V_{i,j} = \frac{C_6}{R^6}. \tag{2.2}$$

Here, $n_i = (\sigma_i^z + 1)/2$ is unity for a Rydberg atom and zero otherwise.

The Ising-Hamiltonian has been extensively studied, both theoretically and experimentally across different platforms, and there are still open questions today. On Rydberg simulators, this type of Hamiltonian has been investigated in 1D [Bernien *et al.*, 2017; Omran *et al.*, 2019], in 2D [Labuhn *et al.*, 2016; Lienhard *et al.*, 2018; Scholl *et al.*, 2021a; Ebadi *et al.*, 2021] and in 3D [Kim *et al.*, 2020]. Especially interesting on tweezer platforms is the ability to explore different lattice geometries, change the interparticle distance and the interaction strengths, as the model offers a variety of different phases and phase diagrams to explore (e.g. [Samajdar *et al.*, 2020]). The phase diagrams can be explored by sweeping parameters quasi-adiabatically, e.g., to try to prepare the ground-state of the system. Furthermore, out-of-equilibrium dynamics of the system can be probed by changing parameters non-adiabatically, e.g., in a quench.

XY-Hamiltonian Another Hamiltonian that can be naturally implemented on our setup is the XY-Hamiltonian. To do so, the spin-qubit is encoded in two different Rydberg states $|nS\rangle = |\downarrow\rangle$ and $|nP\rangle = |\uparrow\rangle$. The dipole-couping gives rise to an interaction potential that scales as $V_{i,j} \propto 1/R_{i,j}^3$ and leads to an exchange of internal state, or "flip-flop" interaction. Using a microwave field with Rabi-frequency Ω and detuning δ, the two states can be coupled with each other and we can write:

$$H = \frac{\hbar\Omega}{2}\sum_i \sigma_i^x - \frac{\hbar\delta}{2}\sum_i \sigma_i^z + \sum_{i<j} \frac{C_3}{R^3}(\sigma_i^+\sigma_j^- + \sigma_i^-\sigma_j^+) \tag{2.3}$$

Here, $\sigma^- = |\downarrow\rangle_i \langle\uparrow|_j$ and $\sigma^+ = |\uparrow\rangle_i \langle\downarrow|_j$ are lowering and raising spin operators. Note that $\sigma_i^+\sigma_j^- + \sigma_i^-\sigma_j^+ = \frac{1}{2}(\sigma_i^x\sigma_j^x + \sigma_i^y\sigma_j^y)$.

This model is equivalent to a hard-core boson hopping Hamiltonian, in which $|\uparrow\rangle = |1\rangle$ corresponds to a particle and $|\downarrow\rangle = |0\rangle$ to an empty site. In this way, the model can be used to describe transport phenomena, in which an excitation can hop

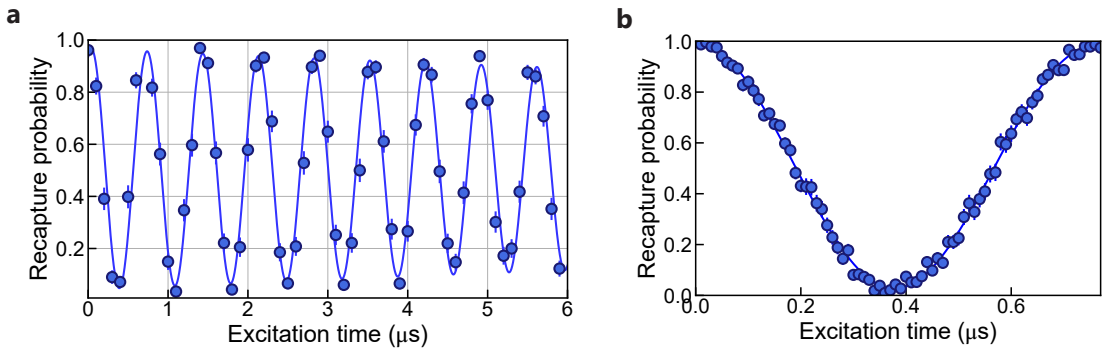

Figure 2.7: Ground state-Rydberg Rabi Oscillation a: Rabi oscillation between the ground state and the $|75S_{1/2}, m_j = 1/2\rangle$ state. **b**: Zoom of the first period with a contrast of approximately 97%. A detailed analysis of contrast and decoherence effects is found in the thesis of Pascal Scholl[Scholl, 2021].

from site to site, or a particle can tunnel between neighboring sites of a lattice. This was implemented on our setup to investigate the Su, Schrieffer and Heeger (SSH) model [de Léséleuc *et al.*, 2019], one of the simplest condensed-matter models displaying topological properties.

2.2.2 Rydberg excitation scheme

To excite ^{87}Rb atoms from the ground to a Rydberg state, we make use of a two-photon transition, since a one-photon transition requires a coherent laser source in the deep UV (<300 nm), which are not readily commercially available. In our scheme, we use a laser at 420 nm to couple the ground state to an intermediate level $|6P_{3/2}\rangle$, and a second laser at 1013 nm coupling the intermediate state to a Rydberg state. The two laser beams are counter propagating along direction of the magnetic field. We can excite $|nS_{1/2}\rangle$ and $|nD_{3/2}\rangle$ Rydberg states. A typical Rabi oscillation between ground- and $|75S_{1/2}, m_j = 1/2\rangle$ is shown in Fig. 2.7.

A new scheme We changed the Rydberg excitation scheme during the time of my PhD. Before, the group was using the intermediate level $|5P_{1/2}\rangle$ and diode lasers. After a careful analysis of the imperfections of the scheme [de Léséleuc *et al.*, 2018], and an experimental demonstration of the scheme using the $|6P_{3/2}\rangle$ intermediate state [Levine *et al.*, 2018], the group decided to change both the laser technology and the intermediate level.

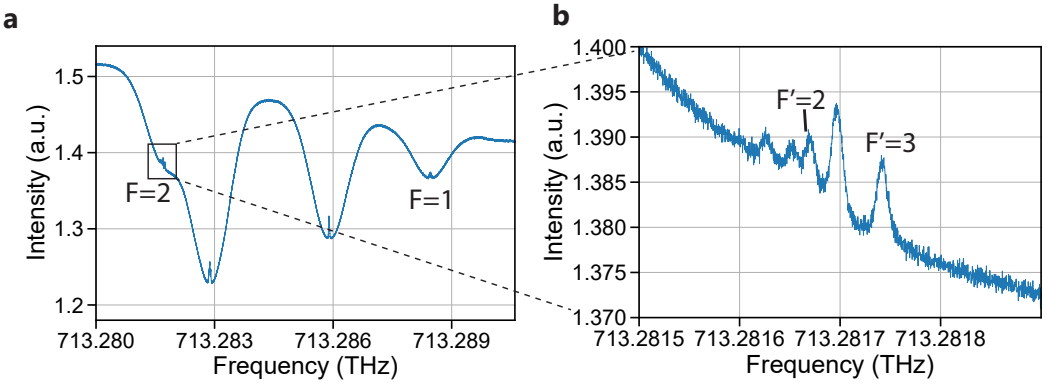

Figure 2.8: Doppler-free spectroscopy of $6P_{3/2}$ level a: Spectrum, including ^{87}Rb and ^{85}Rb lines. Highlighted are the ^{87}Rb $|F = 2\rangle \rightarrow |F'\rangle$ and the $|F = 1\rangle \rightarrow |F'\rangle$ line. **b**: Zoom on the lines relevant for Rydberg excitation. Because of our σ^+-light, we utilize the stretched transition $|F = 2\rangle \rightarrow |F' = 3\rangle$ for the excitation.

The improvements by changing the intermediate level is two-fold. First, with $\tau_{6P_{3/2}} = 113$ ns, the lifetime of the intermediate state is approximately a factor four higher compared to the one of $5P_{1/2}$, reducing decoherence effects from spontaneous emission. Second, to couple the intermediate state to a Rydberg level, where the dipole matrix element is much weaker, we use an infrared laser source, where more laser power is commercially available, e.g., by using a fiber amplifier.

We further changed the laser technology from diode to titanium sapphire lasers to generate the 1013 nm light, and 840 nm light, which is doubled with a BBO-crystal in a cavity. This produces inherently less phase noise compared to a diode laser. Phase noise, especially at a Fourier frequency of approximately 1 MHz is an important source of decoherence for our system, as described in detail in the thesis of Sylvain de Léséleuc [de Léséleuc, 2018].

To probe the new intermediate level with the new titanium sapphire laser, we first set up a Doppler-free spectroscopy, as seen in Figure 2.8. The frequency calibration was done with our wavemeter (High Finesse,WLM SU10) and are consistent with [Glaser *et al.*, 2020].

Layout of the setup The layout of the setup is illustrated in Figure 2.9. The 420 nm laser passes through an EOM, enabling fast switching times of approximately 10 ns and a double-pass AOM to enable temporal shaping of frequency and amplitude during a pulse. The beam arrives with up to 350 mW on the main optical table via a fiber and is focused to a $1/e^2$ waist of $w_{420} = 250\,\mu$m. The 1013 nm laser seeds a

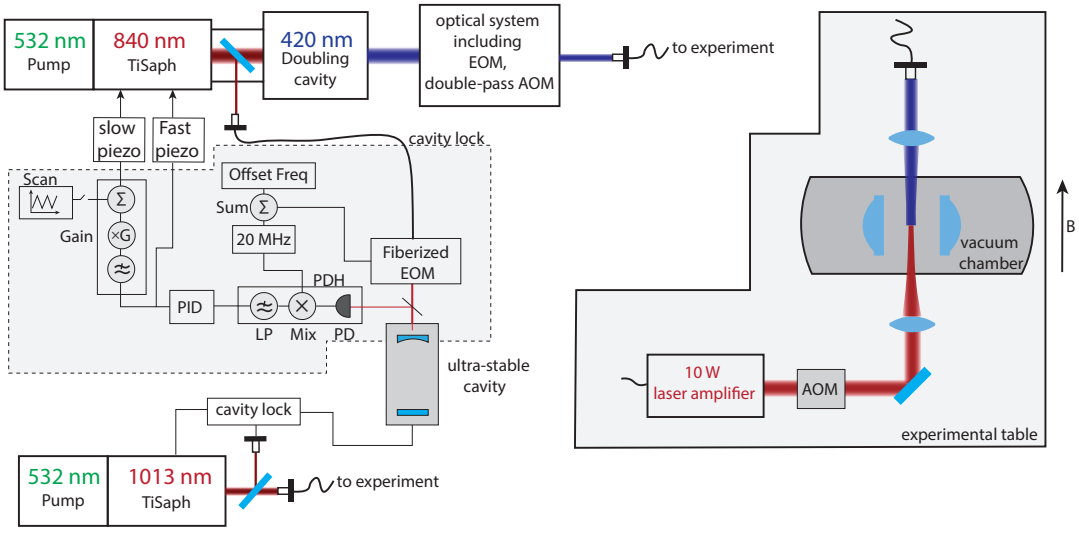

Figure 2.9: Layout of the laser system. The 420 nm light is generated from a frequency-doubled 840 nm titanium sapphire laser. After an AOM and EOM to be able to switch off/on and sweep amplitude and frequency, the light is transferred to the experimental table via a fiber, and up to 350 mW are focused in the vacuum chamber to a waist of 250 µm. The 1013 nm titanium sapphire laser is injected in a 10W laser amplifier, and focused in the vacuum chamber to a waist of 130 µm. Both lasers are frequency stabilized with a PDH-lock to an ultra-stable cavity. A scheme of the locking electronics is shown, where Mix = Mixer, PD = photodiode, LP = lowpass-filter. Whereas the output of the PID is connected to the fast piezo of the titanium saphire laser, an integrated signal is connected to the slow piezo, cancelling slow thermal drifts. Furthermore, the slow piezo is used for scanning the frequency when locking. See text for more detail.

10 W laser amplifier (AzurLight) on the main optical table, after which the setup is free-space. It passes through an AOM, to switch the laser beam, before being focused to a waist of $w_{1013} = 130\,\mu\text{m}$ in the plane of the atoms.

Frequency stabilization A small portion of the light of both the 840 nm and the 1013 nm titanium sapphire lasers are picked up and used to lock them to a ultra-stable laser cavity (with a finesse of $\mathcal{F} = 20000$, by Stable Laser Systems) using the Pound-Drever-Hall (PDH) technique. I built the cavity system similarly to the previous system described in [Ravets, 2014], however, it includes two major changes, highlighted in Figure 2.9: First, I simplified the system by using only one fiberized electro-optical modulator (EOM) to scan the frequency *and* create the sidebands for the PDH lock, where previously this was done with two separate EOMs. This is done by combining the 20 MHz PDH RF signal with a variable RF signal, used to

scan the frequency in experiments, using a power combiner. Second, changing the wavelength of a titanium saphire laser works differently compared to the previously used diode lasers, which required new locking electronics. The used M2 SolsTIS has two intracavity piezos for feedback stabilization of the laser frequency. The first one has a large range ($\pm 15\,\mathrm{GHz}$, $1.5\,\mathrm{GHz\,V^{-1}}$ sensitivity) and can therefore be used to scan the cavity across several free spectral ranges of the ultra-stable cavity (1.5 GHz) which is useful for finding the PDH signal. However, it is comparably slow (up to 50 Hz) and therefore is not used to lock the laser. This is done with the fast piezo (first resonance at 105 kHz). Unfortunately, the range of the fast piezo ($\pm 40\,\mathrm{MHz}$, $4\,\mathrm{MHz\,V^{-1}}$ sensitivity) is smaller than the slow thermal drift of the laser over one hour. Therefore, I implemented feedback electronics with an inner fast servo loop with the fast piezo, and an outer slow loop, using the slow piezo. This enables the system to follow slow thermal drifts which are larger than the range of the fast piezo. The inner loop uses a PID controller that acts on the PDH error signal with the fast piezo. The outer loop, uses the output of the PID controller as error signal and counteracts slow drifts with the slow piezo. This ensures that the output of the PID controller is centered around zero, and the fast piezo always stays centered.

Note that newer versions of the SolsTIS include an intra-cavity EOM that make fast feedback up to 10 MHz possible. Using this system, laser linewidths of approximately 200 Hz have been reported [Graham *et al.*, 2021].

Detection of a Rydberg atom To excite the atoms to the Rydberg states, the optical dipole traps are switched off and the atoms are in free-flight. After having performed a quantum simulation experiment, the dipole traps are switched on again. Only ground-state atoms will be recaptured, as atoms being in the Rydberg state at that point will be ejected from the trap volume due to the ponderomotive force that the weakly-bound electron is experiencing in the oscillating electromagnetic field. For the previously described case of the XY-model, where the spin qubit is encoded in two different Rydberg states, we de-excite one of the Rydberg states to the ground-state before switching on the dipole traps.

2.3 Limitation of current room-temperature setup

Many quantum simulation experiments have been performed with the current room-temperature setup, highlighting the capabilities of Rydberg platforms as analog quantum simulators. However, the total number of particles involved in experiments before the start of my PhD was up to 60 atoms. Due to improvements on the setup (see

Chapter 3), we were able to perform a quantum simulation of the Ising model with up to 200 particles. Even though this was already in a regime, where matrix-product-state simulations of our theory colleagues were taking several weeks to perform with the appropriate bond-dimensions, it is desirable to increase the atom number even further, as especially in two and three dimensions, the increased number of atoms on the boundaries can modify the dynamics of the system drastically. However, on the experimental side it is not a simple task to increase the atom number. The limitations of our current room-temperature setup with respect to increasing the atom number are detailed in the following section.

2.3.1 Number of atoms and lifetime

The first strong limitation for scaling up the number of atoms is the vacuum-limited lifetime of single atoms in the tweezers. Hot molecules from the background gas collide with atoms in the tweezer, leading to an exponential decay of the survival probability with time. The pressure in our room-temperature setup is approximately 10^{-11} mbar, and the measured lifetime is τ_{vac}= 19.8(7) s (see Fig. 2.10a). Even though this timescale seems long compared to the time of a single experiment, it is a major limitation if an ensemble of N atoms is involved, as the lifetime of the whole ensemble is $\tau_{\mathrm{N}} = \tau_{\mathrm{vac}}/N$. With increasing N, the overall lifetime is therefore quickly reduced to experimental timescales of a few hundreds of milliseconds, and is therefore a dominating contributor to atom loss.

As an example, in Fig. 2.10b, the ensemble vacuum lifetime is compared to the time needed to rearrange a N-atom staggered array. As one move takes about 0.9 ms, and on average $N/2$ atoms are not in their target positions, a lower bound on the time to assemble a staggered array can be estimated with $t_{\mathrm{Assembly}} = 50 + 0.9N/2$ (ms), with 50 ms an assumed fixed time for the programs to transfer the image, analyse it and compute the moves.

The two curves intersect, when the assembly time equals the ensemble vacuum lifetime. At this atom number, background gas collisions limit the fidelity of the assembly drastically, and a defect-free shot can only be assembled with a probability of $1/e = 37\%$.

Reducing the assembly time is challenging, as the linear scaling with the atom number is inherent to the problem. The ensemble lifetime on our room-temperature setup for 1000 atoms is 20 ms, which comparable to many experimental timescales, as for example fluorescence images are taken with an exposure time of 20 ms on our

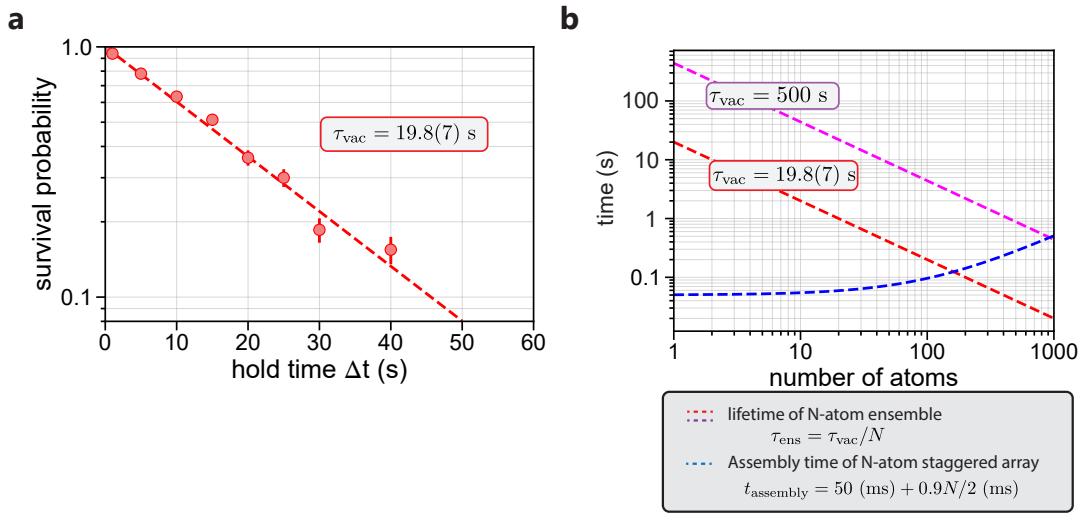

Figure 2.10: Lifetime of room-temperature setup a: Measurement of the vacuum lifetime τ_{vac} **b**: Comparison of the N-atom lifetime and another experimental timescale, the assembly time of a N-atom staggered array.

experiment.

Figure 2.10b illustrates, that the vacuum lifetime needs to be increased by at least a factor 25 to be able to assemble arrays of 1000 atoms with our method. Decreasing the background pressure further on our room-temperature experiment is not simple though, as we are already using standard ultra-high vacuum methods, with copper gaskets, ion pumps and baking out procedures. This motivates the construction of a novel cryogenic tweezer platform, since cryogenic experiments can reach the needed pressure regimes of below 10^{-14} mbar.

2.3.2 Assembly of defect-free atom arrays

Even if a cryogenic environment can mitigate the limiting effect of the vacuum lifetime on the scalability of tweezer platforms, improving the assembly process is beneficial to obtain large defect-free atom arrays. First, a speed-up of the assembly process would lead to higher repetition rates of the experiment. This is desirable on our room-temperature setup due to the limited vacuum lifetime, but also on the cryogenic platform, as it would enable to take a certain amount of statistics in a shorter amount of time. Second, a reduction in the number of moves to assemble an array would lead to a higher success probability, as the probability to move an atom between to traps has a high, yet finite success probability. This single-move success probability is 0.993(1)

for a small array of 10 µm extend [Barredo *et al.*, 2016], but can be significantly lower for arrays with an extend on the order of 100 µm as we shall see in Chapter 3.

Different Assembly schemes First, I give a short review on different existing assembly techniques and compare them to our method:

At KAIST in Korea, the group of Jaewook Ahn uses a spatial light modulator to create reconfigurable arrays of microtraps in multiple dimensions, similar to our group. In contrast, they assemble defect-free arrays by changing the phase pattern on the SLM during each experimental cycle, moving all atoms at once to their target positions. The phase pattern is recalculated with a repetition rate of up to 60 Hz, and using multiple rearrangement cycles, they are able to assemble arrays with up to 30 atoms with a lifetime limited single atom loading efficiency of 0.98 after approximately 9 cycles [Kim *et al.*, 2016]. The feedback cycles are performed with a repetition rate of 0.5 Hz, therefore considerably slower than the method used in our group. Further, we typically reach a single atom loading efficiency of above 0.98 after only two rearrangement cycles, indicating that our experimental imperfections are smaller.

At Harvard, the group of Mikhail Lukin further developed the one-dimensional assembler of [Endres *et al.*, 2016], by combining it with a spatial light modulator. Similar to our group, they combine a 2D-AOD with an SLM. However, they are able to control multiple tweezers at the same time. Moving multiple atoms at a time, and decreasing the ramp-times of the tweezer to 15 µs, they are able to increase the speed of the atom assembly [Ebadi *et al.*, 2021]. Taking less time for the rearrangement, they increase the average filling fraction to 98.5% for one, and 99.2% for two rearrangement cycles, even if the single-move success probability is the same as in our experiment.

Although the second method seems to have a small advantage compared to ours due to its increased speed, the use of multiple tweezers at the same time is limited to regular geometries. Due to changes I have conducted during my PhD, our assembler can also assemble completely arbitrary geometries, as I describe in detail in 3. Furthermore, we conducted algorithmic changes, increasing the efficiency of our assembly scheme.

Limitations of our scheme In our assembly process, the dominating time scale is ramping up and down the intensity of the moving tweezer (see Fig.2.5b). Further, every move has a finite success probability. Therefore, reducing the total number of moves would reduce the assembly time and increase its success probability. The previously described shortest-move-first algorithm however aims only to reduce the total path length of the moving tweezer. Figure 2.11a illustrates a situation in which the

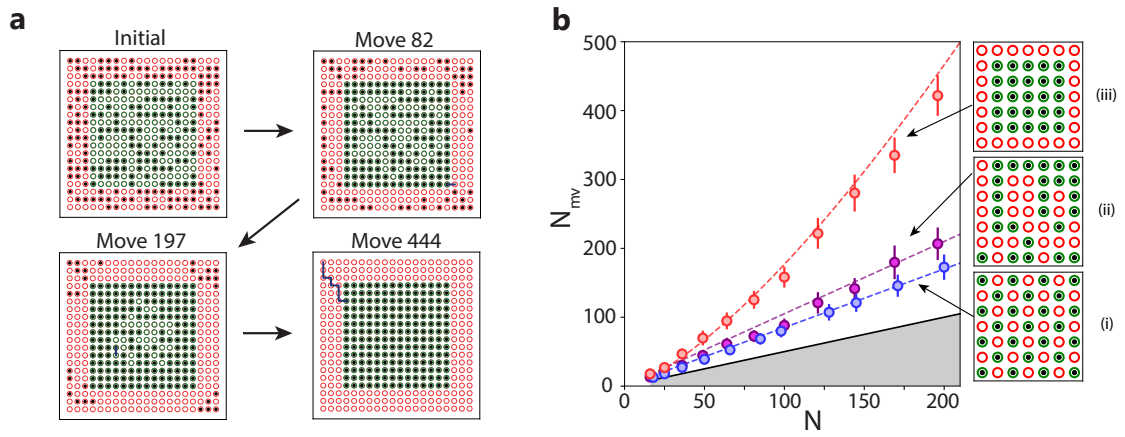

Figure 2.11: Shortcoming of the Shortest-Move-first algorithm. a: Snapshots during the assembly process of a 14x14 array. The macroscopic behaviour reveals that the shortest-move-first algorithm starts by filling the border of the target array (green) with close-by reservoir atoms (red), before the center of the array is filled (e.g. Move 82). These atoms are later obstacles for the last reservoir atoms that are supposed to fill the center (e.g. move 197), leading to a large over-head of moves. **b**: Scaling of the number of moves N_{mv} with the target array size N for staggered (i), random (i) and compact (iii) target arrays. The black line and grey area indicate the ideal minimum number of moves, as on average $N/2$ target traps are empty and need to be filled. While the scaling is especially detrimental in the case of compact arrays due to the reason highlighted in (a), it is also non-ideal for staggered and random target arrays.

shortest-move-first algorithm is leading to a much higher than ideal number of moves. For compact arrays, in which all reservoir atoms lie outside of the target structure, the algorithm tends to fills the target array from the outside to the inside, since the shortest moves are the ones from reservoir atoms in proximity to empty target traps on the border of the array. This however produces a large overhead, since the atoms on the border are obstacles to atoms that are supposed to be moved to the center at a later stage of the process. Figure 2.11b shows the scaling of the algorithm with the number of atoms in the target array. For compact square arrays, the number of moves scales non-lineary as $N_{\mathrm{mv}}^{\mathrm{compact}} = 0.28N^{1.4}$, which can be qualitatively understood, as a significant number of atoms $\propto N$ need to be moved multiple times (about $\sqrt{N}$ times which is the linear dimension of the array). For random arrays the number of moves scales as $N_{\mathrm{mv}}^{\mathrm{compact}} = 1.05N$ and for staggered arrays as $N_{\mathrm{mv}}^{\mathrm{compact}} = 0.85N$. The algorithms described in Chapter 3 improve all of these scalings, but most drastically for compact arrays, where a linear scaling with at most N moves is possible.

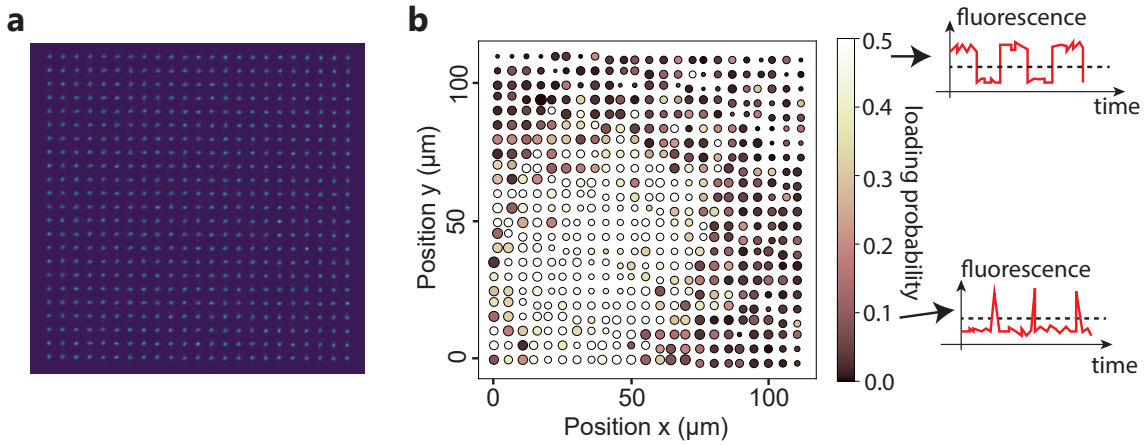

Figure 2.12: Field-of-view and compensated Aberrations a: Intensity equalized trap array of 23×23 atoms, spaced by $5\,\mu\mathrm{m}$. The intensities have a standard deviation of 5% **b**: *in-situ* characterization of the fluorescence signal of the same trap array as in (a). The color represents the loading probability of the trap, 0.5 corresponding to the signal being 50% of the time above treshold and 50% below treshold. Darker traps with less loading have in general less peak intensity. Further, the size of the circles signifies the difference in fluorescence counts between the two levels of the telegraphic signal. If there is too much power in the trap, the step gets smaller due to the induced light-shift. It is evident, that the intensities are not as equal as the image on the CCD camera. Using the intensity equalization method, we achieve a 50% loading probability only (approximately) inside of the field-of-view of the lens.

2.3.3 Limited field-of-view of the aspheric lenses

As previously described, a lens design by Lucas Béguin [Béguin, 2013] was used on our room-temperature quantum simulator CHADOQ. The use of aspheric lenses is a great simplification compared to the microscope objective inside of the vacuum chamber in MIGOU, and the use of the ITO coating on the lenses a clear advantage for Rydberg physics.

A drawback of aspheric lenses however is their limited field of view in comparison to a microscope objective. The performance of an optical system is usually characterised with the Strehl ratio $S = I_{\mathrm{aberr}}/I_{\mathrm{stig}}$ that measures the ratio of peak intensity in the presence of aberrations (I_{aberr}) compared to a perfectly stigmatic optical system (I_{stig}). Off-axis, this ratio decreases due to aberrations and in general $S \geq 0.8$ is quoted for diffraction-limited performance [Sortais *et al.*, 2007].

In ASPHERIX [Sortais *et al.*, 2007], the used lens has a Strehl-ratio of $S \geq 0.8$

for transverse fields of $\pm 25\,\mu m$. On CHADOQ [Béguin, 2013], it was measured that $S \geq 0.8$ for transverse fields of up to approximately $\pm 45\,\mu m$. The reduction in off-axis intensity at the border of the array is not a major concern for trapping atoms, as we can in principle adjust the trap depths with the SLM. However, it reduces the amount of fluorescence photons and aberrations additionally lead to deformation of the trap shape, increasing the size of the waist which in the worst case can slow the light-assisted collision dynamics and increase the probability to trap multiple atoms per tweezer.

Experiments have shown that we can work with a transverse fields of ± 75-$100\,\mu m$. On the border, this reduces the fluorescence counts approximately by 50%, and the traps, while aberrated, still display the typical telegraphic fluorescence signal. When distancing the traps by $5\,\mu m$ in a square array, this would correspond to about 1300 traps in the field of view of the lens, making approximately 650 atoms the maximum size of defect-free arrays utilizing the current model of aspheric lenses.

A further limitation of the setup is that some types of aberrations, such as coma, are compensated by the symmetry of the two aspheric lenses in f-f configuration. Therefore, the intensity pattern on the CCD camera after the chamber is not a direct indication of the intensities in the focal plane of the lenses (see Fig.2.12), especially outside the FOV of the lenses. As a well-equalized trap array is crucial for the preparation of defect-free arrays, the previous intensity-equalization procedure is not good enough for big arrays and new *in-situ* methods need to be implemented. During my PhD, I implemented such a method, leading to the assembly of up to 200 atoms on our room-temperature setup (see Chapter 3) and further improvements of this method are discussed in Chapter 6 .

2.4 Conclusion

In this chapter, I presented the state-of-the-art Rydberg quantum simulator of our group. First, I described all necessary experimental tools to create defect-free arrays of neutral atoms. I pointed out an improvement of the assembly process that I conducted by changing the RF control for the AODs. Then, I explained the tools to utilize the platform for the quantum simulation of spin-models and highlighted our work on changing the Rydberg excitation scheme. Lastly, I presented several limitations of this setup in terms of increasing the number of atoms involved in quantum simulations.

During my PhD, I worked on lifting these limitations. We built a novel cryogenic setup, described in Chapter 4, with lifetimes long enough not to be limiting for the

assembly of over one thousand atoms. Furthermore, I improved the efficiency of the assembly process, leading to an increase in average filling fraction of target traps from 96% reported in [Barredo *et al.*, 2016] for an 25-atom array, up to 98.5% for a 196-atom array. This contribution is twofold: First, a change in algorithms, reported in Chapter 3, leading to fewer moves, faster calculation times and making multiple rearrangement cycles possible. Second, a new *in-situ* equalization scheme for the trap powers, using the fluorescence signal of the atoms instead of the intensity on the CCD-camera, which is described in Chapters 3 and 6.

Chapter 3

Enhanced Assembly of Atom Arrays

In Chapter 2, I introduced the basic principles of the atom assembly. I also discussed limitations of the current algorithms, which motivated an algorithmic improvement on our setup. This chapter will detail the problem at hand, and present three new algorithms that lead to significant experimental improvements. This work led to a publication and is presented in [Schymik *et al.*, 2020] (see Appendix D). Finally, I will show an application of the algorithms for a quantum simulation project of the Ising model [Scholl *et al.*, 2021a] with up to 200 atoms (see Appendix F).

3.1 Defining the problem - pebble motion on a graph

As introduced in Section 2.1.3, we aim to assemble a *target* structure of N atoms. As the loading probability of each trap is around 50%, we start with at least $2N$ traps,

including the N *target* traps, and at least N *reservoir* traps. In a sequential order, we move atoms with a moving tweezer from reservoir to target traps until all target traps are filled. We are interested in finding an algorithm that computes this sequence of moves, while fulfilling the following two criteria:

1. The time to compute the sequence of moves should not surpass a few tens of milliseconds for a few hundred atoms, as we need to run the algorithm at each repetition of the experiment.

2. The algorithm should find the sequence of moves that maximizes the success probability of the assembly process. Because of the vacuum-limited lifetime (see Chapter 2.3.1), the success probability is strongly dependant on minimizing the total assembly time, consisting of the computation time of the algorithm, the number of moves and the total travelled distance.

3.1.1 Assembly time, travelled distance and number of moves

As presented in Section 2.1.3, ramping the intensity of the moving tweezer power is the dominant timescale during the assembly process on our experiment, as it takes about 400 µs, whereas the atoms are moved at a constant speed of 100 µm ms^{-1}. Moving an atom between two traps with a typical experimental distance of 5 – 10 µm therefore consists in a ramping time of 800 µs, and a moving time of 50 – 100 µs. Minimizing the total assembly time is therefore in most cases similar to minimizing the number of individual moves, and minimizing the total travelled distance plays a minor role. Another reason to find a minimal number of moves arises from the finite success probability of each move, due to a non-perfect transfer between the moving tweezer trap and the stationary SLM traps.

In this section, we will see that finding the minimal number of moves is an intractable problem for larger number of atoms and we have to opt for heuristic algorithms finding a near-optimal solution that can be computed in a few tens of ms.

One exception, where we can find the optimal solution on experimental time scales, is the *slalom* moves that have been briefly introduced in Chapter 2.1.3. If the moving tweezer can move between adjacent rows of static SLM traps, the number of moves is fixed and equal to the number of missing atoms in the target array, on average $N/2$. Furthermore, the moves can be performed in *any order*. In this case the task to minimize the assembly time simplifies: Only the travelled distance remains to be

minimized and this problem amounts to a well-known computer science problem, namely the linear sum assignment problem (LSAP) [Cormen *et al.*, 2001]:

Having a set of *source* atoms S and *target* traps T, together with a weight function $C : S \times T \to \mathbb{R}$, we need to find a bijection $f : S \to T$ that minimizes the cost function $\sum C_{a \in S}(a, f(a))$. In our case, we can explicitly write the weight function as the euclidean distance between source atom s and target atom t, with $C(s_i, t_i) = [(s_{i,x} - t_{i,x})^2 + (s_{i,y} - t_{i,y})^2]^{1/2}$. Although there are $(N/2)!$ possible different assignments in our case, there are well-known algorithms solving this problem in polynomial time ($O(N^3)$)), such as the Hungarian algorithm. On our laboratory computer with *Python 3.6*, the calculation takes approximately 3 ms for $N = 200$. We use a modified Joncker-Volgenant algorithm [Crouse, 2016] with no initialization implemented in the *scipy.optimize* package [Virtanen *et al.*, 2020].

However, on the experiment, we are not using *slalom* moves any more. They have been found to have a considerably smaller success probability when the spacing between static traps is around 5 µm and smaller. Instead, the moving tweezer travels along the lattice formed by the SLM traps. This changes the problem considerably, as atoms may lie on the path between a reservoir and a target trap. If an obstacle atom o is in the path between source atom s and target trap t, we cannot perform the move $[s \to t]$ without a *collision*. We can change the sequence of moves, and first move $[o \to t]$ and then $[s \to o]$. Even though the travelled distance has remained unchanged, we hereby increased the number of moves, increasing the assembly time. Furthermore, it is evident that the *order* of the sequence of moves has become crucial, as $[o \to t]$ has to be performed before $[s \to o]$. As a result, we are no longer able to solve the problem with a bijection $f : S \to T$ and this can no longer be considered as an assignment problem. We therefore need to develop new algorithms.

We simplify the problem of minimizing the assembly time, by only considering to minimize the total number of moves, as it is the dominant time scale on the experiment. Then, it is similar to a well-known problem in computer science: the "pebble-motion problem on a graph" in a variant with unlabeled pebbles. Unfortunately, it is intractable for large N [Călinescu, Dumitrescu, and Pach, 2006] and therefore it is impossible to calculate the optimal number of moves on experimental time scales.

Hence, we opt for heuristic algorithms that find a close-to-optimal solution, given they can be computed in a few tens of milliseconds for a few hundred of target traps. However, the optimal number of moves is not known in general, and highly dependent on the initial atom configuration. Because of possible obstacles, it is in most cases not possible to find a sequence of moves that assembles the target array in $N/2$ moves.

Still, we consider $N/2$ as a lower bound on the optimal number of moves. We will see that for compact arrays an upper bound on the optimal number of moves exists too, as it is always possible to find a sequence of maximally N moves for a compact target structure of N atoms.

3.2 A new algorithmic framework

We have developed a new algorithmic framework for the atom assembly that includes the following changes.

First, we have developed three new algorithms that significantly reduce the total assembly time compared to the shortest-move-first algorithm that was introduced in Chapter 2.1.3. Each of the new algorithms has an advantage in a different situation, e.g. depending on the geometry of the target and reservoir traps:

- The *compression* algorithm (see Section 3.2.1 below) is targeted at compact arrays, in which all reservoir atoms lie outside of the target structure, and has the advantage of a fast computation time that scales favorable with the number of atoms (roughly as $N^{1.2}$).
- The two hybdrid algorithms, denoted LSAP1 and LSAP2 (see Section 3.2.2 below), both working for any target/reservoir geometries. While the LSAP1 computes a smaller number of moves in the case of compact geometries, the LSAP2 algorithm is best for staggered configurations, in which reservoir atoms and target trap positions alternate.

Second, I present a new graph-based approach for the assembly. Using graphs, we extended all algorithms to non-regular structures, e.g. when target and reservoir atoms do not lie on a common Bravais lattice. I further describe a new way to generate reservoir trap positions given a target trap array, and finding lattice edges for non-regular structures along which the moving tweezer can travel.

Third, we include the capability of performing multiple rearrangement cycles to increase the probability of obtaining a defect-free atom array.

3.2.1 Compression algorithm

In Figure 2.11, we saw that the shortest-move algorithm leads to a large overhead in number of moves in the case of compact arrays. Instead of filling the center, the

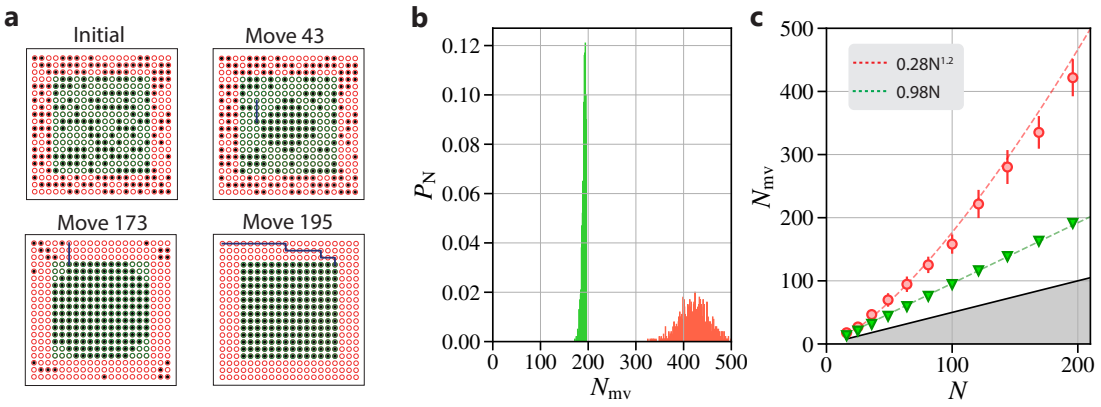

Figure 3.1: The compression algorithm. a A 14×14 target array is assembled in 195 moves. Starting from the center, the traps are filled layer by layer. Each target trap is filled with the closest atom from outside the assembled bulk. **b**: Histogram of the number of moves needed to assemble a 14×14 target array, sampled from 1000 realizations. The shortest-move-first algorithm (red) needs an average of 421 moves, whereas the compression algorithm has a sharp distribution with $N_{\mathrm{mv}} \leq 196$. **c**: Number of moves for the shortest-move-first (red circles) and the compression algorithm (green triangles) for different target array sizes. The black line (grey area) represents $N/2$. Each data point is the average over 1000 randomly loaded realizations, errorbars denote the standard deviation.

algorithm fills the border of the array first. Then, the paths towards the empty center traps are blocked, and additional moves have to be performed to remove these obstacles. As a result, the number of moves required to assemble a compact N atom structure scales non-linearly, with $N_{\mathrm{moves}} \propto N^{1.4}$. In the following, I present a new algorithm that finds a sequence of moves that always fulfills $N_{\mathrm{moves}} \leq N$.

The idea of the *compression* algorithm is to fill the trap array in a predetermined order that naturally avoids collisions. We can start e.g. in the center of the trap array, as it is depicted in Figure 3.1a, and fill it progressively layer by layer until the whole array has been filled. We choose each trap to be filled by the closest trap outside of the already assembled bulk.

As each empty trap is filled with the closest atom from the outside, none of the paths have obstacles. Therefore, the total number of moves is by construction less or equal than the number N of target traps. We have therefore proven that $N/2 \leq N_{\mathrm{moves,min}} \leq N$ for the minimal number of moves to assemble a 50%-loaded N-atom target structure.

The comparison in scaling between the shortest-moves-first and the compression

algorithm is illustrated in Figure 3.1. Taking a 14×14 target structure as an example, the histogram of the number of moves shows the drastic difference between the algorithms. Whereas the shortest-moves-first algorithm has a broad distribution with an average of 421 and a standard deviation of 29 moves, the compression algorithm has a sharp distribution: Over 90% of the realizations require $186 \leq N_{\mathrm{mv}} \leq 196$ moves. For the experiment, the small variance ensures a good shot-to-shot repeatability of the assembly process, especially when compared to the shortest-moves-first algorithm. A further experimental advantage of the sharp distribution is that the maximal number of moves is known, as $N_{\mathrm{mv}} < N$. This is useful, as we fix the time delay between the initial and the assembled fluorescence image on the experimental sequencer for each array. For the shortest-move algorithm, we used to add a buffer of about three standard deviations to the average assembly time to make sure that all initial configurations can be assembled in the given time. This is no longer needed for the compression algorithm. Another advantage is the fast computation time of this algorithm. Because of the predetermined order in which the traps are filled, we can create a look-up table before run-time. The table contains which target traps can be filled from which source traps and is independent of the initial loading. At run-time, the algorithm is left with scanning a one-dimensional list. We found that the computation time of our implementation scales roughly with $N^{1.2}$, and takes about 7 ms for $N = 100$ atoms. Note that our implementation is a simple *Python* program that has not been enhanced, e.g. by using C-extensions, as compared to the LSAP-solver later mentioned in this chapter.

3.2.2 Hybrid algorithms

The compression algorithm shows that it is always possible to find a sequence of at most N moves to assemble a compact N-atom target array. Knowing this, it is interesting to revisit the LSAP algorithm that was mentioned in the case of *slalom* moves. Since the LSAP algorithm finds a bijection between reservoir traps and target atoms, its result contains by definition a matching between N reservoir traps and N target traps.

We previously saw that the order of moves is crucial to avoid collisions, when moving along the lattice sites. The LSAP algorithm however does not return a sequence of moves, but only a unordered matching between traps that minimizes a cost function, e.g. the distance. Moreover, it is unknown, if this matching contains a sequence of moves that would lead to a collision-free assembly.

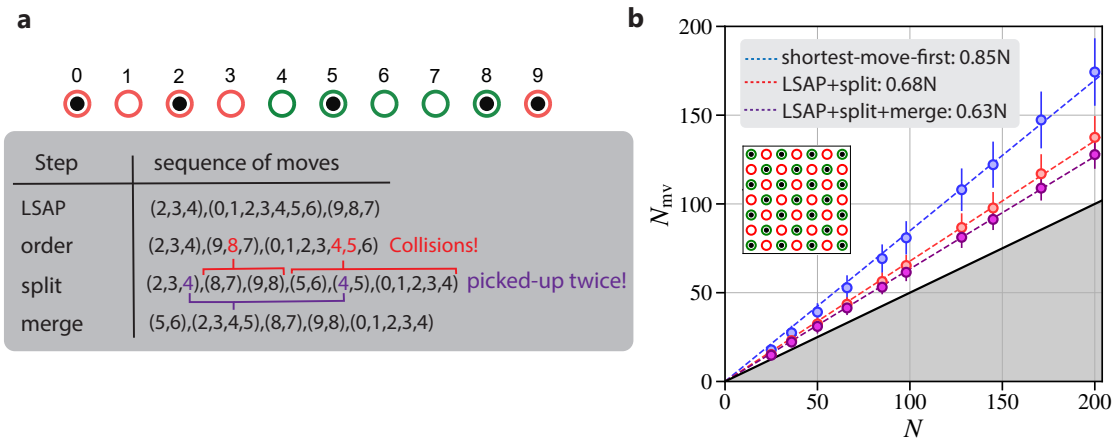

Figure 3.2: The LSAP1 algorithm. a Illustration of the different steps of the algorithm (see text). **b**: Comparison of the scaling of the number of moves N_{mv} with the number of target traps N for staggered arrays (for exemplary array see inset), between the old shortest-move-first algorithm and the different steps of the LSAP1 algorithm. The black line indicates $N/2$, the number of on average unoccupied target traps.

In the following, I present two hybrid algorithms that find a collision-free sequence of moves, starting from an initial LSAP matching.

LSAP1: Standard metric, split and merge

This algorithm starts with a standard LSAP algorithm as previously described. As a cost function, we minimize the total travelled pathlength $\ell_{\mathrm{tot}} = \sum_{\mathrm{moves}\ i} \ell_i$. As illustrated in Figure 3.2a , we order the returned matching by pathlength, from shortest to longest. Then, we post-process the moves, similarly to the shortest-moves-first algorithm, by splitting each path with obstacle into two paths. As an intermediate result, we obtain a collision-free sequence of moves. As we see in Figure 3.2b, after this step the number of moves scale as $0.68N$ for staggered arrays, which is a significant improvement to the shortest-move-first algorithm ($0.85N$). However, it is possible to reduce the number of moves further. In a second iteration, we try to merge moves where an atom is picked up twice, while checking it does not reintroduce a collision. This second step reduces the total number of moves considerably and for staggered arrays, we arrive at a close-to-optimal scaling of $0.63N$.

Next to a close-to-optimal number of moves, this algorithm has the advantage of finding the optimal pathlength, as it starts with an LSAP solver. Therefore, it is a good choice even for systems where ramping the intensity is not the dominant timescale.

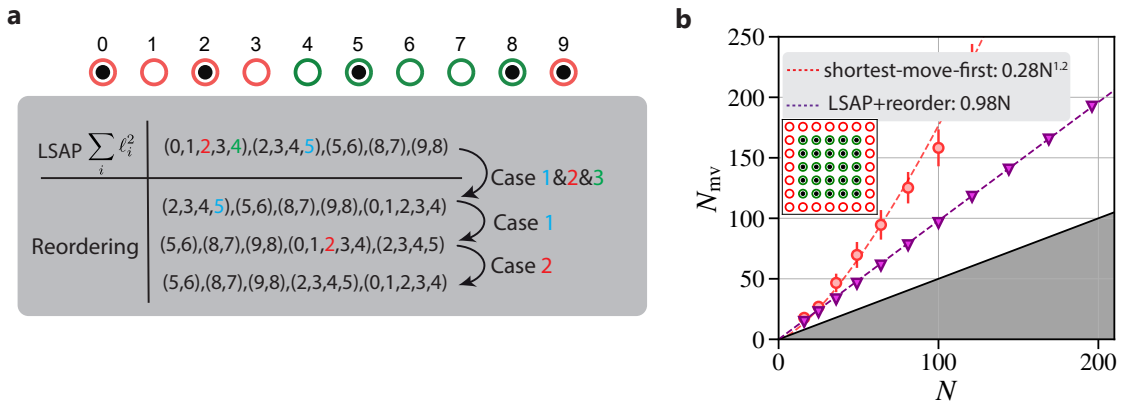

Figure 3.3: The LSAP2 algorithm. a Illustration of the different steps of the algorithm (see text). **b**: Comparison of the scaling of the number of moves N_{mv} with the number of target traps N for compact arrays (for exemplary array see inset), between the old shortest-move-first algorithm and the different steps of the LSAP2 algorithm. The black line indicates $N/2$, the number of on average unoccupied target traps.

Note that the merging technique works for all algorithms which pick up certain atoms more than once. Therefore, it is also applicable to the shortest-move-algorithm. However, we find the smallest number of moves in the above combination with the LSAP matching.

The computation time for a staggered array of 200 target traps is 5 ms and for our atom numbers, we find that it scales roughly as N^2. To save computation time, we precalculate the distances and paths between all trap pairs and store it in a look-up table before runtime. During each assembly cycle, the costmatrix of the LSAP algorithm is then found as a submatrix of this look-up table.

LSAP2: modified metric and reordering

This algorithm starts with an LSAP algorithm with a modified cost function. We consider the sum of the squares of all pathlengths $\sum_{\mathrm{moves}\ i} \ell_i^2$, as it favors shorter moves which avoids collisions[1] . Empirically, we find that the returned matching can be reordered into a collision-free sequence of moves to assemble any target array.

The working principle is reminiscent of the compression algorithm, as the cost to fill an empty target trap is smallest for the closest atom. If there is an obstacle O on the shortest path between source trap S and target trap T, the cost of the

[1]The idea of an LSAP algorithm with a modified metric is similar to [Lee, Kim, and Ahn, 2017]. However, their assembly technique moves all atoms at once. Therefore, contrary to our case, they do not need to find a collision-free sequence of moves.

move $[S \to T]$ is bigger than the combined cost of the moves $[O \to T]$ and $[S \to O]$: $|\boldsymbol{t} - \boldsymbol{s}|^2 > |\boldsymbol{t} - \boldsymbol{o}|^2 + |\boldsymbol{o} - \boldsymbol{s}|^2$, as $|\boldsymbol{t} - \boldsymbol{s}| = |\boldsymbol{t} - \boldsymbol{o}| + |\boldsymbol{o} - \boldsymbol{s}|$.

To get a collision-free sequence, we reorder the matching returned by the LSAP algorithm with the following algorithm, as illustrated in Figure 3.3: We examine each move in the sequence, and, if the target trap of the move is occupied (case 1), or if another trap along the path of the move is filled (case 2), or if the target trap is in the path of another move following in the list (case 3), we postpone the move by putting it at the end of the sequence of moves. Although without proof, we observe that this procedure always converges into a collision-free sequence.

We find that this algorithm works best for compact arrays, where the number of moves scales as $0.98N$, similar to the compression algorithm. Furthermore, the pathlength is close-to-optimal since we start with an LSAP solver, even if we consider the square of all pathlengths. The algorithm takes about 4 ms to compute for a compact array of 100 target atoms and for our atom numbers, we find that the computing time roughly scales with N^2.

Compared to the compression algorithm, the LSAP is faster for smaller atom numbers, mainly due to the highly optimized code of the LSAP. Due to its more favorable scaling, the compression algorithm in our implementation is however faster above a cricital target atom number of $N_c = 300$.

3.2.3 From Bravais lattice to fully-arbitrary graphs

The atom assembler presented in [Barredo *et al.*, 2016] allowed us to create user-defined target trap arrays, with the restrictions that all reservoir and target traps have to lie on an underlying Bravais lattice. During my PhD, we lifted this restriction by changing the framework of the algorithms to a graph-based approach and are now able to assemble truly arbitrary trap arrays.

This work was motivated by several interesting quantum simulations that would require physical structures that can not be described by a Bravais lattice. Totally arbitrary structures can be useful for combinatorial optimization problems such as finding the maximum independent set of a graph [Pichler *et al.*, 2018; Henriet, 2020]. Further non-periodic structures include crystal defects (vacancies, dislocations, grain boundaries), quasi-crystals or disordered arrays for Anderson or many-body localization studies.

When considering to assemble a user-defined target array with arbitrary positions, there are two major differences in comparison to an array that can be described by a

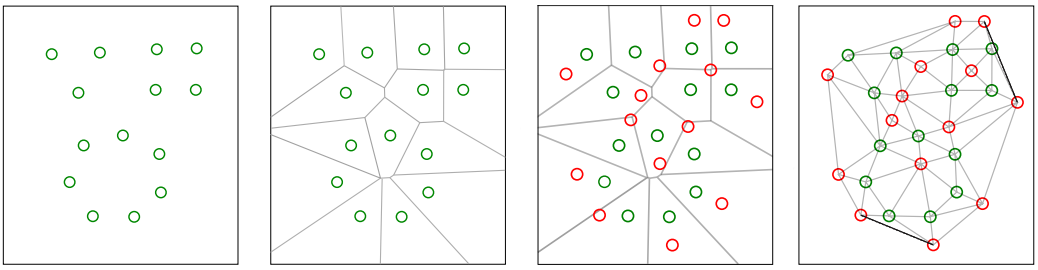

Figure 3.4: Initialization procedure of an arbitrary target array. From left to right: The user-defined target trap pattern (green circles). A Voronoi decomposition (grey lines) of the target trap array. Placement of the reservoir traps (red circles) inside each region, respecting the minimum distance requirement. Delaunay triangulation of the whole trap array (grey lines) to find edges for the moving tweezer to travel along. Edges in black are too close to another trap and are removed.

Bravais lattice. First, the positions of the reservoir traps are not naturally given by a common lattice anymore, necessitating a new procedure to place reservoir traps given the target trap positions. Second, the paths the moving tweezer can travel along are not naturally given by the lattice edges anymore. As the moving tweezer can not travel between any two traps in a direct, straight line without the possibility of collisions with obstacle atoms, this requires finding a set of edges along which to move. We solve these two problems in the following way, as illustrated in Figure 3.4:

The process starts with an arbitrary user-defined trap array with N target traps that we wish to assemble. We then need to place N additional reservoir atoms close to our target trap array. The assembly process needs considerably less moves if each target trap is surrounded by at least one reservoir trap (e.g. staggered configuration), and therefore a reservoir trap should be placed in immediate proximity of each target trap whenever possible. To do so, we use a Voronoi decomposition [Preparata and Shamos, 1985] of the target traps. This divides the plane in N regions, one around each trap T, such that all points of this regions are closer to T than to any other trap. In each of these Voronoi cells, we place a single reservoir trap, as long as it satisfies a minimal distance requirement of 4 µm to all other traps. Note that this procedure recovers a staggered configuration on a square array.

If the target traps are too close to each other, we cannot add enough reservoir traps with this method. Then, we place the extra traps at the periphery of the pattern in a compact triangular array, as it has the highest compactness of 2d Bravais lattices

Next, we have to find the paths along which the moving tweezer can travel. For

this, we use a Delaunay triangulation [Preparata and Shamos, 1985], as illustrated in Figure 3.4. To avoid collisions, we enforce a minimal distance between edges and traps: we post-remove an edge if there is a trap in its vicinity that is closer than 3 µm.

In practice, the triangulation is done with the *scipy* library [Virtanen *et al.*, 2020]. With the triangulation, the problem can be naturally described in a graph language, in which the nodes are the trap positions and the edges the paths along which the moving tweezer can travel. Each edge can be weighted with its length, making it possible to run efficient shortest-path graph-algorithms (e.g. the Dijkstra algorithm [Preparata and Shamos, 1985], to find the shortest path for the moving tweezer between two traps, following the edges of the graph). For the generation of the graphs and the graph-algorithms, we use the *Networkx* library [Hagberg, Swart, and S Chult, 2008].

The graph-based framework is a powerful tool that lets us utilize all prior algorithms on arbitrary trap arrays, without adding any extra computational cost at runtime. We compute the distances and shortest-paths between all traps before runtime, and store them in a look-up table. During the experimental sequence, there are therefore no computations done on the graph structure itself.

In Figure 3.5, we illustrate two different arbitrary patterns. For both of them, the reservoir traps are generated in the above described way, then the array is triangulated to find the paths for the moving tweezer. The two structures were then assembled using the LSAP1 algorithm.

3.2.4 Choosing the right algorithm

Given the algorithmic framework that was introduced in this Chapter, the working-procedure is illustrated in the flowchart in Figure 3.6.

Starting with a set of user-defined target trap positions, we first determine whether they lie on a Bravais lattice. If yes, the reservoir atoms are naturally given, else, they have to be created with the method introduced in the last section.

We then choose the best algorithm according to the following reasoning: For non-compact structures, e.g. staggered arrays, we use the LSAP1 algorithm. For compact arrays, we choose the compression or LSAP2 algorithm. Since the compression algorithm has a more favorable scaling of the computation time with the number of traps, we utilize it above a critical number of 300. Below, we utilize the LSAP2 algorithm. The scalings and computation times are summarized in the table in Figure 3.6.

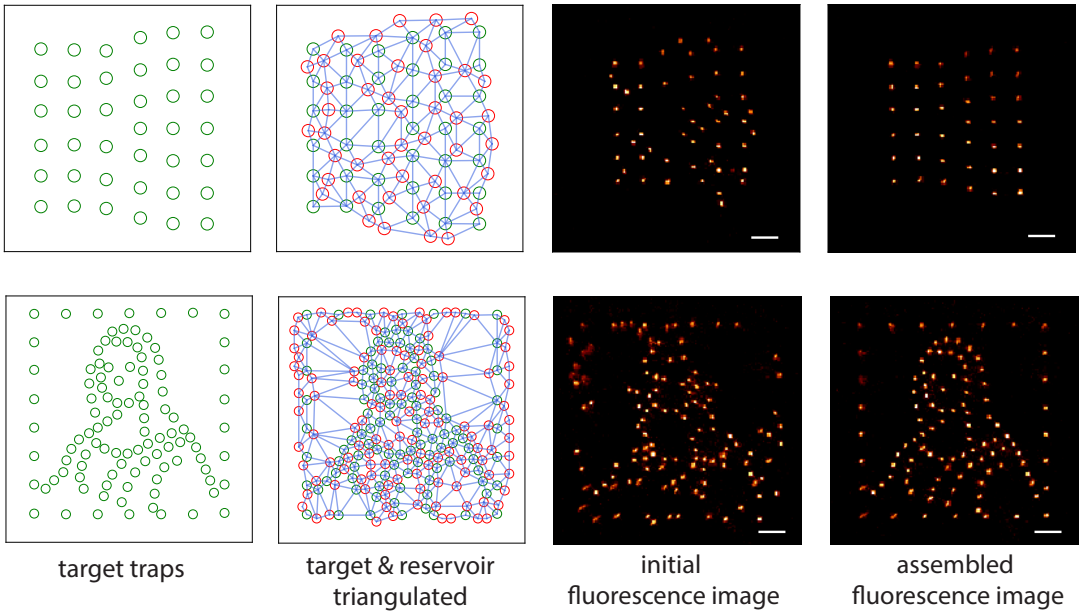

Figure 3.5: Examples of the assembly of two arbitrary target geometries. From left to right: target trap positions (green), triangulated ensemble of target (green) and reservoir (red) traps, connected by the edges (grey) the moving tweezer travels along, an initial fluorescence image determining the trap occupation, a final fluorescence image after the assembly process. **Upper:** Dislocation with 39 atoms. Utilizing the LSAP1 algorithm, the array is assembled in on average 24 moves. **Lower:** Mona Lisa with 106 atoms. With the LSAP1 algorithm, the array is assembled with on average 70 moves. The scale bar in the fluorescence images depicts a distance of $10\,\mu\mathrm{m}$.

3.2.5 Multiple assembly cycles

As previously described, the probability P_0 to obtain a defect-free N-atom array depends strongly on the lifetime τ_{vac} of the atoms in the tweezer, and the time needed to assemble the N-atom array. Ultimately, the probability is limited by:

$$P_0^{\star}(N) = \exp(-\frac{t_{\mathrm{assembly}}(N)}{\tau_{\mathrm{vac}}/N}). \tag{3.1}$$

The assembly time t_{assembly} is a function of the number of atoms and is given by:

$$t_{\mathrm{assembly}} = t_{\mathrm{analysis}} + t_{\mathrm{comp}} + N_{\mathrm{mv}} t_{\mathrm{ramp}} + d_{\mathrm{tot}} v_{\mathrm{mt}}, \tag{3.2}$$

where t_{analysis} is the time needed to analyse a fluorescence image (approximately $50\,\mathrm{ms}$), and t_{comp} the computation time of the algorithm. The moving time for the

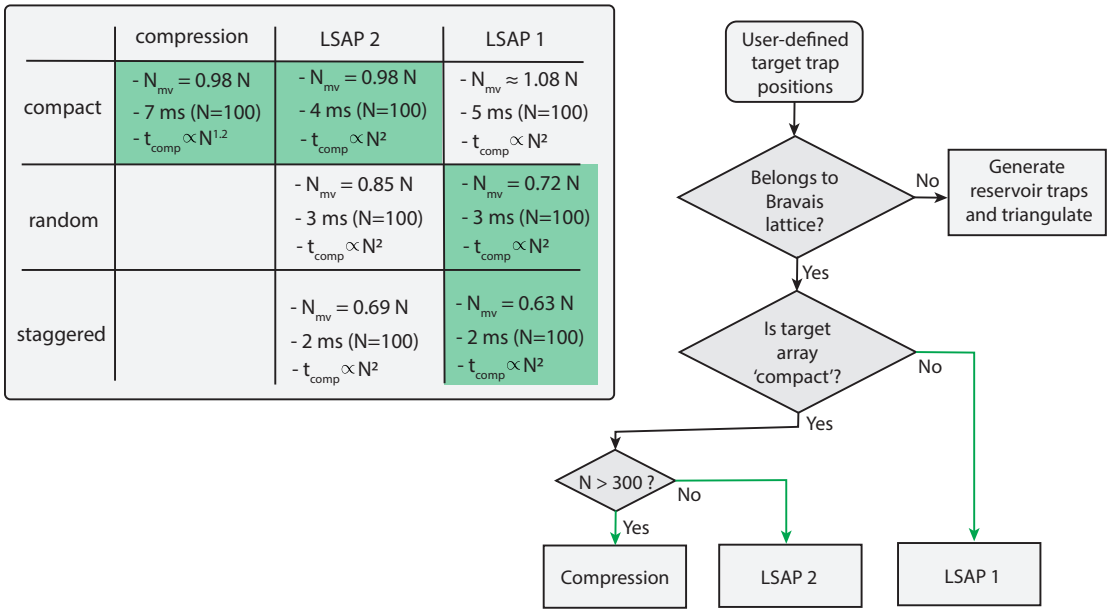

Figure 3.6: Summary of the different algorithms and workflow. Left: Table with summary of the different algorithms. Scaling of the number of moves N_{mv} with the number of target traps N, the calculation time for a target trap number of $N = 100$, and the typical rough scaling of the computation time with the number of target traps. **Right:** Flowchart of our modular approach. The best choice of algorithm depends on the target array.

moving tweezer is influenced by the algorithm and depends mainly on the number of moves N_{mv} and to a lesser extend on the total travelled distance d_{tot}, with ramp time t_{ramp} and the velocity of the moving tweezer v_{mt}, as explained in Section 3.1.1. Note that all these times depend on the number N of target traps!

However, each move only has a finite success probability. In [Barredo *et al.*, 2016], the success probability was found to be $p_{\mathrm{mv}} = 0.993(1)$ between two neighbouring traps with 5 µm. If we consider p_{mv} to be the average success probability of each move, and N_{mv} are needed to assemble the N-atom array, this reduces the probability to obtain a defect-free array to:

$$P_0(N) = p_{\mathrm{mv}}^{N_{mv}} \exp(-\frac{t_{\mathrm{assembly}}}{\tau_{\mathrm{vac}}/N}). \tag{3.3}$$

Note that this is an estimation that assumes that all moves have the same success probability, the average move success probability. Due to experimental imperfections that will be evaluated at the end of this chapter, this is not true in general, and different moves can have different success probabilities. As in general $\prod_i^{N_{mv}} p_i \neq p_{\mathrm{mv}}^{N_{mv}}$,

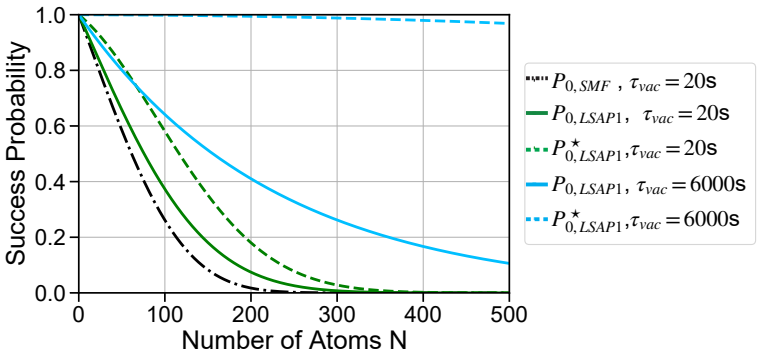

Figure 3.7: Success Probability to assemble a staggered N-atom array. The probabilities P_0 includes the finite success probability of each move (see Eq. 3.3), whereas $P_0^\star$ is the purely lifetime-limited success probability (see Eq. 3.1) that could be achieved in the limit of many rearrangement cycles. The increase in success probability between the old shortest-move-first algorithm and the new LSAP1 algorithm with multiple rearrangement cycles is significant. However, the success probability could be further improved by an increased vacuum lifetime.

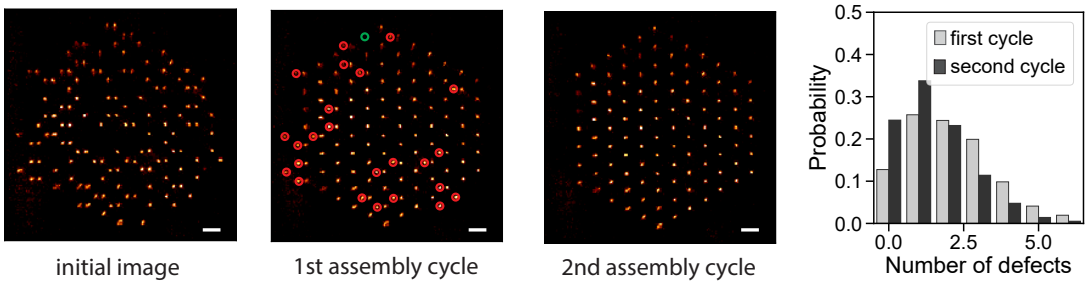

Figure 3.8: Second rearrangement cycle: Example of an 108 atom array, the scale bar denotes $10\,\mu\mathrm{m}$. After the first rearrangement cycle, we do not remove excess reservoir atoms (red) from their traps, but use them to fill the remaining unoccupied target traps (green). This significantly increases the fidelity of a defect-free shot, as shown in the histogram.

this is only a rough estimation. However, it lets us distinguish between the different physical contributions to the success probability.

In Figure 3.7, the different success probabilities of equations (3.1,3.3) are illustrated on an example with a staggered N-atom array. While the success probability is significantly improved for the new algorithms, e.g. the LSAP1 compared to the shortest-move-first, the single move efficiency decreases the success probability drastically compared to $P_0^\star$.

To solve this issue, we implement multiple rearrangement cycles, as illustrated in Figure 3.8. On the shown triangular patch with 108 atoms, there are on average two empty target traps after the first rearrangement cycle. We do not remove excess reservoir atoms after the first cycle, but use them to fill the remaining empty target traps in a second rearrangement cycle. This significantly increases the probability to obtain a defect-free array, as illustrated by the histogram in Figure 3.8. In the limit of many rearrangement cycles, the probability should converge to $P_0^\star$.

On the experiment, we rarely found a significant gain beyond two cycles, partly because of an imperfect trap depth equalization, as illustrated in the next section. In most cases we started with a surplus of reservoir traps of approximately 10% and performed two rearrangement cycles.

Note that in a cryogenic environment with extended single-atom lifetimes of 6000 s, both the probabilities P_0 and $P_0^\star$ are significantly increased (see Figure 3.7).

3.3 Application of enhanced assembly on the quantum simulation of the Ising model

During my PhD, we performed a quantum simulation of the 2D transverse field Ising model with up to 200 atoms. This model has been previously implemented on our room-temperature setup in [Lienhard *et al.*, 2018], where antiferromagnetic ordering and the build-up of correlations has been observed. However, these preliminary studies were limited due to a relatively small coherence time of approximately 1 µs and a limited system size of 36 atoms.

With the improvements of the atom assembly highlighted in this section, and the implementation of a new laser system (see Chapter 2.2.2), we were able to investigate the model with unprecedented system size of up to 200 atoms and coherence time of 20 µs. This work has lead to a back-to-back publication [Scholl *et al.*, 2021a] with the group of Mikhail D. Lukin at Harvard [Ebadi *et al.*, 2021], and is described in detail in the thesis of Pascal Scholl [Scholl, 2021]. In the following, I will describe the preparation of 200-atom arrays and then briefly summarize the quantum simulation experiments.

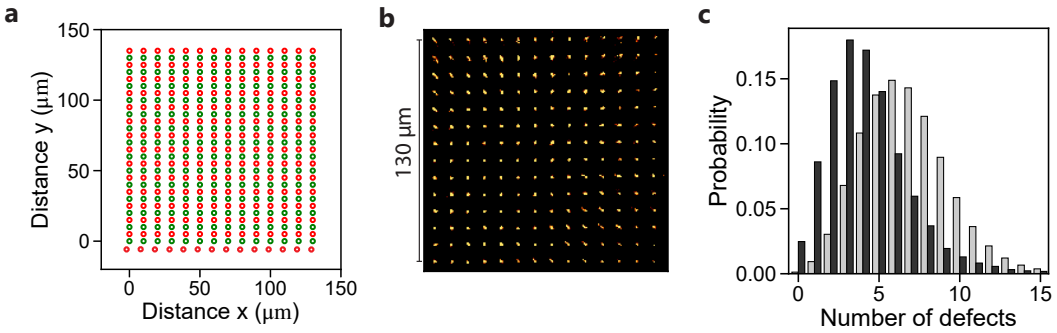

Figure 3.9: Assembly of 14×14 square array. **a**: Target (green) and reservoir trap (red) placement in staggered configuration. **b**: Assembled defect-free fluorescence image. **c**: Probability distribution of number of defects.

3.3.1 Arrays of up to 200 atoms

Preparing defect-free atom arrays with up to 200 atoms is a challenging task on our room-temperature setup and involves using the new algorithmic framework discussed in the previous sections. In the following, I will highlight the used procedure, and point to further experimental limitations, mainly related to the limited field-of-view of the lenses and caused optical aberrations. Solutions to these limitations will be presented in Chapter 6.

For the project, we prepared e.g. defect-free 14×14 square arrays with an interatomic distance of 10 µm. The extent of the array is thus 130 µm and similar to the field-of-view of the aspheric lens. Therefore, we place the reservoir atoms inside of the structure in a staggered configuration (see Figure 3.9a), resulting in an interatomic distance of 5 µm in y- and 10 µm in x-direction. The staggered configuration needs the least number of moves using the LSAP1 algorithm (compare Figure 3.6) and for a 50%-loading, we expect an average number of moves of 123. Using two rearrangement cycles, we obtain a defect-free 196-atom array with a probability of $P_{0,196}$ =2.5% (see Figure 3.9c). This demonstrates the capabilities of our new algorithmic framework, that allows us to reach an unprecedented atom number with a non-negligible preparation fidelity.

Assembling these large arrays, we find however that increasing the atom number has additional experimental challenges next to the algorithmic side. Mainly, these challenges stem from the fact that these large arrays have an extent similar to the field-of-view of the aspheric lenses. As a result, optical aberrations on the border of the array (see Section 2.3.3) are playing a role: the trap depth equalization and the single-move efficiency are worse compared to smaller arrays.

This reduces the efficiency of the assembly process: We find that the success

probability of 2.5% to assemble a defect-free array is reduced compared to the approximately 10% expected from a single cycle with an average single-move efficiency of $p_{\mathrm{mv}} = 0.993(1)$ (compare Equation 3.3, Figure 3.7). Especially, as we find an average of 83 moves — the lower than $N/2$ number of moves is caused by an increased loading probability of approximately 60-65% — and an average total travelled distance of 620 µm when analysing the data for the first rearrangement cycle. The connection between the lower than expected overall success probability and an imperfect trap depth equalization is illustrated in Figure 3.10. It shows the filling probability of each of the 196 traps after two assembly cycles, deduced from the fluorescence images before and after the assembly process. Most target traps are filled in 98.5% of the experimental cycles, except for a few traps that have a significantly smaller filling probability. These traps have a smaller than average trap depth, leading to an increased loss probability.

The probability to assemble a defect-free array, can be found by multiplying the filling probabilities p_i of all traps i and is, as stated above: $P_{0,196} = \prod_i p_i = 2.5\%$. From Figure 3.10b, we see that this probability is limited by a few traps with significantly smaller filling probability. We expect that with an improved trap depth equalization method, all traps have a filling probability distribution with an average probability of $\overline{p}_{\mathrm{avg}} = 0.985$ (red line in Fig. 3.10b). Considering this value leads to a probability of $P'_{0,196} = 5.2\%$ to assemble a defect-free array. This highlights the importance of a better trap depth equalization method and in Chapter 6, I will present a new improved method.

For this project, I implemented a first iteration of a new *in situ* trap depth equalization. The new method improved the success probability of the assembly process considerably compared to the normal intensity equalization. In contrast to the intensity equalization feedback that takes the measured intensities as weights for a feedback algorithm (see Fig. 2.3), the new method relies on taking the loading probability of each trap (see Fig. 2.12) into account. Even though the method resulted in a major improvement, it is still imperfect, as can be seen from the histogram of the filling probabilities in Figure 3.10b.

The additional discrepancy to the expected success probability to obtain zero defects might stem from the fact that for large arrays, the single move efficiency is significantly lower than the $p_{\mathrm{mv}} = 0.993(1)$ quoted in [Barredo *et al.*, 2016]. From the assembly of the 14×14 array, we can estimate the average single move fidelity $\overline{p}_{\mathrm{mv}}$ with:

$$\overline{p}_{\mathrm{mv}}^{N_{\mathrm{mv}}} = \overline{p}_{\mathrm{avg}}^{N} \exp\left(\frac{t_{\mathrm{assembly}}(N)}{\tau_{\mathrm{vac}}/N}\right), \tag{3.4}$$

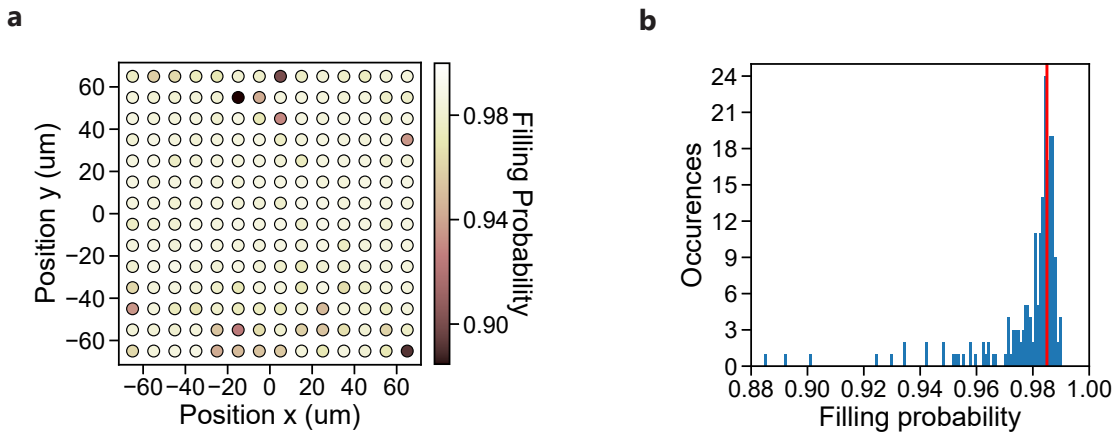

Figure 3.10: Filling Probabilities of 14×14 target array after two rearrangement cycles. a: Target array with filling probability, denoting the assembly success, for each trap. **b:**Histogram of the filling probabilities of a. We can see a peaked distribution around a filling probability of 0.985 (red line), and a tail of traps with smaller filling probabilities.

where N is the number of atoms in the target array, N_{mv} the number of moves, determined by the algorithm, $\overline{p}_{\mathrm{avg}}$ the average filling fraction of the traps after one rearrangement cycle, $\tau_{\mathrm{vac}} = 20$ s the vacuum lifetime on our room-temperature setup. We find an average single move fidelity of $\overline{p}_{\mathrm{mv}} = 0.972(4)$. Again, note that this is only a simple estimation, as we work with average quantities.

We attribute this reduced single move fidelity mainly to more complicated and longer moves (compared to [Barredo *et al.*, 2016]). The laser power in the moving tweezer can vary by approximately 30% over the whole extend of the large array, which can change the transfer efficiency between moving tweezer and SLM traps. Compared to our 14×14 array with an extent of 130 µm, the benchmark in [Barredo *et al.*, 2016] was done with a 3×3 array with an extent of only 10 µm.

3.3.2 Quasi-adiabatic preparation of antiferromagnetic ground states

In the last section, I showed that we can prepare defect-free arrays of 200 atoms with non-negligible fidelities due to the new algorithmic framework. This opens up the possibility to perform a large-scale quantum simulation of the Ising model.

The Hamiltonian of the transverse field Ising model (see Chapter 2.2.1) is naturally implemented on our Rydberg platform:

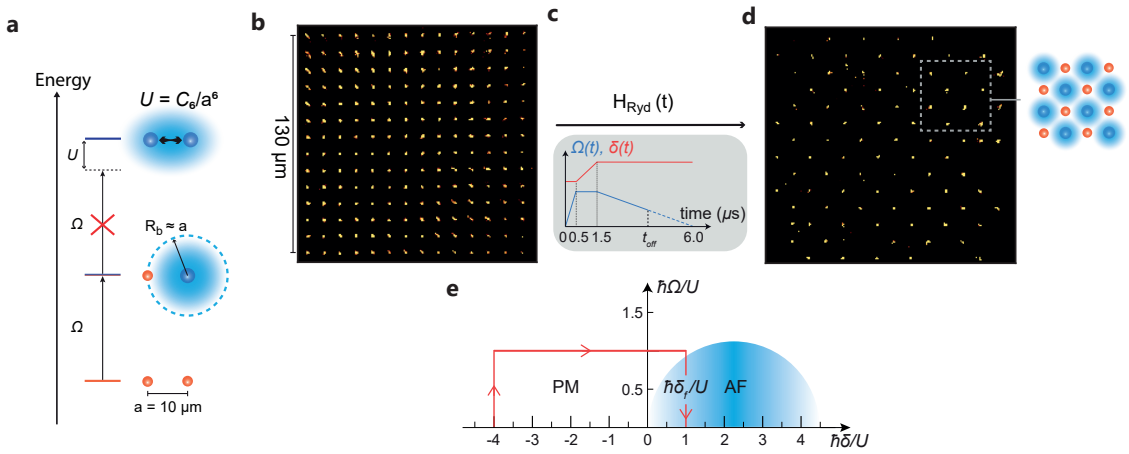

Figure 3.11: Antiferromagnetic ordering in square arrays. a: Illustration of the Rydberg blockade. The strong interaction prevent the simultaneous excitation of two ground-state atoms (red) to the Rydberg state (blue), if their distance is smaller than the Rydberg radius R_b. **b,c,d,e:** Illustration of the experimental cycle. The atoms are initialized in the ground-state representing the paramagnetic phase (b). Then detuning δ and Rabi-frequency Ω are changed (c) to reach the antiferromagnetic ground-state of the system (d). This figure is adapted from [Scholl *et al.*, 2021a].

$$H_{\mathrm{Ryd}} = \sum_{i<j} U_{ij} n_i n_j + \frac{\hbar\Omega}{2} \sum_i \sigma_i^x - \hbar\delta \sum_i n_i, \tag{3.5}$$

where the Rydberg- $\left|75S_{1/2}, m_J = 1/2\right\rangle$ and groundstate $\left|5S_{1/2}, F = 2, m_F = 2\right\rangle$ are mapped onto the spin states $|\uparrow\rangle$ and $|\downarrow\rangle$. Here, $U_{ij} = \frac{C_6}{R^6}$ is the van der Waals interaction, with C_6 the van der Waals coefficient and R the distance between the atoms, σ^x and $n_i = |\uparrow\rangle\langle\uparrow|_i = (1 + \sigma_i^z)/2$ are the Pauli matrices, Ω the Rabi frequency of the laser field with detuning δ.

As illustrated in Figure 3.11, the strong interactions, characterized by the Rydberg radius $R_b = (C_6/\hbar\Omega)^{1/6}$, lead to antiferromagnetic ordering: As the Rydberg radius is similar to the lattice spacing $R_b \simeq a = 10\,\mu\mathrm{m}$, the interactions prevent the simultaneous excitation of two neighbouring atoms.

We prepare the antiferromagnetic ground state of the system, by quasi-adiabatically changing the parameters of H_{Ryd} as can be seen in Figure 3.11 on a 196 atom square array. The array is initialized in the paramagnetic ground state, where all spins are aligned $|\downarrow\downarrow \ldots \downarrow\rangle$. This state is represented by the assembled array, as $|\downarrow\rangle$ is encoded in the ground-state atom (see Fig. 3.11b). In 6 µs, the detuning and Rabi frequency are then changed (see Fig. 3.11c,e), crossing the phase transition and reaching the

antiferromagnetic ground state. The duration of the sweep of 6 µs was found to be a good balance between decoherence effects and quasi-adiabaticity of the sweep.

In this work, we also investigated the phase diagram of the triangular lattice (see Fig. 3.8 for an assembled triangular array). We observe for the first time the creation of two distinct antiferromagnetic orders. For an in-depth analysis of the experiments on the triangular and square lattice, the reader is referred to the thesis of Pascal Scholl [Scholl, 2021].

Increasing the system size is critical, as the phase diagram of our finite size system can change quite drastically from an infinite system size (see [Lienhard *et al.*, 2018],[Scholl, 2021]). Because of the open-boundary conditions, the atoms on the boundary experience fewer interactions as the ones in the bulk: compared to an infinite system, this can lead to more ground-state configurations on the classical line of the phase diagram ($\Omega = 0$), as the atoms on the boundary are more likely to be excited to the Rydberg state for increasing δ.

This work demonstrates that by pushing our platform to unprecedented atom numbers, we can address open questions in many-body physics.

3.4 Conclusion

In this chapter, I presented a new algorithmic framework for the assembly process that allowed us to reach unprecedented atom numbers on our room-temperature setup. This demonstrates the capabilities of our platform to perform large-scale quantum simulations to address open questions in many-body physics.

First, I described three new algorithms that improve the assembly efficiency by significantly reducing the number of moves compared to the previous shortest-move-first algorithm. Together with performing multiple assembly cycles, this allowed us to prepare defect-free atom-arrays of up to 200 atoms with non-negligible fidelities.

Using a new graph-based approach, the algorithms are extended further to non-regular structures that cannot be represented on a Bravais lattice. This approach opens up the possibility to interesting new experiments, like the optimization problem of finding the maximum-independent set on a graph.

Finally, I highlight experimental limitations on our setup. First, the vacuum-limited single-atom lifetime in our tweezers is an ultimate limit on our room-temperature setup. With our new cryogenic platform (see Chapter 4), we can lift this limitation and increase the atom number further. Second, I highlight experimental concerns caused by the big extend of our arrays that is similar to the field-of-view of the aspheric lenses.

This motivates us to improve techniques that have worked well on smaller arrays, like the trap depth equalization, and these improvements will be presented in Chapter 6.

Chapter 4

Designing and Building a Cryogenic Single-Atom Platform

In the last chapters, I presented the vacuum-limited lifetime of a single atom in a tweezer as a major limitation for the scalability of our room-temperature quantum simulation platform. Due to the cryopumping effect, cryogenic experiments routinely achieve a vacuum pressure several orders of magnitude lower than on room-temperature platforms (e.g. [Benvenuti, 1974; Diederich *et al.*, 1998; Gabrielse *et al.*, 1990]). Therefore, we designed and built a novel cryogenic single-atom array platform which I describe in detail in this chapter.

I will describe the design of the new apparatus, starting with an overview of the different components, before detailing them further. Then, I analyse the performance of the cryostat in a series of tests. Specifically, I evaluate the capability of the cryogenic platform to sustain low temperatures while submitted to various heat loads during large-scale quantum simulation experiments.

4.1 Design of the apparatus

As detailed in the introduction, there have been various efforts in the atomic, molecular, optical community (AMO) to build cryogenic experiments, such as in the trapped ion

community ([Pagano *et al.*, 2018; Micke *et al.*, 2019]), or for Bose-Einstein Condensation ([Roux *et al.*, 2008; Bernon *et al.*, 2013]). However, each platform has its own specific constraints, so an adaptation for our tweezer array experiment is not straightforward.

Our system was designed in collaboration with the cryogenic company *MyCryoFirm*. Their flagship product *OptiDry* is an optical-access, closed-cycle (Helium 4) cryostat with temperatures down to 4 K. Our new platform relies on the same cryogenic techniques, albeit being UHV-compatible and adapted for the requirements of a tweezer array experiment.

In our design process, we decided to keep several main technical solutions of our room-temperature setup. This involved the following components: an atom source composed of an oven and a spin-flip Zeeman slower, and a science chamber including two aspheric lenses to generate the tweezers and magnetic field coils for the magneto-optical trap.

This enables us to focus mainly on the design of the cryogenic side of the new platform. I illustrate the platform in two parts: the ultra-high vacuum, closed-cycle cryostat that cools down part of the science chamber to 4 K, and the science chamber containing all necessary elements for the generation of large-scale single-atom arrays. Although reminiscent of our room-temperature setup, all elements inside the science chamber are modified for cryogenic temperatures, necessitated by experimental challenges such as thermal contraction, thermal conduction and electric resistivity at low temperatures.

4.1.1 Overview of the setup

An overview of the setup is illustrated in Figure 4.1. The atomic source is similar to our room-temperature setup. It contains an oven, creating an atomic beam of Rubidium that is slowed down by a spin-flip Zeeman slower before we capture atoms in a magneto-optical trap in the science chamber. The oven-part can be decoupled by a gate valve, blocking the atomic beam. This atomic source has been built by Eric Magnan and is described in more detail in his thesis [Magnan, 2018].

The cryogenic side of the experiment accommodates an ultra-high vacuum closed-cycle cryostat which is encased in a large stainless-steel vacuum chamber at 300 K. It contains a science chamber on one side that is connected to the Zeeman slower, and a pulse-tube-refrigerator on the other. Attached to the cryostat are two pumps, a $300\,\mathrm{L\,s^{-1}}$ titanium-sublimation ion pump and a non-evaporable getter (NEG) cartridge.

Figure 4.2 shows a cross-section of the cryogenic part. The pulse-tube refrigerator

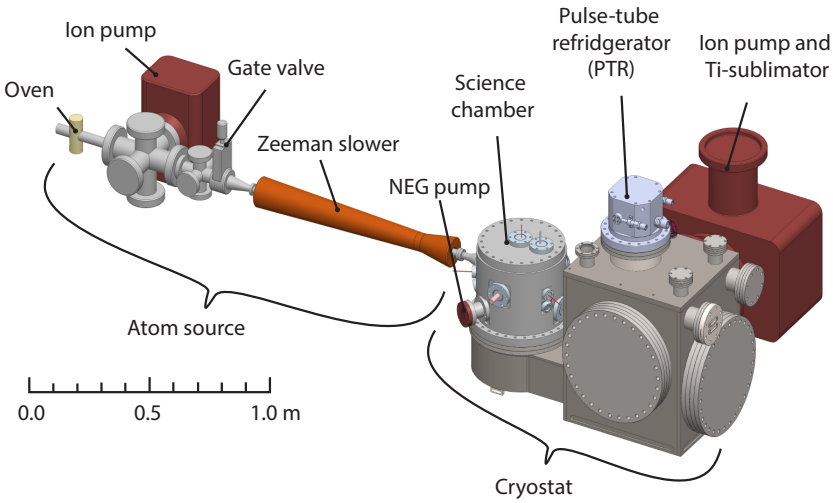

Figure 4.1: Overview of the experimental apparatus. Schematic of the whole setup, including the atom source and the cryostat.

(PTR) has two stages, cooling a first radiation shield to 30 K (light blue) and a second baseplate and heatshield to 4 K (dark blue). The compression of helium inside of the PTR leads to vibration amplitudes typically on the 10 µm level at the cold head. To decouple the optical assembly in the science chamber from these vibrations, the connections between the PTR stage and the thermal shields or baseplate are made out of ultra-soft, high thermal conductivity copper braids.

The science chamber contains super-conducting magnetic-field coils and the optical assembly at a temperature of 4 K. The optics include two aspheric lenses, and two mirrors for beam steering of the Zeeman and MOT beams. We use the same lenses as on our room temperature setup (NA = 0.5, focal length f =10 mm, working distance of 7 mm). To allow optical access from the outside, the thermal shields (30 K and 4 K) are equipped with 5 mm thick fused-silica. The laser beams from the outside therefore propagate through two vacuum viewports and four windows on the thermal shields. In the direction of the Zeeman beam however, the thermal shields have an aperture with a diameter of approximately 13 mm.

4.1.2 Closed-cycle cryostat

To cool down a significant part of the science chamber to 4 K, we built a two-stage closed-cycle cryostat using a pulse-tube refrigerator (PTR) in collaboration with the

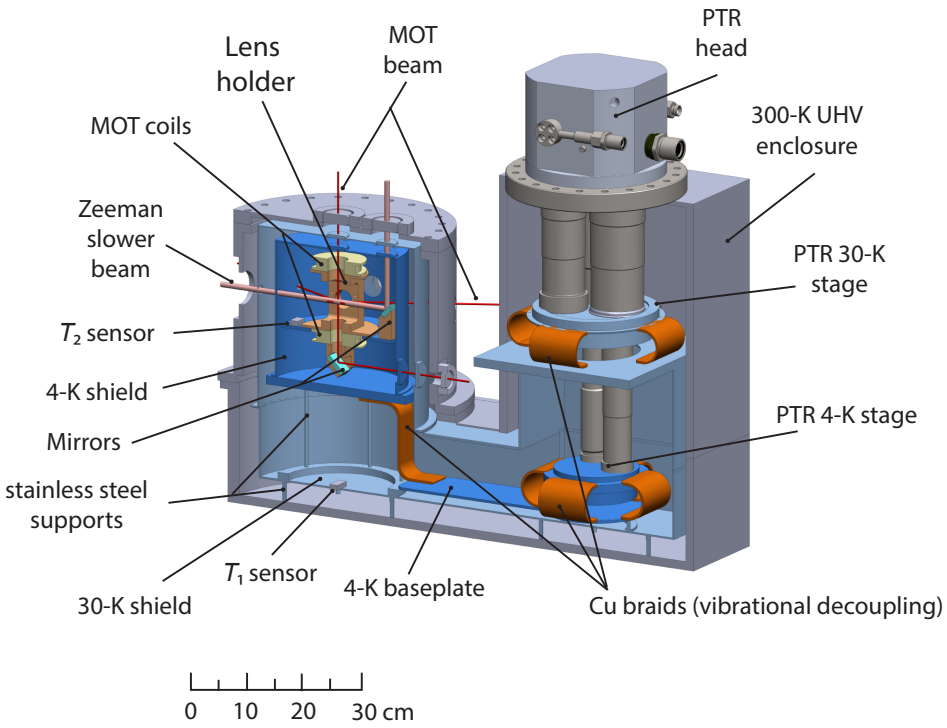

Figure 4.2: Cross-section of the cryostat: A two stage pulse-tube refrigerator (PTR) cools down an optical assembly inside nested radiation shields. The first stage of the PTR is connected via flexible copper links to a 30 K shield (light blue), and the second stage of the PTR to a radiation shield at 4 K (dark blue), inside which the optical assembly is found.

company *MyCryoFirm*. We opt for a nonbakeable system, similar to the commercial OptiDry models from *MyCryoFirm*, as the PTR cannot be heated above temperatures of approximately 60 °C, and a removable PTR makes the design significantly more involved. Additionally, we only use UHV compatible materials inside of the vacuum vessel. This compromise results in a moderate vacuum in the room-temperature chamber (order of 1×10^{-8} mbar). However, we shall see in the following chapter that the cryopumping by the 4 K shield enclosing the atoms results in a vacuum several orders of magnitude better than on our room-temperature setup.

In the following, I describe briefly the working principle of the Gifford-McMahon-type pulse-tube refrigerator that we use. For simplicity, I limit the description to a single-stage, although we use a two-stage PTR. For a more in depth review on cryocoolers, the reader is referred to [de Waele, 2011]. Then, I detail the realization of a closed-cycle cryostat for our experimental purposes.

Working principle of the cryocooler The basic working principle of a Gifford-

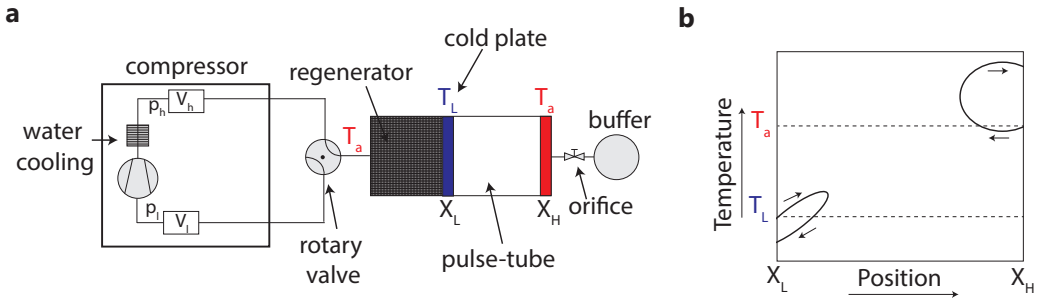

Figure 4.3: Schema of a one stage Pulse-tube refrigerator setup: a The pulse-tube is connected via a rotary valve to the high and low pressure side (p_h,p_l) of a compressor. V_h and V_L are buffer volumes of the compressor. The cooling head has a regenerator, and an isolated pulse-tube. It is connected via an orifice to a buffer volume. **b:** The trajectory of a gas volume close to the cold end X_L or hot end X_H of the pulse-tube. On the right side, the gas volume enters the pulse tube at a lower temperature than leaving it, therefore leading to a net heating effect at the heat exchanger X_H. On the left side, the gas volume leaves the pulse tube at a lower temperature than entering it, leading to a net cooling at X_L. For details see text. Figure adapted from [de Waele, 2011].

McMahon-type pulse-tube refrigerator (PTR) is illustrated in Figure 4.3. The working fluid is helium, with pressures variating between approximately 10 to 25 bar. The hot side of the regenerator is connected alternatingly to the high- and low-pressure side of the compressor. A rotary valve ensures this connection while decoupling the compressor (50Hz) from the cooler, resulting in pulse-tube operating frequencies of about 1-2 Hz

While the working fluid is in good thermal contact with its surrounding in the regenerator, it is thermally isolated from its surroundings in the pulse-tube. Here, pressure changes in the working fluid lead to heating and cooling.

During the compression phase, the gas flows into the pulse-tube via the regenerator — a matrix of solid porous material with high heat capacity and good thermal contact with the working fluid — and the cold heat exchanger X_L. At the hot heat exchanger X_H, gas leaves the pulse tube through an orifice into the buffer at (ambient) temperature T_a until the pressure in pulse-tube and buffer equilibrates. Heat is released via the heat exchanger. When the pressure in the pulse-tube is lower, the gas flows back from the buffer via the orifice. As illustrated in Figure 4.3b, the gas leaves the tube at the hot end X_H with a higher temperature than the inlet temperature T_a, therefore we observe a net heating effect at X_H. Contrarily, the gas enters the pulse tube at the cold end with temperature T_L when the pressure is high, and returns with

a temperature lower than T_L, therefore there is a net cooling effect at X_L.

Compared to other types of cryo-coolers, the pulse-tube has no mechanical displacer near the cold-head that moves the gas through the regenerator. Instead, a buffer volume with flow resistance (orifice) achieves the needed dephasing between the movement of the gas and the temperature or pressure changes. It is therefore less prone to vibrations and electromagnetic interferences. The residual vibrations caused by helium compression and expansion can be successfully decoupled by flexible copper braids. While our standard Helium 4 pulse-tube has two stages at 30 K and 4 K, temperatures down to 1.73 K have been reached using ^{3}He as the working fluid [Jiang *et al.*, 2004] with a three-stage PTR.

Pulse-tube refrigerator Our cryostat is based on a two-stage pulse-tube-refrigerator head (PTR, Sumitomo RP-082B2S) with a cooling capacity of approximately 1 W on the second stage at 4 K. The PTR is connected to a 7 kW compressor (Sumitomo F-70H) running at 50 Hz that is water-cooled with 10 L min^{-1}.

Radiation shields The two stages of the PTR are connected to a nested structure of radiation shields, at temperatures of 30 K and 4 K. These parts are made out of 2 mm-thick polished, gold-plated copper to reduce their emissivity. The shields are fabricated in multiple parts to simplify the assembly through the large CF275 vacuum flanges on the cryogenic side (see Figure 4.2). Custom gold-plated copper parts are added on the shields where the pulse-tube passes through the 30 K shield, to reduce the size of any gaps and limit the blackbody radiation from the exterior. This avoids the use of silver tape often used in cryogenic experiments, as we refrain from the use of any adhesives because of UHV considerations.

Mechanical supports A major technical challenge in building the cryostat is the mechanical connection between parts of different temperatures, such as the 30 K shield and the 300 K chamber, or the 4 K shield and the 30 K shield. These supports have to be mechanically stable, but at the same time their cross-area should be small to reduce the thermal conductance to the cold stages of the cryostat. This is part of the expertise of our collaboration partner *MyCryoFirm*. In their commercial *OptiDry* cryostat, the 30 K shield is connected to the 300 K stainless steel vacuum vessel with epoxied fiberglass tubes. As we refrain from using adhesives such as epoxy, we opt for ultra-thin stainless steel tubes with a wall-thickness of 0.1 mm which are welded to the bottom of the 300 K vessel. Furthermore, these ultra-thin tubes are used in a truss structure, supporting the 4 K shield on the 30 K shield. Because of the thin wall-thickness and the small thermal conductivity of stainless steel — from 4 K to 30 K the heat conductance through the stainless steel supports is approximately a

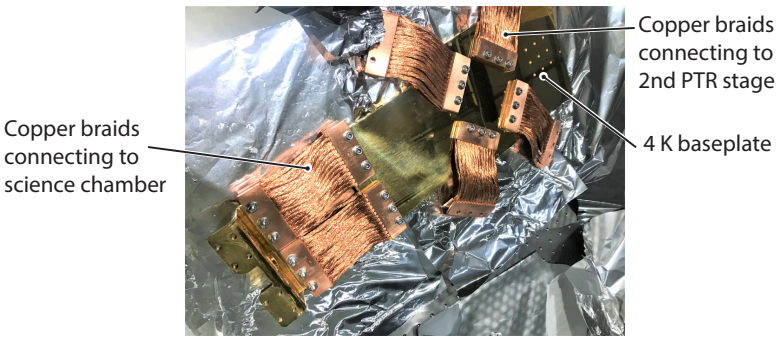

Figure 4.4: Picture of the baseplate and copper braids before assembly: A large gold-plated copper baseplate connects the PTR side of the experiment with the science chamber. To decouple from vibrations, the connections to the 2nd PTR stage, and to the 4 K baseplate in the science chamber is made with flexible copper braids.

factor 700 lower compared to an equivalent (OFHC) copper structure — the heat load on the 4 K platine is kept to a minimum, while the truss structure leads to a good mechanical stability.

Vibrational decoupling To reduce vibrations in the science chamber due to the PTR, the first stage of the PTR is connected to the 30 K radiation shields using ultra-soft, high termal conductivity copper braids (see Figure 4.2). Furthermore, these copper braids are used to connect the second PTR stage at 4 K to a large gold-plated copper baseplate of approximately 6 kg, reaching into the science chamber (see Figure 4.4). There, this copper baseplate is connected by another pair of copper braids to the 4 K baseplate in the science chamber on which the optical assembly is mounted.

This three-fold decoupling leads to a very effective reduction of the vibrational amplitude at the position of the lens holder in the science chamber. In a first test, we measure the vibrations, using a commercial displacement measurement interferometer (attocube IDS3010). Placing the retroreflector of the interferometer at the position of the lens holder, we measure rms vibration amplitudes along the three different axis. At the main vibration frequency component — the operating frequency of the pulse tube at 1-2 Hz — the measured amplitudes are:

- Zeeman axis: 5 nm ,
- Tweezer axis: 11 nm ,
- vertical axis: 5 nm .

The measured background amplitude on the optical table is below 1 nm.

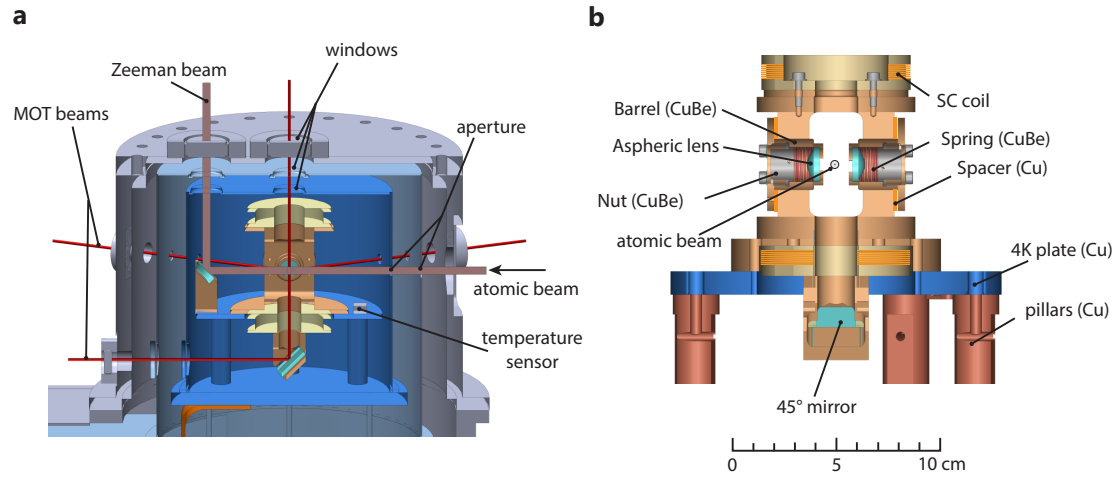

Figure 4.5: Schematic of the optical assembly. a: Cross section of the science chamber. The optical assembly is inside the nested radiation shields. Laser beams enter the chamber through vacuum viewports and windows on the radiation shields. The Zeeman beam and the vertical MOT beams are reflected by $45°$-mirrors at $4\,\mathrm{K}$. Apertures in the heat shields allow atoms to enter from the Zeeman slower. **b**: Cross section of the lens holder, including stress-free mounted aspheric lenses, superconducting coils and the $45°$-mirror for the MOT.

We conclude that the vibrations are sufficiently suppressed for our tweezer experiments. The vibrational amplitude is far smaller than the extent of the tweezer traps ($\sim 1\,\mu\mathrm{m}$) and the atomic motion in the trap ($\sim 100\,\mathrm{nm}$). Furthermore, the main vibration frequency components (1–2 Hz) are far below the trap frequencies (tens of kHz). Therefore the atoms should not experience any heating effects due to vibrations.

4.1.3 Science chamber

The optical assembly is placed inside the $4\,\mathrm{K}$ radiation shield of the science chamber and is illustrated in Figure 4.5. It includes the two stress-free mounted aspheric lenses, and two mirrors for beam steering. Additionally, superconducting coils are mounted on the lens holder. Two temperature sensors are inside of the science chamber, a silicon diode (Lakeshore) next to the lens holder (see Fig 4.5a), and a PT-100 platinum sensor (Lakeshore) on the bottom of the $30\,\mathrm{K}$ radiation shield. In the following, I will detail the different elements of the science chamber.

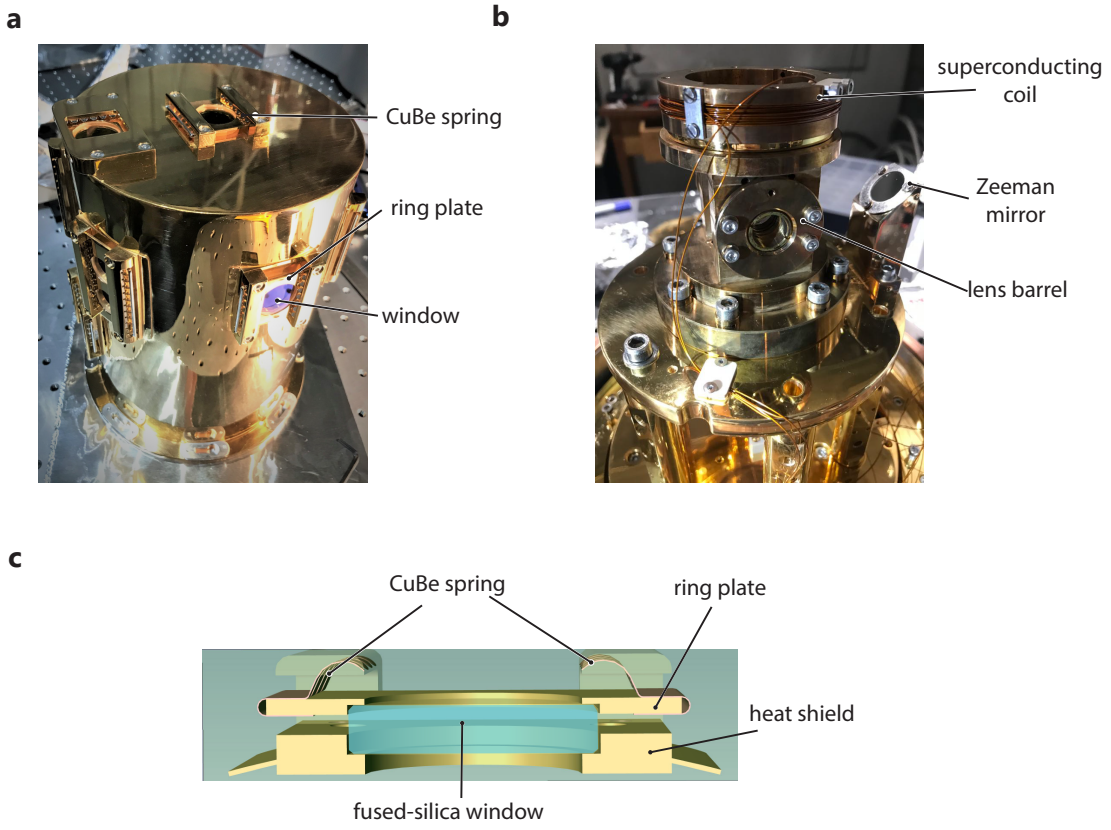

Figure 4.6: Pictures of the setup. a: The 30 K radiation shield with stress-free mounted windows. **b**: The lens holder with superconducting coil. **c**: cross section of a schematic illustrating the stress-free mounted fused-silica window. The window is held in place by a spring-loaded ring plate.

Radiation shields

Inside the science chamber, the radiation shields are two nested cylinders, made out of 2 mm-thick gold-plated copper (see Figure 4.5). Each of the shields has 11 windows, six for the MOT beams, one for the zeeman slower beam, and 4 windows for diagnostic cameras which sit on top or below the horizontal MOT windows. Additionally, each shield has an aperture of 13 mm, to allow atoms to enter the trapping region.

The 5 mm thick fused silica windows are mounted on the heat shield in a stress-free fashion. As we cool down the ensemble from 300 K to 30 K or 4 K, materials contract with different magnitudes: The fused-silica windows contract less than the metal (Copper or Beryllium-Copper) around. Stress from clamping the window, e.g. with a set-screw, can induce optical aberrations due to deformation, but also stress-induced birefringence which would change the polarization of incoming laser beams. Therefore, we designed a stress-free mount for the heat shield windows: they are held in place

with plates that are spring-loaded with a pair of fingerstock gaskets (see Fig. 4.6a).

The top- and bottom MOT and the Zeeman slower windows are anti-reflection coated for blue and infrared light (400 – 500 nm and 750 – 1100 nm) to allow Rydberg excitation. The other windows are coated only for the infrared light.

Optical Assembly

The central structure of the optical assembly — the *lens holder* — is attached to the 4 K baseplate. It features two aspheric lenses, superconducting coils and a 45° mirror. It is milled in a beryllium-copper (CuBe: 98% Cu, 2% Be) block. The material choice is a trade-off, as it has better mechanical properties than copper, while maintaining acceptable thermal conductivity. Furthermore, its electrical conductivity at 4 K is lower than that of copper, reducing the effects of eddy-currents.

Stress-free mounted lenses The two aspheric lenses[1] in f–f configuration are mounted in beryllium-copper barrels (see Fig. 4.5b and 4.6b). Similarly to the windows on the heat shields, the lenses are mounted in a stress-free way, accounting for the differential thermal contraction of CuBe and glass when cooling down. This is especially important to reduce stress-induced optical aberrations or birefringence in the tweezer traps.

The CuBe barrels have a relative thermal contraction between room-temperature and 4 K of [Ekin, 2006]

$$(\Delta L/L)_{\mathrm{CuBe}} \equiv (L_{293\mathrm{K}} - L_{4\mathrm{K}})/L_{293\mathrm{K}} = 0.00316 \quad , \tag{4.1}$$

whereas the lens glass (D-ZLaF52LA, Light Path Technologies) has (at room temperature) a linear coefficient of thermal expansion of

$$\mathrm{CTE} = \frac{1}{L}\frac{dL}{dT} = 6.9 \times 10^{-6}\mathrm{K}^{-1} \quad . \tag{4.2}$$

To account for the differential thermal contraction, we choose the internal diameter of the barrels to exceed the outer diameter of the lenses by 20 µm at room-temperature. This results in a stress-free fit at cryogenic temperatures. To ensure the correct positioning of the lenses at room-temperature and during the cool-down, the lenses are spring-loaded, using a CuBe spring[2] and a nut.

In first tests, the stress-free design was qualitatively verified by a crossed-polariser stress test. This test consisted in placing the sample (the lenses inside of the lens

[1] Lightpath Technologies, NA=0.5, f=10 mm, working distance of 7 mm.
[2] CuBe spring with stiffness of 0.5 N/mm

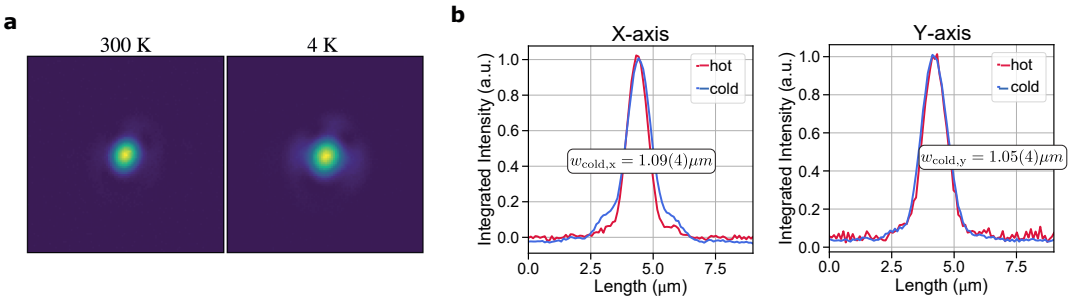

Figure 4.7: Spotsize at room-temperature and 4 K **a**: Camera images of the spotsizes after the chamber. **b**: Comparison of slices integrated along the horizontal or vertical direction. No drastic changes are observed, although minor stress seems to be present in x-direction. Note that the beam passes through 2 vacuum viewports and 4 windows on the heat shields before being imaged onto a CCD camera. The beam has not been realigned at cryrogenic temperatures.

holder) between two crossed-polarizers. Any stress (due to cooling down to 4 K) would lead to stress-induced birefringence and change the transmission through the crossed polarizers. However, no major changes in transmission were detected, leading to the conclusion that our design succesfully prevents stress on the lenses.

In the final setup, we measured the spotsize of a single tweezer before and after the cool-down, to determine if stress is present (see Figure 4.7). Only minor changes in the spotsize are observed.

Compensation for f–f configuration As the CuBe lens holder, and to a lesser extend the lenses, contract when cooling down the ensemble to 4 K, the distance between the two aspheric lenses decreases. Consequently, if the lenses were in f–f configuration at cryogenic temperatures and a laser beam enters and exits the system collimated, the system at room-temperature can be described, in the thin-lens approximation, by a lens with effective focal length f':

$$\frac{1}{f'} = -\frac{\Delta L}{f_{\mathrm{asph}}^2} \quad . \tag{4.3}$$

Here, $f_{\mathrm{asph}} = 10$ mm is the focal length of the aspheric lenses and ΔL the contraction length.

Since the lens-holder is made out of beryllium-copper, its thermal contraction is determined by equation (4.1). We can neglect the thermal contraction of the glass, because of the following argument: In the thin lens approximation, the focal length f

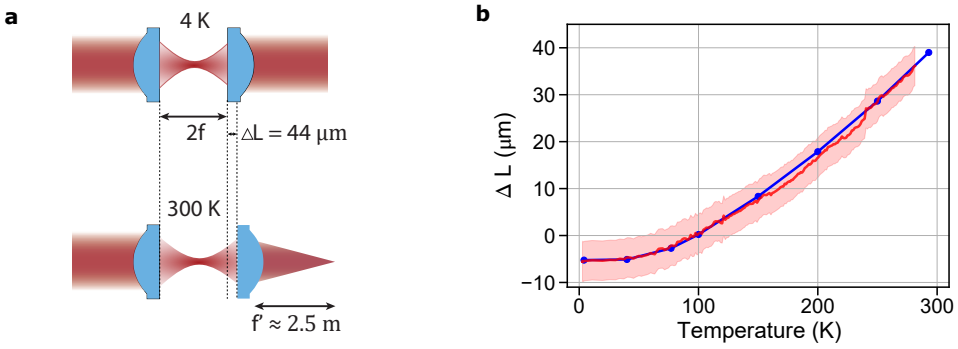

Figure 4.8: Axial Contraction of imaging system. a: Illustration of the f–f configuration, where the distance is gradually reduced when cooling down to cryogenic temperatures. **b**: Measurement of the change in distance ΔL between the lenses, inferred from the size of the beam at a certain distance after the second lens. The red shaded area indicates the standard deviation of the measurement. In blue, the literature values of the relative length contraction of beryllium-copper ([Ekin, 2006]).

is given by:

$$\frac{1}{f} = \frac{n-1}{R} \quad , \tag{4.4}$$

with R the radius of curvature of our plano-convex lens. While the change of R with temperature is governed by the CTE of glass (equation (4.2)), the index of refraction of the lens glass changes similarly:

$$\frac{dn}{dT} = 6.5 \times 10^{-6}\mathrm{K}^{-1} \quad . \tag{4.5}$$

These two effects approximately cancel each other out and we therefore only take into account the contraction of the CuBe lens holder.

Figure 4.8 illustrates the change in effective focal length of our $f-f$ lens setup. Taking into account the distance between the two lenses ($2 \times \mathrm{WD} = 14\,\mathrm{mm}$), we expect a length change of $\Delta L = 44\,\mu\mathrm{m}$. If we neglect the contraction of the lenses, the total system would therefore have a focal length of approximately $f' = 2.5$ m at room-temperature, when collimated at 4 K. As we want the optical system to be collimated at 4 K, we need to pre-compensate the distance between the two lenses at room-temperature by the contraction length ΔL (see Figure 4.8). We realise the pre-compensation with copper spacers between the barrels and holders with a thickness that I gradually reduced by manual lapping until the proper axial spacing between the two lenses was reached.

Figure 4.8b shows a measurement of the contraction of the lens holder, inferred from

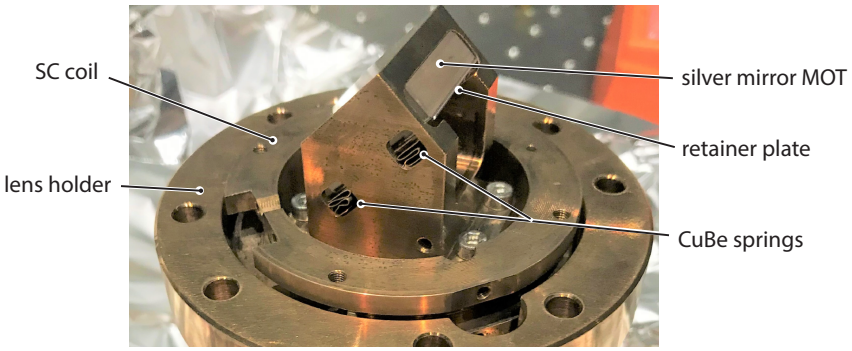

Figure 4.9: Mirror for the vertical MOT beams A silver mirror is mounted in using CuBe springs and a retainer plate, to mitigate stress during cool-down.

the size of the beam at a certain distance after the second lens. In blue, the literature values for the length contraction for beryllium-copper [Ekin, 2006] are compared to our measurement. We find an outstanding agreement between the literature contraction values and the measurement. Furthermore the thickness of the copper spacers is almost perfect, as it deviates only by approximately 5 µm. As a result, we measure that our pre-compensated system has a focal length f' of approximately 2.5 m at room-temperature. At 4 K the system is almost afocal, as the exiting beam focuses at a distance of > 20 m.

Stress-free mounted 45° mirrors Two stress-free mounted 45° silver mirrors are inside the science chamber. A first mirror is mounted on the bottom of the lens holder. It reflects the two vertical MOT beams, as we do not have optical access from the bottom of the chamber. A second mirror is mounted next to the lens holder reflecting the Zeeman beam from the top. This avoids having a cold window at cryogenic temperature facing the hot atomic beam, which would not not transmit the Zeeman laser after becoming opaque due to an accumulation of Rubidium. In contrast, the silver mirror would reflect the laser beam even with accumulation of Rubidium.

Both mirrors are mounted with beryllium-copper springs holding them in place (see Figure 4.9). This mitigates stress due to differential thermal contraction of the materials during cool-down to 4 K.

Superconducting magnetic field coils

Above and below the lens holder are two magnetic field coils (see Fig. 4.5). They can be used for a MOT magnetic field gradient, or for a homogenous bias field, when changing from anti-Helmholtz to Helmholtz configuration.

As current-carrying wires are a major heat source in our cryogenic setup, we opt for superconducting wire for our magnetic field coils. We choose a 0.5 mm diameter, Kapton insulated wire (Supercon Inc.) that has multiple 38 µm-diameter superconducting NbTi wires inside of a copper-matrix, with a copper-to-superconductor ratio of approximately 3:1. The superconductor has a critical temperature of 9.2 K, and we measure the residual resistivity ratio (RRR) of the copper wire to be approximately 230 (see Fig. 4.10).

Each coil is wound around a beryllium-copper form (100 turns with a diameter of 52 mm). The material choice reduces eddy currents compared to copper, as beryllium-copper has a moderate electrical resistivity at cryogenic temperatures (At 10 K [Ekin, 2006]: $\rho_{\mathrm{CuBe}} = 6.92\,\mu\Omega\,\mathrm{cm}$, $\rho_{\mathrm{Cu\ (OFHC,\ RRR\simeq 100)}} = 0.015\,\mu\Omega\,\mathrm{cm}$). In a preliminary test setup at 4 K, we measured characteristic magnetic field decay times of approximately 1 ms. In the final setup however, we notice that the magnetic field the atoms experience is negligible only after 40 ms. This is most likely caused by the presence of pure copper parts (e.g. the 4 K shield) close to the coils in which eddy currents develop.

In (anti-)Helmholtz configuration the coils produce (magnetic field gradients of 4.3 G/cmA) peak magnetic fields of 23 G/A.

Wiring between the cold-plate and the exterior The superconducting coils are connected to the 300 K exterior via a 0.6 mm-diameter Kapton-insulated copper wire, and the connection between the copper and the superconducting wire is made on the 4 K base-plate in the science chamber.

On its way from the 300 K exterior to the 4 K base plate, the wire is thermalised at multiple locations. First, on a 40 mm tall chimney on the 30 K shield. Then, it is wrapped tightly around the pulse tube. In the science chamber, the wire is wound around and clamped on one of the pillars (see Figure 4.5).

For diagnostic purposes, the superconducting coils are furthermore connected to the 300 K outside via an additional 0.25 mm Kapton-insulated copper wire. This second pair of wires for each coil lets us determine the resistance in a four-wire-measurement. Figure 4.10 illustrates a typical 4-wire measurement that was conducted during the cool-down of the cryostat. Below the critical temperature, the coils enter the superconducting phase and the resistance of the coils vanishes. In the measurement the resistance jumped to approximately 1 mΩ around 9.2 K, before vanishing completely below 6 K. This indicates that the superconducting wire is not in perfect thermal contact with the coil holder during the cool-down.

Considerations on wire choice The copper wires from the 300 K exterior to the 4 K cold plate are a significant heat load for the cryostat. This became apparent

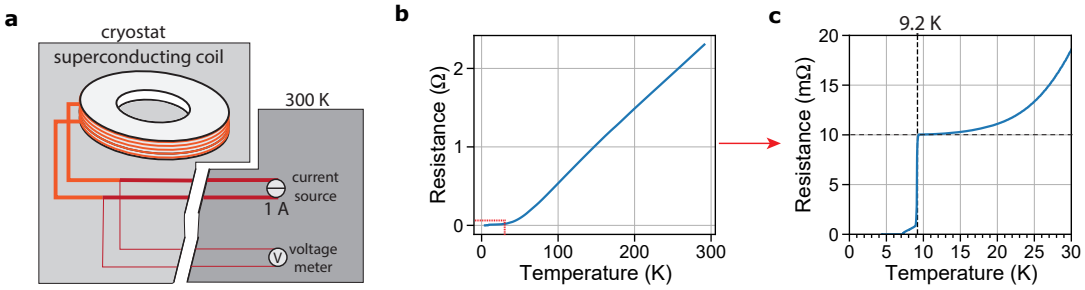

Figure 4.10: Wiring for 4-wire measurement. **a**: Each superconducting coil is connected to two pairs of copper wires leading to the 300 K exterior. The $0.6\,\mathrm{mm}$-wires are the main current-carrying wires, and the $0.25\,\mathrm{mm}$-wires can be used to determine the coils resistance by measuring the voltage drop over the coils at a known current. **b**: Example of a typical 4-wire measurement during cool-down in a test cryostat. **c**: Zoom into (b) for low temperatures. Below the critical temperature of $9.2\,\mathrm{K}$, the coils enter the superconducting phase and their resistance vanishes. The residual resistivity ratio of the copper in the wire is approximately 230, as can be seen from the ratio of resistances at room-temperature (2.3 Ω) and at $10\,\mathrm{K}$ (10 mΩ).

to us, as we first connected the $0.25\,\mathrm{mm}$-diameter copper wire to the superconducting coils. When driving the coils with currents above 1 A using this wire, the heat load on the cold head was too high. We therefore changed to the $0.6\,\mathrm{mm}$-diameter copper wire to drive the coils, leaving the smaller $0.25\,\mathrm{mm}$-diameter copper wire for possible 4-wire measurements to determine the state of the superconducting coils (see above). I detail further considerations for the wire choice in the following.

The diameters for high-current wires have to be chosen to minimize the overall heat load on the 4 K stage of the cryostat, including the heat influx from outside and Joule heating [McFee, 1959].

The heat introduced by a current I flowing through a small length of wire $d\ell$ with cross section A and resistivity ρ is

$$d\dot{q} = \rho(T)\frac{d\ell}{A}I^2, \tag{4.6}$$

and therefore scales inversely with the wire cross-section A and thus with the square of the diameter.

However, the thermal conductance along the wire is

$$\dot{q} = \lambda(T)A\frac{dT}{d\ell}, \tag{4.7}$$

with the thermal conductivity λ. It scales linearly with wire cross-section (square of the diameter).

Whereas one would like to choose the smallest possible diameter to minimize the heat leak from the 300 K exterior down the wires into the cryostat, Joule heating becomes a problem for cables with small diameters, such as for the 0.25 mm-diameter wire in our case. Therefore a compromise has to be considered when selecting the optimal cable diameter: the sum of the heat conduction along the wire and the heat introduced by Joule heating has to be minimized.

In the following, I make a basic approximation of the optimal wire parameters for our cryostat, under the assumption of constant thermal conductivity $\lambda(T) = \lambda$ and electric resistivity $\rho(T) = \rho$. From equation (4.6) and (4.7), one can find the general equation:

$$\dot{q} = I\sqrt{2\rho\lambda(T_{\max} - T)} \quad , \tag{4.8}$$

where $T_{\max}$ is the maximal temperature along the wire.

To minimize the heat flowing into the low-temperature region $\dot{q}_L$, the maximum temperature should be minimal (see eq. (4.8)), that is, when $T_{\max}$ is equal to the temperature T_H at the hot (room-temperature) end of the cable.

From equations (4.6), (4.7) and (4.8) one can then derive the optimal wire parameters:

$$\frac{LI}{A} = \frac{[\dot{q}_L]_{\min}}{\rho I} = \sqrt{2\frac{\lambda}{\rho}(T_H - T_C)} \quad , \tag{4.9}$$

with T_H and T_C the temperatures at the hot and cold end of the wire.

In our case, assuming room-temperature values for λ and ρ, we find an optimal wire size for the connection between 290 K and 4 K with the parameters:

$$LI/A \simeq 4 \times 10^6 \mathrm{A/m} \quad . \tag{4.10}$$

For a wire length of 1 m and a current of 2 A, we find that an optimal wire has a diameter of approximately 0.8 mm. In reality the situation is more complicated, as λ and ρ vary a lot with temperature. However, the value of equation (4.10) only changes by approximately 30% when considering the real parameters. The optimal wire parameters, taking into account the temperature variance of λ and ρ are described in the literature [Ekin, 2006].

This highlights that the wire with 0.25 mm-diameter was too small. It is furthermore interesting to know how much a deviation from the optimal parameters changes the heat load on the cryostat. When the selected cross-section A is bigger than the optimal

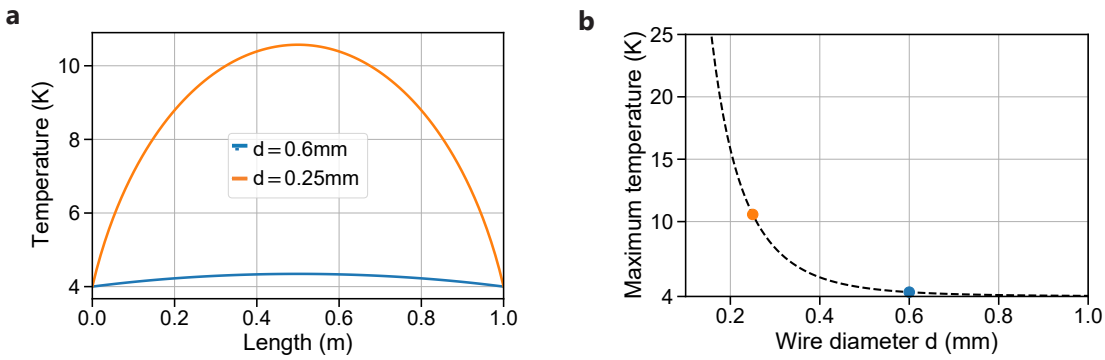

Figure 4.11: Temperature profile of copper wires with different diameters. A 1 m long copper wire with a cross-section diameter d is driven with a current of 1 A. On both sides the wire is thermalised to 4 K. The resulting peak temperature is strongly dependent on the diameter d and can reach temperatures above the critical temperature of the superconducting coil.

one A_{opt}, we can find for the ratio between the non-ideal heat flow $\dot{q_L}$ and the minimal heat flow:

$$\frac{\dot{q_L}}{[\dot{q_L}]_{\text{min}}} = \frac{1}{2}\left[\frac{A}{A_{\text{opt}}} + \frac{A_{\text{opt}}}{A}\right] \quad . \tag{4.11}$$

A similar relation can be found when a smaller cross-section is selected [McFee, 1959].

This means that when the diameter d is wrong by a factor of 2, the heat flow on the cold end of the wire is approximately doubled.

This basic model highlights the importance of choosing the right wire diameter and gives a good idea of the wire diameter that we have to choose. However, the real situation is more complicated, as our cryostat has two stages and the wire is thermalised in multiple places.

Another difficulty is the approximate distance of 1 m between the PTR cold-head and the cold-plate of the science chamber. The wire is thermalised to 4 K in both places, but can significantly heat up in between, especially if the wire diameter is too small for a given current.

The temperature distribution along a wire of length L that is thermalised on both ends to the same temperature of $T_C = 4$ K is symmetric, with a maximum temperature at $L/2$. We are interested in finding the maximum temperature, this time considering the temperature dependence of the thermal conductivity at low temperatures. According to the Wiedemann-Franz-law, the dependence is approximately linear for low temperatures, with:

$$\lambda(T) = \beta T \quad . \tag{4.12}$$

For our copper wire, $\beta = 158$ W/m/K^2 [Ekin, 2006] (assuming RRR = 100).

From equation (4.6) and (4.7), one can derive the differential equation:

$$\frac{d}{dx}(T\frac{d}{dx}T) = \frac{-\rho I^2}{\beta A^2} \quad , \tag{4.13}$$

which can be solved using substitution to arrive at:

$$T(x) = \sqrt{-\alpha(x - c_2)^2 + c_1} \quad , \tag{4.14}$$

where

$$\alpha = \frac{\rho I^2}{\beta A^2} \quad , \tag{4.15}$$

and

$$c_2 = 0.5L, \quad c_1 = \alpha c_2^2 + T_c^2 \quad . \tag{4.16}$$

The maximum temperature is therefore inversely proportional to the area A of the wire. Its strong dependence on the wire diameter is illustrated in Figure 4.11. A wire with a diameter of 0.25 mm can easily reach temperatures above the critical temperature of the superconducting coil. This is especially a problem, when the wire is not perfectly thermalised to 4 K on one or both sides, as we shall see later. The wire diameter choice of 0.6 mm however seems suitable for our purposes.

4.2 Performance characterization of the cryostat

To demonstrate that the new experimental apparatus fulfils all necessary criteria for an operation with large-scale tweezer arrays, we characterized its performance in a series of tests. First, I describe the basic operation of the cryostat. Then, I investigate all possible experimental heat loads and estimate the heat budget. Finally, I characterize the operational regime of the superconducting coils.

4.2.1 Basic operation: cool-down and heat-up

Before operating the Cryostat, we evacuated the system until we reached a residual pressure in the 1×10^{-8} mbar range. First, we connected a turbomolecular pump, and

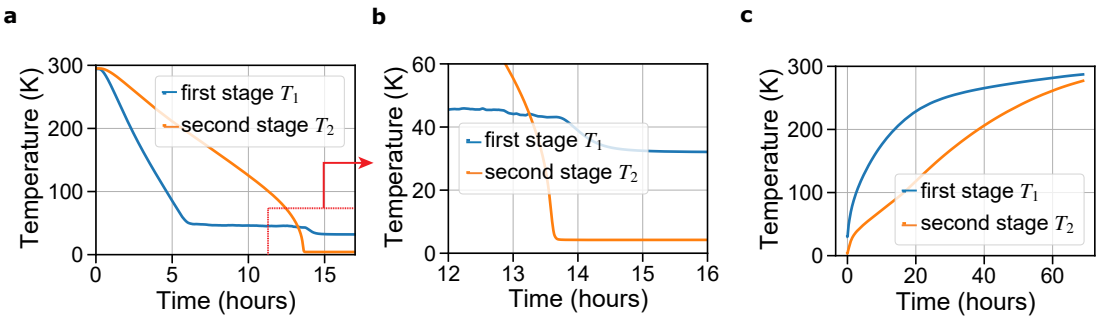

Figure 4.12: Temperature behaviour during cool-down and warm up. a: Typical cool-down, the base temperatures are reached after approximately 15 hours. **b:** zoom into (a) for low temperatures. **c**: Typical warm-up, the system can be opened after approximately 3 days.

degassed and activated the titanium sublimation ion pump and the non-evaporable getter pump at pressures below 5×10^{-7} mbar (as measured by the turbomolecular pump). This pressure is limited mainly by the absence of a bake-out of the system and by the numerous elements inside of the chamber, some of which have a large surface area, such as the copper braids.

Then, we switch on the pulse tube refrigerator, and the temperature decreases until it reaches a steady-state value after approximately 15 hours (see Figure 4.12). The temperature is measured with two thermometers (see Fig. 4.2): a silicon diode (Lakeshore) next to the lens holder on the 4 K-baseplate (T_1) and a PT-100 platinum resistance thermometer (Lakeshore) on the bottom of the 30 K radiation shield in the science chamber (T_2). After the cool-down, the pressure measured by the ion-pump current is approximately 4×10^{-10} mbar.

Warming-up the cryostat to room-temperature takes a minimum of three days, if the pulse-tube is switched off and the vessel is kept under vacuum (see Figure 4.12b). In practice, we usually switched off the cryostat Fridays and opened the vessel Mondays to change the test configuration (see tests below). This could however be accelerated to about half a day by flooding the chamber with dry nitrogen gas to supplement the radiative heat transfer by the much more efficient convective transfer.

4.2.2 Preliminary tests and heat budget evaluation

In a series of tests with various configurations, we evaluated the response of the cryostat to different heat loads that we expect during the operation of the experiment.

Starting with a configuration with a minimal experimental heat load, we sequentially added elements to the science chamber and independently evaluated each contribution.

Cool-down with minimal heat load We first cooled-down the system with a minimal heat load, without the superconducting coils and the wiring from 4 K to 300 K. We further replaced all windows in the heat shields with gold-coated copper plugs and sealed the aperture for the atomic beam in the heat shields. The base-temperature in this configuration is $T_1 = 30.1$ K and $T_2 = 3.2$ K.

In order to determine the cryostats response to a given heat load, we applied controlled power through two heaters and measured the temperature increase, as illustrated in Figure 4.13. The two heaters were positioned next to the lens holder in the science chamber (H_1) and on the 4 K-baseplate just beneath the PTR 4-K stage on the cryostat side (H_2). Temperatures were measured in proximity to the heaters: We added two Cernox temperature sensors next to the lens holder (C_1) and on the PTR 4-K stage (C_2). After we applied a given power through one of the heaters, we waited approximately 5 – 10 minutes for the temperatures to equilibrate before measurement.

As can be seen in Figure 4.13b, the temperature increase is maximal on the lens holder, when a heat load is applied in the science chamber. Above a base temperature of 4 K, this increase is approximately $4\,\mathrm{K\,W^{-1}}$. If the heat load is applied on the cryostat side close to the second PTR stage, the temperature increase is smaller, with approximately $2\,\mathrm{K\,W^{-1}}$.

This heater test serves as a reference, as we can compare future temperature increases caused by additional heat loads to the controlled heating power applied during this test. Note that we removed both the heaters $H_{1,2}$ and the Cernox temperature sensors $C_{1,2}$ for the final configuration.

Cool-down with windows In a second cool-down, we mounted the stress-free fused silica windows on both of the radiation shields, and opened the aperture for the atoms. The Zeeman slower was not connected, but a blind flange was at its place.

The base temperature was barely increased (< 0.1 K). This shows that the windows block most of the black-body radiation from the outside. Furthermore, the small aperture in the heat shields for the atomic beam does not contribute significantly to heating. We repeated the experiment with the heaters $H_{1,2}$, but the results were similar with respect to our measurement precision.

Cool-down with superconducting coils Next, we mounted the superconducting coils on the optical assembly, and connected the four 0.6 mm-diameter copper wires from the 4 K baseplate to the 300 K exterior. Additionally, four 0.25 mm-diameter copper wires were already connected for a potential four-wire measurement (see above).

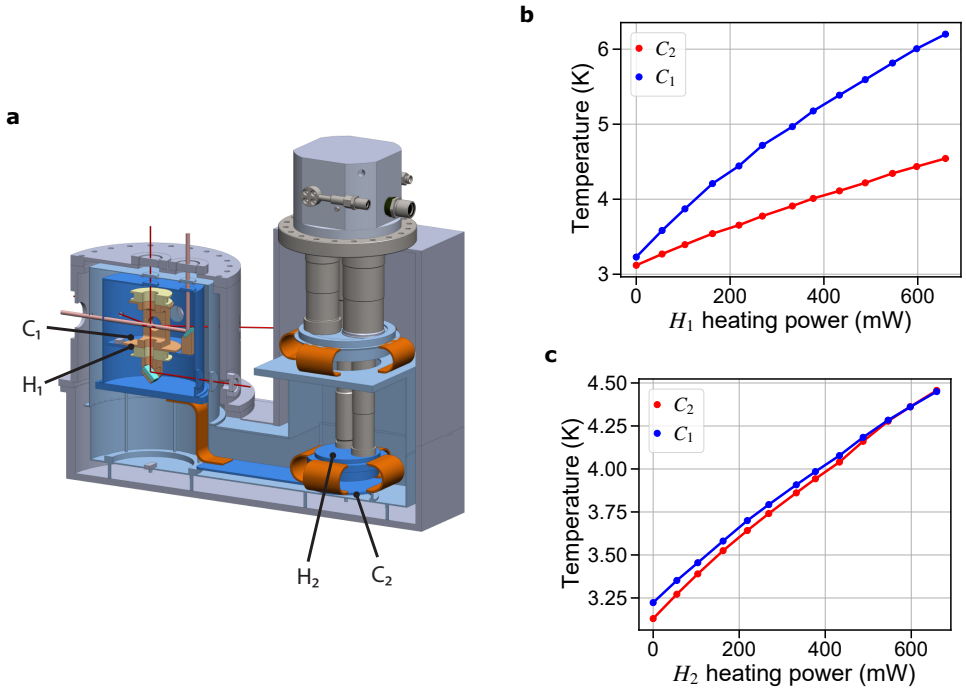

Figure 4.13: Temperature increase for controlled heat load a: Heater positions (H_1,H_2) and temperature sensor positions (C_1,C_2). **b** Heater H_1 next to the lens holder. The temperature increase is maximal next to the lens holder and approximately $4\,\mathrm{K\,W^{-1}}$. **b**: Heater H_2 on the 4 K-baseplate beneath the PTR 4-K stage. The temperature increase is approximately $2\,\mathrm{K\,W^{-1}}$.

After cool-down, we measured a base-temperature of $T_1 = 32.1$ K and $T_2 = 4.2$ K. I compare the temperature increase of 1 K with a basic calculation in the following.

The conduction heat flow $\dot{q}$ along one cable with length L and cross-section A is

$$\dot{q} = \frac{A}{L} \int_{4\mathrm{K}}^{300\mathrm{K}} \lambda(T) dT \tag{4.17}$$

The thermal conductivity λ is strongly dependent on the temperature for high-purity metals, such as copper in electrical cables. Tabulated values of this integral can be found in [Ekin, 2006], and for high-purity (ETP) copper $\int_{4\mathrm{K}}^{300\mathrm{K}} \lambda(T) dT = 165\,\mathrm{kW\,m^{-1}}$.

For our cables with an approximate length of 2 m, we find a combined conduction heat flow of around 425 mW. The 0.6 mm-diameter cables contributes with about 360 mW, whereas the 0.25 mm-diameter cables with about 65 mW. This number roughly agrees with the measurements in Figure 4.13, considering that we did not measure the cable length and do not know the purity of the copper inside of the cable.

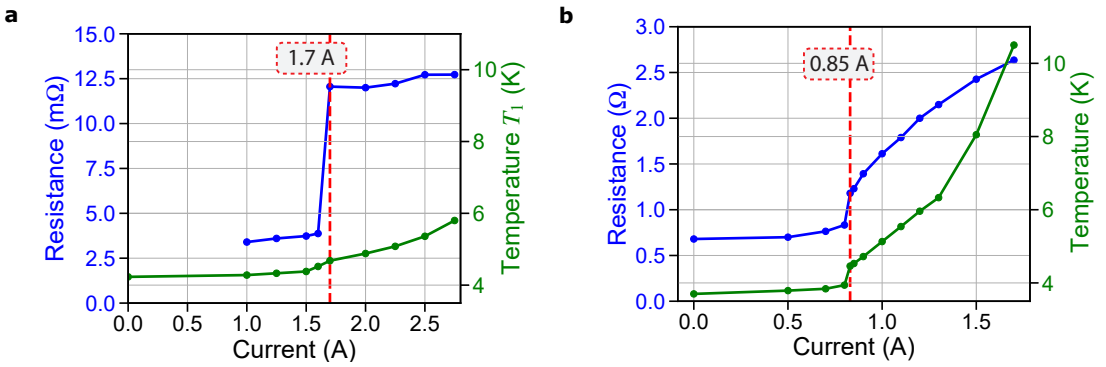

Figure 4.14: Characterization of the SC coils a: In a four-wire measurement, we determine the resistance of the coils for a given current through the coils and measure the increase in temperature T_1 on the baseplate of the lens holder in the science chamber. Above a current of 1.7 A, we observe a jump in the resistance of the coil, indicating a partial transition to the normal state. Whereas the heat load is small in the superconducting state and mainly caused by the connecting copper wires, the whole coil contributes to heating above the transition. **b**: When sending the current through the smaller $0.25\,\mathrm{mm}$ wire, the Joule heating has a drastic effect, highlighting the importance of the correct diameter choice (in our case $0.6\,\mathrm{mm}$). Here, the resistance is the coil plus the copper wires leading to the exterior.

Operation of the superconducting coils Next, we sent current through the superconducting coils to evaluate the additional heat load due to Joule heating of the current-carrying wires. At the same time, we measured the resistance of the superconducting coils in a four-wire measurement (see Fig. 4.10), to determine the state of the superconducting coils.

Figure 4.14a illustrates the measurement of temperature and resistance for increasing current. At a current of 1 A, the increase in temperature is approximately 0.1 K. For currents up to 1.7 A, this temperature increase is mostly attributed to Joule heating in the 0.6 mm-diameter wire connecting to the superconducting coils. For higher currents however, we observe a jump in the resistance of the coils, indicating that the coils partially reach a temperature over the critical temperature of 9.2 K and transition to the normal state. As the temperature of the lens holder is still below the critical temperature, we assume that the thermal contact between the kapton-insulated SC-wire and the CuBe-form of the coil is not sufficient for good thermalization.

Above this transition, the temperature increases in a steeper way with increasing current, as the coil contributes to Joule heating. At a current of 2.5 A, we reach a temperature of 5.4 K. As we shall see in Chapter 5, the reachable magnetic field

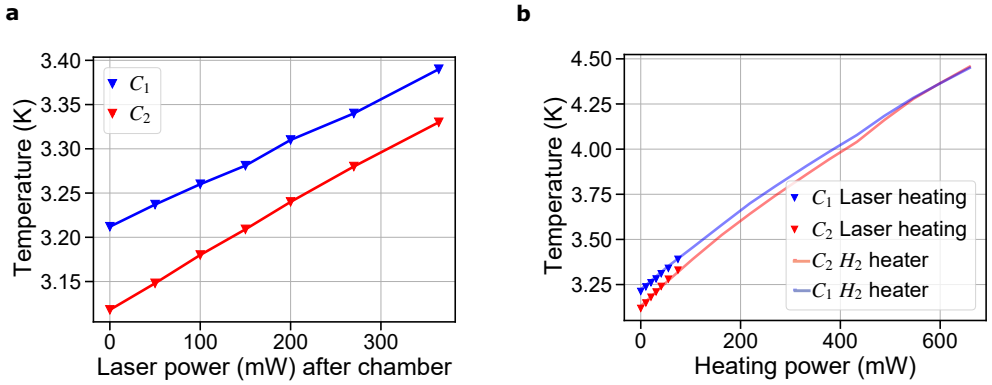

Figure 4.15: Temperature increase for laser power a: Increase in temperature inside the cryostat for a given laser power through the aspheric lenses. The temperature is measured with $C_{1,2}$ (see above), and the laser power is measured after the chamber. **b**: Overlay of the data with Figure 4.13, assuming that the 9% loss of laser power at each lens entirely contributes to heating.

gradients of up to 7.3 G/cm (corresponding to currents of 1.7 A) are more than enough for the operation of a MOT and the loading of a tweezer array.

In a first test before the 0.6 mm-diameter wire was installed, we tested the superconducting coils with the 0.25 mm-diameter wire that we later used for the four-wire measurement setup (see Figure 4.14b). Although we were not able to measure the coils resistance directly in a 4-wire measurement, we still observed a jump in the total resistance (superconducting coils plus the cables to the 300 K exterior). With the smaller than optimal wire (see above), the Joule heating effect was much more pronounced, reaching a temperature of above 10 K for a current of 1.7 A. This highlights the importance of the above discussed choice of wire diameter.

Operation with high laser power To use the platform for large-scale quantum simulation, we need to send a high laser power through the aspheric lenses. For 1000 atoms we need about 2000 traps which equals to approximately 4 W of laser power at the used wavelength of 815 nm. Part of the laser power however is absorbed or reflected by the ITO coating of the lenses and does not exit the cryostat. Therefore, it is a major heat load to consider. Both of the aspheric lenses are coated with a 120 nm thick coating of ITO, which has a specified transmission of 91% at a wavelength of 815 nm. Of the 9% non-transmitted light, about 1–2 percentage points are due to absorption of the ITO, whereas the rest of the light is reflected and may or may not exit the cryostat.

Figure 4.15a shows the temperature increase in the cryostat, measured with the

same sensors $C_{1,2}$ as above, for a given laser power. Again, we let the temperature settle for at least 5 minutes before measurement and measured the laser power after the chamber. In 4.15b, we compare the data to the heater measurement (Fig. 4.13b), assuming that the full 9% of the light per lens is contributing to heating. The data fits remarkably, leading to the conclusion that indeed most of the light that is not transmitted by the lenses stays in the cryostat and is eventually absorbed by the surrounding surfaces. Note however, that the data is overlayed with the H_2 heater data. This leads to the conclusion that most of the laser light is reflected by the ITO coating and absorbed on other parts of the 4 K environment, e.g. the heat shields.

In summary, the absorption of laser power is not a hindrance to utilizing the machine for large-scale quantum computation. Even for 4 W of laser power, the temperature increase would be less than 2 K, as the heat load is about 340 mW per Watt of laser power. Moreover, the thickness of the ITO coating could be reduced.

Summary of all heat loads The performance tests are summarized in Table 4.1. In the final configuration, we create at least 1000 traps and send 1.6 A through the superconducting coils. The combined increase of the base temperature is approximately 1 K, leading to a temperature of $T_1 = 5.2$ K.

The base temperature is therefore still relatively low and significantly lower than the critical temperature of the superconducting coils of 9.2 K. Extrapolating the data, we should be able to use this kind of platform for over 6000 traps, which shows that a cryogenic tweezer platform would be capable of performing large-scale quantum simulation. However, we have not tested the platform in this regime because we do not have the required laser power.

Images of the setup To give the reader an impression of the new cryogenic setup, I have attached images of the experiment in Appendix A.

Test conditions	Temperature 2nd stage
minimal heat load, no wires, no light, plugged windows and atom beam aperture	3.2 K
windows and open atom aperture, no light, no wires	3.3 K
windows and open atom aperture, SC coils and wires, no current, no light	4.2 K
windows and open atom aperture, SC coils and wires, current 1.6 A , no light	4.52 K
windows and open atom aperture, SC coils and wires, current 1.6 A , 2 W laser power	5.2 K

Table 4.1.: Summary of performance tests: Each configuration including the temperature measured on the 4 K baseplate in the science chamber. For the first three tests, the cryostat was opened to change the configuration and cooled-down anew.

4.3 Conclusion

In this chapter, I presented the design and characterization of a new cryogenic tweezer platform for large-scale quantum simulation.

First, I gave an overview over the new cryogenic platform that shares some main characteristics with our room-temperature setup: An atomic source, and a science chamber with aspheric lenses and magnetic field coils, to load single atoms into the tweezer traps. However, the design of the science chamber is heavily modified due to the experimental challenge of cooling down the main parts to 4 K.

After illustrating the ultra-high vacuum cryostat design using a pulse-tube refrigerator, I detailed our solutions to the experimental challenges that involve thermal contraction, conduction and electric resistivity.

Finally, I demonstrated in a series of tests that the new platform indeed manages to keep low temperatures with all heat loads present in an experiment with large tweezer arrays. In the next chapter we shall see, that the large pumping speed of the surfaces at 4 K close to the atoms indeed leads to a vacuum orders of magnitude lower than on our room-temperature setup resulting in long vacuum-limited trapping lifetimes of single atoms in tweezers of over 6000 s, an approximately 300-fold increase over the 20 s lifetime of the room-temperature setup.

Compared to our room-temperature setup, the cryogenic setup does not yet include electrodes to actively control the electrostatic environment in the focal plane of the lenses. For Rybderg experiments, this is a crucial ingredient however and we plan

to include them in the near future. Similarly, we plan to add antennas inside of the chamber to drive microwave transitions between different Rydberg levels.

Chapter 5

Arrays of Single Atoms in a Cryogenic Environment

The last chapter detailed the design of the new cryogenic tweezer platform. In this chapter, I demonstrate the trapping of single ^{87}Rb atoms in a cryogenic environment at 4 K with trapping lifetimes exceeding 6000 s.

First, I detail the laser system used to trap a cloud of Rubidium atoms in a magneto-optical trap (MOT) and the measurement of the lifetime of the atoms in the MOT. Then, we trap single atoms in tweezers, and measure their vacuum-limited lifetime. We shall see, that it is not trivial to measure these long lifetimes, as other effects can lead to losses, such as heating mechanisms. We therefore study these effects carefully, find a suitable measurement method and finally measure a lifetime exceeding 6000 s. Parts of this chapter are published in Physical Review Applied [Schymik *et al.*, 2021](see Appendix E).

Note: After the first set of lifetime measurements, we have noticed a vacuum leak in the flange of the 300 L/s ion pump. After fixing the leak, the vacuum pressure as measured by the ion pump decreased from previously 3×10^{-7} mbar to 4×10^{-10} mbar. Correspondingly, we measured an increase in the single-atom lifetime in the tweezers from previously 335 s to over 6000 s. Note that a part of our data, e.g. the lifetime of the magneto-optical trap, was only measured before fixing the leak. In the following, I will note if a measurement was done pre- or post-leak.

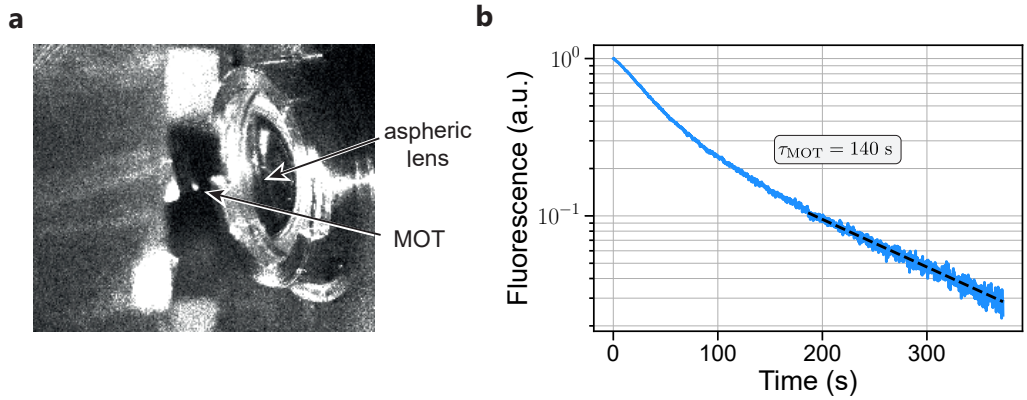

Figure 5.1: Lifetime of atoms in the magneto-optical trap. a: Image of the MOT with a CCD camera. On the right, the aspheric lens can be seen. **b:** Decay of the fluorescence of the MOT. A fit to the low-density tail of the distribution results in a lifetime of 140 s.

5.1 Lifetime of atoms in a magneto-optical trap

Creating a magneto-optical trap is the first step towards loading single atoms in optical dipole traps. As background-gas collisions are also present in a MOT, this furthermore allows us to obtain a first estimation of the trap lifetime. On our room-temperature experiment, the MOT lifetime is with $\tau_{\mathrm{MOT}} = 20$ s similar to the lifetime of the atoms in the tweezer. In cryogenic experiments, MOT lifetimes in excess of 1 h have been measured [Willems and Libbrecht, 1995].

Laser system We operate the oven at approximately 100 °C. The hot atomic beam of ^{87}Rb atoms is slowed with a spin-flip Zeeman slower to trap atoms in a magneto-optical trap in the center of the science chamber. The MOT cooling light consists of three pairs of counter-propagating beams, with an $1/e^2$ radius of 1.7 mm and a power of 1 mW per beam. The light is detuned by -4.5Γ from the $F = 2 \rightarrow F' = 3$ transition of the D_2 line of ^{87}Rb. The laser is frequency-stabilized on the $F = 2 \rightarrow F' = (1, 3)$ cross-over transition using a standard Doppler-free spectroscopy and detuned with a double-pass acousto-optical modulator (AOM). Since the atoms have a small chance of decaying into the $F = 1$ state due to off-resonant scattering over $F' = 2$, we further use a repumping scheme. It consists of three pairs of counter-propagating beams on the same path and and with the same size as the cooling light, but with a power of 0.1 mW per beam. The repump light is frequency-stabilized on the $F = 1 \rightarrow F' = 2$ transition of the D_1 line. We typically apply a magnetic-field gradient of 6 G/cm using the superconducting coils in the science chamber.

MOT lifetime After loading the MOT for approximately 500 ms, we stop any further loading of the MOT by switching-off the Zeeman laser light and closing the gate valve to the oven by hand in about 1 s. The fluorescence decay of the MOT is measured with a CCD camera, as illustrated in Figure 5.1. The atom number loss from the trap is typically modelled with:

$$\dot{n} = -\frac{1}{\tau_{\mathrm{MOT}}} n - \beta n^2, \tag{5.1}$$

where n is the atom density in the trap that is proportional to the measured fluorescence light in our case. For high densities, the decay is dominated by two-body collisions with collisional constant β. For low atom densities, one-body losses are observed with rate τ_{MOT}^{-1} which is usually cause by collisions with the background gas. For a more in depth analysis of collisions in a MOT, see e.g. Ref. [Sesko *et al.*, 1989].

We have furthermore noticed that the decay is also sensitive on the alignment of the relatively small laser beams. We attribute this to a loss from atoms in the outer region of the MOT, where beam intensities are not perfectly balanced.

As illustrated in Figure 5.1, we extract α from the exponential decay at low densities and measure a lifetime of $\tau_{\mathrm{MOT}} = 140$ s, which is seven times higher than on our room-temperature setup. It corresponds to vacuum pressures in the low 10^{-12} mbar regime, and demonstrates the effect of cryopumping of the 4 K-shields surrounding the atoms, especially, since the vacuum pressure in the 300 K part of the system is measured to be in the 10^{-7} mbar regime (as measured by the ion pump current). Note that this measurement was done before fixing the vacuum leak in the ion pump.

5.2 Lifetime of single atoms in tweezer arrays

To create arrays of single atom, we use a 830 nm titanium saphire laser light source and a spatial light modulator, as explained in Section 2.1.2. With the SLM, we create arrays of tweezer traps in the focal plane of the aspheric lenses.

To demonstrate the scalability of the new platform, we would like to measure the vacuum-limited lifetime of an atom in a tweezer, or in other words the survival probability of a single atom in a tweezer as a function of the hold time (see Fig. 2.10). In practice, we use a trap array (e.g. a 9×9 square array), take two fluorescence images with varying time separation and analyse for each initially filled trap if it is still occupied in the second image. To extract a vacuum-limited lifetime from this measurement, we need to be sure that the losses observed in the second fluorescence

image are caused entirely by background gas collisions.

In this section, I show that this is not a trivial task, as different mechanisms lead to atom loss on the long time scales of the lifetime measurement. In the following, I present our careful studies of theses loss mechanisms.

First, I present a study of heating mechanisms in the tweezer traps. Compared to our room-temperature setup, this is especially important on the new cryogenic setup, as heating occurs on a timescale that is shorter than losses due to background collisions at these low vacuum pressure levels. These heating effects can be suppressed by cooling the atoms and I will present how we cool down atoms in the traps to approximately 20 µK using polarization gradient cooling. In this context, I will demonstrate that further loss mechanisms which occur in the presence of cooling light: correlated losses due to collisions with H_2 atoms at 4 K and another loss mechanism in presence of the cooling light that is dependent on the power in the repump laser. Then, I show that on our cryogenic setup, ballistic collisions with atoms from the oven can decrease the lifetime in the traps, which is why we close the gate valve (automatically) between two fluorescence images.

We finally find a measurement method that minimizes the effects of all other loss mechanisms, measuring a trap lifetime exceeding 6000 s, a lower bound on the expected vacuum-limited lifetime. With this, we have achieved the goal of our cryogenic setup to increase the lifetime by several orders of magnitude compared to our room-temperature setup.

5.2.1 Heating mechanisms and polarization gradient cooling

First, we try to measure the lifetime τ by evaluating the atom number loss between two fluorescence images separated by a time Δt. No cooling light is applied in between the two images. If the losses were purely due to background collisions, one would expect an exponential decay of the survival probability $P(t)$ of an atom in a single tweezer:

$$P_{\mathrm{vac}}(t) = \exp(-t/\tau) \tag{5.2}$$

Figure 5.2 illustrates the experiment with a square array of 9× 9 traps with a spacing of 10 µm. We find that the decay is not exponential. Note that this measurement was performed before fixing the leak.

Trap light scattering Although the dipole trap at 830 nm is far red-detuned

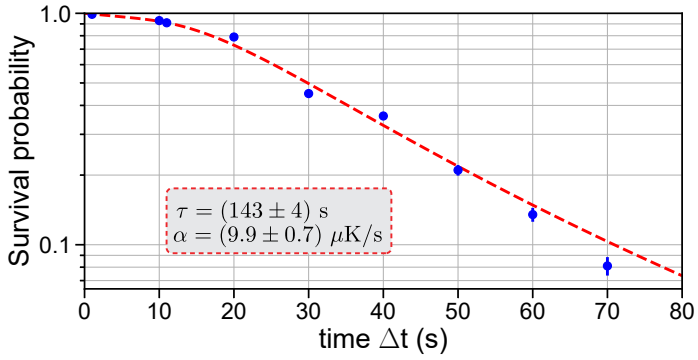

Figure 5.2: Lifetime of an atom in the tweezer without cooling. The survival probability between two images with time separation Δt is not a pure exponential decay. This can be modelled with a linear heating rate due to off-resonant scattering of the trapping laser light [Darquié, 2005].

from the atomic resonance of Rubidium, atoms in the trap scatter photons with a finite rate leading to a linear increase of the atom temperature with time. The scattering rate at this wavelength is $\Gamma_{\mathrm{sc}} = 32\,\mathrm{s}^{-1}$, with a recoil energy of $E_{\mathrm{recoil}} = 0.36\,\mu\mathrm{K}$. We define the linear heating rate as [Grimm, Weidemüller, and Ovchinnikov, 2000]:

$$\alpha_{sc} = 2T_{\mathrm{recoil}}\Gamma_{\mathrm{sc}} = 5.75\,\mu\mathrm{K\,s}^{-1}. \tag{5.3}$$

Assuming a 3D isotropic harmonic trap, it has been shown ([Darquié, 2005]) that linear heating leads to a survival probability of:

$$P_{\mathrm{survival}}(t) = P_{\mathrm{vac}}(t)P_{\mathrm{heat}}(t), \tag{5.4}$$

with:

$$P_{\mathrm{heat}}(t) = 1 - \exp\left(-\frac{U_0}{k_B(T_0+\alpha t)}\right)\left(1 + \frac{U_0}{k_B(T_0+\alpha t)} + \frac{U_0^2}{k_B^2(T_0+\alpha t)^2}\right). \tag{5.5}$$

As can be seen from Figure 5.2, the linear heating rate describes the experimental data well. With an initial temperature of T_0 =20 µK (see below) and a trap depth of U_0/k_B =1 mK, we find a heating rate of $\alpha = (9.9 \pm 0.7)\mu\mathrm{K\,s}^{-1}$ (see Figure 5.2), comparable with the estimate of equation (5.3).

We conclude that contrary to our room-temperature setup, heating due to off-resonant scattering of the trapping laser has a significant contribution when measuring the lifetime in the tweezers. To counteract the heating during this measurement, we therefore need to apply cooling light in between two images. This could be done either

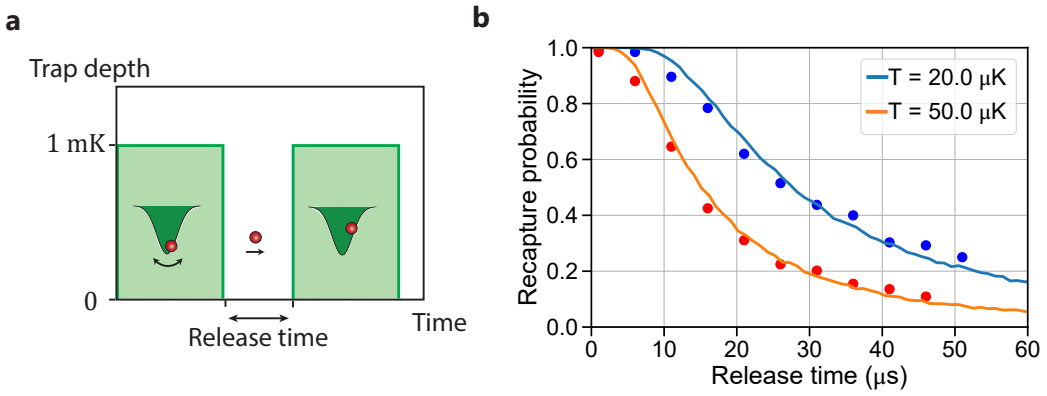

Figure 5.3: Release and Recapture measurement. a The trap is switched off for a certain time, and the atom moves ballistically with a velocity determined by its energy. After a few μs, the trap is switched on again and the atom is lost if its outside of the trapping volume. **b**: The loss can be compared to a Monte-Carlo simulation of the classical atom trajectories given an initial temperature T (solid lines). On our setup, the initial temperature after loading the atoms into the tweezers with the MOT lasers is approximately $50\,\mu\mathrm{K}$ (red dots). Through polarization-gradient-cooling, we are able to cool-down the atoms to approximately $20\,\mu\mathrm{K}$ (blue dots).

continuously, or by a short cooling pulse with a certain repetition rate that resets the temperature every few seconds. If we want the loss due to heating between two cooling pulses to be much less than 1% — therefore $P_{\mathrm{vac}}(1 - P_{\mathrm{heat}}) < 1\%$ — we should send a cooling pulse with a period of $T \leq 10$ s.

Temperature of the atoms Single atoms in tweezers have a well-defined energy which has been proven to follow a thermal Boltzman distribution from experiment to experiment [Tuchendler *et al.*, 2008]. Therefore, we can measure the temperature with the standard release-and-recapture method: We switch the traps off for a short time (typically a few μs) and measure the atom loss as a function of the switch-off time. When the traps are off, the atoms move ballistically with a velocity determined by their initial energy. Only when they are still inside of the trap volume after it is switched on again, they can be recaptured.

We compare the measurement of the atom loss to a Monte-Carlo simulation of the classical trajectories given an initial temperature (see Figure 5.3). With our MOT parameters (see Section 5.1), the temperature is approximately $50\,\mu\mathrm{K}$.

Polarization gradient cooling Even lower temperatures can be reached by using the polarization-gradient cooling (PGC) technique [Wineland, Dalibard, and Cohen-Tannoudji, 1992]. The reachable temperature T of the atoms is $k_B T \sim \Omega^2/\delta$

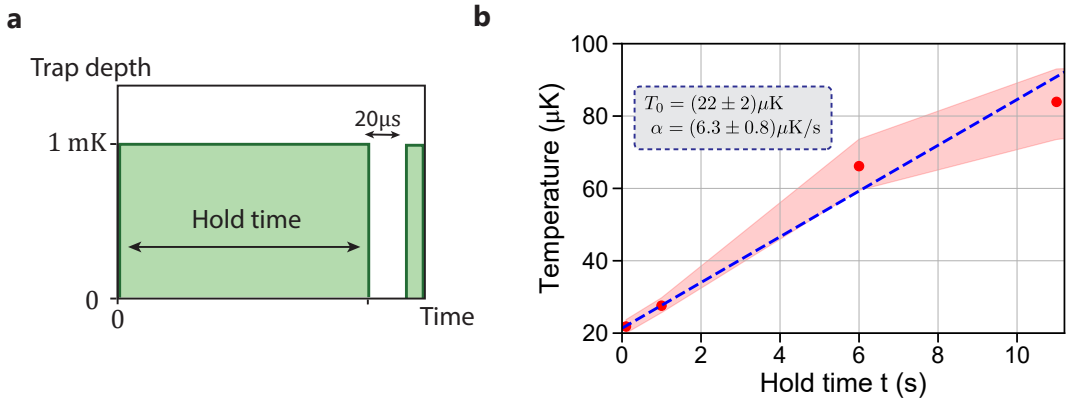

Figure 5.4: Measurement of the temperature increase. a: Schematic of the measurement principle. The atoms are held in the tweezers for a variable time, after which the temperature is determined with the release-and-recapture method with 20 µs switch-off time. **b**: Evolution of the temperature with the hold time. The shaded region corresponds to the standard deviation. We fit the data with a linear heating rate (dotted blue), and find an initial temperature of (22 ± 2)µK and a heating rate of (6.3 ± 0.8)µK s^{-1}.

and proportional to the Rabi-frequency Ω of the MOT beams and their detuning δ from the $F = 2 \rightarrow F' = 3$ transition.

On the experiment, we detune the cooling light to -12Γ and reduce the power to 6 mW, whereas the repump light stays on resonance. Furthermore, we switch-off the MOT gradient, and cancel the static magnetic field with compensation coils around the chamber. With a cooling pulse of 40 ms, we are able to cool-down the atoms from initially 50 µK to approximately 20 µK, as illustrated in Figure 5.3.

Measuring the heating rate Independent of the indirect determination of the heating rate from a lifetime measurement (see above), we can measure directly the temperature increase of the atoms after a certain hold time in the tweezers. The principle is illustrated in Figure 5.4. We hold the atoms in the tweezer for a variable time (a few seconds), after which we determine the temperature with the release-and-recapture method. For the temperature determination, we measure the atom loss with and without switching-off the traps for 20 µs, and compare them to Monte-Carlo Simulations with a given temperature (see above). As seen in Figure 5.4b, we measure a heating rate of approximately 6 µK s^{-1} which is again comparable with equation (5.3), although significantly lower than the value determined with the indirect method.

Further heating mechanisms not considered in this analysis could be technical noise due to laser intensity or pointing noise [Savard, O'Hara, and Thomas, 1997].

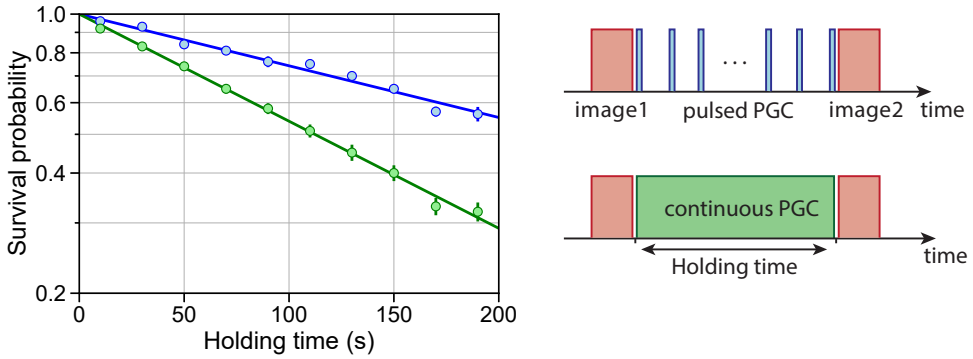

Figure 5.5: Lifetime measurement under cooling. We observe atom loss under continuous PGC cooling, leading to a lifetime of τ_{cont} =162 s, whereas under a pulsed PGC condition, we measure τ_{pulsed} =335 s. In the pulsed condition, we send a short 20 ms cooling pulse every 10 s. The continuous PGC uses the same parameters (detuning, power). Note that these measurements have been performed before fixing the vacuum leak.

5.2.2 Cooling methods: pulsed or continuous?

In our new cryogenic setup, the rate at which atoms are lost by background gas collisions is lower than the heating rates of atoms in the tweezer. Therefore, we need to cool the atoms during the measurement to estimate the vacuum-limited lifetime in the traps.

Continuous PGC cooling As described in the last section, we can use polarization-gradient cooling (PGC) to cool the atoms in the tweezers to 20 µK and mitigate heating effects during a lifetime measurement. Between the two fluorescence images, we therefore shine the PGC light (-12Γ, 6 mW) continuously, as illustrated in Figure 5.5. We measure a lifetime of $\tau_{\text{cont}} = 162$ s which is comparable to the MOT lifetime. However, we observe an atom loss when shining the PGC light which makes this technique not useful to measure the lifetime. I detail these light-dependent losses in the next section.

Pulsed PGC cooling To limit the atom loss we experience during continuous cooling as much as possible, we implement a pulsed PGC scheme. Every 10 s, we reset the temperature with a 20 ms PGC pulse (see Figure 5.5). With this small duty cycle ($\eta = 0.2\%$), the light-dependent losses are minimized, while the losses due to heating are small. Hence, this is the ideal method to determine the vacuum-limited lifetime.

Using the pulsed cooling method, we measured a lifetime of 335 s before fixing a leak in our vacuum system. As we shall see later, the lifetime after fixing the leak is measured to be over 6000 s.

5.2.3 Light induced processes in the presence of cooling light

Even though the continuous cooling method is not suitable to measure the lifetime of the atoms, it is interesting to investigate the causes of the observed losses further, especially as wish not to lose any atoms while shining light, e.g. in imaging conditions. Although we are still investigating this further in the lab, I highlight our current observations in the following. Before that, I recall a subtlety of our lifetime measurement (Fig. 5.5): From the two fluorescence images with varying time delay, we analyse for each initially occupied trap if it is still filled in the second image. This might be different from comparing the total number of atoms in the two images, as discussed below.

Molasses reloading A first reason for losses in continuous PGC conditions might arise from reloading of atoms into the tweezers from a Rubidium molasses between the two fluorescence images. If a reloaded atom enters a tweezer that was already occupied, both atoms will be expelled due to light-assisted collisions. These atoms could originate from the source, or from background Rubidium gas in the chamber. Both of these are unlikely however, as we block the atomic beam during the lifetime measurement with the (motorized) gate valve, and the residual Rb pressure in the 4 K environment is extremely small. Light incident on the inner cryogenic surfaces of the chamber have been reported to lead to the desorption of gas [Willems and Libbrecht, 1995], but mostly Helium, and the small MOT beams are not significantly scattered inside of the chamber.

During the measurement of the lifetime, we never see the atom number increasing which would be the sign of a reloading mechanism from a molasses. We therefore exclude this possibility as a cause for the observed losses.

Collisions with cold background gas At 4 K, the background gas consists mainly of helium and hydrogen, as all other species are well *frozen-out* by the cryogenic surfaces. As hydrogen is very light, the energy gained by a Rubidium atom colliding with a hydrogen atom at 4 K is small: The thermal velocity of H_2 at 4 K is $220\,\mathrm{m\,s^{-1}}$, approximately 9 times smaller than at room-temperature. As a result, the momentum transfer to Rubidium atoms after collisions is reduced and in some cases so small that the Rubidium atom is only heated, but not lost from the trap. Next to low pressures, the decreased Rubidium loss rate from the trap is an additional advantage of a cryogenic platform. A similar observation has been made with cryogenic ion traps [Pagano *et al.*, 2018].

However, specific to our platform, these collisions can influence our lifetime mea-

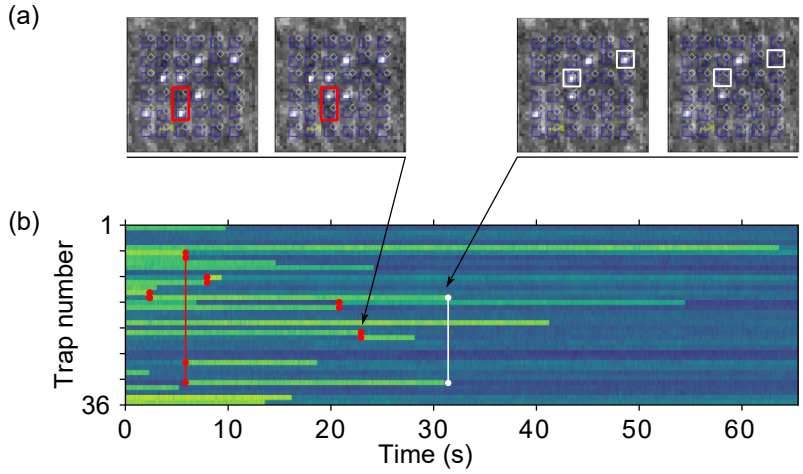

Figure 5.6: Recapture and correlated losses. a: When shining the imaging light continuously, we measure recapture (see a, left) and correlated loss events (see a, right). **b**: Experimental fluorescence traces showing the evolution of the trap occupancy as a function of time. Case (i) recapture events are highlighted in red, whereas case (ii) correlated losses are highlighted in white. We count 6 recapture events and 1 correlated loss event, next to 15 loss events without recapture. The figure is taken from [Schymik *et al.*, 2021].

surement, as detailed in the following. After a head-on collision (worst case) between a H_2 atom, and a Rubidium atom initially at rest, the Rubidium atom gains a velocity of only approximately $10\,\mathrm{m\,s^{-1}}$. This is large enough to expel it from the trap but can be still below the capture-range of a typical Rubidium MOT. Therefore, atoms could be recaptured into a tweezer trap after being previously expelled by a collision. Recaptured Rubidium atoms can (i) enter an unfilled trap, leading to an unchanged total atom number, or (ii) enter an already occupied trap, leading to a secondary loss induced by light-assisted collisions and a total atom number decrease of two.

We illustrate these two cases in an experiment (see Figure 5.6), in which we take images in the *video mode* of the camera, in which images of 50 ms are taken in fast succession (with a dead time of approximately 20 ms). The cooling light is always on, in imaging conditions with a detuning of -4.5Γ, to be able to obtain bright fluorescence images. After loading a MOT, we close the valve and cut the MOT beams briefly to disperse the atomic cloud. We then watch the atom decay *live* on the camera.

In Figure 5.6, we see recapture events with constant total atom number (the atom is lost in one and immediately appears in another trap). Furthermore, we observe correlated losses, where two atoms are lost at the same time, because one lost atom enters an already occupied trap. In this experiment, a fraction of $P_{\mathrm{recap}} \simeq 0.46$ atoms are recaptured, as we count 6 recapture and one correlated loss event, next to 15 times

that an atom is lost without being recaptured. Therefore, a significant fraction of atoms that are lost due to background gas collisions are recaptured when the MOT light is on. This is consistent with the fact that a significant amount of background collisions is with slow hydrogen molecules. Note that the statistics of the experiment in Figure 5.6 does not allow us to make a precise prediction of the recapture probability P_{recap}. Furthermore it could, e.g., depend on the detuning of the cooling light, and the distance between traps.

The effect of the observed recapture events however has a minor influence on the lifetime measurement, as illustrated in Figure 5.7. As previously mentioned, we distinguish between atoms that hop to another unfilled trap (case (i)) and atoms that hop to another filled trap (case (ii)), leading to a correlated loss of two atoms. Compared to the situation in which all background collisions lead to an atom loss ($P_{\text{recap}} = 0$), correlated losses (case (ii)) lead to an increased atom loss, whereas case (i) events decrease the atom loss and can in fact increase the measured lifetime, as an atom can re-enter a trap where an atom previously has been lost. Both of the cases are equally likely when half of the traps are filled, e.g. at the beginning of the measurement. However, as we start to lose atoms due to background collisions, case (i) is more probable than case (ii) as more than half of the number of traps are unfilled. As a result, we measure an initially bigger atom loss (compared to $P_{\text{recap}} = 0$), but for longer times, the atom loss is smaller and we measure an extended lifetime (see Fig. 5.7). Therefore, the influence of secondary losses on the lifetime measurement depends on the considered holding times.

On the experiment, we usually measured holding times smaller than the lifetime (e.g. up to 0.6 lifetimes in Figure 5.5), so correlated losses could play a role. As illustrated in Figure 5.7b, the measured lifetime is maximally reduced to around 90% for a recapture probability of $P_{\text{recap}} = 0.46$. If long times are considered, the case (i) events lead to an increase in measured lifetime.

The lifetime measured in continuous cooling conditions in Figure 5.5 is however reduced by approximately 50% compared to the pulsed cooling condition. Furthermore, the experimental situation is not comparable, as the detuning of the cooling light and therefore the capture velocity of the molasses is different. In Figure 5.5, the light is further detuned (-12Γ) compared to the -4.5Γ in Figure 5.6. Therefore, we would expect the collisions to play an even smaller role in the lifetime measurement with continuous PGC conditions. We conclude that the discrepancy between continuous and pulsed PGC conditions can therefore not be explained with the effect of low-energy collisions.

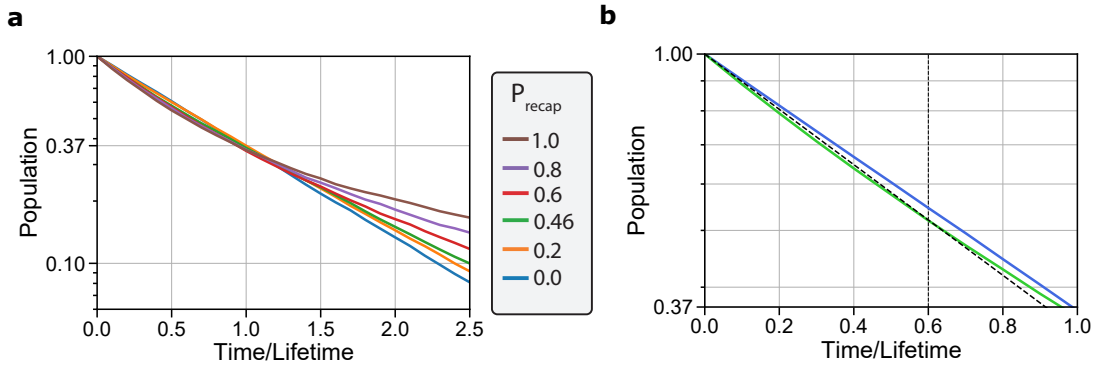

Figure 5.7: Influence of cold collisions on the measured lifetime. a: Monte-Carlo simulation of the measured recapture probability in the initially filled traps (initial filling 50%). At short times, correlated losses (case (ii)) lead to a smaller recapture probability compared to the no-collision case (blue line). However, at longer times, the measured lifetime is longer due to case (i) events. **b**: If we consider only times up to 0.6 lifetimes, the measured lifetime could be decreased to approximately 90%, if $P_{\mathrm{recap}} \simeq 0.46$ (green).

Loss during imaging We observe that the total number of atoms in Figure 5.6 decays much faster than expected from a lifetime of 330 s. As explained in the previous section, this cannot be caused by recapture events. As we observe this decay only in the presence of light, we conclude that we lose a fraction of the atoms, when shining light in imaging conditions. The decay of the total number of atoms in Figure 5.6 agrees roughly with a loss rate of $\beta_{\mathrm{loss}} = 0.04\,\mathrm{s}^{-1}$. This would correspond to a survival probability of approximately $P_{\mathrm{survival}} = 0.998$ for a 50 ms image. Note that the statistics of Figure 5.6 are not enough to conclude on the imaging survival probability with high precision. However, similar numbers for the loss between two consecutive images have been observed on the experiment and this is a topic of further investigation.

A similar experiment is illustrated in Figure 5.8. Here, we take an image every 5 seconds, in between two short PGC pulses. This measurement was taken after fixing the vacuum leak. Initially, this was thought to be an alternative, faster way of estimating the vacuum-limited lifetime, because collecting enough statistics with the usual method takes about 15 hours for the measured lifetime of 100 minutes. However, we again measure a reduced lifetime, due to a finite imaging survival probability.

Similar to before, we observe recapture and correlated loss events, however much rarer in this measurement, as the light is off most of the time. They can be observed by eye in the fluorescence traces in Fig. 5.8a, but also when considering the difference between the decay of the total atom number (that includes recaptured atoms) and the decay of the initial population (that includes recaptured atoms only if the atom is

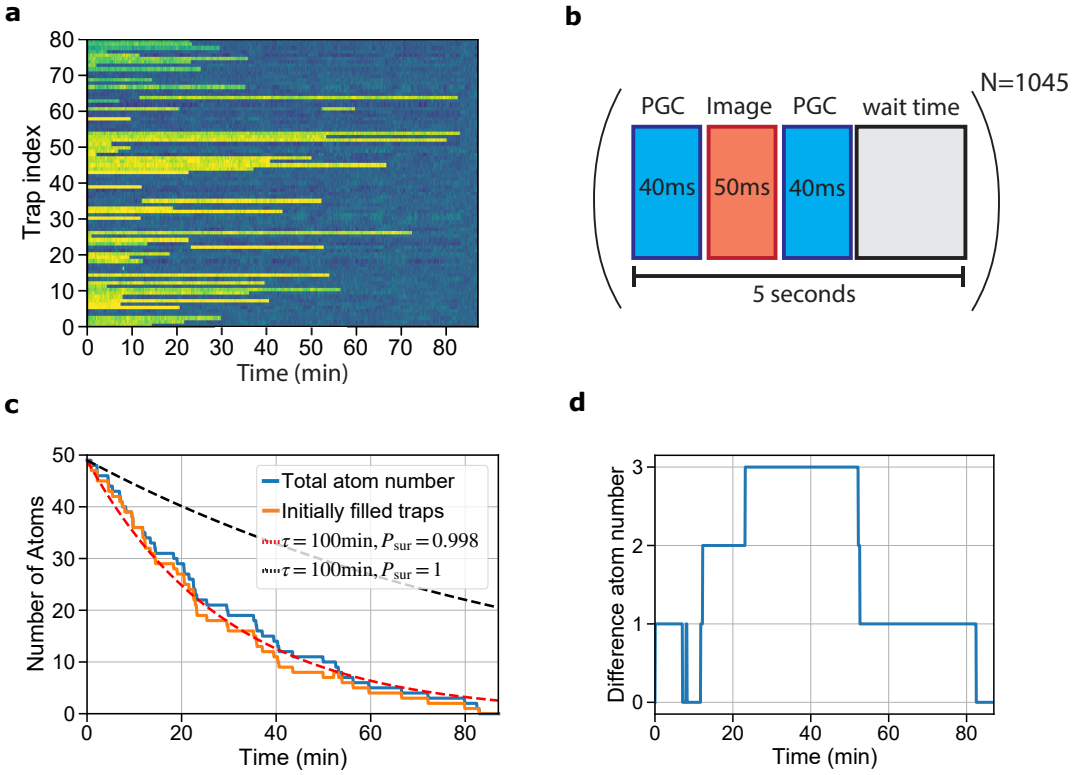

Figure 5.8: Alternative lifetime measurement a: Experimental fluorescence traces, showing the trap occupancy for each trap as a function of time. **b:** Experimental sequence leading to the fluorescence traces in (a). An image is taken every 5 s, with PGC pulses in between to cool the atom. The sequence is repeated 1045 times. **c**: The population decay, regarding only initially filled traps (orange), or the total atom number (blue). It fits with a lifetime of 100 min only when an image survival probability of P_{survival} =0.998 is considered. **c:** Difference in the total atom number and the population in the initially filled traps, consisting of a part of the case (i) recapture events.

recaptured in an initial trap), as illustrated in Figure 5.8c. In one cycle (see Fig. 5.8)b), the probability to have such an event is $P_{\text{case (i)/cycle}} \simeq 1 \times 10^{-4}$.

The decay of the population of the initially filled traps is much faster than the later measured vacuum-limited lifetime of 100 minutes. We explain it, by taking into account an additional loss of $P_{\text{loss/cycle}}$:

$$P_{\text{survival}}(t) = P_{\text{loss/cycle}}^{N_{\text{cycle}}} \exp(-N_{\text{cycle}} \Delta t_{\text{cycle}}/\tau) \quad . \tag{5.6}$$

We find that $P_{\text{loss/cycle}} \simeq 2 \times 10^{-3}$, corresponding to an survival probability of P_{survival} =0.998 for a 50 ms image, a similar number to the experiment before.

The detailed analysis of the imaging survival probability is beyond the scope of

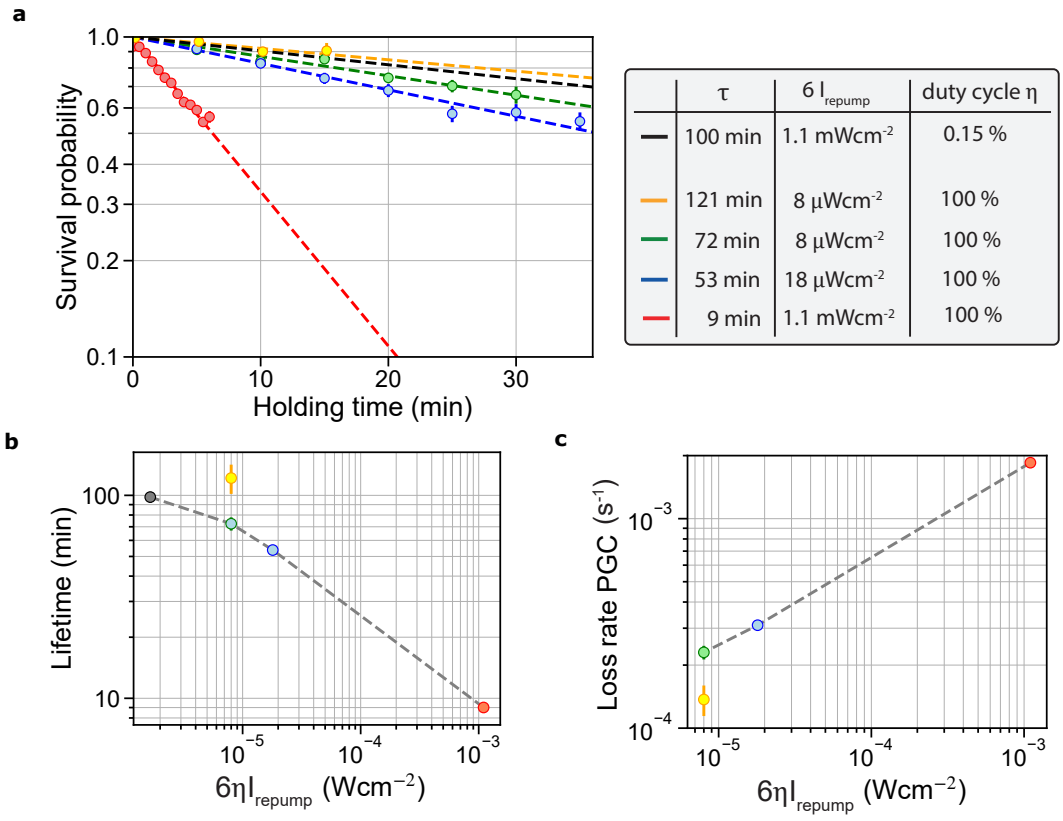

Figure 5.9: Influence of the Repump intensity on the lifetime a: Three different lifetime measurements with continuous PGC conditions on a 9×9 array with open oven valve (red, blue, green), a measurement with continuous PGC condition on a 6×6 array with closed oven valve and the black dotted line represents the measured lifetime of 100 min (pulsed PGC, closed valve). **b:** Demonstration of the extracted lifetime as a function of the repump intensity. **c**: Loss rate for the PGC beams, assuming that for the 100 min lifetime measurement in pulsed conditions, the losses are negligible.

this chapter. However, it is a current topic of research in our group, as a high image survival probability is crucial for large defect-free arrays. Considering the survival probability for a 50 ms image, estimated here to be P_{survival} =0.998 , a 500-atom array can be prepared with a maximum probability of $P_{500} = 0.998^{500} \simeq 0.37$. Therefore it is important to maximise the image survival probability, e.g. by investigating the influence of trap depth, detuning, intensity of the cooling and repump light, as was also attempted in Ref. [Martinez-Dorantes *et al.*, 2018].

Dependence on repumper power We observe that the atom loss in continuous PGC conditions correlates to the power in the repump beam. This observation is illustrated in Figure 5.9 where we compare measurements of the lifetime in different

conditions. For all the measurements, we utilise the continuous PGC conditions, with 6 cooling beams ($F = 2 \rightarrow F' = 3$ transition of the D_2 line) detuned at -10.5Γ with an overall intensity of $6I_{\text{cooling}} = 11$ mWcm^{-1}, and 6 repump beams ($F = 1 \rightarrow F' = 2$ transition of the D_1 line) with varying intensity. The measured lifetime is higher for smaller intensities in the repumper. Most of these measurements (red,blue,green) were done with an open gate valve during the hold time, whereas the highest lifetime (yellow) was measured with a closed gate valve. I detail the influence of closing the gate valve in the next section.

This dependency of the lifetime on the repumper power can explain why the pulsed cooling scheme is favorable for measuring the lifetime, as the repump power over the whole measurement is the comparatively low considering its small duty cycle. At the time of writing, we do not have an explanation of the physical processes involved.

5.2.4 Ballistic collisions with atoms from the oven

We find that the measured lifetime of the atoms in the tweezers correlates with the temperature of the oven, when the gate valve rests open during the measurement: for increasing temperatures of the oven, the lifetime decreases due to collisions with atoms from the oven region.

To demonstrate this, we measure the lifetime in pulsed cooling conditions (see above) for different oven temperatures, as illustrated in Figure 5.10. With increasing oven temperature, the lifetime is measured to be shorter. Furthermore, we find that if we block the atomic beam with the gate vale during the measurement of the lifetime, the measured lifetime does not change with the oven temperature. This indicates collisional losses with atoms from the oven region, which is in a direct line of sight of the tweezers.

The measured survival probability for a lifetime measurement is:

$$P_{\text{survival}} = \exp(-t/\tau) \quad , \tag{5.7}$$

with a total loss rate τ^{-1}, depending on the vacuum lifetime τ_{vac} and a collisional rate $\alpha_{\text{collision}}$:

$$\tau^{-1} = \tau_{\text{vac}}^{-1} + \alpha_{\text{collision}} \quad . \tag{5.8}$$

The loss rate τ^{-1} is illustrated in Figure 5.10b and depends on the temperature of the oven. For temperatures below 340 K, the loss rate due to the lifetime (in this case $\tau_{\text{vac}} \simeq 200$ s) dominates, whereas for higher oven temperatures, the collisions have a

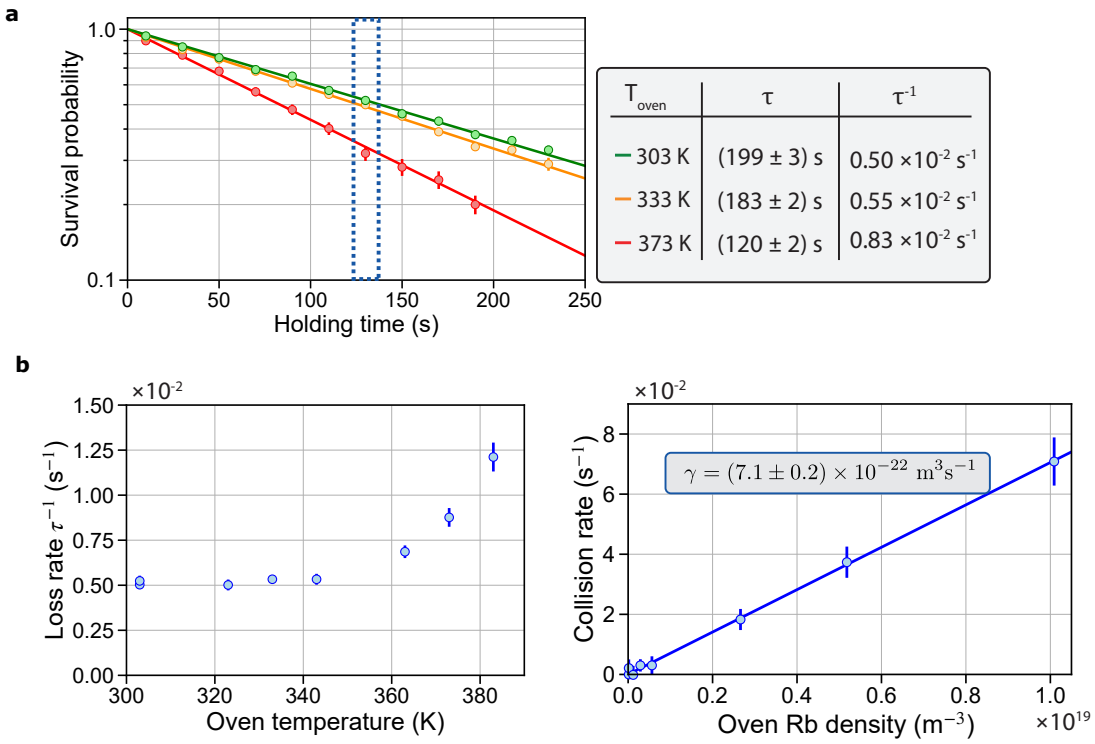

Figure 5.10: Measured influence of the oven temperature on the lifetime. a: Three exemplary lifetime measurements with different oven temperatures. With increasing oven temperature the lifetime is shorter, indicating collisional losses with atoms from the oven. **b:** From a measurement at 130 s hold time (see (a)), we find a loss rate τ^{-1} that correlates with the oven temperature. Above temperatures of 340 K the loss rate increases significantly. **c**: Collisional rate $\alpha_{\text{collision}}$ as a function of the oven Rubidium vapor density. The linear relationship indicates a dependency on the flux of the oven.

significant effect.

The rate of collisions between atoms from the oven and atoms in the tweezer should depend on the oven flux Φ_{oven} and the collisional cross section σ and therefore be proportional to the Rubidium vapor density n_{Rb} in the oven:

$$\alpha_{\text{collision}} = \sigma\Phi_{\text{oven}} \simeq \gamma n_{\text{Rb}} \quad . \tag{5.9}$$

In Figure 5.10c, this dependency is illustrated, using the Rubidium vapor pressure data from [Steck]. We find a scattering rate $\gamma = (7.1 \pm 0.2) \times 10^{-22}$ m^{3}s^{-1}. This result is comparable to an order of magnitude estimation, regarding the geometry of our setup and lets us infer a Rubidium-Rubidium collisional cross section, as is discussed in Appendix B.

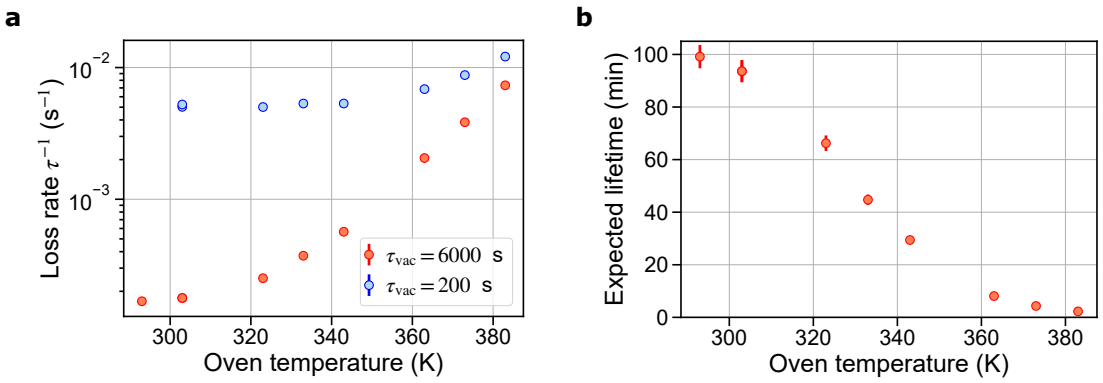

Figure 5.11: Expected influence of the oven flux for a lifetime of 6000 s. Using the estimated scattering rate γ (see Fig. 5.10) together with equations 5.7 – 5.9, we analyse the influence of the oven flux for a lifetime of 6000 s. **a:** Comparison of the loss rate τ^{-1} of Figure 5.10 (blue) with an estimation for the loss rate for a lifetime of 6000 s (red) based on γ. **b:** With a lifetime of over 6000 s, the influence of collisions with atoms from the oven is non-negligible, even for low temperatures.

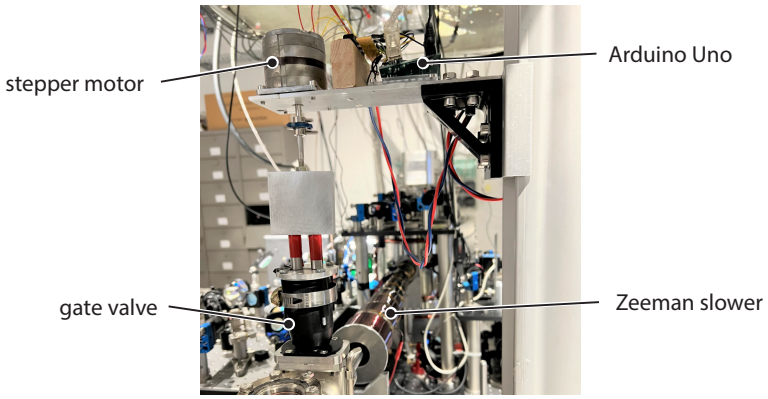

Figure 5.12: Motorized gate valve. The gate valve is opened or closed using a stepper motor that is controlled with an Arduino. We close the valve in approximately 1 s during the measurement of the lifetime.

As this data was taken with a comparatively low lifetime, I illustrate the estimated effect of the collisions on the later measured lifetime of 6000 s in Figure 5.11. Here, it is evident that $\alpha_{\text{collision}}$ is comparable to τ_{vac}^{-1} even at low oven temperatures, limiting the lifetime.

In summary, we have shown that collisions with atoms from the oven region are a loss mechanism for atoms in the tweezers. To benefit from long lifetimes, we therefore work at oven temperatures below 340 K. Additionally, we built a computer controllable

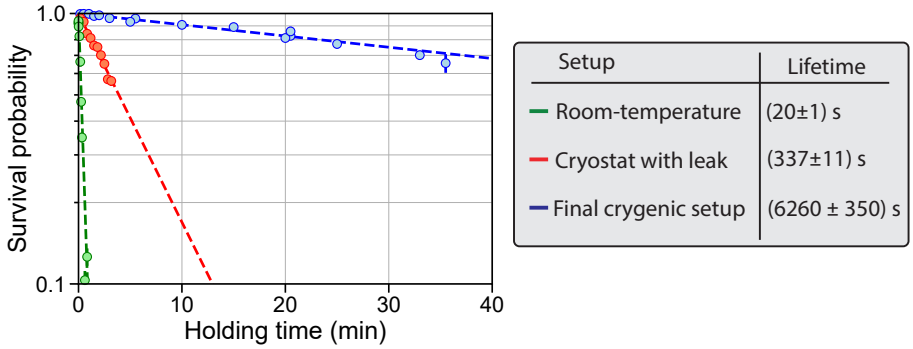

Figure 5.13: Comparison of measured lifetimes. In our final cryogenic setup, we measure a lifetime of approximately 6300 s, a 300-fold increase to the lifetime on our room-temperature setup. The values are corrected for imaging loss.

actuator of the gate valve (see Figure 5.12), that closes and opens the valve during the measurement of the lifetime. Using this homebuilt actuator, we ensure that the atomic beam is blocked during the measurement, and collisions do not influence our measurement regardless of the oven temperature.

Since it takes approximately one second to close the valve, this is however not suited for experiments with high repetition rate. Therefore, we plan to include a computer controllable beam flag in a future setup that can block the atomic beam fast and therefore still allow a high experimental repetition rate of 1-2 Hz. Alternatively, a 2D-MOT instead of a Zeeman slower in the atomic source could be a solution to decrease the influence of the flux of atoms from the oven.

5.2.5 Measurement of a lifetime of over 6000 s

I have shown that a measurement of the vacuum-limited lifetime is not a trivial task. Atoms are not only lost by background gas collisions, but further loss mechanisms have to be considered in order to asses the true vacuum-limited lifetime. First, collisions from the oven can cause atom losses. To minimize this effect, we therefore operate at low oven temperatures of 30 °C, and additionally close the gate valve during measurement to cut the atomic beam. Second, the atoms are heated due to off-resonant scattering of trap light which can cause atom loss. To keep these losses to a minimum, we employ PGC cooling. Third, as we observe a loss mechanism when the PGC light is continuously on, we try to minimize the duty cycle of the cooling light. We opt for a relatively short PGC cooling pulse of 20 ms every 10 s. Finally, in imaging conditions,

we have a finite survival probability of approximately P_{survival} =0.998 for a 50 ms. In the following measurement, we therefore correct the values by the imaging loss, by dividing all measured survival probabilities by the imaging loss.

After fixing the a leak in the vacuum system, we use the described optimal measuring conditions, and perform another lifetime measurement on a 9×9 tweezer array. The average lifetime in the array is $\tau = (6260 \pm 350)$ s. Note that even without correcting for the imaging loss, the lifetime is above 6000 s. In Figure 5.13, we compare the measurements on different setups. The cryogenic lifetime estimate is approximately a factor 300 longer than on our room-temperature setup. As the lifetime is a major limitation on our room-temperature setup for the scalability of the platform, the extended lifetime in the new cryogenic setup opens up the path towards large-scale tweezer arrays.

5.3 Conclusion

In this chapter, we have estimated the vacuum-limited lifetime of atoms at 4 K in our novel cryogenic tweezer platform. We measure a lifetime of approximately 6300 s, a 300-fold improvement over our room-temperature. The measured lifetime gives a lower-bound to the vacuum-limited lifetime — although we believe it to be fairly close — as multiple loss mechanisms complicate the measurement. This very promising result opens the path to scale-up the tweezer platform for future large-scale quantum simulation.

I have analysed in detail different loss mechanisms, such as the influence of collisions from the oven region, heating due to off-resonant scattering of the trap laser light and losses due to imaging light. Using this information, we have found a measurement protocol that is the least influenced by the different losses and allowed us finally to measure a lifetime of approximately 6300 s.

We have found that further improvements are important for scaling up the number of atoms on our platform. First, we should analyse in more detail the survival probability of an atom during a fluorescence image. With a lifetime of over 6000 s, the imaging losses are dominant in the experimental cycle. As an example, in between two fluorescence images with a 200 ms delay, the expected loss of one atom due to the vacuum limited lifetime is approximately $P_{\text{loss,vac}} \simeq 3 \times 10^{-5}$, compared to an expected imaging loss of $P_{\text{loss,image}} \simeq 2 \times 10^{-3}$. It would be essential to decrease the imaging loss, e.g. by choosing a right parameter set of light detuning, intensity and trap depth. Note that the loss due to the lifetime on our room-temperature is $P_{\text{loss,vac}} \simeq 1 \times 10^{-2}$, an order

of magnitude higher than the imaging loss.

Second, collisions with atoms from the oven have a significant effect on the lifetime of the atoms in the tweezer. For the lifetime measurements, we have found a way to mitigate this effect, by decreasing the oven temperature to 30 °C, and blocking the atomic beam by operating the gate valve. This procedure however does not allow a high repetition rates of the experiment, as the MOT loading time is reduced drastically which such a low oven temperature, and the operation of the gate valve takes approximately 1 s. Therefore, in a future setup, we should include an atomic beam shutter that operates at high repetition rate.

An interesting further measurement could be the one of the lifetime for different temperatures of the cryostat. This could give valuable insight on the pressures at different temperatures, and whether it would be possible to work at higher temperatures with similarly long lifetimes.

To improve the lifetime even further, the ultimate step would be to have a bakeable cryogenic system. This is technically more difficult, as it requires a removable PTR. Instead of physical connections using copper braids between the PTR head and the heatshields and coldplate, this requires the use of radiators in a chamber filled with buffer gas. An intermediate improvement would also be to improve the vacuum in the non-cryogenic part of the system, e.g. the atomic source part, by the use of differential pumping stages.

Chapter 6

Towards Larger Atom Arrays

As we have seen in the previous chapters, the vacuum-limited lifetime of a single atom in a tweezer is a major limitation for scaling up the number of atoms on our room-temperature quantum simulation platform. During my PhD, we lifted this limitation with a new cryogenic setup in which the single atom lifetime is over 6000 s, an approximately 300-fold increase over our room-temperature setup. Together with the improved algorithmic framework for the assembly process (see Chapter 3), we are currently working on creating large arrays of atoms. This chapter describes the work in progress to assemble up to 500 atoms.

First, I describe the current state of the assembly process on our setup and demonstrate that we can assemble defect-free arrays of 231 atoms, however with small success probability. Even with the extended lifetime on our cryogenic setup, other imperfections currently prevent us from assembling larger arrays with high fidelity. I have identified these technical imperfections in previous chapters: In Chapter 3, we have seen that the imperfect trap depth equalization has a major impact on the assembly efficiency. Furthermore, the single move efficiency is not the same, considering a small array with extent of 10 µm (0.993), or a big array with extent 130 µm (0.97). Finally, in Chapter 5, we have identified that losses during imaging have an impact on the overall efficiency to have a defect-free shot. Once we have solved these technical imperfections, we can fully benefit from the extended atom lifetime and assemble large arrays with high fidelities.

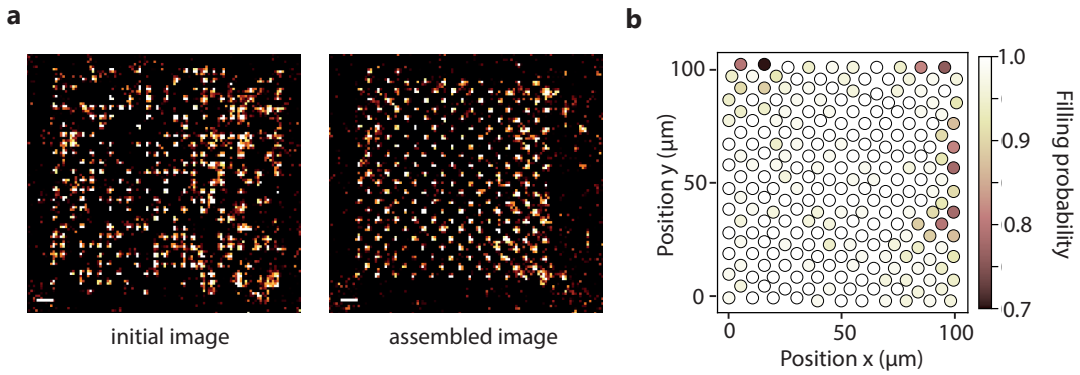

Figure 6.1: Assembly of a 231-atom array. a: Exemplary fluorescence images of the initial array and the array after 2 assembly processes. The scale bar denotes $10\,\mu\mathrm{m}$. **b:** The probability of a trap site to be filled in the last (assembled) fluorescence image. We can see that the overall success probability of the assembly process (found as the product of all filling probabilities) is mainly limited by a few traps at the border of the array with a significantly lower filling probability.

In this chapter, I detail the current progress on these topics at the time of writing. This mainly involves work on the trap depth equalization which we have identified as the currently strongest limitation. As both the single move efficiency and the imaging survival probability depend on the trap depth, a small spread in trap depths is also crucial to evaluate these imperfections. I start by detailing how the current method [Nogrette *et al.*, 2014] does not produce reliable results in the limit of trap arrays with an extent larger than the field-of-view of the lenses. Next, I analyse whether we can use the fluorescence signal of the atoms to estimate the trap depths and I propose a new equalisation scheme involving this analysis.

6.1 Assembling large arrays on the cryogenic setup

On the new experimental setup, we implemented an atom assembler relying on the same experimental techniques as on our room-temperature setup (see Chapter 2.1.3 for details). This involves the use of a computer controlled 2D-acousto-optical deflector (2D-AOD) that can transport an atom between reservoir and target traps. To find the sequence of moves to assemble the user-defined target array, we use the new algorithmic framework described in Chapter 3.

Figure 6.1 illustrates the current state of the atom assembler. We are able to assemble atom arrays of over 230 atoms. However, the success probability of obtaining

a defect-free is relatively low: the probability to assemble the array at hand with at most one defect is approximately 12%. Similar to the analysis in Chapter 3, we find that this is mainly due to a few traps that have a significantly lower filling probability (see Figure 6.1b), coinciding with a smaller trap depth. We conclude that we need to find a better trap depth equalization method before we can increase the number of atoms further to the regime of 500 atoms.

6.2 Rethinking the trap depth equalization

In Chapter 2.1.2, I illustrated a trap depth equalization method based on the trap light [Nogrette *et al.*, 2014]. Using the second aspheric lens and an imaging system, we image the light intensity distribution in the atomic plane (the focal plane of the aspheric lens) onto a CCD camera. The peak intensity of a trap on the CCD camera image gives us an estimation of the trap depth in the focal plane of the lenses. With this information, we then equalize the trap depths of an array using an iterative algorithm, involving the spatial-light modulator and the CCD camera.

In the past, this method worked reasonably well on our experiment. However, the trap arrays used for quantum simulation consisted of up to around 40 atoms and the spatial extent was usually below 70 µm. Upon increasing the atom number during the time of my PhD we have noticed that for larger arrays, e.g. the 196 atom array with an extent of 130 µm described in Chapter 3, the method did not work sufficiently well.

In this section, I detail that for large arrays, compared to the field-of-view (FOV) of the lens, the peak intensity of a trap on the CCD camera is not a reliable estimate for the trap depth in the focal plane of the aspheric lenses. We therefore need to find a new equalization scheme based on an *in situ* estimation of the trap depth. Other groups have measured the AC-Stark shift of each trap to estimate the trap depth for an equalization procedure ([Endres *et al.*, 2016; Jenkins *et al.*, 2021; Singh *et al.*, 2021]). Here, I analyse whether we can find an alternative and potentially less involved estimation using the telegraphic fluorescence trace during the loading of traps. Finally, I will suggest a new method using this estimate.

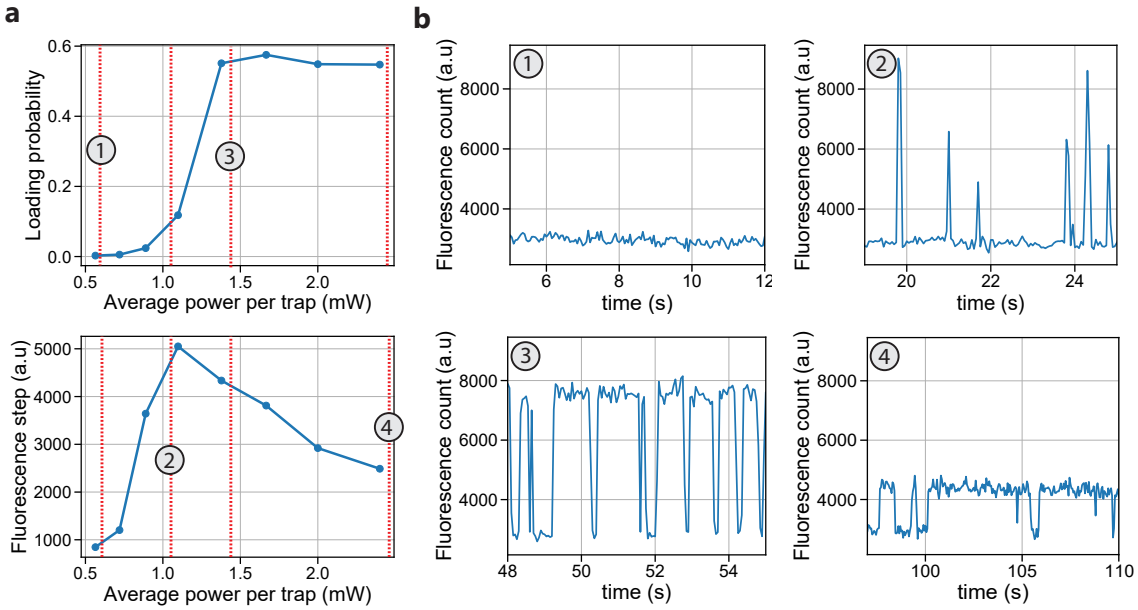

Figure 6.2: Fluorescence traces at different laser powers. The wavelength in this example is 815 nm. **a:** The loading probability and fluorescence step size (difference between maximum and minimum fluorescence count) of a trap as a function of the average laser power (total laser power divided by the number of traps) exhibit characteristic features. **b:** Examples of the fluorescence trace at different powers. The loading probability rises from zero to 50–60%. As the light shift decreases with decreasing trap power, the fluorescence step is higher for lower trap powers. However, below a certain threshold the atom cannot be trapped for the full duration of an image and the fluorescence step drops to the noise level.

6.2.1 The problem of a trap depth equalization method based on a trap light analysis

As described in Chapter 2, we load cold atoms from a MOT into our micron-sized tweezers and rely on light-assisted-collision processes to isolate single atoms. Choosing the right parameters for the trap depth leads to either one or zero atoms being in the trap at any time with a loading probability of around 50-60%.

In Figure 6.2, I illustrate the dependence of the loading probability of a single trap on the laser power and therefore on the trap depth. Above a certain power threshold, we achieve a constant loading of approximately 50-60% (panel 3 and 4). If the power is too low, we do not trap any atoms (panel 1), but, for a range of powers below the threshold, the trap depth is still large enough to occasionally trap an atom (panel 2). The atom is however quickly heated out of the trap, leading to a loading probability

below 50% and a *spiky* fluorescence signal.

As we increase the power in the traps, we light-shift the atoms with respect to the atomic resonance. As a result, the scattering rate decreases with increasing trap power. For the fluorescence signal, the decreased scattering rate leads to a smaller fluorescence step, i.e. the difference in the two fluorescence levels of the telegraphic trace. In the limit of high trap powers, the fluorescence step can be on the same order as the background noise on the camera (see Fig. 6.2 panel 4). This leads to an increase of detection errors: the possibility to measure an atom, even though there is none, or vice versa.

The trap depth equalization is crucial for our platform for two main criteria: First, we would like to have a loading probability around 50% at each trap site. Second, we would like the highest possible fluorescence step size to decrease detection errors. A large spread in trap depths would make it impossible to fulfil these two criteria on all trap sites. As the current equalization method is not perfect, we often have to accept a small fluorescence step size for some traps to have at least 50% loading probability on all trap sites.

To fulfil the mentioned two criteria, a reliable method to determine the depth of each trap is needed. In the past, this was deduced by the peak intensity of a trap on the CCD camera image. As previously mentioned, the peak intensity is only a reliable estimate for the trap depth for arrays with a small extent compared to the FOV of the lens. This is illustrated in Figure 6.3, where the intensity distribution, as measured on the CCD camera, is compared to the loading probability on each trap site. In this example, the intensities are equal with a standard deviation of approximately 8% over the full array. In contrast, the loading probability of each trap, as calculated from the fluorescence signal, is 50% only in an area comparable to the FOV of the lens, while it decreases to zero on the borders of the array. As the loading probability depends on the trap depth (see Figure 6.2), this comparison suggests that the traph depths do not correlate with the measured intensities over the full array. This is most likely caused by optical aberrations, such as coma that are compensated by the symmetry of the two aspheric lenses in f-f configuration. Therefore, we do not measure these aberrations on the CCD camera (after the second aspheric lens), although they are present in the focal plane of the aspheric lens.

As a consequence, we are in need of a new, reliable estimation method for the trap depth. Preferably, this method would be *in situ*, meaning it uses the atomic signal itself to deduce the trap depth. This could be done for example by measuring the trapping frequencies of each trap. Assuming the waist of each trap is the same, one

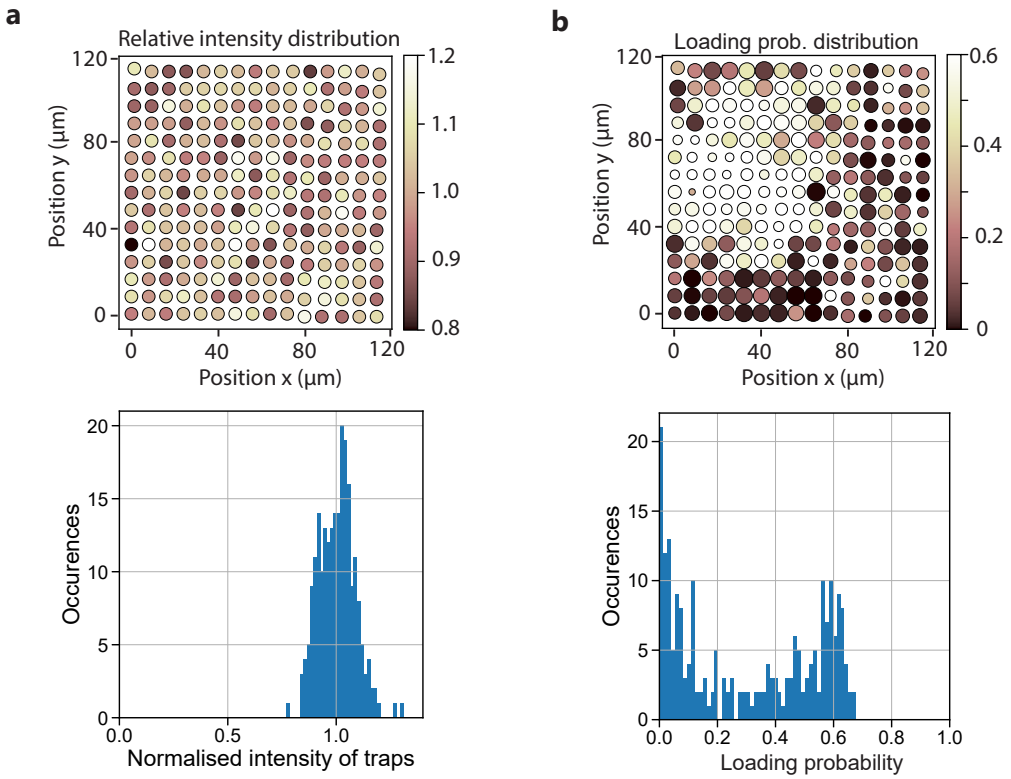

Figure 6.3: Intensity distribution and loading probability on a 15×15 array. a: The intensity distribution over the array is homogenous and its distribution has a standard deviation of 8%. **b**: The distribution of the loading probability over the array is inhomogeneous: an area with a diameter of approximately 70 µm on the left has a similar loading probability of 50%, while on the border of the array, the traps are barely loaded. The histogram shows a bimodal distribution, with two peaks around zero and 60%. We conclude from this comparison that the intensity distribution measured on the CCD camera is not a valid estimate of the trap depth over the full extent of the array.

could estimate the relative trap depth. Similarly, one could measure the AC Stark shift (e.g. [Endres *et al.*, 2016; Jenkins *et al.*, 2021; Singh *et al.*, 2021]).

A different method could be to find an equalization method using the loading probability and/or the fluorescence step size of each trap, similar to Figure 6.2, as the goals (a 50% loading, and a large fluorescence step size) can be described with these two quantities. This could be easier and faster to measure than the trap frequencies or the Stark shift.

6.2.2 Inferring the trap depth from the fluorescence signal

To evaluate whether we can use the fluorescence trace as a valuable tool to estimate the trap depth and equalize the trap array, we have to analyse it further. In the following, I discuss whether its shape is a universal feature and to which extent it could prove as a valid estimate.

Loading probability From Figure 6.2a, we find that the loading probability is only sensitive to the trap power for small trap powers. Above, it is constantly 50–60%, even for increasing power. Therefore, the loading probability alone is not a useful quantity to estimate the trap depth.

The first iteration of an *in situ* method that I implemented on our room-temperature setup (see Chapter 3.3) used the loading probability as weights. For the method to work well, all traps had to have loading probabilities of $0 < P_{\text{loading}} < 50\%$. Since this is rarely the case for large arrays at the beginning, this method required many iterations and, while drastically improving the result obtained by a simple intensity equalisation, was still imperfect.

The functional form of the loading probability as a function of the power in the trap experiences a sharp rise which is quite sensitive to the trap power (Fig. 6.2a). With enough data points, one can fit an error function to the loading probability P_{loading} as a function of the average trap power p_{trap}:

$$P_{\text{loading}} = 0.5 P_{\text{max}} \left[\text{erf}(c(p_{\text{trap}} - p_{\text{half}})) + 1\right] \quad . \tag{6.1}$$

Here, the maximal loading rate (50-60%) is denoted with P_{max}. Furthermore the half-way rise power is denoted as p_{half}, and c is a measure for the sharpness of the rise.

We fit equation (6.1) to all fluorescence traces on the 15×15 array (same as in Figure 6.3). We then find that it is possible to overlay all the traces by normalising the power of each trace with its half-way rise power p_{half}, as illustrated in Figure 6.4a,b. As all traces collapse onto one curve when normalizing the power, we conclude that the shape is universal and that p_{half} is an estimate for the trap depth U:

$$\frac{p_{\text{half},i}}{\overline{p_{\text{half}}}} = \frac{U_i}{\overline{U}} \quad . \tag{6.2}$$

This indicates that the sharpness of the rise (parameter c) is similar for most of the traps, as can be verified in Figure 6.4d. We believe that the sharpness parameter c is related to the spotsize of the trap, even though we do not measure a difference in spot size with the CCD camera. This could however be related to the symmetry of the f-f

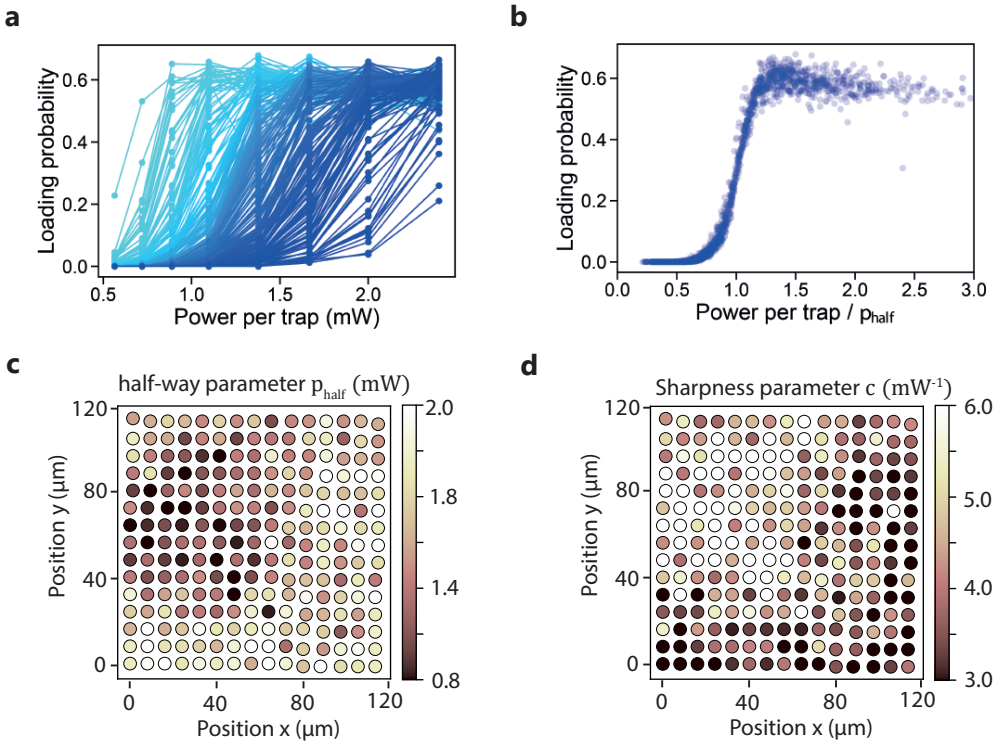

Figure 6.4: Overlaying all loading probabilities. a: For each trap in a 15×15 array, we record the loading probability for 8 different powers. Each of the points is averaged for at least 60 s, with a relatively low loading rate into the tweezer of about 2 atoms per second (compare e.g. Figure 6.2). **b:** Overlay of all datapoints, by fitting the traces with equation 6.1 and normalising the power by the half-way power. **c:** Distribution of the fit parameter half-way power p_{half} reveals a large spread over the array, for the corresponding intensity distribution on the CCD camera, see Fig. 6.3. **d:** Distribution of the sharpness fit parameter c. It seems correlated to the half-way power, indicating that the difference in loading probability is correlated to a change of the trap size.

configuration (see above). Furthermore, we observe that the sharpness is higher in the top left than the bottom of the array. As it is not radially symetric, it indicates that the trapping laser is not perfectly on the optical axis of the aspheric lens. In the future, this could prove as a useful alignment tool.

From the recorded traces, it is possible to determine the half-way power p_{half} of each trap site with a relative precision of approximately 1%. Here, I recorded each trace for at least 60 s at eight specific trap power values, therefore the measurement took approximately 10 minutes. While this is comparatively long compared to imaging the trap intensities with the CCD camera, we might only have to do it once in the

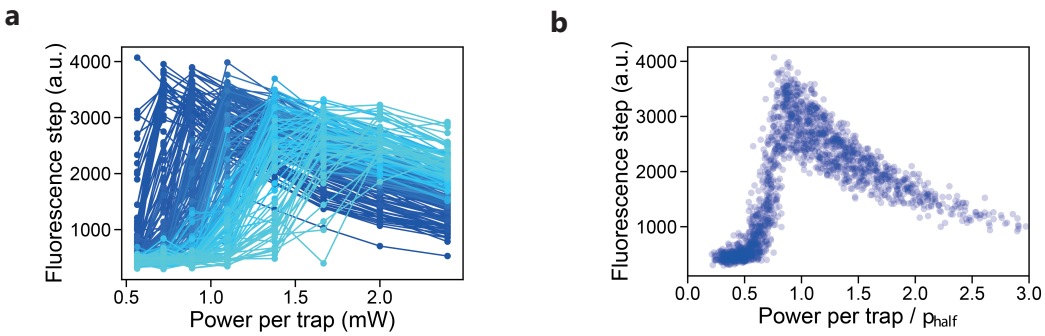

Figure 6.5: Overlaying the fluorescence step sizes. a: For each trap in a 15×15 array, we record the maximum fluorescence step size for 8 different powers. Each of the points is averaged for at least 60 s, with a relatively low loading rate into the tweezer of about 2 atoms per second (compare e.g. Figure 6.2). **b:** Overlay of all datapoints, by using p_{half} previously determined by the loading probability. The spread in the maximum fluorescence count indicates that the collection efficiency is not the same for all traps.

equalisation scheme, as I will discuss in the next section. Note that it is crucial for the loading rate of atoms from the MOT into the tweezer to stay constant. If the loading rate changes during measurement, the sharpness of the rise of the loading probability in the intermediate regime will change which makes the determination of p_{half} less precise. It should however not pose a big issue for the loading rate to be approximately constant over a duration of 10 minutes.

Fluorescence step size From Figure 6.2, we find that the fluorescence step size has a maximum and is not a monotonous function of the trap power. This is explained by two competing effects: First, the light-shift is smaller for a decreasing trap power, leading to a bigger fluorescence step for low powers. Second, we need a finite trap power to be able to trap the atom that is dependent on the temperature of the atom. Below that power, the step size decreases to the noise level. In an intermediate regime, the atom is captured for less than the duration of a fluorescence image, and the fluorescence step size increases with increasing trap depth.

Using the fit parameter of the half-way power p_{half} from the analysis of the loading probabilities, we can rescale the fluorescence traces, as illustrated in Figure 6.5. Again, we find that we can overlay the traces reasonably well, however the spread in the peak fluorescence step is significant. This can be explained by the fact that the amount of collected fluorescence light also depends on the position. Off the axis of the aspheric lens, we collect a significantly smaller number of photons.

We note therefore that the number of counts $N_{\mathrm{counts},i}$ obtained with the fluorescence camera from an atom in a tweezer trap i depends on (i) the number of photons

$N_{\text{photons},i}$ emitted by the atom, (ii) the position dependent collection efficiency η_i and (iii) the conversion ϵ from photons to digital counts in the camera:

$$N_{\text{counts},i} = \epsilon \eta_i N_{\text{photons},i} \quad . \tag{6.3}$$

The number of scattered photons is given by the scattering rate $R_{\text{sc},i}$ and the duration of a fluorescence image (here $t_{\text{image}} = 50\,\text{ms}$). For a two-level atom, the steady state total photon scattering rate is given by

$$N_{\text{photons},i} \propto R_{\text{sc},i} = \left(\frac{\Gamma}{2}\right) \frac{I/I_{\text{sat}}}{1 + I/I_{\text{sat}} + 4(\Delta_i/\Gamma)^2} \quad . \tag{6.4}$$

Here, Γ is the natural decay rate from the excited state, I_{sat} the saturation intensity, I the intensity of the laser and Δ the detuning of the laser from the atomic resonance. The detuning Δ_i at each trap i is given by the detuning of the MOT laser beams δ_{MOT} and the light-shift of the ground and excited state $\delta_{\text{light shift},i}$, with $\Delta_i = \delta_{\text{MOT}} + \delta_{\text{light shift},i}$. The light-shift depends on the trap depth of each trap and is therefore proportional to the average laser power per trap:

$$\delta_{\text{light shift},i} = \delta_i^* p_{\text{trap}} \quad , \tag{6.5}$$

with δ_i^* the light-shift per mW of average trap power.

In Figure 6.6a, the fluorescence step is fitted with equations (6.3),(6.4), having the conversion factor $C_{\text{tot}} = \epsilon \eta_i t_{\text{image}}$ and the light shift per mW of average trap power δ_i^* as free parameters. We see that the decrease of the fluorescence step is well captured by the effect of reduced scattering rate. Similar to the analysis of the loading probability, we try to overlay all the traces onto one curve in Figure 6.6c. As the trace collapse onto one curve, the light shift per mW δ_i^* therefore is a good estimate for the trap depth. However, not all the traces had enough data points above 50% loading probability (compare e.g. Fig. 6.4), and therefore we could not determine δ_i^* for all traps, as can be seen in Figure 6.6d.

In conclusion, we find that the decrease of the fluorescence step with increasing power can indeed be described with a light-shift from the atomic resonance. Furthermore, we can estimate the trap depth from the decrease of the fluorescence step with increasing trap power. However, from the given data, we could not estimate the trap depth for all traps. Therefore, the fluorescence step size should be recorded for more values of the power. The estimation of the absolute value of the light shift with our method is not very precise, because (i) most of the traces do not have sufficient data points to

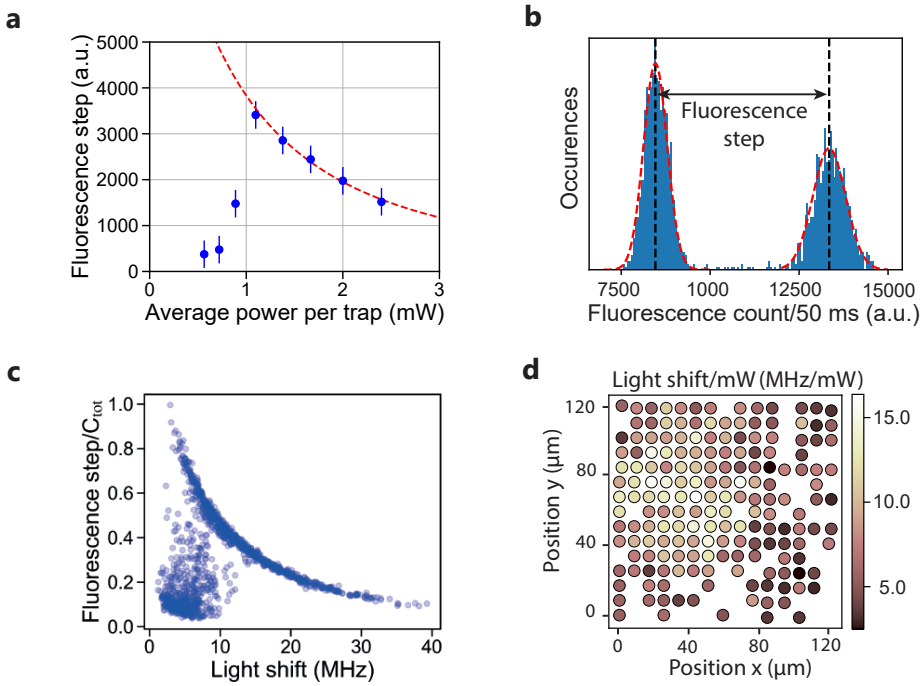

Figure 6.6: Overlaying the fluorescence step sizes. a: The fluorescence step size for a trap (blue points) is proportional to the scattering rate. The decrease with increasing power is caused by the light-shift. The red dotted line is a fit to the data using the scattering rate (eq. (6.4)). **b**: Example of histogram of a fluorescence trace (not from this data set) that allows us to extract the fluorescence step. The error on the fluorescence step is given by the gaussian distribution (see text). **c**: We can overlay all data points by rescaling the axis with the fit parameters. **d**: The light shift per mW of laser power δ^* for all traps, as obtained from the fits. For a few shallow traps, not enough data points at high power were available to fit equation (6.4).

fit, (ii) the errors for the fluorescence step are for us on the order of 10% (see 6.6b), mainly given by the photon-shot noise and conversion processes in the camera (see e.g. Ref. [Alberti *et al.*, 2016]). Furthermore, the precision could be improved with a calibration of the camera, to be able to extract the number of photons (see e.g. Ref. [Bergschneider *et al.*, 2018]) and fix the parameter C_{tot}.

Comparing both the analysis of the fluorescence step and of the loading probability, the latter seems preferable for a trap equalization method. From the given data, the fitting procedure of the loading probability lead to a smaller uncertainty for the trap depth estimate p_{half}. Furthermore, less data points for lower powers can be taken compared to the procedure for the fluorescence step that did not work for all traps.

6.2.3 A new proposed scheme

As we have seen in the previous section, the loading probability as a function of the trap power allows us to compare the trap depths between traps with relatively high precision. Therefore, we should be able to use the determined half-way power $p_{\mathrm{half},i}$ of each trap i for a trap depth equalization scheme. In the following, I propose two new schemes to equalize the trap depths which are illustrated in Figure 6.7.

Iterative Scheme A first scheme might use the half-way power $p_{\mathrm{half}}/\overline{p}_{\mathrm{half}}$ to substitute the previously measured peak intensity $I_i/\bar{I}$. Then the equalization scheme is similar to the method described in Chapter 2.1.2, as illustrated in Figure 6.7 . The advantage of this method is that it entirely relies on the EMCCD camera that records the fluorescence traces and the SLM. The CCD camera is not needed any more. The disadvantage however is the comparatively long duration of the equalisation scheme. In each iteration, we have to record the fluorescence trace for multiple overall trap powers, which can easily take 5 to 10 minutes. Therefore this method would take at least one hour to equalize the trap depths reasonably well (usually about 10 iterations).

Combined Scheme In a second scheme, we avoid measuring the half-way power p_{half} in each iteration. Instead, we measure it once to calibrate the CCD camera. We assume that on each trap site i, the measured peak intensity I_i^* on the CCD camera is proportional to the trap depth U_i in the focal plane of the aspheric lens:

$$U_i \propto p_{\mathrm{half},i} = \beta_i I_i^* \quad . \tag{6.6}$$

The proportionality factor β_i is not equal for all traps i, as we have previously seen, e.g. in Figure 6.3. However, on each trap site there is a linear relationship between the measured between U_i and I_i^*, as has been verified.

After this calibration, we can use the CCD camera and the SLM for the feedback algorithm. The advantage of this method is that the time consuming measurement of the half-way powers $p_{\mathrm{half},i}$ is done only once, and afterwards is substituted for the fast intensity measurement of the CCD camera.

6.3 Conclusion

In this Chapter, I have illustrated current progress on the experiment to solve technical imperfections in order to assemble large arrays of atoms. These technical imperfections

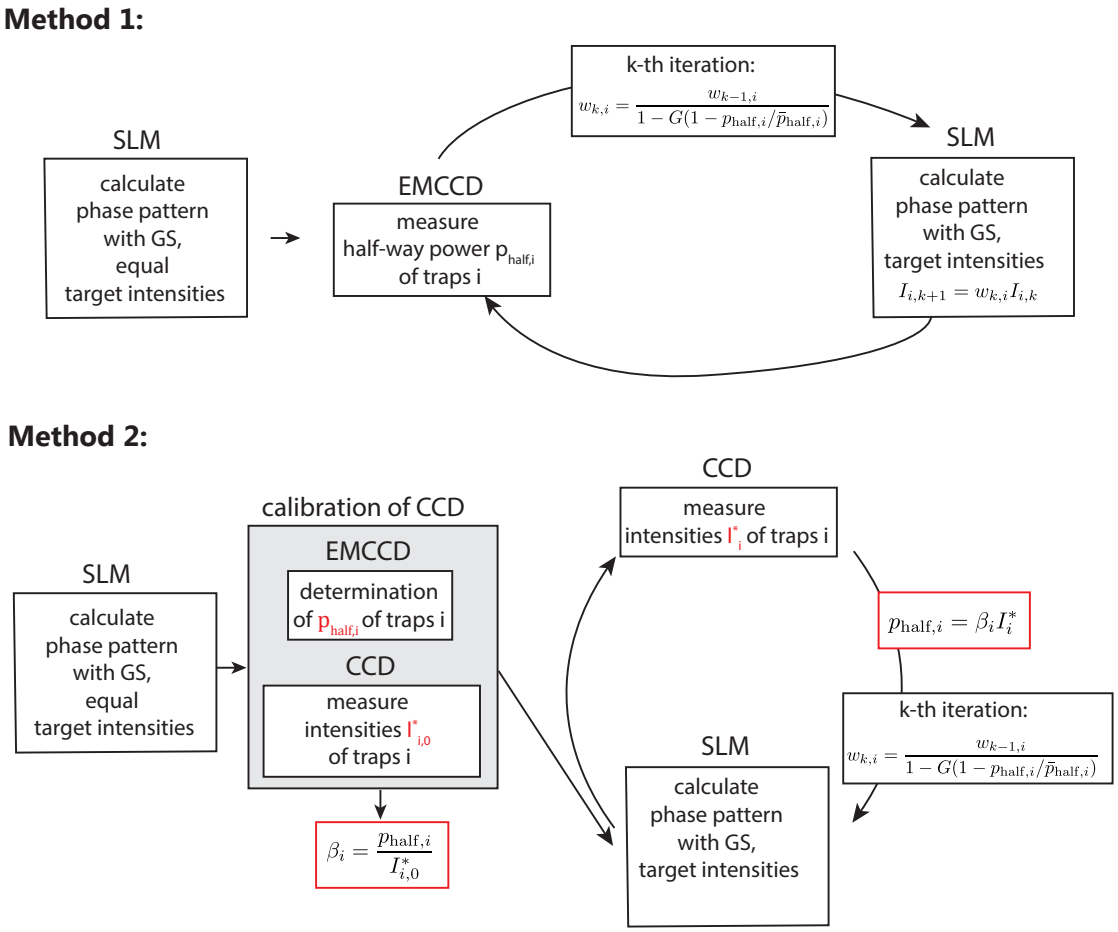

Figure 6.7: Schematic of the proposed equalization schemes. Method 1: This method relies on the determination of the trap depths with the *in situ* atomic signal recorded by the EMCCD camera. From the determination of the half-way power $p_{\mathrm{half},i}$ for each trap i, we can then calculate weights in a similar fashion to before and use them in the next iteration of the SLM algorithm. This method does not use the CCD camera anymore to measure the intensity distribution in the focal plane of the aspheric lens. **Method 2:** This method first calibrates the measured intensities on the CCD camera, by determining the corresponding $p_{\mathrm{half},i}$ for all traps. Using the conversion factor β_i for each trap, we then perform the equalization purely with the CCD camera and the SLM.

have been analysed in the course of this thesis and are (i) the imperfect trap depth equalization, (ii) the decreased assembly efficiency for large arrays, and (iii) the finite imaging survival probability. Once these imperfections have been resolved, we can fully profit from the extended vacuum lifetime of the cryogenic setup and should be able to assemble up to 500 atoms.

This chapter focuses mainly on the trap depth equalization. I first state the issues of the current method that uses the CCD camera to estimate the trap depths. Then, I analyse whether we can obtain more reliable estimates from the fluorescence trace. I find that we can estimate the trap depth from measuring the decrease in scattering rate for increasing light-shift. However, it is more reliable to estimate the trap depth from the change of loading probability as a function of trap depth. I then propose two new methods that use this new metric. The big advantage of the proposed methods is that they require only simple tools to estimate the trap depth (only the MOT lasers).

Next steps I have recorded and analysed the data of this chapter at the time of writing and we have not demonstrated the proposed methods yet. In the immediate future, we will however test both methods experimentally and evaluate whether the fluorescence trace can be used for a new improved trap depth equalization method.

One disadvantage of the proposed method is the required overall laser power. This is usually a limited resource; however, we need to change it over a large range during the measurement of the loading probability curve (see Figure 6.4). If the initial spread of trap depths is too big, we will not have a large enough range in power to take the full calibration curve for all the traps. Therefore we need some pre-equalization method for large (larger than the FOV) arrays, to smoothen out the initial trap depth pattern (see circle in Figure 6.3). This is easily done however, by doing one calibration measurement of the positions (with less traps), and then saving the weights. We can then do intensity equalization in the beginning using these weights, to arrive at a pre-equalized pattern.

Another solution could be to partition the trap array into two (or more) equal parts and change the trap depths in the two parts using the SLM. While the first part is ramped from full trap depth to almost zero trap depth, the second part is ramped in the opposite way. This way, the overall laser power will always be constant, however, the trap depths can be changed over a large range.

Other imperfections A well equalized trap array will not only be important to assemble large arrays of atoms, but also to examine the other two technical imperfections in more detail.

The survival probability of an atom during an image depends on the trap depth, as we have already seen in this Chapter. If the trap depth is too small, the atoms are trapped for less than the duration of an image, leading to a *spiky* fluorescence trace. Related to this observation, the detuning of the imaging light from resonance should play an important role, and its intensity, as we saw in the previous chapter for a reduced lifetime for high repump intensities. In Chapter 5, we have seen that we

currently obtain a survival probability of approximately 0.998 for an atom during a 50 ms fluorescence image. However, it is important to increase this further. With Strontium e.g., it has been shown that high survival probabilities of 0.99932(8) can achieved [Covey *et al.*, 2019].

The reduced single move efficiency for large arrays also depends on the trap depth, as has been shown in [Barredo *et al.*, 2016]. We think that reduction of this single move efficiency — when comparing arrays of 10 µm extent to those bigger than 100 µm — is mainly due to the change of trap depth of the moving tweezer over the whole extent of a large array, caused by the changing diffraction efficiency of the AODs. This could however be calibrated in the future such that the trap depth is kept constant over the full array using feed-forward.

Chapter 7

Conclusion and Outlook

Similar to most quantum simulation platforms, the tweezer atom array experiment of our group faces a major challenge in increasing the number of individually controlled quantum objects. In this manuscript, I have presented work on lifting some important limitations for the scalability of our platform, involving the construction of a new cryogenic tweezer array experiment and improved assembly algorithms for large defect-free arrays.

Assembly of defect-free atom arrays The atom-by-atom assembly scheme of our group was first presented in 2016 [Barredo *et al.*, 2016]. With it, we could assemble regular (Bravais) lattice geometries with excellent efficiencies and later the method was extended to three dimensions [Barredo *et al.*, 2018]. The ability to produce defect-free atom arrays together with the flexibility in choice of lattice geometries (e.g. triangular, square, Kagome) opened up a variety of possible applications in the field of quantum simulation. During my PhD, we have improved this method in two regards: (i) the scalability of the technique and (ii), its flexibility by extending it to the assembly of arbitrary geometries.

With new algorithms that need less elementary moves to assemble a defect-free atom structure, we improved the overall efficiency of the assembly process [Schymik *et al.*, 2020]. As a result, we were able to increase the number of atoms from around forty up to 200 for a quantum simulation of the Ising model on our room-temperature setup [Scholl *et al.*, 2021a]. With the total atom number increase, the ratio between bulk and boundary atoms also improves and both allows us to investigate phenomena that were previously limited by atom number and boundary effects.

Using the new algorithmic framework, we can now assemble arbitrary geometries. This further extends the number of physics questions that can be investigated on our platform. Next to condensed matter models with non-periodic features such as crystal defects (interstitial defects, vacancies, dislocations, grain boundaries), this includes recent proposals for optimization problems on graphs [Henry *et al.*, 2021; Pichler *et al.*, 2018; Henriet, 2020; Minhyuk *et al.*, 2021]. As an example, finding the maximum independent set (MIS) of a unit-disc graph is an optimization problem that

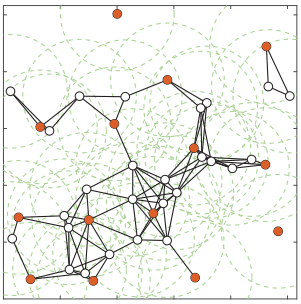

Figure 7.1: Maximum independent set for unit-disc graphs. On the unit-disc graph, two vertices are connected if they are closer than a unit distance, symbolised be green circles. Finding the maximum independent set (red) is an optimization problem that can be mapped onto a Rydberg quantum simulator. Hereby, the Rydberg blockade radius corresponds to the unit distance, and the MIS is the ground-state for an Ising-like Hamiltonian. This figure is extracted from Ref. [Pichler *et al.*, 2018].

can be mapped on a Rydberg quantum simulator. A unit-disc graph is a collection of vertices with an edge between two vertices, if they are closer than a unit distance, as illustrated in Figure 7.1. Finding the MIS of a given graph consists in finding the largest subset of vertices, such that no two two vertices in the MIS are connected by an edge. The decision version of the MIS problem — deciding whether the size of an MIS is larger than a given integer on an arbitrary graph — is known to be *np*-hard.

The Rybderg blockade prevents the simultaneous excitation of two connected vertices on a graph, if the atomic configuration is chosen such that connected vertices have a large van der Waals interaction energy. The ground state of the system would then correspond to the maximum independent set of the unit-disc graph. The ability to assemble arbitrary geometries is hereby essential to be able to choose the right atomic configuration for a given graph.

Cryogenic tweezer platform In Chapter 4, I have presented the construction of a new cryogenic tweezer platform. Due to the high pumping speed of the cryogenic surfaces at 4 K, the vacuum at the position of the atoms is orders of magnitude better than on our room temperature setup. This drastically reduces the loss rate of ^{87}Rb atoms from the tweezer due to background gas collisions. As demonstrated in Chapter 5, the lifetime of an atom in the tweezer is over 6000 s, compared to our room-temperature setup an increase by a factor of approximately 300.

On our room-temperature setup, the lifetime is a major limitation to scaling up the number of atoms. With a lifetime of over 6000 s however, its effect is almost negligible

even for an array with over 1000 atoms. This is a promising result for the creation of large arrays of atoms on tweezer platforms and shows its potential for large-scale quantum simulation or computation. Recently, the attractiveness of the Rydberg tweezer platform has lead to a large interest in the cold atom community, with the construction of many similar (but non-cryogenic) platforms in labs all over the world, and even at the industrial level in companies, such as QuEra [Bluvstein *et al.*, 2021], ColdQuanta [Graham *et al.*, 2021], Atom Computing [Barnes *et al.*, 2021] or PASQAL [Henriet *et al.*, 2020]. The work of this thesis is relevant for these companies as well, as most of them promise 1000 qubit processors or computers by 2024.

In a series of tests, we have investigated several experimental heat loads on our cryogenic platform, like current carrying wires or incident laser power (see Chapter 5). We have demonstrated the capability of our system to keep low temperatures despite these heat loads, as the temperature of the cold plate rises only to 5.2 K, when operated with approximately 1000 tweezer traps. Therefore, our cryostat is well-suited for experiments with large tweezer arrays.

In the near future, it would be interesting to measure the lifetime at different (cryogenic) temperatures, above the critical temperature of the superconducting coils and e.g. up to the temperature of liquid nitrogen. Although the lifetime surely decreases at higher temperatures, the requirements for acceptable heat loads soften. As an example, one could use non-superconducting coils at higher temperatures, if the decrease in lifetime is acceptable. In view of the industrialisation of these platforms, this information could be valuable.

Future directions In Chapter 6, I have illustrated important steps towards the assembly of up to 500 atoms on our cryogenic platform. This involves improving several technical imperfections such as the trap depth equalisation, the single-move efficiency of the moving tweezer, and the survival probability of a fluorescence image. In the near future, we will work on solving these imperfections to demonstrate the assembly of large arrays with high fidelities.

To further extend the assembly capabilities, we could implement the 3D plane-by-plane assembly scheme of our group [Barredo *et al.*, 2018]. The third dimension would help to alleviate the constraint of the field-of-view of the lens, as more traps could be created in the volume of the FOV. The technical implementation includes electric tunable lenses to change the focal plane of the moving tweezer and the fluorescence camera. As each plane is imaged separately, the plane-by-plane assembly usually takes longer than assembling a single plane. This should not be limiting any more with the extended lifetime on our cryogenic setup. However, the limited image survival

probability could still be of concern. Therefore, it could be useful to implement another SLM in the fluorescence plane to image several planes simultaneously [Haeun *et al.*, 2021]. With these changes and the promising results of the thesis, we hope to reach the regime of 1000 traps in three dimensions soon. An additional improvement with techniques to increase the loading probability way above 50% [Sompet *et al.*, 2013; Lester *et al.*, 2015; Brown *et al.*, 2019; Aliyu *et al.*, 2021; Jenkins *et al.*, 2021] could be helpful to lift the constraint of laser power and reduce the assembly time.

In the near future, we will add the capabilities for Rydberg atoms to our setup. This involves a laser system for the Rydberg excitation, similar to the one I have described in Chapter 2.2.2. Furthermore, electrodes should be added to the lens holder, similar to our room-temperature setup [Béguin, 2013], to actively control the electrostatic environment in the focal plane of the lenses. To drive transitions between different Rydberg states, we would also add microwave antennas inside the 4 K shield. As our cryogenic system is not baked out, these simple upgrades in the science chamber can be done on a relatively fast time scale, as we have seen during the tests described in Chapter 4.

A first interesting experiment with Ryberg atoms would be the measurement of the Rydberg lifetime. As explained in Chapter 1, the lifetime should be extended in a cryogenic environment, due to the suppression of black-body induced transitions. The measurement of Rydberg lifetimes has been measured recently in our room-temperature setup by trapping Rydberg atoms in three-dimensional holographic bottle beam traps [Barredo *et al.*, 2020]. In this work, the trapping lifetimes of states with principal quantum numbers $60 \leq n \leq 90$ coincided with the Rydberg lifetimes in a 300 K environment. A similar experiment could be conducted on the cryogenic experiment, demonstrating the effect of reduced black-body radiation on the Rydberg lifetime.

Afterwards, we would work towards large-scale quantum simulations of spin-Hamiltonians, e.g. the described Ising or XY-Hamiltonian, in two and three dimensions.

Appendix A

The Experiment in Practice: A Photo Gallery

In this Appendix, I illustrate the experimental setup with a few photos from the lab (Figure A.1).

The whole cryogenic setup is in the middle of the room on a 1.5 m × 2.5 m optical table. The atomic source part (oven and Zeeman slower) is mounted on a moveable breadboard, while the stainless-steel case of the cryogenic part is clamped to the optical table. Not shown in the images is a chain hoist above the experimental table that we used during construction to lift and place the science chamber. Above the experimental table are shelves, upon which the rotary valve is mounted. The helium lines on the rotary valve are connected to the cold head (PTR) of the cryostat, and also to a compressor that is sitting in the corner of the room. The compressor is water-cooled and connected to the water circuit of the air-conditioning.

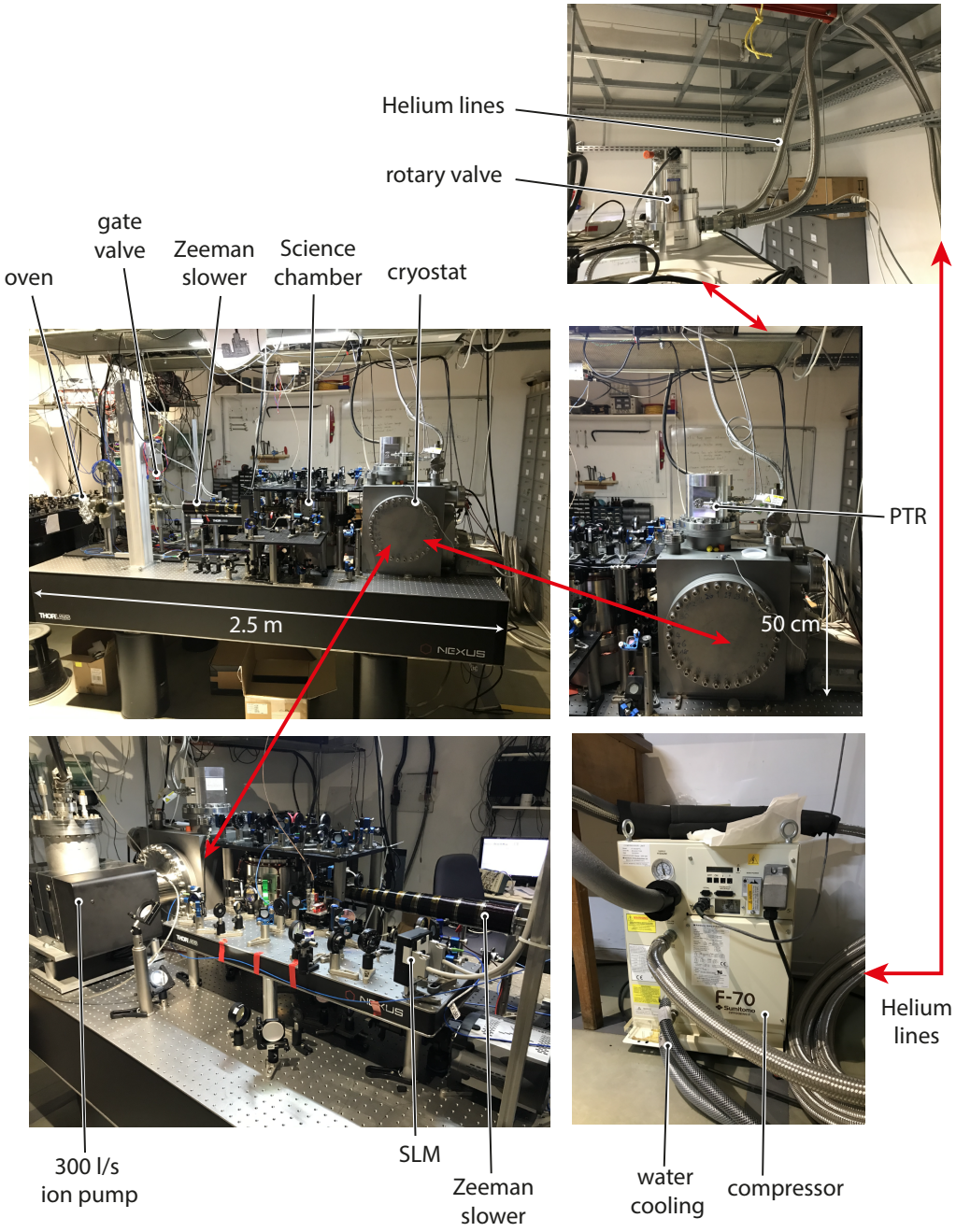

Figure A.1: Pictures of the experiment. Left: Front and backside of the experiment. **Right:** A rotary valve is connected to the PTR head and sits above the experiment. Helium lines are connecting the rotary valve to a water-cooled compressor that sits in a corner of the lab.

Appendix B

Estimate of the Rubidium-Rubidium Collisional Cross Section

In this Appendix, I show that the measured scattering rate between Rubidium atoms in the tweezer and Rubidium atoms from the oven (see Figure B.1a) agrees with a simple estimation given the geometry of the oven, but neglecting any effect of the trap. From the scattering rate, we can infer a Rb-Rb collisional loss cross section of $\sigma = 340\,\text{Å}^2$. This is within a factor of five to a classical calculation including the trap depth. It also agrees within approximately a factor seven with the total collisional cross section literature value of $\sigma_{\text{lit}} = 2500\,\text{Å}^2$ [Bali *et al.*, 1999].

B.1 Inferring the Rb-Rb collisional loss cross section from oven losses

In Chapter 5, we measured atom losses as a function of oven temperature. From this, we inferred a collision rate β that depended linearly on the Rubidium density in the oven

$$\beta = \gamma n_{\text{oven}}, \tag{B.1}$$

with the experimental determined parameter $\gamma = 7.1 \times 10^{-22}\,\text{m}^3\text{s}^{-1}$ (see Figure B.1).

Even though several experimental parameters, such as the oven temperature, are not known with high precision, we can estimate a Rb-Rb collisional cross section from this measurement with a simple model.

The collision rate β depends on the particle flux Φ in the chamber — the number of particles per unit time and unit area — and the Rb-Rb collisional cross section:

$$\beta = \sigma_{\text{loss}} \Phi_{\text{chamber}}. \tag{B.2}$$

To find the flux Φ_{chamber}, we use the following model. We consider an effusive oven, consisting of a Rubidium metal that is in equilibrium with its vapor, corresponding to the saturated vapor pressure $P_{\text{sat}}(T)$ at oven temperature T. The density of Rubidium

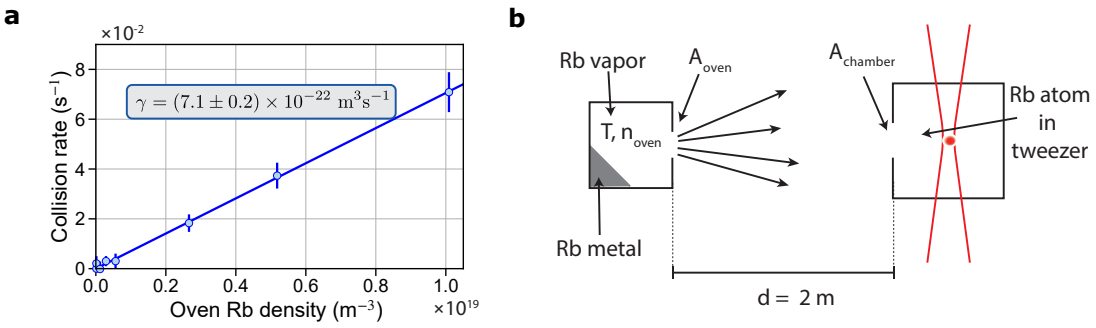

Figure B.1: Atom losses in the tweezer due to collisions with oven atoms a: Same as Figure 5.10, we measure a linear dependence between the collision loss rate and the Rb density in the oven. **b:** Sketch of the simplified model with the oven on the left and the science chamber on the right. Fast atoms exit the oven and fly towards the chamber where they scatter on the Rb atom in the tweezer.

in the oven is $n_{\text{oven}} = \frac{P_{\text{sat}}(T)}{k_B T}$. The gas inside the oven with aperture $A_{\text{oven}} = \pi(2.5\,\text{mm})^2$ is in equilibrium and follows the Maxwell-Boltzman distribution:

$$f(v_x, v_y, v_z) = \left(\frac{m}{2\pi k_B T}\right)^{3/2} \exp\left(\frac{-m(v_x^2 + v_y^2 + v_z^2)}{2k_B T}\right) \quad . \tag{B.3}$$

Using spherical coordinates, the probability of having a particle with velocity v within the solid angle $\mathrm{d}^2\Omega = \sin\theta\ \mathrm{d}\theta\ \mathrm{d}\phi$ then reads

$$\mathrm{d}^3 P = \left(\frac{m}{2\pi k_B T}\right)^{3/2} v^2 \exp\left(\frac{-m(v_x^2 + v_y^2 + v_z^2)}{2k_B T}\right) \mathrm{d}^2\Omega\ \mathrm{d}v \quad . \tag{B.4}$$

The number of atoms flying out of the oven per unit time and unit area, denoted flux Φ, can be found as:

$$\Phi_{\text{oven}} = \frac{1}{4} n_{\text{oven}} \bar{v} \quad , \tag{B.5}$$

with $\bar{v}$ the mean velocity in the vapor:

$$\bar{v} = \sqrt{\frac{8k_B T}{\pi m}} \quad . \tag{B.6}$$

For small solid angles, one finds that the flux of atoms into the chamber at a distance of $d = 1.5$ m is then given by:

$$\Phi_{\text{chamber}} = \Phi_{\text{oven}} \frac{A_{\text{oven}}}{\pi d^2} \quad . \tag{B.7}$$

Combining equations (B.2),(B.5) and (B.7), we find

$$\beta = \sigma_{\text{loss}} \frac{A_{\text{oven}} \bar{v}}{4\pi d^2} n_{\text{oven}}, \tag{B.8}$$

and using equation (B.1), we finally find the loss cross section as a function of the measured parameter γ:

$$\sigma_{\text{loss}} = \gamma \frac{4\pi d^2}{A_{\text{oven}} \sqrt{\frac{8k_B T}{\pi m}}} \simeq 340\,\text{Å}^2 \quad . \tag{B.9}$$

B.2 Classical estimate of the collisional loss cross section

To estimate the collisional cross section, we can use our knowledge of the experimental situation (see Figure B.2) to make a simplifying approximation. An atom leaves the oven in x-direction with velocity v (typically $300\,\text{m}\,\text{s}^{-1}$) and is scattered in the xy-plane on an atom in a dipole trap inside of the science chamber. The atom from the oven has a high kinetic energy compared to the shallow trap with a depth of approximately 1 mK. We are interested in finding the impact parameter b_0, at which the trapped atom receives enough momentum to leave the trap. If this was for small impact parameters b, e.g. a near head-on collision, the imparted momentum on the trapped particles is large and both particles would change directions. Here, the full two-body problem would have to be solved for which we would change to the center-of-momentum frame. In our case however, we know that even collisions with large impact parameter will lead to a loss of the trapped atom. In this limit, the deviation angles of the atom from the oven are small. We assume the atom is not deflected at all and its trajectory is fixed along $y = b$ with uniform velocity v. In this limit, the calculation of the collisional loss cross section simplifies and we can use the laboratory frame.

First, we calculate the imparted momentum $\Delta p_y(b)$ on the Rubidium atom in the dipole trap with trap depth U_0 as a function of the impact parameter b. At distance $b = b_0$ the Rubidium atom receives enough energy to leave the trap (see Figure B.2b), if

$$\frac{\Delta p_y(b = b_0)^2}{2m_{\text{Rb}}} > U_0. \tag{B.10}$$

Then, the collisional loss cross section is

$$\sigma_{\text{loss}} = \pi b_0^2. \tag{B.11}$$

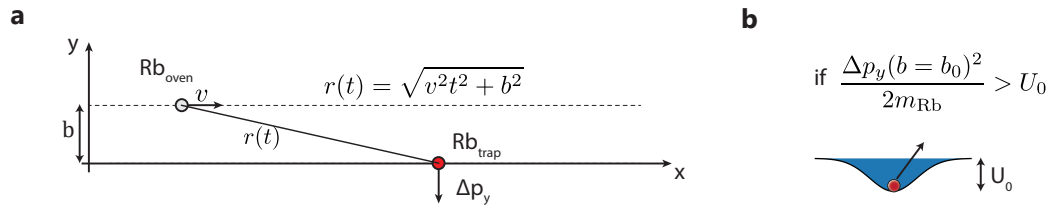

Figure B.2: Collisions under small angles. a: A Rubidium atom from the oven with a velocity v_{oven} scatters on a stationary Rubidium atom in a dipole trap. Under large enough distances ρ, the scattering angle θ is small. The trapped Rubidium atom has momentum Δp_y after the scattering event. **b:** For distances smaller than the impact parameter b, the atom leaves the trap after the collision.

The potential U between the two Rubidium atoms is given by the van-der-Waals C_6 coefficient:

$$U(r) = \frac{-C_6}{r^6} = \frac{-C_6}{(v^2t^2 + y^2)^3} \quad , \tag{B.12}$$

where $C_{6,\text{Rb}} = 4667\ \text{Ha}a_0^6$ in atomic units [Gould and Bučko, 2016] and r is the distance between the two atoms (see Fig. B.2a).

The imparted momentum along y is

$$\Delta p_y = \int_{-\infty}^{\infty} -\frac{\partial U}{\partial y} \mathrm{d}t \quad . \tag{B.13}$$

Using equation (B.12) and the fact that the oven atom is moving along a straight line $y = b$, we get

$$\Delta p_y = -6bC_6 \int_{-\infty}^{\infty} \frac{\mathrm{d}t}{(v^2t^2 + b^2)^4}. \tag{B.14}$$

Finally, we find

$$\Delta p_y(b) = \frac{15\pi C_6}{8vb^6} \quad , \tag{B.15}$$

Using equation (B.11) and (B.10), we find for the loss cross section:

$$\sigma_{\text{loss}} = \pi \left[\frac{1}{2mU_0} \left(\frac{15\pi C_6}{8v} \right)^2 \right]^{1/6} \quad . \tag{B.16}$$

The collisional loss cross section is therefore proportional to $U_0^{-1/6}$ and $v^{-1/3}$. Using the mean velocity of Rubidium atoms[1] out of an oven at 100 °C $v = 300\,\text{m}\,\text{s}^{-1}$ and a trap depth $U_0 = 1\,\text{mK}$, we arrive at:

[1]For this estimate, we refrain from taking into account the velocity distribution and instead use $\bar{v}$.

$$\sigma_{\text{loss}} \simeq 1600\,\text{Å}^2 \quad . \tag{B.17}$$

In comparison, the simple estimation of the collisional cross section (eq. (B.9)) from experimental loss rates lies within a factor of five of the calculated value. Note however that the experimentally inferred collisional cross-section is only a crude approximation, as our setup leads to several technical uncertainties. The temperature of the oven is not known with high precision. The oven is wrapped in heating tape and connected to a temperature controller together with a single temperature sensor that is attached to the oven. Due to the wrapping, the temperature might not be uniform in the oven region, and the temperature sensor is in close proximity to the heating tape.

Appendix C

Magnetic Field Coils for the Magneto-Optical Trap

This appendix gives details about the magnetic field coils in the science chamber used for the magneto-optical trap.

The coils consist of a copper-beryllium holder, with an external diameter of $d_{\text{ext}} = 52\,\text{mm}$ around which the superconducting wire is wound with $N = 100$ turns. The two coils are separated by $d_{\text{coils}} = 80\,\text{mm}$ and can be operated in (anti-)Helmholtz configuration (see Fig. C.1a).

The magnetic field B on axis ($x = y = 0$) as a function of the position z for the two coils is calculated as follows:

$$B(z) = \frac{\mu_0 N I}{d_{\text{ext}}}\left[\left(\frac{d_{\text{ext}}/2}{\sqrt{\frac{1}{4}d_{\text{ext}}^2 + (z + d_{\text{coils}})^2}}\right)^3 \underset{(-)}{+} \left(\frac{d_{\text{ext}}/2}{\sqrt{\frac{1}{4}d_{\text{ext}}^2 + (z - d_{\text{coils}})^2}}\right)^3\right] \quad . \tag{C.1}$$

The calculated field and gradient for our geometry is illustrated in Figure C.1b. In anti-Helmholtz configuration, we reach a magnetic field gradient of 4.3G/cm/A at the position of the atoms. For the operation of the MOT, we usually use a current of around 1.7 A, leading to a magnetic field gradient of approximately 7G/cm/A.

For Helmholtz configuration (plus sign in equation (C.1)), the field and gradient is illustrated in Figure C.1c.

The Kapton-insulated superconducting wire (Supercon Inc.) has a diameter of 0.5 mm. Inside, it has multiple 38 µm-diameter superconducting NbTi wires inside of a copper-matrix, with a copper-to-superconductor ratio of approximately 3:1. The superconductor has a critical temperature of 9.2 K, the residual resistivity ratio (RRR) of the copper wire is approximately 230.

Per coil, we use an approximate length of L =16 m of wire. We measure the resistance of each coil to be $R_{\text{coil,T=300K}} = 2.1\,\Omega$.

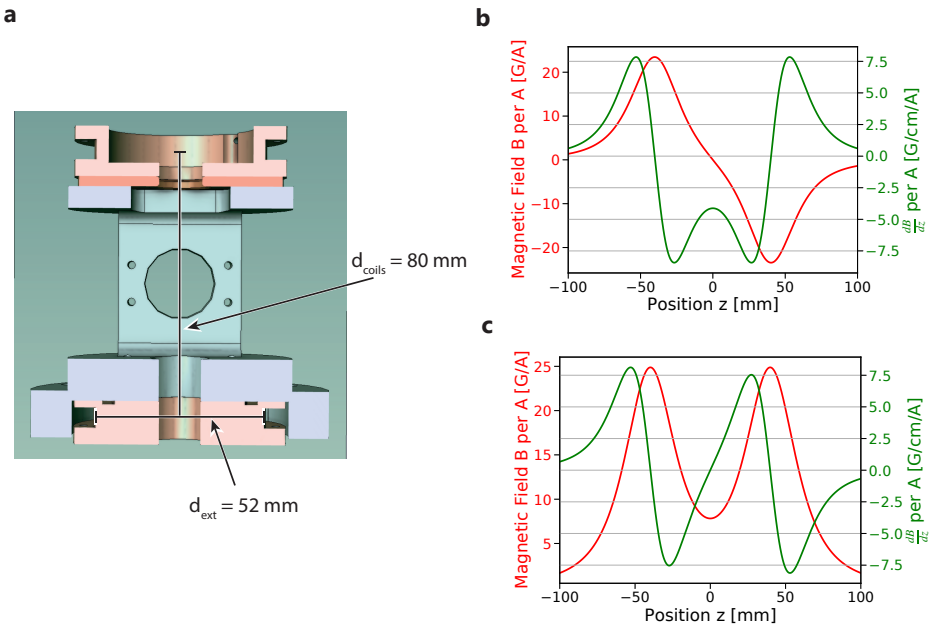

Figure C.1: Magnetic field coils. a: Cross-section through the lens-holder containing the magnetic-field coils. **b:** Calculated magnitude of magnetic field and magnetic field gradient as a function of the position. We reach a typical magnetic field gradient of $4.3\mathrm{G/cm/A}$ at the center of the coils in anti-Helmholtz configuration. **c**: Magnetic field and gradient as a function of the position at the center of the coils in Helmholtz-configuration.

Appendix D

Article: *Enhanced Atom-by-Atom Assembly of Arbitrary Tweezer Arrays*

This appendix reproduces the following published article:

Kai-Niklas Schymik, Vincent Lienhard, Daniel Barredo, Pascal Scholl, Hannah Williams, Antoine Browaeys, and Thierry Lahaye. *Enhanced atom-by-atom assembly of arbitrary tweezer arrays*. Physical Review A **102**, 063107 (2020)

Editors' Suggestion

Enhanced atom-by-atom assembly of arbitrary tweezer arrays

Kai-Niklas Schymik, Vincent Lienhard, Daniel Barredo, Pascal Scholl, Hannah Williams, Antoine Browaeys, and Thierry Lahaye

Université Paris-Saclay, Institut d'Optique Graduate School, CNRS, Laboratoire Charles Fabry, 91127 Palaiseau, France

(Received 13 October 2020; accepted 20 November 2020; published 10 December 2020)

We report on improvements extending the capabilities of the atom-by-atom assembler described by Barredo *et al.* [Science **354**, 1021 (2016)] that we use to create fully-loaded target arrays of more than 100 single atoms in optical tweezers, starting from randomly loaded, half-filled initial arrays. We describe four variants of the sorting algorithm that decrease the number of moves needed for assembly and enable the assembly of arbitrary, nonregular target arrays. We demonstrate experimentally the performance of this enhanced assembler for a variety of target arrays.

DOI: 10.1103/PhysRevA.102.063107

I. INTRODUCTION

Over the past few years, arrays of single laser-cooled atoms trapped in optical tweezers have become a prominent platform for quantum science, in particular for quantum simulation [1]. They allow single-atom imaging and manipulation, fast repetition rates, and high tunability of the geometry of the arrays. When combined with excitation to Rydberg states, these systems naturally implement quantum spin models, with either Ising [2–6] or XY [7] interactions. They can also be used to realize quantum gates with fidelities approaching those of the best quantum computing platforms [8–11].

A crucial ingredient of the atom array platform is the atom-by-atom assembly of fully loaded arrays, starting from the partially loaded arrays (with a typical filling fraction of 50%–60%) obtained when loading optical tweezers with single atoms [12]. This technique, first demonstrated in [13–15], can follow different approaches. A fast and effective approach for realizing one-dimensional chains uses an acousto-optic deflector (AOD) driven with multiple radio-frequency tones to generate all the traps [14]; after loading, empty traps are then switched off and the remaining ones are brought to their target position, thus achieving a fully loaded chain in a single step. However, directly extending this approach to more than one dimension is challenging [16]. A different approach consists in using a spatial light modulator (SLM) to generate arbitrary patterns of traps in one, two, or three dimensions, load them with atoms, and then dynamically change the SLM pattern to rearrange the atoms in space [17]. However, SLMs are slow, making the rearrangement time prohibitive, which limits this approach to small atom numbers. Another approach is using a static trap array and combining it with a moving tweezer [13,18].

Our experiment [13] follows this strategy and uses an SLM that produces a user-defined fixed pattern of optical tweezers which includes the final (target) array, combined with a moving tweezer. This extra microtrap, controlled by a two-dimensional (2D) AOD, is used to move the atoms one by one to reach a fully loaded target array. The heuristic shortest-moves-first algorithm used in [13] to find the set of needed moves is versatile, as any target array included in an initial regular array can be assembled. It works well up to a few tens of atoms, but it has some limitations. First, the algorithm was written for regular arrays, such as square and triangular lattices. On completely arbitrary arrays, lattice edges along which atoms can be moved are not naturally given, and using straight paths between source and target traps would lead to unwanted losses, as another target trap already containing an atom may be in the way. Another limitation is that the number of moves needed for ordering is not optimal and minimizing this number becomes more crucial when the number N of assembled atoms increases beyond a few tens.

Here we describe four improved algorithms that can be used without any change in the hardware; the choice of the most efficient approach depends on the characteristics of the target array. We first recall in Sec. II the problem we need to solve and review our previous approach and its shortcomings (Sec. III). We then discuss in Sec. IV a compression algorithm which is well adapted for compact arrays (here, by compact we mean that no trap other than target ones lies within the target array). The number of moves is then at most N, which significantly reduces the assembly time. We show in Sec. V that a similar scaling can be obtained for all arrays (compact or not) by using algorithms based on a linear sum assignment problem solver. In Sec. VI we extend these algorithms to the case of fully arbitrary two-dimensional patterns (i.e., they are not embedded in a regular Bravais lattice). Finally, in Sec. VII we experimentally implement these approaches in a variety of arrays.

II. STATEMENT OF THE PROBLEM

Our goal is to obtain a fully loaded array of N traps, whose positions are given by the user (this defines the *target* array, denoted by green circles in this paper). To do so, we start from a larger array, with $\sim 2N$ traps, containing the target array and extra, *reservoir* traps (these will be denoted by red circles). The entire array is loaded in a stochastic way with an $\sim$50% filling fraction at each realization of the experiment.

Therefore, we have, with high probability, at least N atoms in the full array. Using a moving optical tweezer, we then transport the atoms one by one, from an initial trap to one of the target traps, until the target array is fully filled.

To maximize the success probability of the assembly process, we need to minimize the total assembly time. One reason for that arises from the vacuum-limited lifetime of a trapped atom, which, in our experiments, is $\tau_{\mathrm{vac}} \sim 20$ s. This means that for an array with N atoms, the lifetime of the configuration is τ_{vac}/N. It is thus important, when N increases, to minimize the total assembly time to reduce atom losses during rearrangement. As atoms are moved between traps at a constant velocity (typically $\sim$100 nm/μs, meaning we need $\sim$50 μs to move over a typical nearest-neighbor distance of 5 μm) and as it requires a comparatively longer time (600 μs) to capture or release an atom [13], minimizing the arrangement time mainly amounts to minimizing the number of moves and, but to a lesser extent, the total travel distance (defined as the sum of the lengths of the successive straight paths over which an atom is moved). A second reason for minimizing the number of moves is that each transfer from a source trap to a target trap has a finite success probability p (typically around $p \sim 0.98$–0.99 in our experiments), partly due to the already mentioned vacuum-limited losses, but also due to, e.g., inaccuracy in the positioning of the moving tweezers or residual heating. Beyond the number of moves and the total travel distance, the time it takes for the algorithm to compute the moves at each repetition of the experiment contributes to the total assembly time.

In [13] we distinguished two types of moves for reordering. The first approach (which we called type 1) corresponds to the situation where the atom can be moved in between adjacent rows of traps. Then, as on average $N/2$ atoms are out of place initially, the mean number of needed moves is $N_{\mathrm{mv}} = N/2$ and we have to solve a linear sum assignment problem [19]. Using the Hungarian algorithm (as in [20]) then minimizes the assembly time. However, type-1 moves require a large distance (at least 5 μm) between any two traps to avoid atom loss due to disturbances of the trap potential. In practice, many experimental reasons (the finite field of view of the lenses used to focus the tweezers, the need to have large interaction strength between Rydberg atoms, and to have uniform Rydberg excitation lasers over the array) call for having smaller distances in the arrays. Furthermore, as we will see in Sec. VI, type-1 moves are not well suited for the assembly of truly arbitrary geometries. For these reasons, we here focus on solving our problem using just type-2 moves, where an atom can only be moved along a straight path between adjacent traps.

In the case of type-2 moves, assigning any source trap to any target trap is not possible, since other traps might be in the way. While an atom can be moved over an empty trap as the moving tweezer is $\sim$10 times as deep as the stationary traps, having filled traps on the path would lead to collisions and atom loss. Finding the optimal set of moves is thus nontrivial since it requires finding a collision-free assignment with a well-defined ordering of the moves. In computer science, this problem is known as the pebble motion on a graph (in a variant with unlabeled pebbles) and is intractable for large N [21], even more so in practice as we need to solve it in a time short compared to the configuration lifetime. Therefore, we opt for heuristic algorithms, provided they give a solution not too far from the optimum and run in a few tens of milliseconds at most for up to a few hundred atoms. In the next section, we will see that the algorithm used in [13] actually meets these criteria only when the target array is not too compact and when N is not too large.

III. OUR PREVIOUS ASSEMBLER: PRINCIPLE OF OPERATION AND LIMITATIONS

The atom-by-atom assembler described in [13,22] allowed us to create user-defined arrays in one, two, and three dimensions at unit filling. Nonperiodic structures, or complex lattices such as ladder, honeycomb, kagome, or pyrochlore geometries could also be obtained by selecting a subset of target traps on an underlying Bravais lattice.

We chose a heuristic approach to the problem that had the advantage of requiring a short computation time, scaling as $O(N^2)$, albeit at the expense of not guaranteeing the optimal assignment. This greedy algorithm, which we will call the shortest-moves-first algorithm, works as follows. We first compute a matrix of distances $D = d_{ij}$ between each out-of-place atom s_i and each (empty) target t_j trap. Then we order the entries of this matrix by increasing length and select the first $N/2$ elements with the condition that only one element per row or column is chosen (i.e., that each atom or target trap is only assigned once).

This initial matching is not collision-free, as already filled traps may lie in between a matched reservoir atom and an empty target trap. Therefore, in a second step, we postprocess this assignment by applying a rule that splits each move $S \to T$ from a source atom S to a target trap T in two moves $O \to T$ and $S \to O$ for each obstacle atom O that is found in the path. Note that this process leaves the travel distance unchanged but increases the number of moves, therefore increasing the total assembly time.

Figure 1 shows the number of moves N_{mv} returned by the above algorithm to assemble a target array of N atoms embedded in a square array, for three different geometries: (i) a staggered pattern, (ii) a random pattern, and (iii) a compact square in the center. The number of moves is averaged over 1000 realizations of the initial random loading. We observe that N_{mv} is only slightly above $N/2$ for the cases (i) and (ii) where the reservoir and target traps are strongly mixed. However, in the case (iii) of compact geometries, where all the reservoir atoms lie outside the target array, we observe that this procedure scales as $N_{\mathrm{mv}} \propto N^{\alpha}$, with $\alpha \simeq 1.4$ (red dashed line), making it unsuitable for large arrays.

The reason for this is illustrated in Fig. 2, which shows a few snapshots of the reordering process. The shortest moves are those connecting out-of-place atoms with target traps on the border of the array; therefore, the algorithm starts by filling the outermost shell. Once this is done, it is no longer possible to fill the (empty) inner traps without performing extra operations to displace the atoms that lie in the way, giving rise to many extra moves to fill the inner part of the target array. For the initial configuration in Fig. 2(b), the 14×14 target array is assembled in 444 moves. As picking up and releasing an atom takes extra time, this behavior leads to prohibitive rearrangement times, even if the distance traveled is close to optimal.

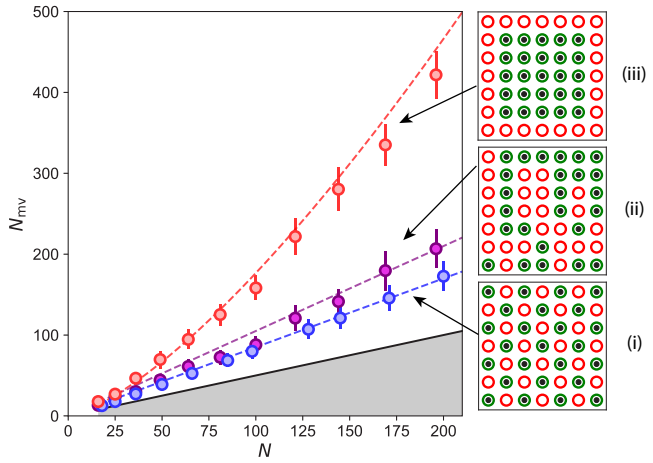

FIG. 1. Scaling of the number of moves for different geometries, with the shortest-moves-first approach. The plot shows the number N_{mv} of moves (averaged over 1000 realizations of the random loading; the error bars indicate the standard deviation of the distribution of N_{mv}) as a function of the size N of the target array. For staggered configurations (blue), where a target trap and a reservoir trap alternate, the overhead as compared to the lower bound $N/2$ (indicated by the solid black line above the gray-shaded area) is small. For a random subset of target traps in a square array (purple), the number of postprocessing moves due to obstacles is already bigger, but the scaling is still linear with N. A drastic change appears in the case of compact geometries (red), where the target array is surrounded by reservoir atoms. Here the number of moves does not increase linearly with N, but rather as $N^{1.4}$ (dashed line) and many postprocess moves are needed. This means that the current algorithm is unsuited for large compact geometries.

This behavior is problematic, as many arrays of interest for quantum simulation are compact. Therefore, it is crucial to find an assignment between the reservoir and target traps which really minimizes the number of moves. For assembling compact arrays, a much better approach, where the maximum number of moves is at most N, is the compression algorithm that we now describe.

IV. IMPROVED ASSEMBLY OF COMPACT ARRAYS BY THE COMPRESSION ALGORITHM

From the above considerations it is clear that we need to prevent the formation of the outer shell during the assembling process. A simple way to do this and have a collision-free assignment without any postprocessing is to fill the target traps in a determined order. We first fill the central traps and progressively, one layer after the other, we fill the compact structure until we reach its border. To fill the traps, we choose the closest atoms lying outside the already assembled bulk. An asset of this compression approach is that we can calculate once, independently of the initial loading, a lookup table. The table stores which source traps can be used to fill a given target trap. In combination with the predetermined order in which the target traps are filled, the lookup table reduces the calculation time of a particular instance. We observe that it scales roughly as $N^{1.2}$ with the number of target traps and amounts, in our implementation, to about 7 ms for $N = 100$ on a regular desktop computer with 16 GB of RAM.

Figure 3(a) illustrates how the algorithm works on a small square array. The target array is first assembled from the bottom left corner, then the diagonal, and finally the top right corner. Using this algorithm, atoms which initially occupy target traps can be displaced, which means additional moves with respect to an optimal solution. However, as we always use the atoms closest to the border of the compact structure to assemble it, the path is always obstacle-free and therefore we do not need any postprocessing. Consequently, each atom is moved *at most once* during the assembling process, which sets the upper bound $N_{mv} \leqslant N$ and ensures on average a smaller number of moves using the compression algorithm with respect to the shortest-moves-first algorithm of the preceding section. As N_{mv} cannot be lower than $N/2$ on average, our solution, while not optimal for many initial loading instances, is generally close to optimal. Figure 3(b) shows how this

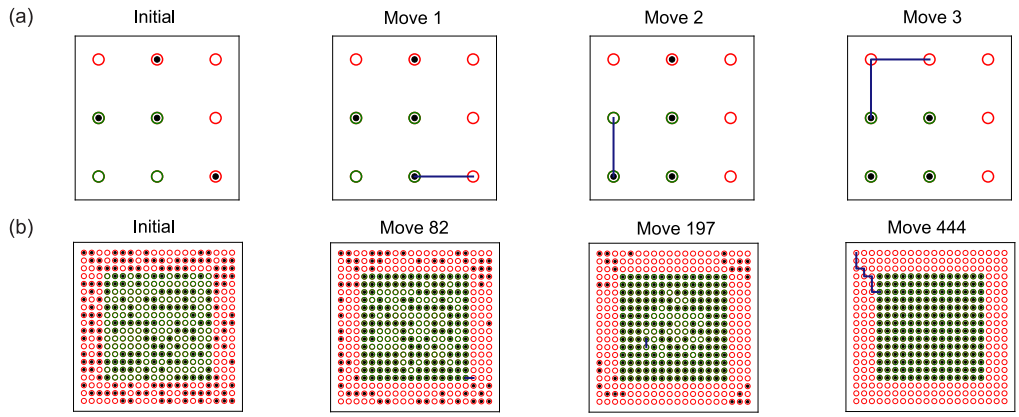

FIG. 2. Assembling of a compact array using the shortest-moves-first algorithm. (a) Microscopic view. The first set of moves (blue lines) connects out-of-place atoms with target traps on the outer shell of the structure (e.g., move 1). Once the border is populated, it is no longer possible to fill the inner traps without performing extra moves (move 2). (b) The macroscopic behavior on a 14×14 array reveals that the algorithm starts by filling the border of the target array (green circles) with atoms from reservoir traps (red circles), while inner traps are still empty (e.g., move 82), leading to a large overhead in the number of moves for successful assembling.

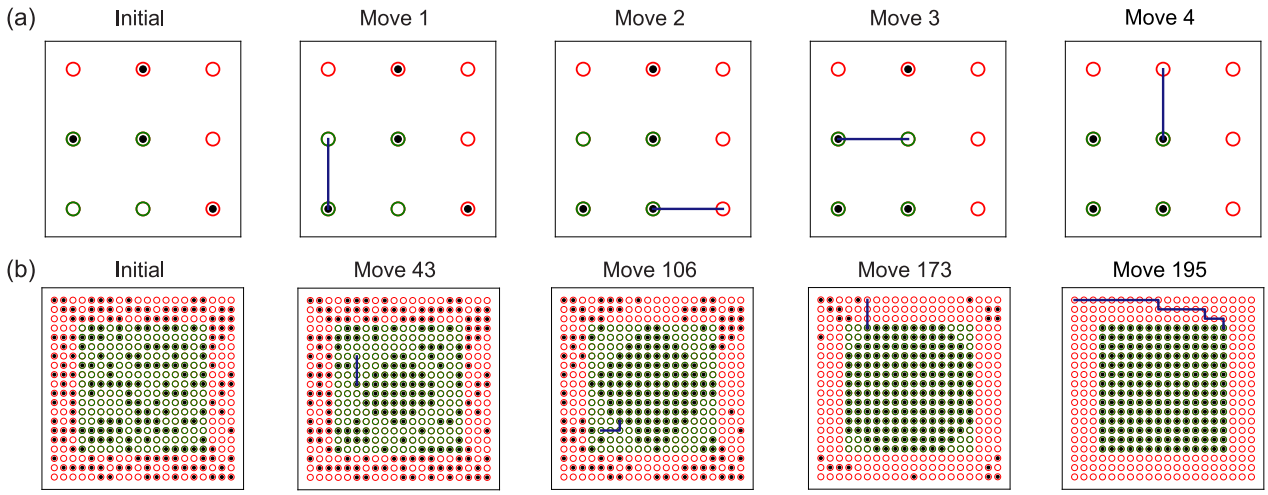

FIG. 3. Compression algorithm. (a) Illustration of the compression procedure for a 2×2 target array, requiring four moves. (b) A few assembling steps using the compression algorithm to assemble a 14×14 target array in only 195 moves, to be contrasted with the 444 moves needed previously.

compression algorithm outperforms the shortest-moves-first one. The 196 target atoms are assembled in 195 moves, whereas the same initial configuration required 444 moves to be sorted with our previous approach.

As can be seen in Fig. 4(a), not only is the average number of moves smaller than before, but the distribution of N_{mv}, calculated for 1000 random initial loading instances of the array, is also strongly sub-Poissonian, as well as asymmetric, with a sharp cutoff at N. This is an appealing feature, as it indicates that the success probability of the assembly process should be more consistent from one shot to another, as compared to the previous approach. Figure 4(b) shows the linear scaling of N_{mv} with N.

This technique can be naturally extended to the case of compact structures in other lattices (e.g., triangular) and also to arbitrary geometries, as we will see in Sec. VI.

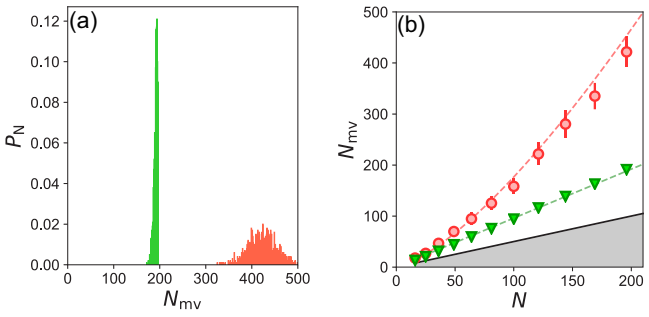

FIG. 4. Compression vs shortest-moves-first algorithms. (a) Histogram of the number of moves needed to fill a 14×14 square array for 1000 initial random loading instances. The compression algorithm (green) has a narrow distribution which is bounded by N. The shortest-moves-first algorithm (red) has a broad distribution and requires on average many more moves since the initial assignment is not collision-free. (b) Comparison of the scaling of N_{mv} as a function of N between the two algorithms. The compression algorithm gives a number of moves linear in N. Error bars are the standard deviation of the distribution.

V. USING A LINEAR SUM ASSIGNMENT PROBLEM SOLVER

In view of minimizing the number of moves, it is interesting to revisit the approach of the problem as a linear sum assignment problem (LSAP), which was mentioned above for the case of type-1 moves. However, for the type-2 moves we are interested in here, a direct application of the LSAP matching with the travel distance ℓ as a cost function does not yield a collision-free assignment and requires postprocessing, which in general increases the number of moves. We describe in this section two different algorithms that first use a LSAP solver and then reprocess the moves, which leads to a low number of moves. The LSAP solver we use in practice is a modified Jonker-Volgenant algorithm with no initialization [23], which is implemented in the `scipy.optimize` PYTHON package [24].

The first algorithm (LSAP1) uses the total travel distance $\sum_{\mathrm{moves}\ i} \ell_i$ as the cost function, while the second one (LSAP2) uses a modified metric $\sum_{\mathrm{moves}\ i} \ell_i^2$, which favors shorter paths [Fig. 5(a)]. In both cases, the set of returned moves is postprocessed to eliminate collisions and reduce the number of moves.

A. LSAP1: Standard metric and merging

Our first approach, described using a simple example in Fig. 5(b), starts with the LSAP algorithm using the travel distance between the source and target traps as a cost function. We first sort the returned moves from shortest to longest. Since the found assignment leads to collisions, we then postprocess the set of moves by splitting the paths with obstacles into two or more moves, just as in the shortest-moves-first approach. However, in a second iteration, we merge again some moves in which an atom is picked up twice, thereby reducing the number of moves considerably, checking at each step that we do not reintroduce any collision in doing so. Note that this second merging iteration can in principle be applied to any algorithm, but yields the smallest number of moves when

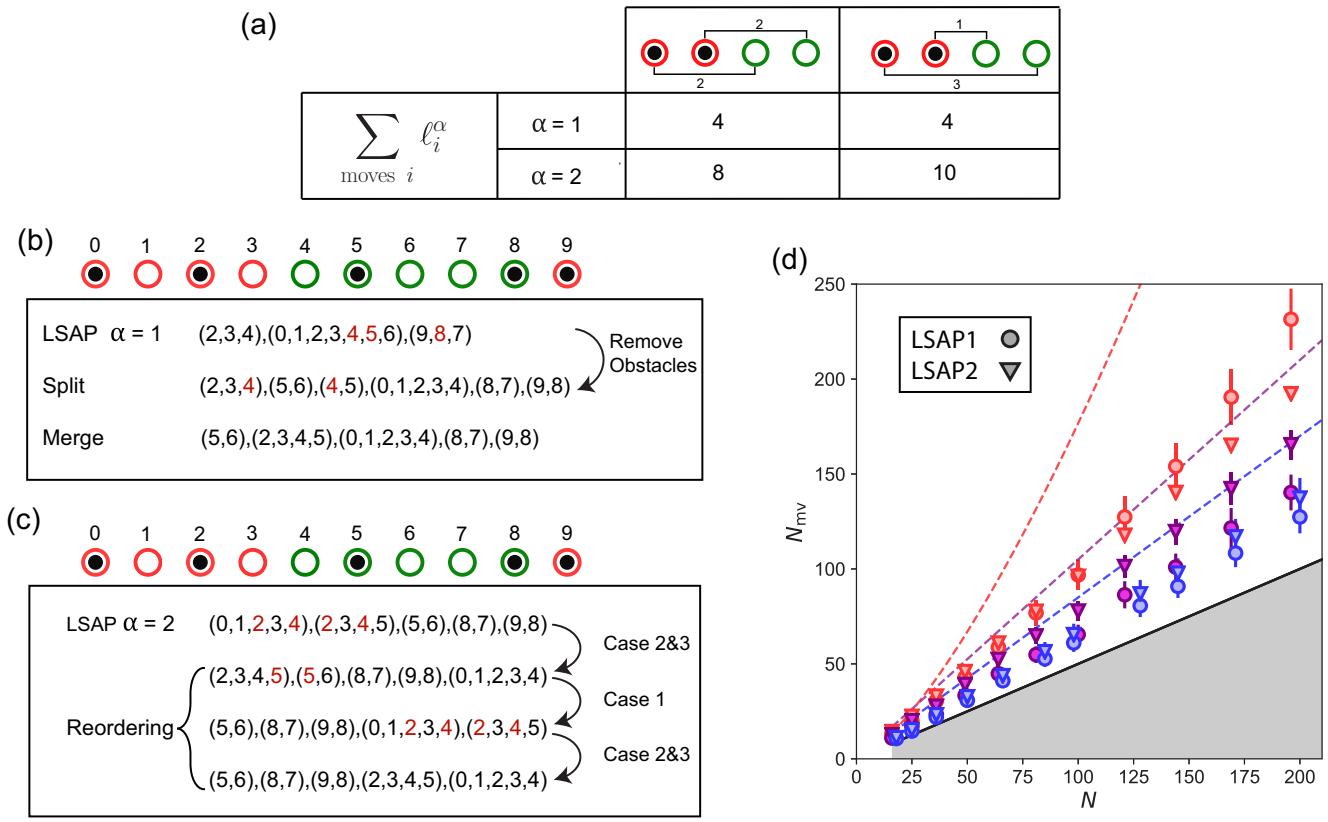

FIG. 5. Modified LSAP algorithms. (a) Using a cost function with $\alpha = 2$ (see the text) in a LSAP solver favors short moves. (b) The algorithm LSAP1 first uses a LSAP solver with $\alpha = 1$, which returns a list of moves [here (2,3,4) means that the atom initially in trap 2 is moved, via trap 3, to trap 4]. Some moves lead to collisions (denoted in red) and thus the set of moves is postprocessed as in the shortest-moves-first algorithms, by splitting the problematic moves into two or more stages. However, in a second step, two moves that share the same trap as final and initial positions (denoted in red) can be merged together, reducing the total number of moves. (c) The algorithm LSAP2 uses a modified cost function with $\alpha = 2$, which returns a set of short moves; to avoid collisions, the moves are then reordered by applying successively three rules (see the text) until the rearrangement can be performed without collisions. Numbers in red highlight the breaking of a rule. (d) Number N_{mv} of needed moves as a function of N to assemble a staggered target array (blue), a random target array (purple), or a compact target array (red), for the LSAP1 and LSAP2 algorithms. The dashed lines reproduce the fits of Fig. 1 for comparison.

starting from the LSAP matching. The computation time for this approach is on average 4 ms for 100 target traps in a staggered geometry and roughly scales as N^2.[1,2]

Figure 5(d) shows the number of moves N_{mv} as a function of N for LSAP 1 (disks). The performance is very satisfactory for staggered or random target arrays, as the number of moves is only 20–30 % higher than the absolute lower bound $N/2$. For compact arrays, the number of needed moves is slightly larger than N, making this approach less efficient than the compression algorithm described in Sec. IV.

B. LSAP2: Modified metric and reordering

Long moves lead to many collisions; therefore, it is beneficial to avoid them. In our second approach we achieve this by using a modified cost function $\sum_{\text{paths } i} \ell_i^2$. A similar idea was introduced in [20], but here the moves are sequential and we thus need to find the right ordering in which the moves have to be performed to avoid collisions.

To do so, we apply the following rules. We examine each move in the list and if the target trap of the move is occupied (case 1), if another trap along the path of the move is filled (case 2), or if the target trap is in the path of another move following in the list (case 3), we postpone this move and put it at the end of the list of moves. We find empirically that this procedure always produces a collision-free set of moves. This approach is illustrated in Fig. 5(c). The whole algorithm (LSAP and reordering) has an average computation time of 4 ms for $N = 100$ target traps in a compact geometry and scales roughly as N^2.

Whatever the target array, the maximum number of moves is bounded by N, the size of the cost matrix. As can be seen in Fig. 5(d) (triangles), the number of moves returned by

[1]In the worst case, the Hungarian matching algorithm is known to scale as N^3; however, we observe empirically that for the current problem and for the values of N up to a few hundreds considered here, the average runtime of our LSAP and reordering algorithm scales roughly as N^2.

[2]To reduce the computation time during the experiment, we precalculate a lookup table with the shortest paths and path lengths between all trap pairs. During each assembly cycle, the cost matrix for the LSAP algorithm is found as a submatrix of the lookup table.

LSAP2 is slightly larger than LSAP1 for sparse arrays, but is smaller for compact arrays, where it gives essentially the same performance as the compression algorithm. The latter, however, has the advantage of a shorter calculation time for $N > N_c$, with a critical atom number $N_c \sim 300$ in our current implementation.

VI. ARRAYS WITH COMPLETELY ARBITRARY GEOMETRY

Condensed-matter models are often studied on specific crystalline arrangements which are described by a Bravais lattice, e.g., a square or a triangular lattice. Our previous assembler was therefore based on such an underlying lattice, which simplifies the problem in two ways. First, this naturally defines the paths along which the moving tweezer can travel and, because these lattice edges are separated by a constant spacing, it automatically ensures that a minimal distance between atoms in traps and the moving tweezer is always kept during the rearrangement. Second, it simplifies the distance calculation between two traps by defining the metric in terms of lattice coordinates (Manhattan distance).

Not all physical structures of interest for quantum simulation, however, can be described by a Bravais lattice. Examples of such nonperiodic features include crystals with defects (interstitial defects, vacancies, dislocations, and grain boundaries), quasicrystals, disordered arrays for Anderson or many-body localization studies, and even totally arbitrary structures in the context of combinatorial optimization problems such as finding the maximum independent set of a graph [25,26]. To examine such systems, we developed a variant of our algorithms, which is not based on an underlying lattice and therefore allows us to assemble truly arbitrary structures.

The starting point for our algorithm is the set of N target traps, whose positions are provided by the user. Because of the stochastic loading, we have to place N additional reservoir traps close to the arbitrary N-atom target configuration. This reservoir generation works as follows [Fig. 6(a)]. Whenever possible, to reduce the number of moves, a reservoir trap should be placed in immediate proximity to each target trap. To do so, we compute the Voronoi diagram [27] of the set of target traps (i.e., divide the plane in N regions, one around each target trap T, such that all points of this region are closer to T than to any other trap). We then add in each Voronoi cell a single reservoir trap, provided it can be placed at a distance larger than a "safety" distance d_m (typically $\sim 4\ \mu$m) from all other traps. If successful, this procedure ensures that for each target trap there is a single reservoir close to it [Fig. 6(b)]. If, however, the density of the target traps is already comparable to $1/d_m^2$, then we cannot add enough reservoir traps in this way and so we place extra traps at the periphery of the pattern in a compact triangular array [Fig. 6(c)].

The next step is to find paths along which an atom can travel to an empty target trap. Contrary to the case of Bravais lattices, no obvious edges are *a priori* connecting the traps along which the moves can be performed. Direct straight-line paths from the reservoir to the target trap are also not possible, since there can be other traps in the way, leading to collisions and atom losses. We thus define the set of allowed paths by using a Delaunay triangulation [27] of the full set of traps

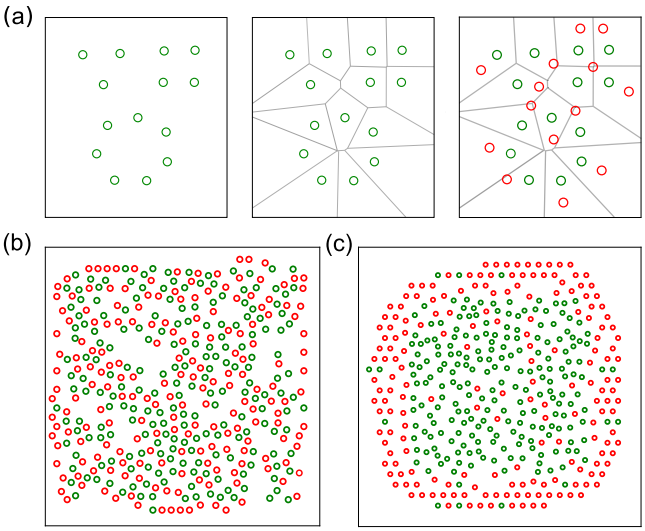

FIG. 6. Generating the reservoir arrays for arbitrary target arrays. (a) Starting from the user-defined target array (left), we compute its Voronoi diagram (middle) and in each cell we add a reservoir trap, shown in red, if there is enough room (right); otherwise we add it at the periphery (see the text for details). Also shown are examples of generated reservoirs for an $N = 200$ target array, (b) without and (c) with the need to add reservoirs at the periphery.

(target and reservoir) as shown in Fig. 7. In practice, we implemented the triangulation in PYTHON 3.0 with the SCIPY library [24]. To enforce the above-mentioned constraint of a minimal passing distance, we postremove edges that do not meet this requirement (see dashed lines in Fig. 7). We emphasize that the generation of the reservoir traps and of the allowed edges is done just once for any given target array, and not at each repetition of the experiment, which considerably relaxes the constraints on the speed of this algorithm. In practice, arrays with hundreds of target traps can be processed in a few seconds.

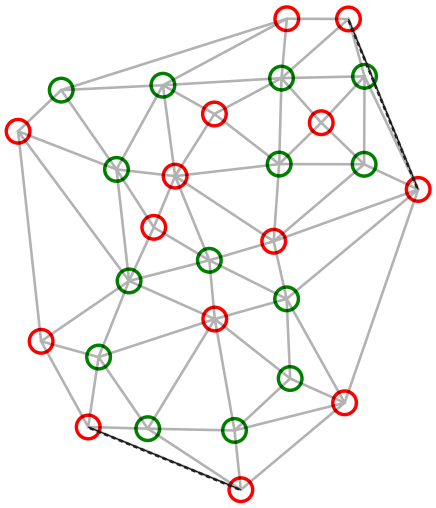

FIG. 7. Generating the allowed paths between traps. We first perform the Delaunay triangulation of the atom array. In a second step, we remove edges which do not fulfill a minimal passing-distance requirement (dotted line).

This triangulation then allows us to naturally describe the whole structure in terms of graph language, connecting the nodes (trap positions) by edges along which the atoms are allowed to move. In this way, we eliminate the necessity to describe the problem with an underlying Bravais lattice. Furthermore, it allows the implementation of efficient shortest-path graph algorithms (e.g., the Dijkstra algorithm [19]) to find the shortest path between a matched initial and target trap, following the allowed edges of the graph. For the generation of the graphs and graph algorithms the NETWORKX library [28] is used. With these modifications, it is now possible to extend the algorithms discussed above to arbitrary patterns. The scaling and performance of the algorithms (in terms of computation time and the number of moves) are essentially unchanged as compared to the case of regular lattices.

VII. EXPERIMENTAL DEMONSTRATION

The experimental setup has been described in [13]. Using an SLM (Hammamatsu X10468-02), a fixed pattern of optical dipole traps at 850 nm is generated in the focal plane of a high-numerical-aperture (equal to 0.5) aspheric lens. With an available laser power of ∼1 W, we can generate up to 200 traps with a $1/e^2$ radius of ∼1 μm and a typical trap depth of ∼1 mK, resulting in a radial (longitudinal) trapping frequency around 100 kHz (20 kHz). Initially, the traps are stochastically loaded with single atoms at a temperature of ∼10 μK from a magneto-optical trap of ^{87}Rb atoms; the typical loading time is ∼150 ms. An initial fluorescence image (20 ms) determines the initial occupancy of the traps, which is 50–60% on average.

To assemble a target array, we use a single 850-nm dipole trap with a $1/e^2$ radius of ∼1.3 μm, steered by a 2D AOD, which can pick up an atom from a static trap by ramping up its depth to ∼10 mK and subsequently moving and then releasing the atom at the position of an empty static trap. After the assembly, a fluorescence image with an exposure time of 20 ms determines the occupancy of the target array, before we perform an actual experiment, e.g., quantum simulation of a spin model, by exciting the atoms to Rydberg levels [1]. This technique allows us to perform experiments with a typical repetition rate of ∼3 Hz.

Once the trap array has been generated, we equalize the trap intensities using the fluorescence signal of the loaded traps.[3] Then the choice of the optimal algorithm to be used for assembly, among the three described above, is made according to the characteristics of the target array to assemble, as described in Fig. 8.

Finally, in order to further improve the success probability of assembling a defect-free array, we apply multiple rearrangement cycles (similar to [14,18]). At the end of the first rearrangement process, we keep the excess atoms and determine the defects with a fluorescence image. We then fill these defects [Fig. 9(a)]. This process can be repeated until a defect-free array is obtained and excess atoms are removed. However, since this procedure requires more than N initial

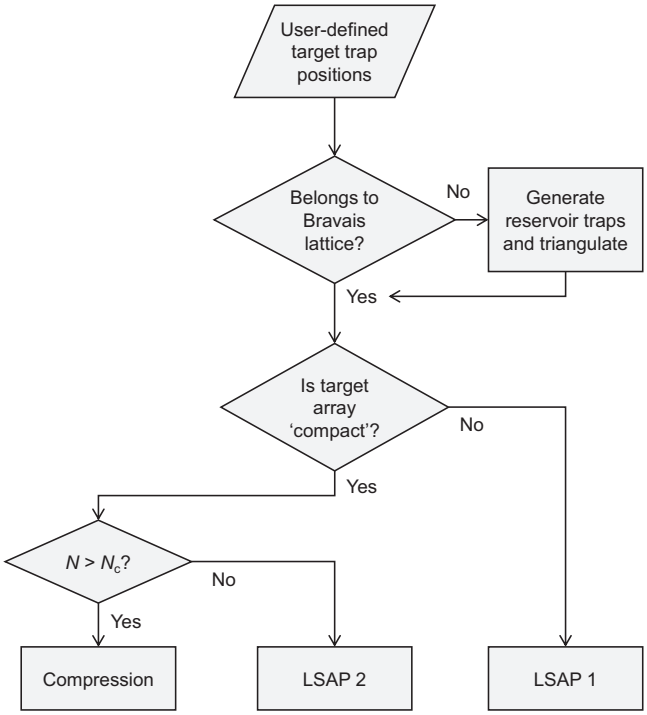

FIG. 8. Algorithm choice flowchart. The best-suited algorithm to be used depends on the characteristics of the target array. The critical atom number N_c is defined at the end of Sec. V.

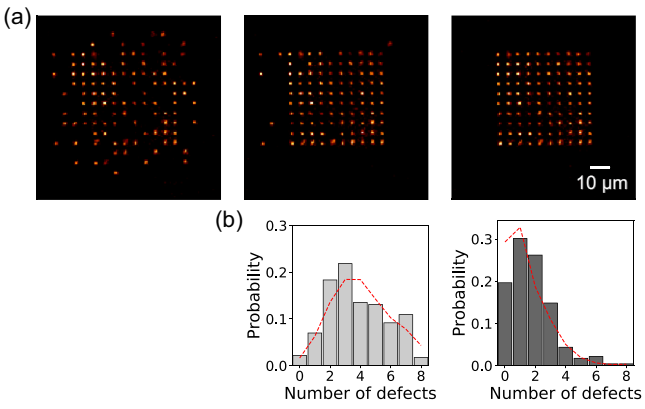

FIG. 9. Multiple rearrangement cycles. The probability to assemble a defect-free array can be increased by starting with more than N atoms and repeating the rearrangement cycle more than once. (a) On the shown 10×10 compact target square array, we can increase the probability to create a defect-free array by a factor 10 (from 2% to 20%), when starting with 225 atoms and performing a second cycle. (b) A Monte Carlo simulation (red) of the first cycle and second cycle, including the measured efficiencies of performing the moves and vacuum lifetime, reproduces the experimental distribution of defects reasonably well.

[3]It is of importance that all microtraps have a good optical quality and in particular the same depth such that (i) single-atom loading does indeed occur with a probability of ∼1/2 and (ii) the fluorescence signal from any given trap allows for efficient identification of the presence of a single atom. We now equalize the trap depths by a direct optimization of the fluorescence time trace of each single trap, altering the trap intensity until we fulfill criteria (i) and (ii). A detailed description of this procedure is left for future work.

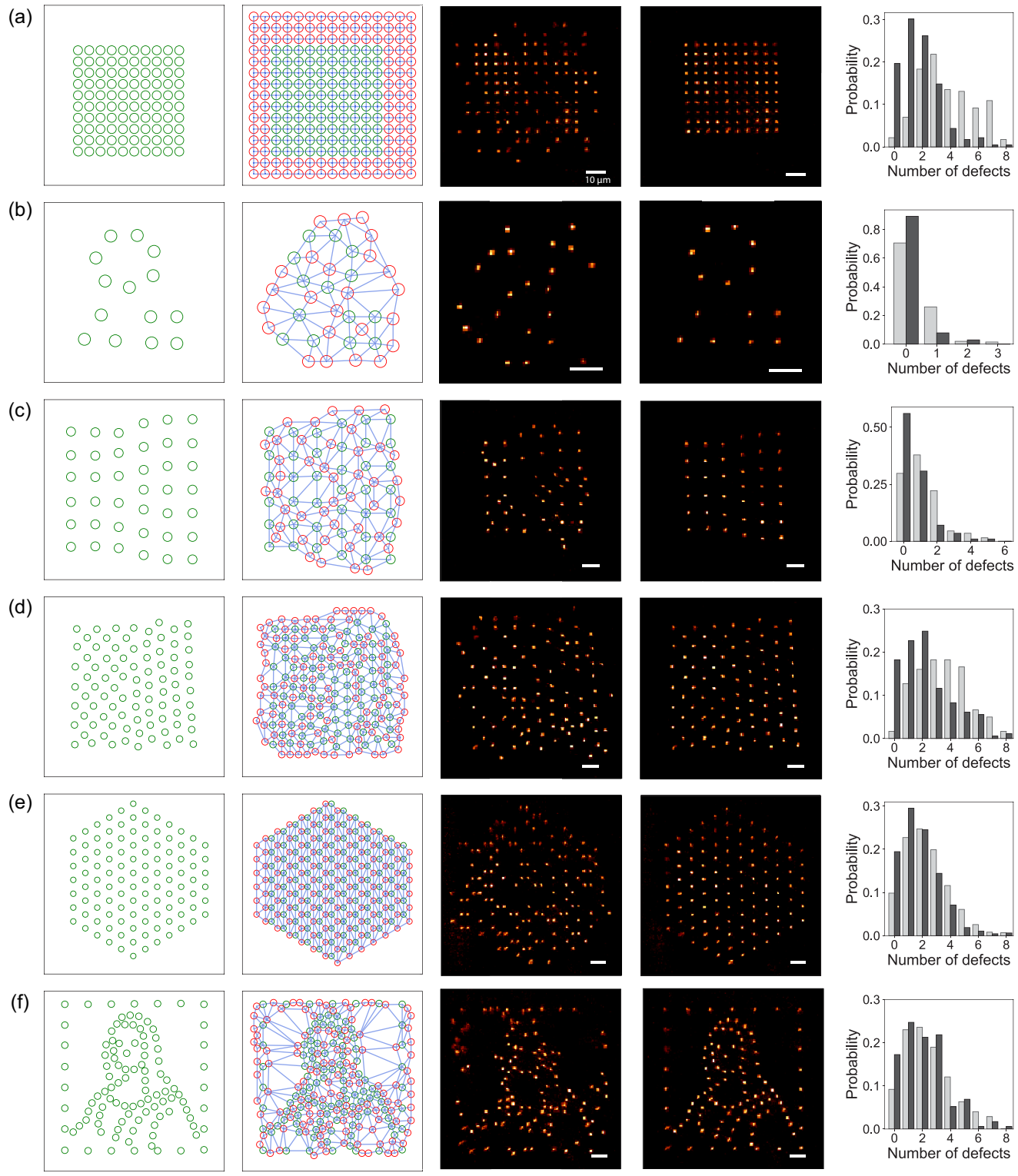

FIG. 10. Gallery of assembled arbitrary structures. Shown from left to right are the target structure, the structure with the generated reservoir traps (in red) and the allowed paths connecting traps, the fluorescence image of an initial random loading, the fluorescence image of the assembled structure, and the probability distribution of the number of defects after a rearrangement cycle (gray) and after two such cycles (dark gray). All white scale bars are 10 μm. (a) Compact square array ($N = 100$), (b) the arbitrary array used as an example in Sec. VI ($N = 14$), (c) an edge dislocation in a square lattice ($N = 39$), (d) a grain boundary between a square and a triangular lattice ($N = 91$), (e) a patch of a triangular lattice ($N = 108$), and (f) an atomic rendering of Mona Lisa ($N = 106$).

atoms, a high efficiency of a single rearrangement cycle is still essential as laser power is a limiting factor for scaling up the number of atoms. Figure 9(b) shows the probability distribution of the number of defects (missing atoms) after a single (left) or two (right) rearrangement cycles, showing the benefit of performing several cycles.

Examples of assembled structures of various types, with up to $N = 108$ atoms, can be seen in Fig. 10. The probability to have a given number of defects in the final array is shown in the histograms on the right, for a single rearrangement (gray) and for two cycles (dark gray). In the latter case, even for $N > 100$, defect-free arrays are obtained in about 20% of the shots. Using a trapping wavelength closer to resonance (820 nm) in order to generate more traps for a given laser power, we have been able to assemble arrays of up to 209 atoms without any given defects.

VIII. CONCLUSION

In this paper, we have shown how, without any change in the hardware used in [13], improved algorithms can significantly improve the capabilities of a moving-tweezer atom-by-atom assembler, both in terms of possible array geometries and in terms of achievable atom numbers due to the fact that fewer moves are required.

The algorithms demonstrated here can be used directly for the plane-by-plane assembly of three-dimensional structures [22]. Extending them to a full three-dimensional assembly with atoms being moved also longitudinally, along the lens optical axis, will require significant changes due to the fact that transverse moves (using an AOD) and longitudinal moves (done with an electrically tunable lens) do not obey the same constraints.

Another natural extension of this study, which we leave for future work, is to use multiple tweezers working in parallel, in the spirit of [14]. This approach should be particularly easy to adapt to the compression algorithm for assembling compact regular structures; then, assuming that the laser power for generating the multiple tweezers is not a limit, the assembly time could scale as $\sqrt{N}$, making it possible to assemble structures with several hundreds of atoms. Combined with other technical improvements, using, e.g., cryogenic environments to drastically extend the vacuum-limited lifetime, reaching a scale of 1000 atoms or more thus seems realistic in the relatively near future, which would open up a variety of exciting applications in quantum science and technology.

ACKNOWLEDGMENTS

We thank Loïc Henriet and Henrique Silvério for useful discussions and Gilles Kuhorn for contributions to testing some of the algorithms. This project received funding from the European Union's Horizon 2020 research and innovation program under Grant Agreement No. 817482 (PASQuanS) and from the Région Île-de-France in the framework of DIM SIRTEQ (Project CARAQUES).

[1] A. Browaeys and T. Lahaye, Many-body physics with individually controlled Rydberg atoms, Nat. Phys. **16**, 132 (2020).

[2] H. Labuhn, D. Barredo, S. Ravets, S. de Léséleuc, T. Macrì, T. Lahaye, and A. Browaeys, Tunable two-dimensional arrays of single Rydberg atoms for realizing quantum Ising models, Nature (London) **534**, 667 (2016).

[3] H. Bernien, S. Schwartz, A. Keesling, H. Levine, A. Omran, H. Pichler, S. Choi, A. S. Zibrov, M. Endres, M. Greiner, V. Vuletić, and M. D. Lukin, Probing many-body dynamics on a 51-atom quantum simulator, Nature (London) **551**, 579 (2017).

[4] V. Lienhard, S. de Léséleuc, D. Barredo, T. Lahaye, A. Browaeys, M. Schuler, L.-P. Henry, and A. M. Läuchli, Observing the Space- and Time-Dependent Growth of Correlations in Dynamically Tuned Synthetic Ising Models with Antiferromagnetic Interactions, Phys. Rev. X **8**, 021070 (2018).

[5] H. Kim, Y. Park, K. Kim, H.-S. Sim, and J. Ahn, Detailed Balance of Thermalization Dynamics in Rydberg-Atom Quantum Simulators, Phys. Rev. Lett. **120**, 180502 (2018).

[6] A. Keesling, A. Omran, H. Levine, H. Bernien, H. Pichler, S. Choi, R. Samajdar, S. Schwartz, P. Silvi, S. Sachdev, P. Zoller, M. Endres, M. Greiner, V. Vuletić, and M. D. Lukin, Quantum Kibble-Zurek mechanism and critical dynamics on a programmable Rydberg simulator, Nature (London) **568**, 207 (2019).

[7] S. de Léséleuc, V. Lienhard, P. Scholl, D. Barredo, S. Weber, N. Lang, H. P. Büchler, T. Lahaye, and A. Browaeys, Observation of a symmetry-protected topological phase of interacting bosons with Rydberg atoms, Science **365**, 775 (2019).

[8] H. Levine, A. Keesling, A. Omran, H. Bernien, S. Schwartz, A. S. Zibrov, M. Endres, M. Greiner, V. Vuletić, and M. D. Lukin, High-Fidelity Control and Entanglement of Rydberg-Atom Qubits, Phys. Rev. Lett. **121**, 123603 (2018).

[9] H. Levine, A. Keesling, G. Semeghini, A. Omran, T. T. Wang, S. Ebadi, H. Bernien, M. Greiner, V. Vuletić, H. Pichler, and M. D. Lukin, Parallel Implementation of High-Fidelity Multiqubit Gates with Neutral Atoms, Phys. Rev. Lett. **123**, 170503 (2019).

[10] T. M. Graham, M. Kwon, B. Grinkemeyer, Z. Marra, X. Jiang, M. T. Lichtman, Y. Sun, M. Ebert, and M. Saffman, Rydberg-Mediated Entanglement in a Two-Dimensional Neutral Atom Qubit Array, Phys. Rev. Lett. **123**, 230501 (2019).

[11] I. S. Madjarov, J. P. Covey, A. L. Shaw, J. Choi, A. Kale, A. Cooper, H. Pichler, V. Schkolnik, J. R. Williams, and M. Endres, High-fidelity entanglement and detection of alkaline-earth Rydberg atoms, Nat. Phys. **16**, 857 (2020).

[12] N. Schlosser, G. Reymond, I. Protsenko, and P. Grangier, Sub-Poissonian loading of single atoms in a microscopic dipole trap, Nature (London) **411**, 1024 (2001).

[13] D. Barredo, S. de Léséleuc, V. Lienhard, T. Lahaye, and A. Browaeys, An atom-by-atom assembler of defect-free arbitrary two-dimensional atomic arrays, Science **354**, 1021 (2016).

[14] M. Endres, H. Bernien, A. Keesling, H. Levine, E. R. Anschuetz, A. Krajenbrink, C. Senko, V. Vuletic, M. Greiner, and M. D. Lukin, Atom-by-atom assembly of defect-free one-dimensional cold atom arrays, Science **354**, 1024 (2016).

[15] H. Kim, W. Lee, H.-g. Lee, H. Jo, Y. Song, and A. Jaewook, *In situ* single-atom array synthesis using dynamic holographic optical tweezers, Nat. Commun. **7**, 13317 (2016).

[16] M. O. Brown, T. Thiele, C. Kiehl, T.-W. Hsu, and C. A. Regal, Gray-Molasses Optical-Tweezer Loading: Controlling Collisions for Scaling Atom-Array Assembly, Phys. Rev. X **9**, 011057 (2019).

[17] W. Lee, H. Kim, and J. Ahn, Three-dimensional rearrangement of single atoms using actively controlled optical microtraps, Opt. Express **24**, 9816 (2016).

[18] D. Ohl de Mello, D. Schäffner, J. Werkmann, T. Preuschoff, L. Kohfahl, M. Schlosser, and G. Birkl, Defect-Free Assembly of 2D Clusters of more than 100 Single-Atom Quantum Systems, Phys. Rev. Lett. **122**, 203601 (2019).

[19] T. H. Cormen, C. E. Leiserson, R. L. Rivest, and C. Stein, *Introduction to Algorithms*, 2nd ed. (MIT Press, Cambridge, 2001).

[20] W. Lee, H. Kim, and J. Ahn, Defect-free atomic array formation using the Hungarian matching algorithm, Phys. Rev. A **95**, 053424 (2017).

[21] G. Călinescu, A. Dumitrescu, and J. Pach, LATIN 2006: Theoretical Informatics, in *Proceedings of the 7th Latin American Symposium, Valdivia, 2006*, edited by J. R. Correa, A. Hevia, and M. Kiwi, Lecture Notes in Computer Science Vol. 3887 (Springer, Berlin, 2006), pp. 262–273.

[22] D. Barredo, V. Lienhard, S. de Léséleuc, T. Lahaye, and A. Browaeys, Synthetic three-dimensional atomic structures assembled atom by atom, Nature (London) **561**, 79 (2018).

[23] D. F. Crouse, On implementing 2D rectangular assignment algorithms, IEEE Trans. Aerosp. Electron. Syst. **52**, 1679 (2016).

[24] P. Virtanen, R. Gommers, T. E. Oliphant, M. Haberland, T. Reddy, D. Cournapeau, E. Burovski, P. Peterson, W. Weckesser *et al.*, SciPy 1.0: Fundamental algorithms for scientific computing in Python, Nat. Methods **17**, 261 (2020).

[25] H. Pichler, S.-T. Wang, L. Zhou, S. Choi, and M. D. Lukin, Quantum optimization for maximum independent set using Rydberg atom arrays, arXiv:1808.10816.

[26] L. Henriet, Robustness to spontaneous emission of a variational quantum algorithm, Phys. Rev. A **101**, 012335 (2020).

[27] F. P. Preparata and M. Shamos, *Computational Geometry: An Introduction* (Springer, New York, 1985).

[28] A. A. Hagberg, D. A. Schult, and P. J. Swart, in *Proceedings of the 7th Python in Science Conference (SciPy2008), Pasadena, 2008*, edited by G. Varoquaux, T. Vaught, and J. Millman (unpublished), pp. 11–15.

Appendix E

Article: *Single Atoms with 6000-Second Trapping Lifetimes in Optical-Tweezer Arrays at Cryogenic Temperatures*

This appendix reproduces the following published article:

Kai-Niklas Schymik, Sara Pancaldi, Florence Nogrette, Daniel Barredo, Julien Paris, Antoine Browaeys, and Thierry Lahaye *Single Atoms with 6000-Second Trapping Lifetimes in Optical-Tweezer Arrays at Cryogenic Temperatures*. Physical Review Applied **16**, 034013 (2021)

Single Atoms with 6000-Second Trapping Lifetimes in Optical-Tweezer Arrays at Cryogenic Temperatures

Kai-Niklas Schymik,[1] Sara Pancaldi,[1] Florence Nogrette,[1] Daniel Barredo,[1,2] Julien Paris,[3] Antoine Browaeys,[1] and Thierry Lahaye[1,*]

[1] *Université Paris-Saclay, Institut d'Optique Graduate School, CNRS, Laboratoire Charles Fabry, Palaiseau Cedex 91127, France*

[2] *Nanomaterials and Nanotechnology Research Center (CINN-CSIC), Universidad de Oviedo (UO), Principado de Asturias, El Entrego 33940, Spain*

[3] *My Cryo Firm, 20 Villa des Carrières, Fontenay-sous-Bois 94120, France*

(Received 14 June 2021; revised 23 July 2021; accepted 30 July 2021; published 7 September 2021)

We report on the trapping of single Rb atoms in tunable arrays of optical tweezers in a cryogenic environment at approximately 4 K. We describe the design and construction of the experimental apparatus, based on a custom-made UHV-compatible closed-cycle cryostat with optical access. We demonstrate the trapping of single atoms in cryogenic arrays of optical tweezers, with lifetimes up to 6000 s, despite the fact that the vacuum system has not been baked out. These results open the way to large arrays of single atoms with extended coherence, for applications in large-scale quantum simulation of many-body systems and, more generally, in quantum science and technology.

DOI: 10.1103/PhysRevApplied.16.034013

I. INTRODUCTION

For most applications of quantum science and technology, whatever the experimental platform, scaling up the number of individually controlled quantum objects is a major subject of research, as this is a necessary condition for practical use [1]. Over the past few years, tweezer atom arrays have emerged as a very versatile platform for quantum science, with applications ranging from quantum simulation of many-body systems [2] to quantum metrology [3,4] and quantum computing [5,6]. Large arrays with up to approximately 200 atoms are now used for quantum simulation of spin systems [7,8]. They are assembled atom by atom, using moving optical tweezers, from an initially disordered configuration. One of the current challenges in the field is to scale up the atom number while preserving, or even increasing, the coherence of the system.

A natural way to achieve this goal is to operate the tweezer arrays in a cryogenic environment at a temperature of a few kelvin. A first beneficial effect is that the residual pressure is considerably smaller than at room temperature, which reduces collisions of the trapped atoms with the residual gas. This allows us to increase the trapping lifetime of atoms in the tweezers, which is one of the limiting factors in the assembly of large arrays, as the assembly time increases with the system size. For a sequential assembly scheme, as used, e.g., in Ref. [9], increasing the trapping lifetime by a factor of α allows for an increase in the atom number by roughly $\sqrt{\alpha}$ [10]. A second benefit is that black-body radiation (BBR), which scales as T^4, is considerably reduced in such an environment, making BBR-induced transitions between Rydberg levels almost negligible. For low-angular-momentum Rydberg states, this results in a typical increase of the Rydberg lifetime by a factor of between 2 and 3 [11], with a direct impact on coherence and gate fidelities [12]. The inhibition of BBR-induced transitions would also be beneficial for Rydberg dressing experiments, where they are a serious limitation [13,14]. For circular states, the lifetime increases by several orders of magnitude in a cryogenic environment [15], motivating their use for quantum computing and simulation [16–18]. Finally, cryogenic single-atom trapping is also required, albeit at much lower temperatures, for coupling single atoms to microwave resonators in order to build hybrid systems [19].

Here, we demonstrate the trapping of single atoms in arrays of optical tweezers in a cryogenic environment at 4 K. We first describe the design, construction, and characterization of the setup, based on a closed-cycle cryostat where we use only UHV-compatible components. We then show how laser cooling and trapping of Rb atoms in the setup is obtained without any strong change as compared to a room-temperature setup. We finally show that we can trap single atoms in arrays of tweezers, with measured lifetimes in the tweezers up to 6000 s, a 300-fold improvement compared to our current room-temperature setup.

*thierry.lahaye@institutoptique.fr

II. EXPERIMENTAL APPARATUS

A. Cryostat design

The adaptation of an atom-tweezer setup for operation at cryogenic temperatures comes with many specific technical constraints. This means that a straightforward use of the cryogenic solutions previously developed in the atomic, molecular, and optical (AMO) community, e.g., for ion trapping [20,21] or for Bose-Einstein condensation [22,23], is not possible.

In this work, we have chosen to keep, whenever possible, the technical solutions adopted in our existing room-temperature setup, e.g., the use of in-vacuum high-NA aspheric lenses or that of a Zeeman slower as an atom source [24]. This has allowed us to focus mainly on the design of the cryogenic part. We base our design on the use of a closed-cycle cryostat using a pulse-tube refrigerator (PTR), with the technical constraint of using only UHV-compatible materials. However, to keep the design of our custom-made cryostat close to that of a commercial model [25], we opt for a nonbakeable system, as the PTR cannot be baked out without being damaged (having a removable PTR to allow for bake-out of the rest of the system makes the design significantly more involved). This trade-off results in having a moderate vacuum in the room-temperature chamber but, as we shall see, cryopumping by the 4-K shield enclosing the atoms still results in long trapping lifetimes.

Figure 1(a) shows a general view of the system. The cryostat is enclosed in a large stainless-steel vacuum chamber at 300 K that accommodates the PTR on one side and a science chamber on the other side. An atomic source, comprising a rubidium oven followed by a Zeeman slower, is connected to the science chamber and can be isolated from it using a gate valve actuated with a stepper motor. The cryostat chamber is pumped using a 300-L/s ion pump (that includes a titanium sublimator), as well as with a nonevaporable getter (NEG) cartridge.

A cross section of the cryostat assembly is shown in Fig. 1(b). The two cooling stages of the PTR at 30 K and 4 K are thermally connected to nested gold-plated copper radiation shields, which extend all the way to the science chamber. This connection is made using ultrasoft high-thermal-conductivity copper braids for vibration decoupling. On the thermal shields, antireflection-coated 5-mm-thick fused-silica windows allow for optical access along all the needed directions [26]. The vibrational decoupling with copper braids is highly efficient: with the PTR in operation, we measure, along the three orthogonal directions, residual vibrations on the 4-K baseplate below 10 nm (rms), the main frequency components being in the hertz range.

The optical assembly for atom trapping is bolted on the 4 K baseplate, in the center of the science chamber, and comprises a beryllium-copper (Cu-Be) lens holder and two mirrors for beam steering. The four magneto-optical trap (MOT) beams in the horizontal plane, as well as the tweezer beam along the optical axis of the aspheric lenses, propagate in a straight line from outside the chamber, through a total of two vacuum view ports and four windows on the thermal shields, and exit the chamber on the other side. Three beams, on two axes (the Zeeman slower beam and the vertical MOT beams) are reflected inside the chamber on 45° metallic mirrors held by Cu-Be supports. This allows (i) for the vertical MOT axis, to avoid having beams coming from below the chamber, which would make the construction of the cryostat quite involved, and (ii) for the Zeeman slower beam, to avoid having a cold window facing the atomic beam, where Rb would accumulate, rendering it opaque. Two apertures with a diameter of 13 mm, one in each thermal shield, allow the atomic beam from the Zeeman slower to enter the trapping region.

Figure 1(c) shows a cross-section view of the lens mount. It is milled in a Cu-Be block; this choice of material is a trade-off to retain good thermal conductivity while having better mechanical properties than copper [27]. The two aspheric lenses (LightPath Technologies, NA 0.5, focal length 10 mm, working distance 7 mm) are mounted in Cu-Be barrels. To account for the differential thermal contraction between Cu-Be and glass upon cooling, the barrels are machined such that, at room temperature, their internal diameter exceeds the outer diameter of the lenses by 20 μm, resulting in a perfect match of diameters at 4 K. The flat face of the lens is pressed against a shoulder at the end of the barrel using a Cu-Be spring and a nut to ensure the correct positioning of the lens at the end of the barrel. In a preliminary set of experiments, we check, using white-light illumination between crossed polarizers, that no stress-induced birefringence occurs in the lenses when cooling down the system.

The two lenses are mounted with a spacing such that at 4 K, they are in an ideal f-f configuration. Due to the thermal contraction of the Cu-Be lens holder, and to a lesser extent to that of the aspheric lenses, this means that at room temperature an incident collimated beam will focus at a finite distance, calculated to be approximately 2.5 m, after passing through both lenses. Using copper spacers between the barrels and the holder, with a thickness that we gradually reduce by lapping, the longitudinal positioning of the lenses is carefully adjusted until the proper spacing is obtained. When cooled down to 4 K, the system becomes almost afocal, as a collimated incident beam focuses at a distance > 20 m after the second lens.

In view of future experiments with Rydberg atoms, the face of the lens facing the atoms is coated with a transparent but conductive layer of indium-tin oxide (ITO), with a thickness of 120 nm (giving an overall transmission of the lens of about 90% at the tweezer wavelength of 830 nm).

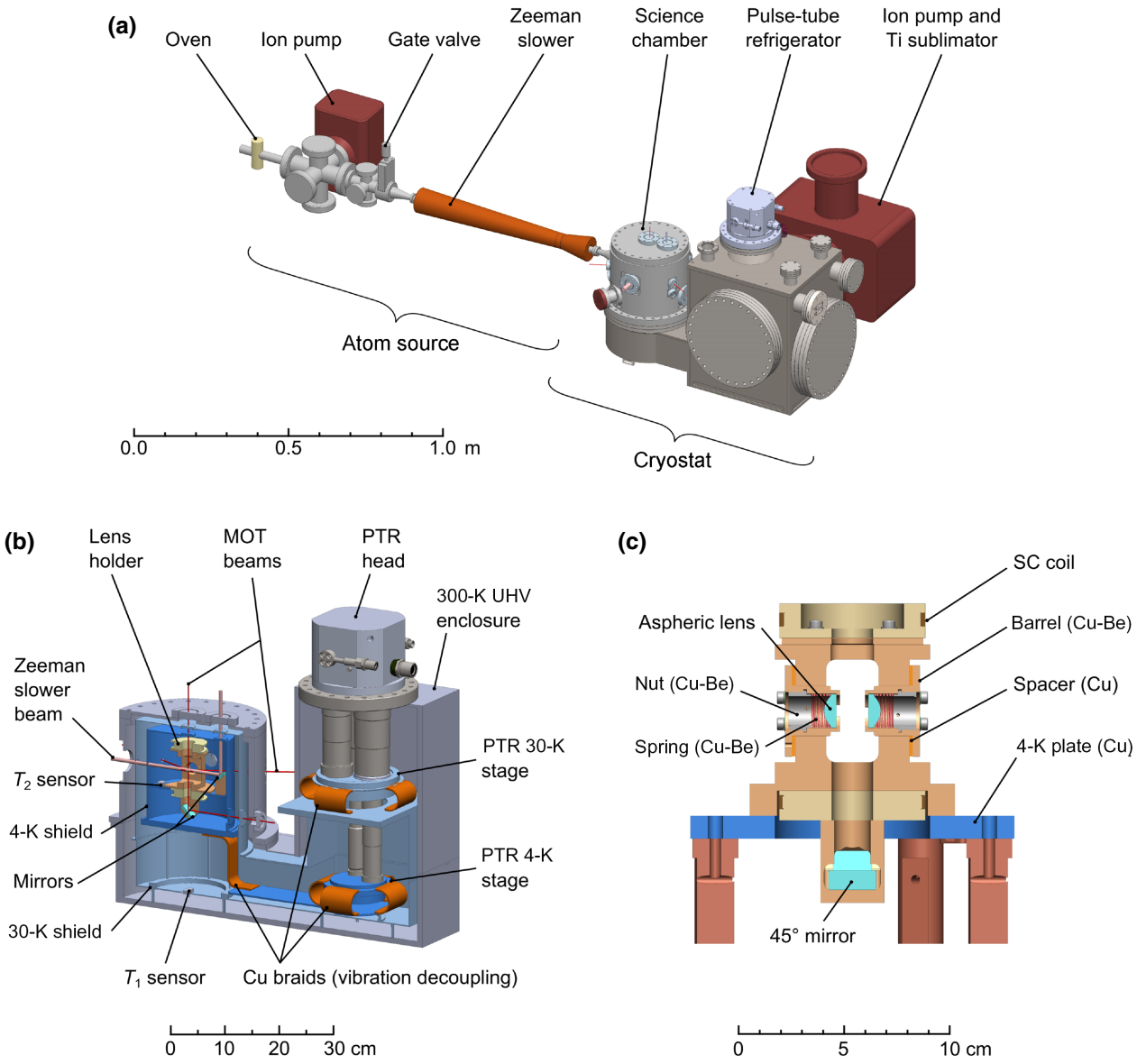

FIG. 1. The experimental setup. (a) A schematic rendering of the entire apparatus, comprising the atomic source and the cryostat. (b) A longitudinal cross section of the cryostat, showing the pulse-tube refrigerator with its two stages at 30 K and 4 K, together with the corresponding thermal shields to which they are connected through vibration-decoupling copper braids. (c) An enlarged cross section of the lens-holder piece.

The lens holder also accommodates two independent superconducting (SC) coils, wound with 0.5-mm diameter Nb-Ti wire, which can be used to produce the MOT magnetic field gradient or a homogeneous bias field when switching from an anti-Helmholtz to a Helmholtz configuration. They are connected to the exterior of the cryostat via 0.6-mm-diameter kapton-insulated copper wire (the chosen diameter is a trade-off that minimizes the heat conduction from room temperature to 4 K and the Joule heating in the wire, for the design current of 2 A [27]). To minimize the effect of eddy currents when switching the magnetic field on and off, the coil form is made of Cu-Be which, unlike pure copper, has a moderate electrical conductivity even at cryogenic temperatures. In a preliminary experiment in a test cryostat at 4 K, we measure decay times of approximately 1 ms for the magnetic field; however, there, the copper thermal shields are quite remote from the coils. In the final configuration of the cryostat, when operating a MOT (see Sec. III A) and turning off the field, we observe that the magnetic field experienced by the atoms fully settles after only approximately 40 ms, most likely due to

the presence of pure copper parts (in particular, the 4-K thermal shield) close to the coils. While this is not an issue for loading optical tweezers, as we show below, one could improve on this in future designs by replacing some copper parts by Cu-Be ones when possible and by cutting out narrow slits in the shields at appropriate locations to break the paths of eddy currents. Finally, we check that for relevant repetition rates of current switching, eddy currents do not lead to any appreciable heating.

B. Performance of the cryostat

To operate the cryostat, we first evacuate the system with turbomolecular pumps, until we reach a residual pressure in the 10^{-8}-mbar range. This pressure is due to (i) the absence of bake-out of the setup and (ii) the large number of elements under vacuum, especially those having a large surface-to-volume area, such as the copper braids, for which outgassing is very slow. We then switch on the PTR and, within about 15 h, the temperatures T_1 and T_2 measured by sensors on the first-stage ("30-K") and on the second-stage ("4-K") shields reach steady values. The pressure in the chamber, as measured by the 300-L/s ion-pump current, is then around 4×10^{-10} mbar [28]. Warming up to room temperature takes about 100 h when keeping the chamber under vacuum; if needed, faster cycling times could be achieved by flushing the chamber with dry nitrogen to enhance heat exchange.

We characterize the performance of the cryostat in a series of preliminary experiments in various configurations, which allow us to evaluate its response to the various heat loads to which it is subjected in operation. We first cool down the system in a configuration minimizing the heat load (no wiring for the SC coils, windows in the thermal shields replaced by gold-plated copper blanks, and openings for the atomic beam sealed) and measure $T_1 = 30.1$ K and $T_2 = 3.2$ K, which gives the base temperature that the system can reach. By applying controlled power to heaters located on the 4-K plate, we measure a temperature increase of around 4 K/W, which gives an estimate of the acceptable heat load. In a second configuration, where the fused-silica windows are mounted on the thermal shields and the apertures for the atomic beam are open, the measured temperature is barely affected, showing that most of the BBR is effectively blocked by the windows. In the final configuration, the SC coils are connected using their four 0.6-mm-diameter wires; the measured temperature (without any current flowing in the coils) is then $T_2 = 4.2$ K, consistent with the heat load due to heat conduction along the wires.

Finally, we test the cryostat performance in the presence of the two extra heat load sources that appear when trapping atoms, namely laser light for the tweezer array and current flowing through the coils. Concerning laser power, due to the ITO coating on the lenses, a significant part (about 20%) of the light at 830 nm is absorbed or reflected by the pair of lenses and does not exit the cryostat; part of it is thus a direct heat load for the 4-K environment. For an incident power of 1 W (enough to generate about 500 optical tweezers), we measure a temperature increase of the lens holder by about 1 K. Concerning the operation of the coils, we observe a slight temperature increase (0.1 K for 1 A) when we run a current through them. For small currents, up to 1.7 A (corresponding to a MOT gradient of 7.3 G/cm), we attribute this to Joule heating of the (non-SC) wires connecting the coils to the room-temperature connectors. Beyond this value, we observe a jump in the coil resistance, indicating that they partially reach a temperature above the Nb-Ti critical temperature of 9.2 K and transition to the normal state, most likely because the thermal contact between the kapton-insulated SC wire and the Cu-Be coil form is not sufficient for proper thermalization. Then, the temperature increase is steeper, with the lens-holder sensor reaching a temperature of 5.4 K when the current is 2.5 A. This is more than enough for operating a MOT in order to load the tweezer array, as we discuss in Sec. III A.

III. SINGLE-ATOM TRAPPING IN ARRAYS OF OPTICAL TWEEZERS

A. Magneto-optical trap

We now describe the operation of the setup for atom trapping, starting with the realization of a ^{87}Rb MOT. To do so, we typically operate the rubidium oven at 100 °C. The resulting atomic beam is slowed down via the Zeeman slower and loads a magneto-optical trap in the science chamber. The MOT uses six counterpropagating laser beams with a $1/e^2$ radius of 1.7 mm and a power of 1 mW each, detuned by -4.5Γ from the $F = 2 \rightarrow F' = 3$ transition of the D_2 line (the natural line width of which is $\Gamma = 2\pi \times 6$ MHz). Repumping light is combined with these six beams, with a power 0.1 mW per beam; it is resonant with the $F = 1 \rightarrow F' = 2$ transition of the D_1 line. The typical magnetic field gradient used for MOT loading is 6 G/cm.

After loading the MOT for typically 500 ms, we turn off the Zeeman slower beam and close the gate valve to stop any further loading of the magneto-optical trap. The decay of the MOT fluorescence, measured with a CCD camera, is shown in Fig. 2. At short times, the MOT decays relatively quickly, due to a combination of (i) light-assisted collisions in the dense central region of the cloud and (ii) the escape of atoms from the outer regions of the MOT, where the beam intensities are not perfectly balanced (making this initial decay quite sensitive to the alignment of the MOT beams). At long times, the fluorescence decay is exponential, with a $1/e$ lifetime of about 140 s, much less sensitive to beam

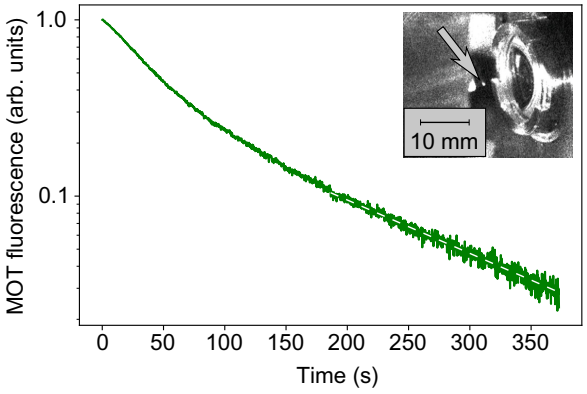

FIG. 2. The fluorescence decay of the MOT. An exponential decay fit at long times (white dashed line) gives a $1/e$ decay time of about 140 s. The inset shows the MOT cloud (arrow) facing one of the aspheric lenses.

alignment. Such a MOT lifetime is typical of vacuum systems with pressures in the low-10^{-12}-mbar range, showing the dramatic effect of cryopumping by the 4-K surfaces surrounding the atoms, despite the relatively low vacuum in the room-temperature chamber. This measured lifetime gives a lower bound on the vacuum-limited lifetime that we can expect for atoms in optical tweezers [29].

B. Arrays of optical tweezers

We then study the loading of single atoms into optical tweezers, which are created using light at 830 nm. Using a spatial light modulator, we create arbitrary tweezer arrays in the focal plane of the aspheric lens [30]. For the work reported here, we use a 9×9 square array (see the average fluorescence image in the inset of Fig. 3). The fluorescence emitted by trapped atoms is collected, using the same aspheric lenses, on an electron-multiplication camera with a typical exposure time of 50 ms. We observe that despite the large number of optical surfaces the beams go through and the high reflectivity of the gold-plated thermal shields, stray light is barely higher than in our room-temperature setup and does not significantly affect the detection of single atoms.

For a power of 3 mW per optical microtrap, we measure, using parametric heating, an axial (radial) trapping frequency 8 kHz (70 kHz). The trap depth is $U_0/k_B \simeq 0.8$ mK. Using a release-and-recapture method [31], we measure the atomic temperature in the tweezers to be around 50 μK after the atoms have been cooled for 50 ms by polarization-gradient cooling (PGC) with a detuning of -4.5Γ. We cool the atoms down further to 20 μK, using a -10.5Γ-detuned light pulse of 40 ms.

To measure the time evolution of the probability of keeping an atom in the optical tweezers, we record a first fluorescence image to identify the traps initially containing

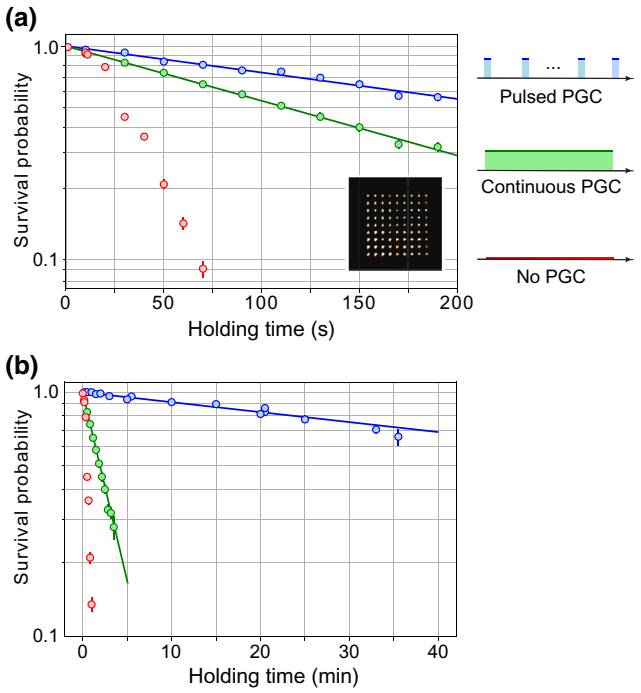

FIG. 3. (a) The survival probability of a single atom as a function of the time it is held in optical tweezers, without PGC (red), with continuous PGC (green), and with a 15-ms pulse of PGC every 10 s (blue). The exponential-decay fits (solid lines) give $1/e$ decay times of about 162 s for continuous PGC and of 335 s for pulsed PGC. The inset shows an averaged fluorescence image of the 9×9 tweezer array, with a spacing of 10 μm between adjacent microtraps. (b) Lifetime measurement for pulsed PGC (blue) after improvement of the vacuum [28,29], note the change in the horizontal scale. The $1/e$ decay time is now 6050 s (solid line). For comparison, the no-PGC and continuous-PGC curves from panel (a) are plotted again.

atoms; we then wait for a time t_{hold} and we finally take a second image to identify the remaining atoms.

Without any cooling light during the hold time, half of the atoms are lost after about 30 s and the decay of the recapture probability with time is nonexponential (see the red dots in Fig. 3). This is explained by a linear heating rate, which we measure in a separate experiment to be of about 8 μK/s, originating from off-resonant scattering of the 830-nm trapping light. An obvious way to mitigate this heating is to leave the PGC on during the hold time. With a detuning of -10.5Γ, the recapture probability is then increased drastically, giving an exponential decay with a $1/e$ decay time of 162 s (green dots). However, a careful inspection of the second image shows that occasionally, an initially empty trap is occupied in the final image. A more detailed analysis (see the Appendix) shows that from time to time, some atoms that are expelled from a trap via collisions with background-gas molecules are still slow enough to be recaptured in the optical molasses and

then reloaded in another optical microtrap, either giving rise to a trap loading (if this other trap is initially empty) or to the correlated loss of two atoms (if the other trap is already occupied). This suggests that the trap lifetime can be further increased.

To do so, we pulse the PGC cooling light, sending a 15-ms PGC pulse at -10.5Γ every 10 s. These timings fulfill the following conditions: the PGC pulse is long enough to fully cool the atom again and is repeated often enough such that the increase in temperature induced by the 830-nm light over the period of 10 s remains well below the trap depth. At the same time, the overall duty cycle $\eta = 0.15\%$ is very small, such that the probability of correlated atom loss, now multiplied by η, becomes entirely negligible. In these conditions, we measure a background-collision-limited lifetime of 335 s (blue), i.e., an improvement by a factor of approximately 16 as compared to our room-temperature setup [29]. Finally, after improving the vacuum, we repeat the pulsed-PGC lifetime measurement and obtain a $1/e$ lifetime of 6050 s as shown in Fig. 3(b). The pulsed-PGC cooling is entirely compatible with atom-by-atom rearrangement, meaning that we can benefit from this lifetime increase for assembling large arrays.

IV. CONCLUSION

In this work, we demonstrate, using a relatively simple setup, the trapping of single atoms in arrays of optical tweezers in a 4-K environment, with long lifetimes of over 6000 s, that open up exciting prospects. We now discuss possible ways to improve the performance in the future.

Using the same setup, the next step will consist in realizing large rearranged arrays with hundreds of single atoms. Defect-free arrays of approximately 800 atoms seem to be within reach in our setup (the necessary 1600 optical tweezers still correspond, for a trapping wavelength of 830 nm, to an acceptable heat load for the cryostat). In the current stage, with ITO coating on the aspheric lenses and appropriate antireflection coatings on the windows, the setup is compatible with Rydberg excitation, albeit without the possibility of electric field control. A direct measurement of Rydberg-level lifetimes using a ponderomotive bottle-beam trap [32] would be interesting, to check the increase in the Rydberg-state lifetime due to the suppression of BBR-induced transitions. The addition of a set of electrodes on the lens holder, and possibly a microwave antenna for coherent manipulation in the Rydberg manifold, will be a relatively simple upgrade of the current setup.

To improve the residual pressure even further, the ultimate step would be to make the system bakeable. For that, the design needs to use a removable PTR, which requires us to use radiators in a chamber filled with buffer gas as the vibration-decoupling heat exchanger, in place of the copper braids used here. Another possible improvement would be to maximize the cryopumping efficiency using porous materials such as activated charcoal. Such a setup, although more involved than the one used in the current work, is perfectly realistic. Cryogenic setups will certainly allow us to reach 1000-atom-scale tweezer arrays, and maybe even more if combined with techniques [33–36] that allow for an initial loading efficiency of the array considerably above 50%, thus reducing both the assembly time and the required trapping laser power.

ACKNOWLEDGMENTS

We thank Eric Magnan and Sam R. Cohen for contributions in the early stages of the experiment, as well as Michel Brune, Jean-Michel Raimond, and Clément Sayrin for useful discussions, and Igor Ferrier-Barbut for a careful reading of the manuscript. Mohammed Sharazi and Franck Ferreyrol from My Cryo Firm were involved in the design and construction of the custom-made cryostat. K.N.S. acknowledges funding from the Studienstiftung des deutschen Volkes. S.P. is partially supported by the Erasmus+ program of the European Union (EU). D.B. acknowledges support from the Ramón y Cajal program (Grant No. RYC2018-025348-I). This project has received funding from the Région Île-de-France through the Major Interest Domain (DIM) "Science and engineering in Ile-de-France Region for Quantum Technologies" (SIRTEQ) project CARAQUES and from the EU Horizon 2020 research and innovation program, under Grant Agreement No. 817482 (Programmable Atomic Large-Scale Quantum Simulation, or PASQuanS).

APPENDIX: CORRELATED LOSS AND RECAPTURE UNDER CONTINUOUS POLARIZATION-GRADIENT COOLING

The fact that the measured trapping lifetime for an atom in optical tweezers is reduced under continuous-PGC conditions can arise due to two different effects, the relative importance of which depends on the experimental parameters.

The first effect is simply that when the PGC beams are always on, a steady-state very dilute cloud of laser-cooled atoms (loaded either from slow atoms from the source or from a residual Rb pressure in the chamber), always surrounds the tweezer array; this yields occasional loading of single atoms in a microtrap that is already occupied, resulting in the loss of both atoms. In the present case, this effect should be negligible, as the atom source is mechanically blocked by the stepper-motor-actuated valve, and the residual Rb pressure in the 4-K environment is extremely low.

The second effect is the following. The energy that is imparted to a trapped Rb atom by a molecule from the residual gas in the vacuum chamber (consisting mostly of H_2 molecules, as most other species are extremely

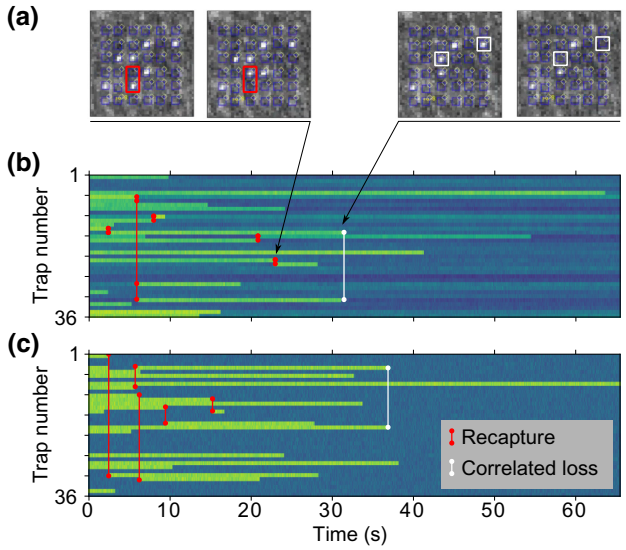

FIG. 4. (a) Examples of fluorescence images of a 6×6 array, showing, between successive frames, either the loss of an atom accompanied by the loading of a previously empty trap (left) or the "simultaneous" loss of two atoms (right). (b) Experimental fluorescence traces, showing the evolution of the array occupancy as a function of time, with correlated loss-and-recapture events highlighted in white and red, respectively. (c) The result of a Monte Carlo simulation of the simple model discussed in the text, showing the same qualitative behavior as the experimental traces in (b).

well cryopumped by the 4-K walls) can be small enough that the Rb atom, while expelled from the approximately 1-mK-deep optical tweezers, is still captured in the optical molasses [37]. This atom can then be very quickly loaded in another trap of the array, that is either empty or loaded. In the first case, two successive frames of the camera that monitors the fluorescence of the array will show the same number of trapped atoms, but with one trap having lost its atom and another one being suddenly loaded [Fig. 4(a), left]. In the second case, the second frame will show two fewer atoms than the first one [Fig. 4(a), right].

Analysis of the successive images acquired during continuous PGC (but taken with a detuning of -4.5Γ to obtain relatively bright fluorescence images) shows that several of those correlated loss-and-recapture events can be identified during the full decay of the array and that they contribute significantly to the trapping lifetime. A typical example of such an analysis is shown in Fig. 4(b). Figure 4(c) shows the result of a very simple stochastic modeling of the process. At each time step, corresponding to an imaging frame, each atom in a filled trap i has a probability p_{coll} of undergoing a collision with the background gas; if a collision does occur, it leaves the trap but has a probability p_{rec} of being recaptured in *any* trap j of the array (including i), chosen randomly, giving rise to either a recapture or to correlated loss. We find that values around $p_{\mathrm{rec}} \sim 0.2$ reproduce qualitatively the main features of the experimental traces.

A quantitative investigation of the dependence of p_{rec} on various parameters (the temperature of the environment, the parameters of the PGC) is beyond the scope of this paper but could be an interesting extension of the present work.

[1] Yu. Alexeev, D. Bacon, K. R. Brown, R. Calderbank, L. D. Carr, F. T. Chong, B. DeMarco, D. Englund, E. Farhi, and B. Fefferman *et al.*, Quantum computer systems for scientific discovery, PRX Quantum **2**, 017001 (2021).

[2] A. Browaeys and T. Lahaye, Many-body physics with individually controlled Rydberg atoms, Nat. Phys. **16**, 132 (2020).

[3] I. S. Madjarov, A. Cooper, A. L. Shaw, J. P. Covey, V. Schkolnik, T. H. Yoon, J. R. Williams, and M. Endres, An Atomic-Array Optical Clock with Single-Atom Readout, Phys. Rev. X **9**, 041052 (2019).

[4] M. A. Norcia, A. W. Young, W. J. Eckner, E. Oelker, J. Ye, and A. M. Kaufman, Seconds-scale coherence on an optical clock transition in a tweezer array, Science **366**, 93 (2019).

[5] M. Saffman, Quantum computing with atomic qubits and Rydberg interactions: Progress and challenges, J. Phys. B **49**, 202001 (2016).

[6] L. Henriet, L. Béguin, A. Signoles, T. Lahaye, A. Browaeys, G.-O. Reymond, and C. Jurczak, Quantum computing with neutral atoms, Quantum **4**, 327 (2020).

[7] P. Scholl, M. Schuler, H. J. Williams, A. A. Eberharter, D. Barredo, K.-N. Schymik, V. Lienhard, L.-P. Henry, T. C. Lang, T. Lahaye, A. M. Läuchli, and A. Browaeys, Quantum simulation of 2D antiferromagnets with hundreds of Rydberg atoms, Nature **595**, 233 (2021).

[8] S. Ebadi, T. T. Wang, H. Levine, A. Keesling, G. Semeghini, A. Omran, D. Bluvstein, R. Samajdar, H. Pichler, W. W. Ho, S. Choi, S. Sachdev, M. Greiner, V. Vuletic, and M. D. Lukin, Quantum phases of matter on a 256-atom programmable quantum simulator, Nature **595**, 227 (2021).

[9] K.-N. Schymik, V. Lienhard, D. Barredo, P. Scholl, H. Williams, A. Browaeys, and T. Lahaye, Enhanced atom-by-atom assembly of arbitrary tweezers arrays, Phys. Rev. A **102**, 063107 (2020).

[10] If the single-atom lifetime is τ, the lifetime of an N-atom configuration is τ/N. As the rearrangement time scales roughly linearly with N, an improvement by a factor α of τ results in an increase of the maximal atom number that one can rearrange during the lifetime of a configuration by only $\sqrt{\alpha}$.

[11] I. I. Beterov, I. I. Ryabtsev, D. B. Tretyakov, and V. M. Entin, Quasiclassical calculations of blackbody-radiation-induced depopulation rates and effective lifetimes of Rydberg nS, nP, and nD alkali-metal atoms with $n \leq 80$, Phys. Rev. A **79**, 052504 (2009).

[12] I. Cong, S.-T. Wang, H. Levine, A. Keesling, and M. D. Lukin, *Hardware-Efficient, Fault-Tolerant Quantum Computation with Rydberg Atoms*, arXiv:2105.13501.

[13] E. A. Goldschmidt, T. Boulier, R. C. Brown, S. B. Koller, J. T. Young, A. V. Gorshkov, S. L. Rolston, and J. V. Porto, Anomalous Broadening in Driven Dissipative Rydberg Systems, Phys. Rev. Lett. **116**, 113001 (2016).

[14] J. Zeiher, R. van Bijnen, P. Schauß, S. Hild, J.-Y. Choi, T. Pohl, I. Bloch, and C. Gross, Many-body interferometry of a Rydberg-dressed spin lattice, Nat. Phys. **12**, 1095 (2016).

[15] S. Haroche, Nobel lecture: Controlling photons in a box and exploring the quantum to classical boundary, Rev. Mod. Phys. **85**, 1083 (2013).

[16] T. Xia, X. L. Zhang, and M. Saffman, Analysis of a controlled phase gate using circular Rydberg states, Phys. Rev. A **88**, 062337 (2013).

[17] T. L. Nguyen, J. M. Raimond, C. Sayrin, R. Cortiñas, T. Cantat-Moltrecht, F. Assemat, I. Dotsenko, S. Gleyzes, S. Haroche, G. Roux, T. Jolicoeur, and M. Brune, Towards Quantum Simulation with Circular Rydberg Atoms, Phys. Rev. X **8**, 011032 (2018).

[18] S. R. Cohen and J. D. Thompson, *Quantum Computing with Circular Rydberg Atoms*, arXiv:2103.12744.

[19] J. D. Pritchard, J. A. Isaacs, M. A. Beck, R. McDermott, and M. Saffman, Hybrid atom-photon quantum gate in a superconducting microwave resonator, Phys. Rev. A **89**, 010301(R) (2014).

[20] G. Pagano, P. W. Hess, H. B. Kaplan, W. L. Tan, P. Richerme, P. Becker, A. Kyprianidis, J. Zhang, E. Birckelbaw, M. R. Hernandez, Y. Wu, and C. Monroe, Cryogenic trapped-ion system for large scale quantum simulation, Quantum Sci. Tech. **4**, 014004 (2018).

[21] P. Micke, J. Stark, S. A. King, T. Leopold, T. Pfeifer, L. Schmöger, M. Schwarz, L. J. Spieß, P. O. Schmidt, and J. R. Crespo López-Urrutia, Closed-cycle, low-vibration 4 K cryostat for ion traps and other applications, Rev. Sci. Instrum. **90**, 065104 (2019).

[22] C. Roux, A. Emmert, A. Lupascu, T. Nirrengarten, G. Nogues, M. Brune, J.-M. Raimond, and S. Haroche, Bose-Einstein condensation on a superconducting atom chip, EPL **81**, 56004 (2008).

[23] S. Bernon, H. Hattermann, D. Bothner, M. Knufinke, P. Weiss, F. Jessen, D. Cano, M. Kemmler, R. Kleiner, D. Koelle, and J. Fortágh, Manipulation and coherence of ultra-cold atoms on a superconducting atom chip, Nat. Commun. **4**, 2380 (2013).

[24] L. Béguin, Ph.D. thesis, Institut d'Optique Graduate School (2013).

[25] In our case, the "OptiDry" model from My Cryo Firm.

[26] In order to avoid stress-induced birefringence upon cooling down, the windows are not rigidly mounded on the thermal shields but held by a retaining ring that is simply pressed against the shields using Cu-Be strips of fingers.

[27] J. W. Ekin, *Experimental Techniques for Low-Temperature Measurements* (Oxford University Press, (Oxford), 2006).

[28] The pressure values stated here were measured after an improvement of the room-temperature vacuum. Indeed, after acceptance of the paper, we noticed a leak in the titanium sublimation pump. Repairing the issue improved the room-temperature vacuum, as measured by the ion pump, by 2 orders of magnitude.

[29] Here, the stated lifetime values were measured before the vacuum was improved. At cryogenic temperatures, the improvements resulted in a 20-fold increase of the measured single-atom lifetimes in the optical tweezers of over 6000 s (see Fig. 3(b)).

[30] F. Nogrette, H. Labuhn, S. Ravets, D. Barredo, L. Béguin, A. Vernier, T. Lahaye, and A. Browaeys, Single-Atom Trapping in Holographic 2D Arrays of Microtraps with Arbitrary Geometries, Phys. Rev. X **4**, 021034 (2014).

[31] C. Tuchendler, A. M. Lance, A. Browaeys, Y. R. P. Sortais, and P. Grangier, Energy distribution and cooling of a single atom in an optical tweezer, Phys. Rev. A **78**, 033425 (2008).

[32] D. Barredo, V. Lienhard, P. Scholl, S. de Léséleuc, T. Boulier, A. Browaeys, and T. Lahaye, Three-Dimensional Trapping of Individual Rydberg Atoms in Ponderomotive Bottle Beam Traps, Phys. Rev. Lett. **124**, 023201 (2020).

[33] P. Sompet, A. V. Carpentier, Y. H. Fung, M. McGovern, and M. F. Andersen, Dynamics of two atoms undergoing light-assisted collisions in an optical microtrap, Phys. Rev. A **88**, 051401(R) (2013).

[34] B. J. Lester, N. Luick, A. M. Kaufman, C. M. Reynolds, and C. A. Regal, Rapid Production of Uniformly Filled Arrays of Neutral Atoms, Phys. Rev. Lett. **115**, 073003 (2015).

[35] M. O. Brown, T. Thiele, C. Kiehl, T.-W. Hsu, and C. A. Regal, Gray-Molasses Optical-Tweezer Loading: Controlling Collisions for Scaling Atom-Array Assembly, Phys. Rev. X **9**, 011057 (2019).

[36] M. M. Aliyu, L. Zhao, X. Q. Quek, K. C. Yellapragada, and H. Loh, *Increasing the scalability of atom arrays with magic wavelength tweezers*, arXiv:2105.15047.

[37] At $T = 4$ K, a H_2 molecule has a typical thermal velocity of $\sqrt{3k_BT/m_{H_2}} \simeq 220$ m/s. Even in the worst-case scenario of a head-on collision, a molecule with this velocity will give to the heavy ^{87}Rb atom (initially almost at rest in its tweezers) a velocity of only approximately 10 m/s (and obviously considerably less for grazing-incidence collisions). Thus, a very significant fraction of the collisions with the residual gas give Rb atoms with a velocity within the capture range of the optical molasses. At room temperature, the effect would be considerably less frequent, as the thermal velocity of H_2 molecules is higher by a factor of almost 9.

Appendix F

Article: *Quantum Simulation of 2D Antiferromagnets with Hundreds of Rydberg Atoms*

This appendix reproduces the following published article:

Pascal Scholl, Michael Schuler, Hannah J. Williams, Alexander A. Eberharter, Daniel Barredo, Kai-Niklas Schymik, Vincent Lienhard, Louis-Paul Henry, Thomas C. Lang, Thierry Lahaye, Andreas M. Läuchli and Antoine Browaeys *Quantum simulation of 2D antiferromagnets with hundreds of Rydberg atoms*. Nature **595**, pages 233-238 (2021)

Article

Quantum simulation of 2D antiferromagnets with hundreds of Rydberg atoms

https://doi.org/10.1038/s41586-021-03585-1

Received: 21 December 2020

Accepted: 27 April 2021

Published online: 7 July 2021

Check for updates

Pascal Scholl[1,6]✉, Michael Schuler[2,6], Hannah J. Williams[1,6], Alexander A. Eberharter[3,6], Daniel Barredo[1,4], Kai-Niklas Schymik[1], Vincent Lienhard[1], Louis-Paul Henry[5], Thomas C. Lang[3], Thierry Lahaye[1], Andreas M. Läuchli[3] & Antoine Browaeys[1]

Quantum simulation using synthetic systems is a promising route to solve outstanding quantum many-body problems in regimes where other approaches, including numerical ones, fail[1]. Many platforms are being developed towards this goal, in particular based on trapped ions[2–4], superconducting circuits[5–7], neutral atoms[8–11] or molecules[12,13]. All of these platforms face two key challenges: scaling up the ensemble size while retaining high-quality control over the parameters, and validating the outputs for these large systems. Here we use programmable arrays of individual atoms trapped in optical tweezers, with interactions controlled by laser excitation to Rydberg states[11], to implement an iconic many-body problem—the antiferromagnetic two-dimensional transverse-field Ising model. We push this platform to a regime with up to 196 atoms manipulated with high fidelity and probe the antiferromagnetic order by dynamically tuning the parameters of the Hamiltonian. We illustrate the versatility of our platform by exploring various system sizes on two qualitatively different geometries—square and triangular arrays. We obtain good agreement with numerical calculations up to a computationally feasible size (approximately 100 particles). This work demonstrates that our platform can be readily used to address open questions in many-body physics.

Previous studies have demonstrated the potential of Rydberg-based quantum simulators with up to a few tens of atoms[14–16], including high-fidelity manipulations[17–19]. In particular, the transverse-field Ising (TFI) model has been studied in one dimension with up to 51 atoms[14,15,20], in two-dimensional (2D) square arrays—but with a limited degree of coherence[16,21], making it difficult to observe genuine quantum features—and recently in three dimensions with 22 atoms[22]. Here we implement the TFI model in two dimensions, combining much larger atom numbers (up to around 200) and a high degree of coherence. In our implementation, we explore two geometries that exhibit qualitatively different phase diagrams: the bipartite square lattice and the geometrically frustrated triangular lattice[23]. On the square lattice, we prepare the Néel state that is characteristic of antiferromagnets with unprecedented probability. On the triangular lattice, we observe the creation of two distinct antiferromagnetic (AF) orders. The large number of atoms involved and the non-equilibrium nature of the experiment makes a direct comparison with accurate numerical simulations challenging. To validate the dynamics of our simulator, we have pushed matrix-product-state simulations to their limit and are able to simulate the dynamics of up to 100 atoms in two dimensions. We obtain an impressive agreement between the simulation and the experiment up to this number, which is one of the largest for which a direct comparison has been performed. Finally, by comparing the experiment to classical Monte Carlo calculations, we demonstrate that our results cannot be reproduced by a classical equilibrium distribution at the same mean energy, and that the experiment features an enhanced probability of finding classical ground states.

2D quantum Ising model on a Rydberg simulator

For arrays of atoms coupled by the (repulsive) van der Waals interaction, when excited to Rydberg states, the Hamiltonian of the TFI model is:

$$H_{\mathrm{Ryd}} = \sum_{i<j} U_{ij}\, n_i n_j + \frac{\hbar\Omega}{2} \sum_i \sigma_i^x - \hbar\delta \sum_i n_i, \qquad (1)$$

where the Rydberg and ground states are mapped onto the (pseudo-) spin states $|\uparrow\rangle$ and $|\downarrow\rangle$, respectively. Here $U_{ij} = C_6/r_{ij}^6$ is the van der Waals interaction, C_6 is the van der Waals coefficient, r_{ij} is the distance between atoms i and j, $n_i = |\uparrow\rangle\langle\uparrow|_i = (1+\sigma_i^z)/2$, σ_i are the usual Pauli matrices and $\hbar$ is the reduced Planck's constant. The two spin states are coupled via a laser field with a Rabi frequency Ω and a detuning δ, which act as transverse and longitudinal fields, respectively. AF ordering in the system appears as a consequence of the strong interactions characterized by the Rydberg blockade radius R_b, as illustrated in Fig. 1a[24]. The type of AF ordering depends on the geometry of the array and the Hamiltonian parameters.

[1]Laboratoire Charles Fabry, Institut d'Optique Graduate School, Université Paris-Saclay, CNRS, Palaiseau, France. [2]Vienna Center for Quantum Science and Technology, Atominstitut, TU Wien, Vienna, Austria. [3]Institut für Theoretische Physik, Universität Innsbruck, Innsbruck, Austria. [4]Nanomaterials and Nanotechnology Research Center (CINN–CSIC), Universidad de Oviedo (UO), Principado de Asturias, El Entrego, Spain. [5]Zentrum für Optische Quantentechnologien, Institut für Laser-Physik, Universität Hamburg, Hamburg, Germany. [6]These authors contributed equally: Pascal Scholl, Michael Schuler, Hannah J. Williams, Alexander A. Eberharter. ✉e-mail: pascal.scholl@institutoptique.fr

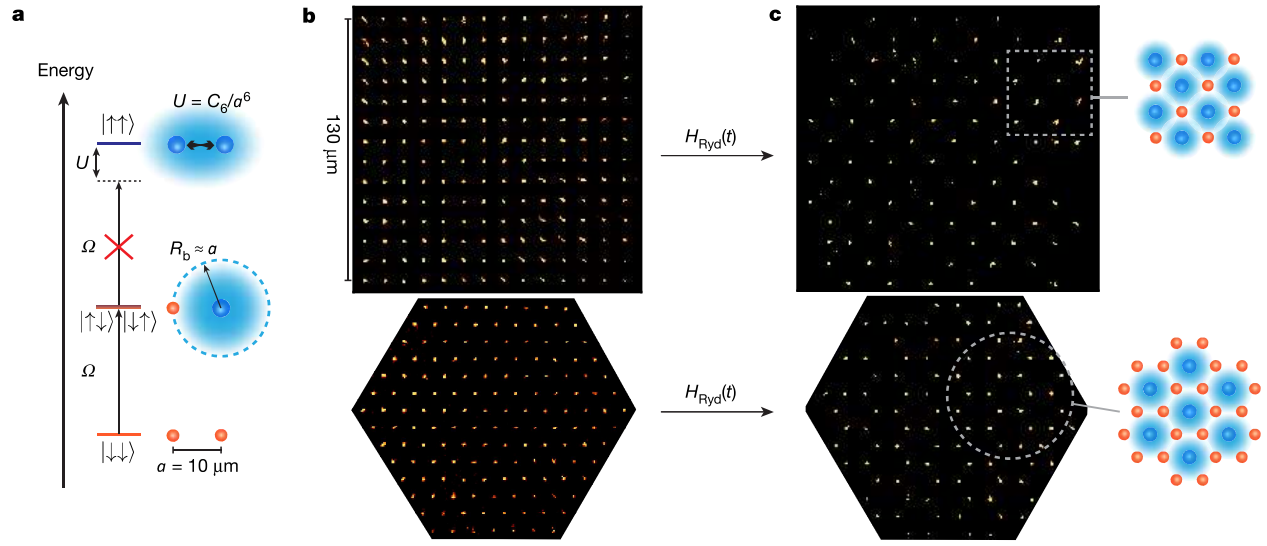

Fig. 1 | Emergence of AF ordering from the Rydberg blockade in square and triangular arrays. a, Illustration of the Rydberg blockade with two atoms, whereby the strong interactions prevent the simultaneous excitation of two atoms from the ground state (red circles) to the Rydberg state (blue circles) within the Rydberg blockade radius R_b at which $U = \hbar\Omega$. **b**, **c**, Single-shot fluorescence images of ground state ($|\downarrow\rangle$) atoms in a 14 × 14 square array (top) and a 147-atom triangular array (bottom) with an atomic separation of $a = 10$ µm. **b**, Initial PM states. **c**, Nearly perfect AF ordering.

We create defect-free square and triangular arrays of up to 196 and 147 ^{87}Rb atoms, respectively, using an optimized atom-by-atom assembly protocol[25] (Fig. 1b). We define $|\downarrow\rangle = |5S_{1/2}, F = 2, m_F = 2\rangle$ and $|\uparrow\rangle = |75S_{1/2}, m_J = 1/2\rangle$ (F and m_F are the hyperfine quantum numbers and m_J is the magnetic quantum number for the fine structure), which are coupled via the intermediate state $|6P_{3/2}, F = 3, m_F = 3\rangle$ with two counter-propagating laser beams with wavelengths of 420 nm and 1,013 nm (ref. [26]) (see 'Experimental setup' section). We achieve a single atom excitation probability of 99.1(8)% and a coherence time of 20 µs, about 20 times longer than in our previous work[16] (see 'Coherence of single-atom laser excitation' section). We use arrays with atomic spacing a = 10 µm, leading to a nearest-neighbour interaction of $U/h \approx 1.95$ MHz.

To probe the phase diagram of H_{Ryd}, we sweep Ω and δ over time, and transfer the system from its initial paramagnetic (PM) ground state $|\downarrow\downarrow\ldots\downarrow\rangle$ into the AF phase. A quantum phase transition (QPT) separates these two phases. Ideally, one would adiabatically drive the system such that it remains in the instantaneous ground state. However, the energy gap at the QPT decreases with the atom number N, (proportional to $1/\sqrt{N}$ on a square lattice and exponentially for the triangular lattice[27,28]). This leads to timescales that are experimentally impractical due to decoherence effects, dominated by spontaneous emission from the intermediate state. Hence, we choose sweep times (about 6 µs) that are short enough to avoid sizeable decoherence but sufficiently long to quasi-adiabatically probe the phase diagram (see 'Benchmarking the 4 × 4 array' section). We record fluorescence images of the atoms remaining in $|\downarrow\rangle$. Examples of single-shot images of the largest square and triangular arrays before (and following) the preparation sweeps are shown in Fig. 1b, c. The final images show almost-perfect AF ordering. For the results presented here, we typically repeat the sequence 1,000 times.

Antiferromagnet on the square lattice

We first focus on the square lattice, using arrays of size $N = L \times L$, with an even linear system size L so that the two Néel states have the same energy. In Fig. 2a, we sketch the (bulk) phase diagram. In the case of the van der Waals interaction implemented here, the AF phase region is expected to extend up to the critical point $\hbar\Omega_c \approx 1.25U$ at $\hbar\delta \approx 4.66U/2$ (ref. [29]). More complex phases[30], explored in a companion paper[31], appear at the lower and upper boundaries of $\hbar\delta/U$ in the AF region. The applied sweeps are shown in Fig. 2a, with the QPT being crossed during the ramp down of $\Omega(t)$. Figure 2b presents an experimental histogram of the states recorded at the end of the sweep for the 8 × 8 array. Remarkably, out of $2^{64} \approx 2 \times 10^{19}$ possible states, we obtain a perfectly ordered state with a probability of around 2.5% (including detection errors; even if the sweeps were fully adiabatic, the probability of measuring perfect AF ordering would be about 27% due to our detection errors), as can be seen by the two prominent peaks. The fluorescence images show the two corresponding Néel states. To characterize the magnetic ordering of the states prepared during the sweep, we measure the order parameter, which is the normalized staggered magnetization $m_{stag} = \langle|n_A - n_B|\rangle/(N/2)$, giving the difference in the number of excitations on each sublattice (A and B), averaged over many realizations. The two perfect AF states correspond to one of the two sublattices being fully excited, such that $m_{stag} = 1$. We access the dynamics of the system during the sweep by rapidly turning off the excitation laser at different times t_{off} (Fig. 2a). Figure 2c shows the evolution of m_{stag} for the 6 × 6 array and the 10 × 10 array, using the same sweep. Over the first 1.5 µs of the sweep, the system is in the PM phase, where fluctuations lead to small but finite $m_{stag} \propto 1/\sqrt{N}$. We then observe the growth of m_{stag} during the drive of the system from the PM to the AF phase.

To benchmark our platform, we perform a systematic comparison of the dynamics with matrix product state (MPS) numerical simulations (see 'Matrix product states' section). We consider both the programmed and the real parameters, the latter of which include independently calibrated experimental imperfections (detection errors, inhomogeneities of the excitation beams, pulse shapes and residual disorder in the atomic positions, described in detail in the 'Effect of imperfections on larger arrays' section), with the exception of decoherence effects. For the 6 × 6 array, we observe a good agreement between the experimental results and the MPS simulations, for both situations. For the 10 × 10 array, the experiment and the real MPS simulations also agree well. The difference between the programmed and the real MPS simulations highlights that the imperfections have a more severe impact on larger systems. In addition, the reduced final value of m_{stag} for the programmed MPS on the 10 × 10 array indicates that as the system size grows, adiabaticity is indeed harder to achieve.

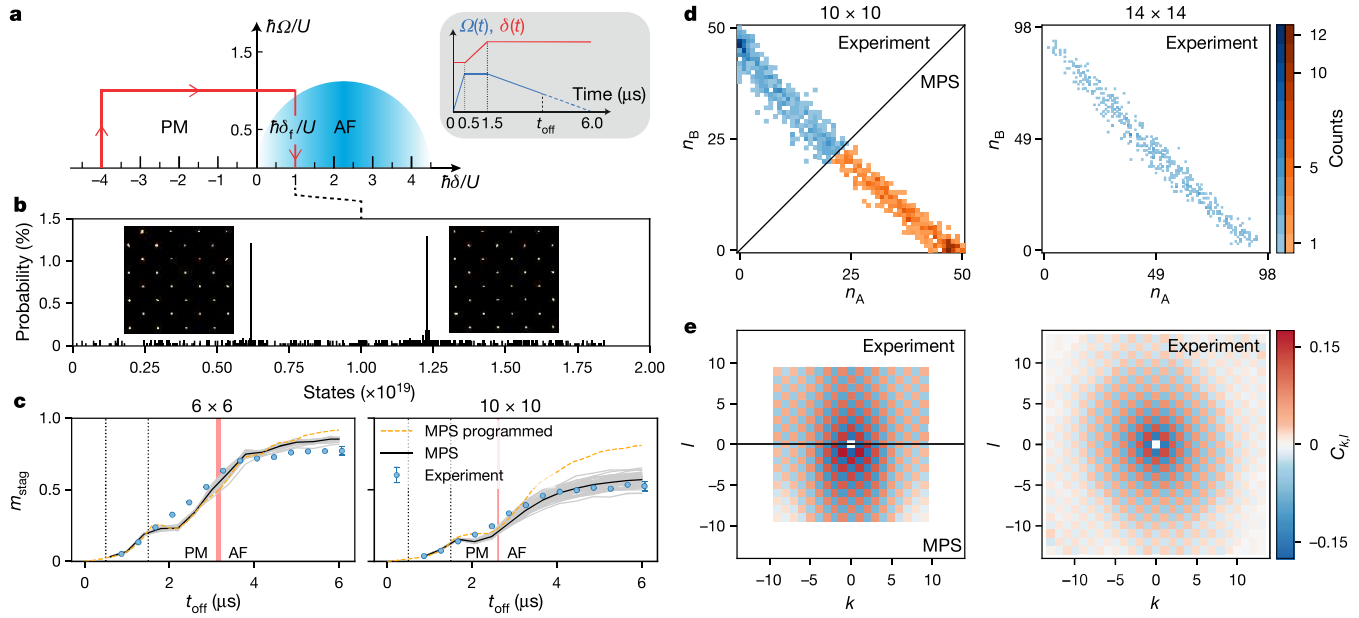

Fig. 2 | The Ising model on a square lattice. a, Sketched bulk phase diagram for the square lattice. The inset shows the sweep shape, with t_{off} the switch-off time of the excitation laser. The corresponding trajectory in the phase diagram is shown as a red arrow. **b**, State histogram for the 8 × 8 array at the end of the sweep. The insets show fluorescence images of the two perfect AF states, which are obtained with 2.5% probability. **c**, Growth of the staggered magnetization during the sweep for the 6 × 6 array (left) and the 10 × 10 array (right). The blue circles are experimental results with standard errors on the mean smaller than the markers size. The error bar on the final point is indicative of the long-term stability of the experimental setup (see 'Long-term stability' section). MPS simulations without (dashed line) and with (grey lines) experimental imperfections for which 50 (6 × 6 array) and 77 (10 × 10 array) disorder instances are shown, with their average shown in black. The vertical dotted lines correspond to the turning points in the sweep. The vertical red regions depict the finite-size phase boundaries between the PM and AF phases, obtained from the inflection point of m_{stag} using ground state density matrix renormalization group. **d**, Final staggered magnetization histograms for the 10 × 10 array (left) and the 14 × 14 array (right). **e**, The correlation maps for the 10 × 10 array (left) and the 14 × 14 array (right), with the MPS results shown in the lower half for the 10 × 10 array.

We now characterize the final state obtained at the end of the sweep ($\Omega = 0$). First, we visualize the shot-wise contributions to m_{stag} using a 2D histogram of the probability $P(n_A, n_B)$ of the $|\uparrow\rangle$ populations n_A and n_B of the two sublattices A and B. Here the two Néel states appear as points at $(N/2, 0)$ and $(0, N/2)$. The results are plotted in Fig. 2d for the 10 × 10 array and the 14 × 14 array. For both systems, we observe the presence of points along the diagonal, highlighting that the average Rydberg density is about 50%. For the 10 × 10 array, we observe a conglomeration of points around the two corners belonging to the Néel states. Owing to the imperfections and the scaling of the energy gap, the state preparation becomes more challenging with increasing system size. The elongated histogram for the 14 × 14 array demonstrates that, remarkably, we prepare strongly AF ordered states ($m_{stag} = 0.391(1)$), even for such large systems. This is also evident in the fluorescence image in Fig. 1c, which shows 184 atoms (out of 196) obeying AF ordering. For a comparison with simulations, we have devised an algorithm to stochastically sample the MPS wavefunction, thereby obtaining snapshots as in the experiment (see 'Sampling of MPS wavefunctions' section). The lower half of Fig. 2d shows the so-obtained histogram for the 10 × 10 lattice, which matches the experiment very well. For even larger atom numbers, accurate MPS simulations become intractable.

Second, we compute the connected spin–spin correlation function defined as

$$C_{k,l} = \frac{1}{N_{k,l}} \sum_{i,j} \langle n_i n_j \rangle - \langle n_i \rangle \langle n_j \rangle, \quad (2)$$

where the sum runs over all pairs of atoms i and j separated by $k\mathbf{e}_1 + l\mathbf{e}_2$, with $\mathbf{e}_{1(2)}$ denoting the two vectors of the underlying lattice, k and l are two integer numbers, and $N_{k,l}$ being the number of such pairs. Figure 2e shows the $C_{k,l}$ correlation maps corresponding to the m_{stag} histograms shown in Fig. 2d. The plots show the alternation of correlation and anti-correlation, expected for AF ordering, whose values would be ±1/4 for the Néel state. The spatial decay of the correlations is well described by correlation lengths of $\xi \approx 7a$ and $\xi \approx 5.5a$ for the two system sizes, respectively, showing that the sweeps produce highly AF ordered states (the residual anisotropy observed is due to the finite size of the excitation beams, which is comparable to the width of the array (130 μm)). Again, we observe good agreement between the experimental and real MPS results for the 10 × 10 array, confirming that the simulations capture well the experimental conditions (for a real-time analysis of the correlations during the sweep, see the 'Growth of antiferromagnetic order' section).

Comparison with classical thermal equilibrium

To further quantify the AF ordering, we analyse the distribution of AF cluster sizes[32]. For each run of the experiment, we decompose the snapshot into individual clusters obeying local AF ordering (see examples in Fig. 3a, b). We count the number of atoms inside each individual cluster, and record the largest size, s_{max}. From the full set of snapshots, we reconstruct the probability distribution $P(s_{max})$. For a perfectly AF-ordered state, this distribution presents as a single peak of unit probability at $s_{max} = N$, while imperfect ordering shows up as a distribution broadened towards smaller s_{max}. In Fig. 3c, d we show $P(s_{max})$ at the end of the sweep for the 10 × 10 array obtained from the experiment (Fig. 3c) and from MPS simulations (Fig. 3d). We observe that more than 27% (30%) of the shots in the experiment (MPS) contain AF clusters of at least 90 sites, that is, $s_{max} \geq 90$.

The fact that we obtain a distribution of final states raises the question whether the system has thermalized during the finite duration of the sweep[14,33]. To answer this question, we compare the observed distribution $P(s_{max})$ to the corresponding distribution obtained from a classical

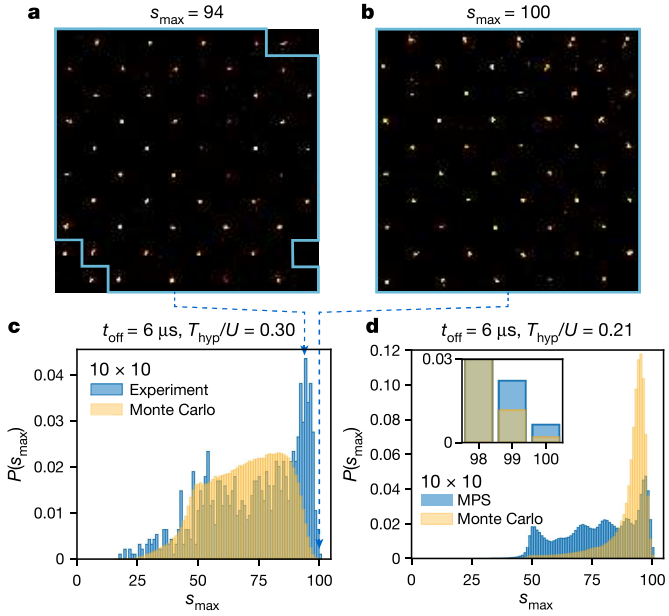

Fig. 3 | Quantum real-time evolution versus classical equilibrium. **a**, **b**, Fluorescence images on a 10 × 10 array illustrating how we extract the largest AF domains comprising 94 (**a**) and 100 (**b**) sites, indicated by the blue boundaries. **c**, **d**, Distributions of s_{max} at the end of the sweep (blue) compared with the classical equilibrium result (yellow) with the corresponding hypothetical temperature T_{hyp}, obtained from the experiment (**c**) and MPS simulations (**d**). The inset in **d** is a zoom into the distribution of the largest AF domains.

equilibrium setup with a hypothetical temperature T_{hyp}. We focus on a classical description for two reasons: (1) the classical energy is the one accessible in the experiment and (2) at the end of the sweep, $\Omega = 0$ and the quantum and classical statistical mechanics descriptions coincide.

To determine T_{hyp}, we match the classical Ising energy $E_{class}(t_{off})$ of the experimental system with $E^{MC}_{class}(T)$ from the corresponding classical statistical mechanics system for a given temperature T estimated from a Monte Carlo sampling (one could also use other observables to match a hypothetical temperature, but as temperature is the variable conjugate to the energy in thermodynamics, it is the most natural choice). We refer to the 'Extracting a classical temperature' section for a thorough discussion of T_{hyp} during the sweep. In Fig. 3c, d, we show $P(s_{max})$ for the corresponding classical equilibrium distributions, and observe that they do not reproduce the distribution of the experimental and MPS results. In particular, the probability of creating perfectly ordered states is higher in the quantum real-time evolution than in the classical equilibrium case. The classical equilibrium approach also results in shorter correlation lengths. A similar analysis during the sweep and for the MPS real-time evolution shows similar features (see the 'Experiment versus classical equilibrium during the sweep' and 'MPS time evolution versus classical equilibrium' sections). Our analysis therefore reveals that despite residual imperfections, the experiment does not thermalize during the state preparation protocol and is well reproduced by a unitary quantum mechanical real-time description. Furthermore, the enhanced probability of finding the targeted classical states is promising for future applications of the Rydberg platform, for example, as a quantum annealer to solve optimization problems of various types[34–36].

The 1/3 and 2/3 phases on the triangular lattice

Having explored the square lattice, we now consider the more complex triangular array. Here the TFI model features a richer phase diagram, with prominent ordered phases at 1/3 and 2/3 Rydberg filling, as sketched in Fig. 4a. The 1/3 phase is the analogue of the AF ordering on the square lattice, where the Rydberg blockade prevents neighbouring sites from being excited simultaneously, leading to one of the three sublattices being filled with Rydberg excitations, illustrated in Fig. 1c. The 2/3 phase is the 'particle–hole' inverse of this, with two sublattices being fully excited and one sublattice containing ground-state atoms. In between these phase regions, at 1/2 filling, the classical Ising model ($\Omega = 0$) is strongly frustrated for nearest-neighbour interactions, with an exponentially large (in N) ground-state manifold[23]. Finite Ω stabilizes yet another ordered phase in a process called 'order by disorder' (OBD)[29,37–41].

To explore the triangular phase diagram, we consider hexagonal clusters of various sizes, built shell by shell around a central three-atom triangle (Fig. 1b). We apply the sweeps shown in Fig. 4a for two different final detunings, δ_f, to create the 1/3 and the 2/3 phases. To quantify the state preparation process, we again measure the temporal dynamics of the order parameter, the normalized staggered magnetization. For the triangular array, this is defined as $m_{stag} = \langle |n_A + e^{i2\pi/3} n_B + e^{-i2\pi/3} n_C| \rangle / (N/3)$, where $n_{A,B,C}$ is the Rydberg population on each of the three sublattices. We plot the results in Fig. 4b for the experiment and two types of MPS simulation (programmed and real) for a 75-atom array, with δ_f chosen to prepare the 1/3 phase. We observe the growth of the AF ordering both in the experiment and the simulations, which agree well during the first 5 µs of the sweep. After this, the experimental results plateau at a lower value of m_{stag} than expected from the MPS. The inclusion of experimental imperfections decreases the final value of m_{stag}; however, there is still a discrepancy with the experimental results. A possible explanation could be the enhanced sensitivity of the QPT from PM to the 1/3 AF phase (believed to be first order[27]) to the residual experimental imperfections not included in the MPS simulation. Confirming the origin of this effect will be the subject of future work.

To further characterize the prepared final states, we consider $C_{k,l}$, defined similarly to equation (2). Here the perfect AF state would have $C_{k,l} = +2/9$ and $C_{k,l} = -1/9$ for correlated and anticorrelated sites, respectively. In Fig. 4c, e, we show the final-state correlation maps for the 1/3 (2/3) phases on atom arrays of 75, 108 and 147 sites (108 sites). We observe a pattern characteristic of three-sublattice ordered states, throughout almost the entire bulk of our systems, with a correlation length $\xi \approx 3$–$3.7a$ for the 1/3 phase and $\xi \approx 2a$ for the 2/3 phase. In Fig. 4d, f, we plot the corresponding distributions of the complex order parameter. For perfectly ordered 1/3 (2/3) systems, one would expect peaks at the three corners of the bounding hexagon, marked by red (green) dots. We observe correspondingly aligned triangular distributions with good agreement between the experimental and MPS results. There is a higher accumulation of points at the corners in the MPS results, which corresponds to a higher value of m_{stag}. Although the distributions spread almost fully to the corners in the 1/3 phase results, for the 2/3 phase the size of the triangle is visibly reduced. This reduction is due to finite-size cluster effects: the boundary is filled with Rydberg excitations, which reduces the maximal possible extent of the distribution to the inner hexagon (dashed lines) (see 'Triangular 2/3 plateau' section). The above results demonstrate the preparation of the 1/3 and 2/3 phases using a synthetic quantum many-body system. Despite the experimental imperfections, and the finite sweep duration, we are able to produce highly ordered states on even the largest 147-atom array. This is highlighted in Fig. 1c, which shows a fluorescence image of the 1/3 phase on the 147-atom array with almost perfect AF ordering. Finally, similar to the square array, we observe an enhanced probability of finding highly ordered states compared with a classical equilibrium system at the same energy, as revealed by experimental order parameter distributions that are centred at larger values (see details in the 'Time evolution versus classical equilibrium on the triangular lattice' section).

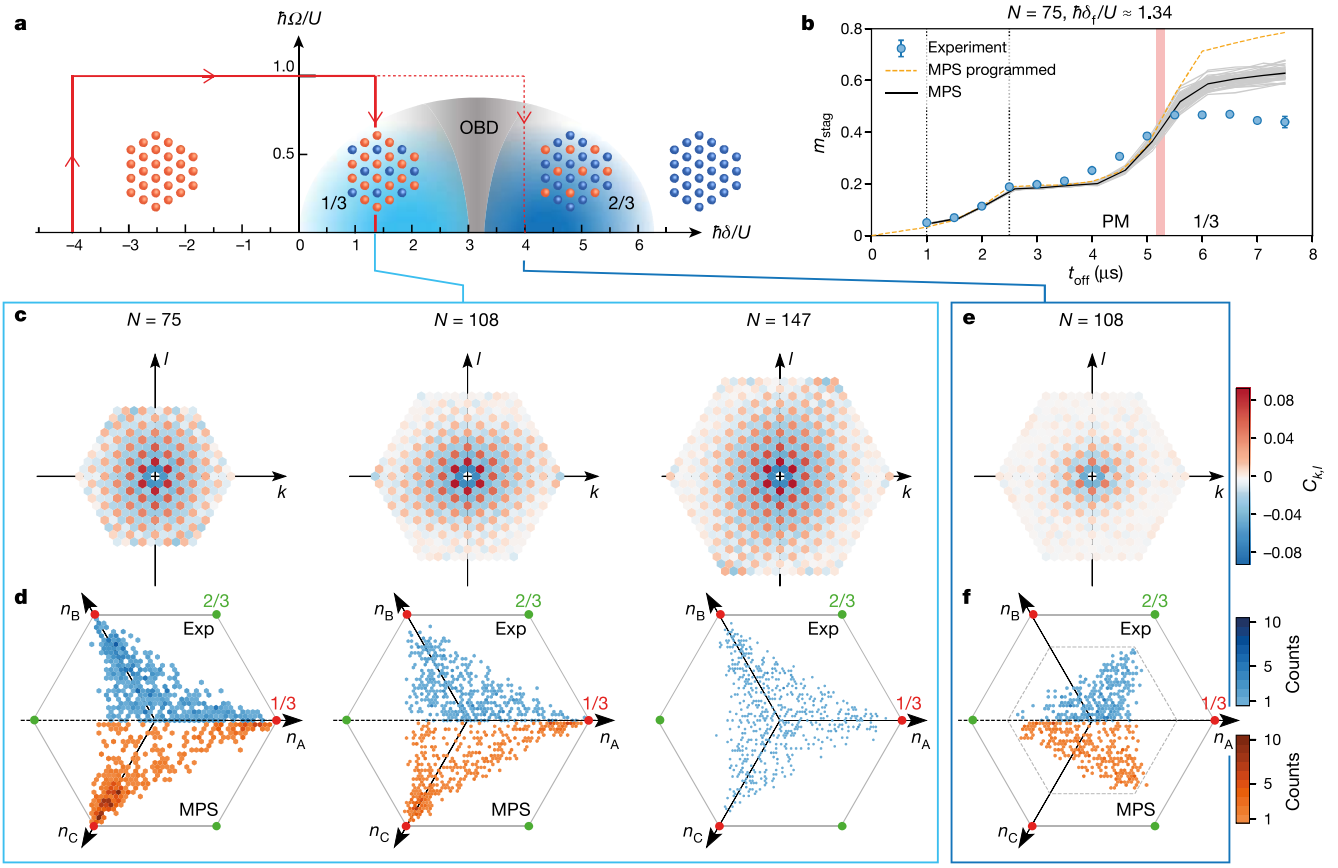

Fig. 4 | AF ordering on a triangular array. a, Sketched bulk phase diagram for the triangular lattice. The red arrows show the sweeps used to prepare the phases at 1/3 and 2/3 filling. **b**, Growth of the staggered magnetization during the sweep for a 75-atom array. The blue circles are experimental results with standard errors on the mean smaller than the markers size. The error bar on the final point is indicative of the long-term stability of the experimental setup (see 'Long-term stability' section). MPS simulations without (dashed line) and with (grey lines) experimental imperfections for which 50 disorder instances are shown, with their average shown in black. The vertical dotted lines correspond to the turning points in the sweep. The vertical red region depicts the finite-size phase boundary between the PM and the 1/3 AF phase phases obtained from density matrix renormalization group. **c**, **d**, Final experimental correlation maps (**c**) and corresponding staggered magnetization histograms plotted in the complex plane (**d**) for the 75-site (left), 108-site (middle) and 147-site (right) triangular arrays for the sweep preparing the 1/3 phase. For the 75-site and 108-site arrays, the lower half of the histograms show the analogous MPS results. **e**, **f**, Final experimental correlation map (**e**) and corresponding staggered magnetization histogram (**f**) for the 108-site triangular array for the sweep preparing the 2/3 phase. The lower half of **f** shows the corresponding MPS results.

Conclusions and outlook

We have probed the quantum dynamics of Ising magnets in square and triangular geometries, beyond situations that can be exactly simulated classically. We have validated the experimental results with comprehensive numerical simulations up to computationally feasible sizes. We have shown a high degree of coherence and control, over a large number of atoms. Combined, this demonstrates that our platform is now able to study quantum spin models in regimes beyond those accessible via numerical investigations. We have also identified a potential advantage of Rydberg quantum simulators to prepare targeted classical states, compared with classical equilibrium systems. Natural extensions of this work include a thorough investigation of the dynamics of the 2D QPT, and further explorations of the effects of frustration, in particular the observation of the elusive OBD phase. Finally, our benchmark provides a roadmap for improving the platform even further, thus opening exciting prospects beyond quantum simulation, for example, for optimization[34,36], quantum sensing[42,43] and quantum computing[44–46].

Independent work exploring other phases and dynamics on a square array with a Rydberg quantum simulator is reported in a companion publication[31].

Online content

Any methods, additional references, Nature Research reporting summaries, source data, extended data, supplementary information, acknowledgements, peer review information; details of author contributions and competing interests; and statements of data and code availability are available at https://doi.org/10.1038/s41586-021-03585-1.

1. Georgescu, I. M., Ashhab, S. & Nori, F. Quantum simulation. *Rev. Mod. Phys.* **86**, 153–185 (2014).
2. Blatt, R. & Roos, C. F. Quantum simulations with trapped ions. *Nat. Phys.* **8**, 277–284 (2012).
3. Monroe, C. et al. Programmable quantum simulations of spin systems with trapped ions. *Rev. Mod. Phys.* **93**, 025001 (2021).
4. Gärttner, M. et al. Measuring out-of-time-order correlations and multiple quantum spectra in a trapped-ion quantum magnet. *Nat. Phys.* **13**, 781–786 (2017).
5. Song, C. et al. 10-qubit entanglement and parallel logic operations with a superconducting circuit. *Phys. Rev. Lett.* **119**, 180511 (2017).
6. King, A. D. et al. Observation of topological phenomena in a programmable lattice of 1,800 qubits. *Nature* **560**, 456–460 (2018).
7. Kjaergaard, M. et al. Superconducting qubits: current state of play. *Annu. Rev. Condens. Matter Phys.* **11**, 369–395 (2020).
8. Bloch, I., Dalibard, J. & Zwerger, W. Many-body physics with ultracold gases. *Rev. Mod. Phys.* **80**, 885–964 (2008).
9. Bloch, I., Dalibard, J. & Nascimbène, S. Quantum simulations with ultracold quantum gases. *Nat. Phys.* **8**, 267–276 (2012).

10. Gross, C. & Bloch, I. Quantum simulations with ultracold atoms in optical lattices. *Science* **357**, 995–1001 (2017).
11. Browaeys, A. & Lahaye, T. Many-body physics with individually controlled Rydberg atoms. *Nat. Phys.* **16**, 132–142 (2020).
12. Yan, B. et al. Observation of dipolar spin-exchange interactions with lattice-confined polar molecules. *Nature* **501**, 521–525 (2013).
13. Zhou, Y. L., Ortner, M. & Rabl, P. Long-range and frustrated spin–spin interactions in crystals of cold polar molecules. *Phys. Rev. A* **84**, 052332 (2011).
14. Bernien, H. et al. Probing many-body dynamics on a 51-atom quantum simulator. *Nature* **551**, 579–584 (2017).
15. Keesling, A. et al. Quantum Kibble–Zurek mechanism and critical dynamics on a programmable Rydberg simulator. *Nature* **568**, 207–211 (2019).
16. Lienhard, V. et al. Observing the space- and time-dependent growth of correlations in dynamically tuned synthetic Ising antiferromagnets. *Phys. Rev. X* **8**, 021070 (2018).
17. Levine, H. et al. Parallel implementation of high-fidelity multiqubit gates with neutral atoms. *Phys. Rev. Lett.* **123**, 170503 (2019).
18. Omran, A. et al. Generation and manipulation of Schrödinger cat states in Rydberg atom arrays. *Science* **365**, 570–574 (2019).
19. Madjarov, I. S. et al. High-fidelity entanglement and detection of alkaline-earth Rydberg atoms. *Nat. Phys.* **16**, 857–861 (2020); correction **17**, 144 (2021).
20. Schauß, P. et al. Crystallization in Ising quantum magnets. *Science* **347**, 1455–1458 (2015).
21. Guardado-Sanchez, E. et al. Probing the quench dynamics of antiferromagnetic correlations in a 2D quantum Ising spin system. *Phys. Rev. X* **8**, 021069 (2018).
22. Song, Y., Kim, M., Hwang, H., Lee, W. & Ahn, J. Quantum simulation of Cayley-tree Ising Hamiltonians with three-dimensional Rydberg atoms. *Phys. Rev. Res.* **3**, 013286 (2021).
23. Wannier, G. H. Antiferromagnetism. The triangular Ising net. *Phys. Rev.* **79**, 357–364 (1950).
24. Jaksch, D. et al. Fast quantum gates for neutral atoms. *Phys. Rev. Lett.* **85**, 2208–2211 (2000).
25. Schymik, K.-N. et al. Enhanced atom-by-atom assembly of arbitrary tweezer arrays. *Phys. Rev. A* **102**, 063107 (2020).
26. Levine, H. et al. High-fidelity control and entanglement of Rydberg-atom qubits. *Phys. Rev. Lett.* **121**, 123603 (2018).
27. Janke, W. & Villanova, R. Three-dimensional 3-state Potts model revisited with new techniques. *Nucl. Phys. B* **489**, 679–696 (1997).
28. Laumann, C. R., Moessner, R., Scardicchio, A. & Sondhi, S. L. Quantum adiabatic algorithm and scaling of gaps at first-order quantum phase transitions. *Phys. Rev. Lett.* **109**, 030502 (2012).
29. Fey, S., Kapfer, S. C. & Schmidt, K. P. Quantum criticality of two-dimensional quantum magnets with long-range interactions. *Phys. Rev. Lett.* **122**, 017203 (2019).
30. Samajdar, R., Ho, W. W., Pichler, H., Lukin, M. D. & Sachdev, S. Complex density wave orders and quantum phase transitions in a model of square-lattice Rydberg atom arrays. *Phys. Rev. Lett.* **124**, 103601 (2020).
31. Ebadi, S. et al. Quantum phases of matter on a 256-atom programmable quantum simulator. *Nature* https://doi.org/10.1038/s41586-021-03582-4 (2021).
32. Stoli, E. & Domb, C. Shape and size of two-dimensional percolation clusters with and without correlations. *J. Phys. A* **12**, 1843–1855 (1979).
33. Kim, H., Park, Y., Kim, K., Sim, H.-S. & Ahn, J. Detailed balance of thermalization dynamics in Rydberg-atom quantum simulators. *Phys. Rev. Lett.* **120**, 180502 (2018).
34. Pichler, H., Wang, S.-T., Zhou, L., Choi, S. & Lukin, M. D. Quantum optimization for maximum independent set using Rydberg atom arrays. Preprint at https://arxiv.org/abs/1808.10816 (2018).
35. Henriet, L. Robustness to spontaneous emission of a variational quantum algorithm. *Phys. Rev. A* **101**, 012335 (2020).
36. Serret, M. F., Marchand, B. & Ayral, T. Solving optimization problems with Rydberg analog quantum computers: realistic requirements for quantum advantage using noisy simulation and classical benchmarks. *Phys. Rev. A* **102**, 052617 (2020).
37. Villain, J., Bidaux, R., Carton, J.-P. & Conte, R. Order as an effect of disorder. *J. Phys. France* **41**, 1263–1272 (1980).
38. Moessner, R., Sondhi, S. L. & Chandra, P. Two-dimensional periodic frustrated Ising models in a transverse field. *Phys. Rev. Lett.* **84**, 4457–4460 (2000).
39. Moessner, R. & Sondhi, S. L. Ising models of quantum frustration. *Phys. Rev. B* **63**, 224401 (2001).
40. Isakov, S. V. & Moessner, R. Interplay of quantum and thermal fluctuations in a frustrated magnet. *Phys. Rev. B* **68**, 104409 (2003).
41. Koziol, J., Fey, S., Kapfer, S. C. & Schmidt, K. P. Quantum criticality of the transverse-field Ising model with long-range interactions on triangular-lattice cylinders. *Phys. Rev. B* **100**, 144411 (2019).
42. Madjarov, I. S. et al. An atomic-array optical clock with single-atom readout. *Phys. Rev. X* **9**, 041052 (2019).
43. Norcia, M. A. et al. Seconds-scale coherence on an optical clock transition in a tweezer array. *Science* **366**, 93–97 (2019).
44. Saffman, M., Walker, T. G. & Mølmer, K. Quantum information with Rydberg atoms. *Rev. Mod. Phys.* **82**, 2313–2363 (2010).
45. Henriet, L. et al. Quantum computing with neutral atoms. *Quantum* **4**, 327 (2020).
46. Morgado, M. & Whitlock, S. Quantum simulation and computing with Rydberg qubits. *AVS Quantum Sci.* **3**, 023501 (2021).

Appendix G

Résumé en Français

Au cours des dernières décennies, la capacité à manipuler des systèmes quantiques individuels s'est améliorée à un rythme rapide, ce qui amène de nombreux chercheurs à penser que nous sommes à l'aube d'une deuxième révolution quantique. Plusieurs nouvelles technologies quantiques, qui utilisent des propriétés quantiques individuels pour obtenir un avantage sur leurs homologues classiques, ont été développées ces dernières années et leur industrialisation a permis de réaliser des percées dans divers domaines. Ces technologies reposent sur le contrôle précis d'objets quantiques uniques qui peuvent être mis en œuvre dans une variété de systèmes physiques, des particules uniques aux dispositifs à de physique du solide. En outre, elles trouvent des applications dans différents domaines qui peuvent être classés dans les catégories suivantes : détection et métrologie quantiques, communication quantique, informatique quantique et simulation quantique.

Les systèmes quantiques sont très sensibles aux perturbations de leur environnement, une caractéristique qui est exploitée pour construire des capteurs quantiques. Par exemple, les centres NV dans le diamant sont des systèmes solide dont le spin électronique est sensible aux perturbations externes telles que la déformation, les champs électriques ou magnétiques. Leur petite taille rend ces capteurs particulièrement intéressants pour les applications industrielles.

La sensibilité des systèmes quantiques peut également être utilisée pour la communication sécurisée. En utilisant les propriétés quantiques des photons, les données peuvent être transférées de manière sécurisée. Le domaine de la communication quantique s'efforce d'étendre cette recherche d'un environnement de laboratoire à une échelle industrielle, et ces dernières années, une distribution de clés quantiques entre un satellite et la Terre sur une distance de 1200 km a été démontrée.

Même si les lois fondamentales de la physique quantique sont bien connues, de nombreuses questions ouvertes se posent dans les systèmes fortement corrélés avec un nombre de particules plus important. En présence de fortes interactions entre les particules quantiques, l'étude numérique de ces systèmes est difficile. Par exemple, si l'on enregistre la fonction d'onde d'un système de N particules de spin-1/2 dans la

mémoire d'un ordinateur, les données nécessaires augmentent de manière exponentielle, atteignant plusieurs milliers de téraoctets de données pour seulement 50 particules. Comme l'a suggéré Feynman, il est plus pratique d'utiliser un autre système quantique contrôlable pour simuler un modèle de mécanique quantique. Un tel simulateur quantique n'aurait besoin que de N qubits pour stocker la fonction d'onde complète d'un système à N particules.

La simulation quantique pourrait être mise en œuvre à l'aide d'un ordinateur quantique, un outil général qui peut simuler une grande classe d'Hamiltoniens. Il repose sur le fait que toute opération unitaire peut être décomposée en portes quantiques universelles. Comme un grand nombre de ces portes doivent être appliquées à la suite les unes des autres, des fidélités très élevées sont nécessaires. Cependant, même avec des probabilités d'erreur finies par porte, il est possible de construire des architectures tolérantes aux erreurs avec des codes de correction d'erreurs quantiques, lorsque l'erreur par porte est inférieure à un certain seuil. Cela nécessite des ressources importantes: les codes de correction d'erreurs quantiques combinent de nombreux qubits physiques avec une erreur par porte finie pour obtenir un qubit logique. Cette exigence en matière de ressources est difficile à satisfaire, ce qui souligne la nécessité d'une plateforme à plusieurs qubits avec de faibles erreurs de porte. Actuellement, les plates-formes fonctionnent dans le régime NISQ (¡¡ noisy intermediate scale quantum era ¿¿), où les fidélités et les tailles de système sont trop petites pour obtenir une tolérance aux erreurs avec de nombreux qubits. L'un des principaux défis de ces plates-formes consiste à augmenter le nombre de qubits tout en maintenant des fidélités élevées.

Une autre approche de la simulation quantique, à plus court terme, est la simulation quantique analogique. Si l'Hamiltonien d'un modèle d'un système quantique peut être mis en correspondance avec un système de simulation, le simulateur peut être utilisé pour produire des propriétés intéressantes, comme les fonctions de corrélation ou l'état fondamental. Même si le simulateur peut être limité à une classe d'Hamiltoniens, il peut être beaucoup plus tolérant aux erreurs qu'un simulateur quantique universel.

Dans ce manuscrit, je décris un tel simulateur quantique analogique basé sur des atomes de rubidium, piégés dans des pinces optiques, qui sont excités vers des états de Rydberg. En combinant les géométries programmables des réseaux de pinces avec les interactions dues à l'excitation de Rydberg, notre plateforme est capable de simuler des modèles de matière condensée emblématiques du magnétisme quantique, tels que le modèle d'Ising et le modèle XY.

Le dispositif experimental à l'état de l'art construit de notre groupe est cependant limitée en termes d'augmentations des particules, la plus grande géométrie assemblée

avant mon doctorat étant de 72 atomes. Cette limitation est due à deux échelles de temps concurrentes : Premièrement, un certain temps, appelé temps d'assemblage, est nécessaire pour assembler une structure à N atomes, et varie linéairement avec N. Deuxièmement, la durée de vie d'un atome dans la pince est de 20 s et limitée par le vide, car les collisions avec le gaz entraînent des pertes d'atomes. La durée de vie d'un réseau de N atomes est inversement proportionnelle à N. En raison de ces deux échelles de temps, la probabilité d'assembler un réseau sans défaut de plus de 300 atomes sur notre expérience à température ambiante est d'environ 1 %.

Dans ce manuscrit, je décris le travail effectué pour lever ces deux principales limitations afin de réaliser de grands réseaux d'atomes sans défaut avec une grande fidélité. Dans le chapitre 3, je décris un nouveau cadre algorithmique, qui a un temps de calcul rapide et nécessite moins de mouvements élémentaires pendant le processus d'assemblage, conduisant à l'assemblage d'un réseau de 196 atomes sur notre installation à température ambiante. Nous construisons ensuite un nouveau dispositif expérimental cryogénique, décrit en détail dans le chapitre 4. Dans un environnement cryogénique, les expériences bénéficient d'une pression de vapeur totale considérablement réduite. Le gaz résiduel ¡¡ gèle ¿¿ lorsqu'il entre en contact avec une surface à des températures cryogéniques — un effet appelé cryopompage — et ne se désorbe pas. À des températures de 4 K, tous les gaz sont condensés ou gelés. En conséquence, la durée de vie d'un atome de rubidium dans la pince est de plus de 6000 s , soit une amélioration de 300 fois par rapport à notre expérience à température ambiante.

Chapitre 2

Dans ce chapitre, je présente le simulateur quantique Rydberg existant dans notre groupe. Tout d'abord, je décris le piégeage d'atomes de Rubidium dans des pinces optiques et l'utilisation d'un modulateur spatial de lumière pour créer des géométries de piège arbitraires en plusieurs dimensions. Je décris ensuite tous les outils expérimentaux nécessaires pour créer des matrices d'atomes sans défaut. Je présente une amélioration du processus d'assemblage que j'ai réalisée en modifiant le contrôle de la radio-fréquence utilisée pour les déflecteurs acousto-optiques. En outre, j'explique comment nous utilisons cette plateforme pour la simulation quantique de modèles de spin et je souligne notre mise en œuvre d'un nouveau schéma d'excitation Rydberg. Enfin, je présente plusieurs limites de cette expérience en termes d'augmentation du nombre d'atomes impliqués dans les simulations quantiques, notamment la durée de vie limitée

des atomes dans la pince, le temps d'assemblage et les aberrations optiques dues au champ limité des lentilles asphériques utilisées.

Chapitre 3

Le temps d'assemblage est une échelle de temps limitante pour la création de grands réseaux sans défaut. Dans ce chapitre, je présente un nouveau cadre algorithmique pour le processus d'assemblage qui nous a permis de réduire considérablement le temps d'assemblage et d'atteindre des nombres d'atomes sans précédent sur notre installation à température ambiante. Cela démontre les capacités de notre plateforme à réaliser des simulations quantiques à grande échelle pour répondre à des questions ouvertes en physique à N corps.

Tout d'abord, je définis le problème à résoudre : trouver un algorithme qui retourne le temps d'assemblage total le plus petit possible, y compris le temps de calcul de l'algorithme lui-même et le temps nécessaire pour déplacer tous les atomes de manière séquentielle. Ensuite, je détaille nos contraintes expérimentales, et montre que le problème est lié à un problème d'optimisation dit LSAP (¡¡ linear sum assignment problem ¿¿) dans un cas particulier. En général, cependant, l'ordre de la séquence des déplacements est crucial, ce qui souligne la nécessité de développer de nouveaux algorithmes. Nous trouvons qu'après avoir pris en compte nos contraintes expérimentales, le problème en question est similaire à un problème bien connu en informatique, le problème du mouvement des cailloux sur un graphe, qui est intractable pour un grand nombre d'atomes. Il est donc impossible de calculer le nombre optimal de mouvements à l'échelle de temps expérimentale et nous optons donc pour des algorithmes heuristiques.

Je décris trois nouveaux algorithmes qui améliorent l'efficacité de l'assemblage en réduisant considérablement le nombre de mouvements par rapport à l'algorithme utilisé précédemment. Combiné avec l'exécution de plusieurs cycles d'assemblage, cela nous permet de préparer des matrices d'atomes sans défaut, jusqu'à 200 atomes, avec des fidélités non négligeables.

Grâce à une nouvelle approche basée sur les graphes, les algorithmes sont étendus à des structures non régulières qui ne peuvent être représentées sur un réseau de Bravais. Cette approche ouvre la voie à de nouvelles expériences intéressantes, comme l'étude de l'effet des défauts cristallins dans les matériaux magnétiques ou le problème d'optimisation consistant à trouver la taille maximum d'un ensemble indépendant d'un graphe.

Chapitre 4

Dans ce chapitre, je présente la conception et la caractérisation d'une nouvelle plateforme cryogénique de pinces optiques pour la simulation quantique à grande échelle.

Tout d'abord, je donne un aperçu de la nouvelle plateforme cryogénique qui partage certaines caractéristiques principales avec notre expérience à température ambiante : Une source atomique, et une chambre de science avec des lentilles asphériques et des bobines de champ magnétique, pour charger des atomes uniques dans les pièges. Cependant, la conception de la chambre est fortement modifiée en raison du défi expérimental que représente le refroidissement des principales parties à 4 K.

Après avoir illustré la conception du cryostat à ultravide à l'aide d'un tube pulsé, je détaille nos solutions aux défis expérimentaux qui impliquent la contraction thermique, la conduction thermique et la résistivité électrique.

Enfin, je démontre dans une série de tests que la nouvelle plateforme parvient effectivement à maintenir de basses températures avec toutes les charges thermiques présentes dans une expérience avec de grands réseaux de pinces. La grande vitesse de pompage des surfaces à 4 K près des atomes conduit effectivement à un vide de plusieurs ordres de grandeur inférieur à celui de notre installation à température ambiante, comme nous voyons dans le chapitre 5, ce qui permet d'obtenir des durées de vie de piégeage limitées par le vide d'atomes uniques dans les pinces optiques de plus de 6000 s.

Chapitre 5

Dans ce chapitre, je démontre le piégeage d'atomes uniques de Rubidium dans un environnement cryogénique à 4 K avec des durées de vie de piégeage dépassant 6000 s. Ce résultat très prometteur ouvre la voie au passage à l'échelle de la plateforme des pinces optiques pour la simulation quantique à grande échelle.

Tout d'abord, je détaille le système laser utilisé pour piéger un nuage d'atomes de Rubidium dans un piège magnéto-optique (PMO) et la mesure de la durée de vie des atomes dans le PMO. Ensuite, nous piégeons des atomes dans des pinces optiques et mesurons une durée de vie d'environ 6300 s, soit une amélioration de 300 fois par rapport à notre installation à température ambiante.

Pour mesurer la durée de vie, nous avons analysé en détail les différents mécanismes

de perte, et trouvé un protocole de mesure robuste contre ces pertes. Tout d'abord, les collisions entre les atomes de la région du four et les atomes de la pince optique peuvent entraîner des pertes importantes. Pour les supprimer, nous fermons la vanne entre la source atomique et la chambre de science pendant la mesure à l'aide d'un actionneur maison contrôlé par ordinateur. En outre, l'échauffement dû à la diffusion non-résonante de la lumière laser du piège entraîne des pertes, ce qui nécessite un refroidissement laser pendant la mesure. Cependant, comme nous trouvons également des pertes dues à la lumière d'imagerie, nous utilisons finalement un schéma de refroidissement laser pulsé pendant la mesure.

Chapitre 6

Dans ce chapitre, j'illustre les progrès au moment de la rédaction du présent rapport de l'expérience visant à résoudre les imperfections techniques afin d'assembler de grands réseaux d'atomes. Ces imperfections techniques ont été analysées au cours de cette thèse et sont (i) l'égalisation imparfaite de la profondeur des pièges, (ii) la diminution de l'efficacité de l'assemblage pour les grands réseaux, et (iii) la probabilité finie de survie des atomes pendant l'imagerie de fluorescence. Une fois ces imperfections résolues, nous pourrons profiter pleinement de la durée de vie prolongée du vide de la configuration cryogénique et devrions être en mesure d'assembler jusqu'à 500 atomes.

Ce chapitre se concentre principalement sur l'égalisation de la profondeur des pièges. Je présente d'abord les problèmes de la méthode actuelle qui utilise une caméra CCD pour estimer la profondeur des pièges. Ensuite, j'analyse si nous pouvons obtenir des estimations plus fiables de la profondeur du piège à partir de la trace de fluorescence. Je constate que nous pouvons estimer la profondeur du piège en mesurant la diminution du taux de diffusion pour un décalage lumineux croissant. De plus, la profondeur du piège peut être estimée à partir du changement de la probabilité de chargement en fonction de la profondeur du piège. Je propose ensuite deux nouvelles méthodes qui utilisent cette nouvelle métrique. Le grand avantage des méthodes proposées est qu'elles ne nécessitent que des outils simples pour estimer la profondeur des pièges.

Bibliography

Aharonov, D. and Ben-Or, M., *"Fault-tolerant quantum computation with constant error rate,"* SIAM J. Comput. **38**, 1207 (1999) [cited in page 12].

Alberti, A., Robens, C., Alt, W., Brakhane, S., Karski, M., Reimann, R., Widera, A., and Meschede, D., *"Super-resolution microscopy of single atoms in optical lattices,"* New Journal of Physics **18**, 053010 (2016) [cited in page 125].

Alexeev, Y., Bacon, D., Brown, K. R., Calderbank, R., Carr, L. D., Chong, F. T., DeMarco, B., Englund, D., Farhi, E., Fefferman, B., Gorshkov, A. V., Houck, A., Kim, J., Kimmel, S., Lange, M., Lloyd, S., Lukin, M. D., Maslov, D., Maunz, P., Monroe, C., Preskill, J., Roetteler, M., Savage, M. J., and Thompson, J., *"Quantum computer systems for scientific discovery,"* PRX Quantum **2**, 017001 (2021) [cited in page 15].

Aliyu, M. M., Zhao, L., Quek, X. Q., Yellapragada, K. C., and Loh, H., *"D1 magic wavelength tweezers for scaling atom arrays,"* (2021), arXiv:2105.15047 [physics.atom-ph] [cited in page 134].

Arute, F., Arya, K., and Babbush, R. e. a., *"Quantum supremacy using a programmable superconducting processor,"* Nature **574**, 505–510 (2019) [cited in pages 12 and 17].

Ashkin, A., *"Acceleration and trapping of particles by radiation pressure,"* Phys. Rev. Lett. **24**, 156 (1970) [cited in page 22].

Aspect, A., Grangier, P., and Roger, G., *"Experimental realization of Einstein-Podolsky-Rosen-Bohm Gedankenexperiment: A new violation of Bell's inequalities,"* Physical Review Letters **49**, 91 (1982) [cited in page 11].

Bakr, W. S., Gillen, J. I., Peng, A., Fölling, S., and Greiner, M., *"A quantum gas microscope for detecting single atoms in a Hubbard-regime optical lattice,"* Nature **462**, 74 (2009) [cited in page 14].

Balasubramanian, G., Chan, I., Kolesov, R., Al-Hmoud, M., Tisler, J., Shin, C., Kim, C., Wojcik, A., Hemmer, P., Krueger, A., Hanke, T., Leitenstorfer, A., Bratschitsch, R., Jelezko, F., and Wrachtrup, J., *"Nanoscale imaging magnetometry with diamond spins under ambient conditions,"* Nature **445**, 648–651 (2008) [cited in page 11].

Bali, S., O'Hara, K. M., Gehm, M. E., Granade, S. R., and Thomas, J. E., *"Quantum-diffractive background gas collisions in atom-trap heating and loss,"* Phys. Rev. A **60**, R29 (1999) [cited in page 137].

Ball, P., *"First quantum computer to pack 100 qubits enters crowded race,"* Nature **599**, 542 (2021) [cited in page 14].

Barnes, K., Battaglino, P., Bloom, B. J., Cassella, K., Coxe, R., Crisosto, N., King, J. P., Kondov, S. S., Kotru, K., Larsen, S. C., Lauigan, J., Lester, B. J., McDonald, M., Megidish, E., Narayanaswami, S., Nishiguchi, C., Notermans, R., Peng, L. S., Ryou, A., Wu, T.-Y., and Yarwood, M., *"Assembly and coherent control of a register of nuclear spin qubits,"* (2021), arXiv:2108.04790 [quant-ph] [cited in page 133].

Barredo, D., Labuhn, H., Ravets, S., Lahaye, T., Browaeys, A., and Adams, C. S., *"Coherent excitation transfer in a spin chain of three Rydberg atoms,"* Physical Review Letters **114**, 113002 (2015) [cited in page 15].

Barredo, D., de Léséleuc, S., Lienhard, V., Lahaye, T., and Browaeys, A., *"An atom-by-atom assembler of defect-free arbitrary two-dimensional atomic arrays,"* Science **354**, 1021 (2016) [cited in pages 19, 28, 32, 41, 45, 55, 59, 63, 64, 129, and 131].

Barredo, D., Lienhard, V., de Léséleuc, S., Lahaye, T., and Browaeys, A., *"Synthetic three-dimensional atomic structures assembled atom by atom,"* Nature **561**, 79 (2018) [cited in pages 25, 28, 131, and 133].

Barredo, D., Lienhard, V., Scholl, P., de Léséleuc, S., Boulier, T., Browaeys, A., and Lahaye, T., *"Three-dimensional trapping of individual Rydberg atoms in ponderomotive bottle beam traps,"* Phys. Rev. Lett. **124**, 023201 (2020) [cited in page 134].

Barredo, D., Ravets, S., Labuhn, H., Béguin, L., Vernier, A., Nogrette, F., Lahaye, T., and Browaeys, A., *"Demonstration of a strong Rydberg blockade in three-atom systems with anisotropic interactions,"* Phys. Rev. Lett. **112**, 183002 (2014) [cited in page 16].

Béguin, L., Measurement of the van der Waals interaction between two Rydberg atoms, Ph.D. thesis, Université Paris-Saclay (2013) [cited in pages 21, 23, 43, 44, and 134].

Bennett, C., Bessette, F., Gilles, B., Louis, S., and Smolin, J., *"Experimental quantum cryptography,"* Journal of Cryptology **5**, 3 (1992) [cited in page 11].

Bennett, C. and Brassard, G., *"Quantum cryptography: public key distribution and coin tossing,"* in Proceedings of IEEE International Conference on Computers Systems and Signal Processing (1984) p. 175 [cited in page 11].

Benvenuti, C., *"Characteristics, advantages, and possible applications of condensation cryopumping,"* Journal of Vacuum Science and Technology **1**, 591 (1974) [cited in pages 18 and 69].

Bergschneider, A., Klinkhamer, V. M., Becher, J. H., Klemt, R., Zürn, G., Preiss, P. M., and Jochim, S., *"Spin-resolved single-atom imaging of* ^{6}Li *in free space,"* Physical Review A **97**, 063613 (2018) [cited in page 125].

Bernien, H., Schwartz, S., Keesling, A., Levine, H., Omran, A., Pichler, H., Choi, S., Zibrov, A. S., Endres, M., Greiner, M., Vuletić, V., and Lukin, M. D., *"Probing many-body dynamics on a 51-atom quantum simulator,"* Nature **551**, 579 (2017) [cited in pages 15, 16, 17, and 34].

Bernon, S., Hattermann, H., Bothner, D., Knufinke, M., Weiss, P., Jessen, F., Cano, D., Kemmler, M., Kleiner, R., Koelle, D., and Fortágh, J., *"Manipulation and coherence of ultra-cold atoms on a superconducting atom chip,"* Nature Communications **4**, 2380 (2013) [cited in pages 18 and 70].

Beterov, I. I., Ryabtsev, I. I., Tretyakov, D. B., and Entin, V. M., *"Quasiclassical calculations of blackbody-radiation-induced depopulation rates and effective lifetimes of Rydberg ns, np, and nd alkali-metal atoms with* $n \leq 80$*,"* Phys. Rev. A **79**, 052504 (2009) [cited in page 18].

Blatt, R., *"Quantum simulations with long strings of trapped ions,"* URL: https://quantumoptics.at/en/research/quiqs.html, accessed on: January 20, 2022 [cited in page 16].

Blatt, R. and Roos, C., *"Quantum simulations with trapped ions,"* Nature Physics **8**, 277 (2012) [cited in page 13].

Bloch, I., Dalibard, J., and Nascimbène, S., *"Quantum simulations with ultracold quantum gases,"* Nature Physics **8**, 267 (2012) [cited in page 13].

Bloch, I., Dalibard, J., and Zwerger, W., *"Many-body physics with ultracold gases,"* Review of Modern Physics **80**, 885 (2008) [cited in page 14].

Bluvstein, D., Levine, H., Semeghini, G., Wang, T. T., Ebadi, S., Kalinowski, M., Keesling, A., Maskara, N., Pichler, H., Greiner, M., Vuletic, V., and Lukin, M. D., *"A quantum processor based on coherent transport of entangled atom arrays,"* (2021), arXiv:2112.03923 [quant-ph] [cited in pages 15 and 133].

Browaeys, A. and Lahaye, T., *"Many-body physics with individually controlled Rydberg atoms,"* Nature Physics **16**, 132 (2020) [cited in pages 13 and 33].

Brown, M. O., Thiele, T., Kiehl, C., Hsu, T.-W., and Regal, C. A., *"Gray-molasses optical-tweezer loading: Controlling collisions for scaling atom-array assembly,"* Phys. Rev. X **9**, 011057 (2019) [cited in pages 28 and 134].

Călinescu, G., Dumitrescu, A., and Pach, J., *"Reconfigurations in graphs and grids,"* in in: Proc. LATIN '06 (Latin American Theoretical INformatics conference), Lecture Notes in Computer Science 3887 (Springer, 2006) pp. 262–273 [cited in page 49].

Cohen, S. R. and Thompson, J. D., *"Quantum computing with circular Rydberg atoms,"* PRX Quantum **2** (2021), 10.1103/prxquantum.2.030322 [cited in page 19].

Cormen, T., Leiserson, C., Rivet, R., and Stein, C., Introduction to Algorithms, 2nd ed. (The MIT Press, 2001) [cited in page 49].

Covey, J. P., Madjarov, I. S., Cooper, A., and Endres, M., *"2000-times repeated imaging of strontium atoms in clock-magic tweezer arrays,"* Phys. Rev. Lett. **122**, 173201 (2019) [cited in page 129].

Crouse, D. F., *"On implementing 2d rectangular assignment algorithms,"* IEEE Transactions on Aerospace and Electronic Systems **52**, 1679 (2016) [cited in page 49].

Darquié, B., MANIPULATION D'ATOMES DANS DES PIÈGES DIPOLAIRES MICROSCOPIQUES ET ÉMISSION CONTRÔLÉE DE PHOTONS PAR UN ATOME UNIQUE, Theses, Université Paris Sud - Paris XI (2005) [cited in page 99].

Di Leonardo, R., Ianni, F., and Ruocco, G., *"Computer generation of optimal holograms for optical trap arrays,"* Optics Express **15**, 1913 (2007) [cited in pages 25 and 26].

Diederich, M., Häffner, H., Hermanspahn, N., Immel, M., Kluge, H., Ley, R., Mann, R., Quint, W., Stahl, S., and Werth, G., *"Observing a single hydrogen-like ion in a penning trap at t = 4 k,"* Hyperfine Interactions **115**, 185 (1998) [cited in pages 18 and 69].

Dietsche, E., Larrouy, A., Haroche,, S.,, Raimond, J., Brune, M., and Gleiyzes, S., *"High-sensitivity magnetometry with a single atom in a superposition of two circular rydberg states."* Nature Physics **15**, 326 (2019) [cited in page 14].

Ebadi, S., T., W., Levine, H., Keesling, A., Semeghini, G., Omran, A., Bluvstein, D., Samajdar, R., Pichler, H., Ho, W., Choi, S., Sachdev, S., Greiner, M., Vluetic, V., and Lukin, M., *"Quantum phases of matter on a 256-atom programmable quantum simulator,"* Nature **595**, 227 (2021) [cited in pages 16, 34, 41, and 61].

Eckel, S., Lee, J., Jendrzejewski, F., Murray, N., Clark, C., Lobb, C., Phillips, W., Edwards, M., and Campbell, G., *"Hysteresis in a quantized superfluid 'atomtronic' circuit."* Nature **506**, 200 (2014) [cited in page 13].

Egan, L., Debroy, D., Noel, C., Risinger, A., Zhu, D., Biswas, D., Newman, M., Li, M., Brown, K., Cetina, M., and Monroe, C., *"Fault-tolerant control of an error-corrected qubit,"* Nature **598**, 281 (2021) [cited in page 14].

Einstein, A., Podolsky, B., and Rosen, N., *"Can quantum-mechanical description of physical reality be considered complete?"* Phys. Rev. **47**, 777 (1935) [cited in page 11].

Ekin, J. W., Experimental Techniques for Low-Temperature Measurements (Oxford University Press (Oxford), 2006) [cited in pages 78, 80, 81, 82, 84, 86, and 89].

Endres, M., Bernien, H., Keesling, A., Levine, H., Anschuetz, E. R., Krajenbrink, A., Senko, C., Vuletic, V., Greiner, M., and Lukin, M. D., *"Atom-by-atom assembly of defect-free one-dimensional cold atom arrays,"* Science **354**, 1024 (2016) [cited in pages 28, 41, 117, and 120].

Feldman, S., *"20 years of quantum computing growth,"* (2019), url: https://www.statista.com/chart/17896/quantum-computing-developments, accessed on: January 20, 2022 [cited in page 16].

Feynman, R., *"Simulating physics with computers,"* International Journal of Theoretical Physics **21**, 467 (1982) [cited in page 12].

Fuhrmanek, A., Bourgain, R., Sortais, Y. R. P., and Browaeys, A., *"Light-assisted collisions between a few cold atoms in a microscopic dipole trap,"* Phys. Rev. A **85**, 062708 (2012) [cited in page 24].

Gabrielse, G., Fei, X., Orozco, L. A., Tjoelker, R. L., Haas, J., Kalinowsky, H., Trainor, T. A., and Kells, W., *"Thousandfold improvement in the measured antiproton mass,"* Phys. Rev. Lett. **65**, 1317 (1990) [cited in pages 18 and 69].

Gaebler, J. P., Tan, T. R., Lin, Y., Wan, Y., Bowler, R., Keith, A. C., Glancy, S., Coakley, K., Knill, E., Leibfried, D., and Wineland, D. J., *"High-fidelity universal gate set for $^{9}Be^{+}$ ion qubits,"* Phys. Rev. Lett. **117**, 060505 (2016) [cited in page 14].

Georgescu, I. M., Ashhab, S., and Nori, F., *"Quantum simulation,"* Review of Modern Physics **86**, 153 (2014) [cited in page 13].

Gibney, E., *"First quantum computer to pack 100 qubits enters crowded race,"* Nature **574**, 461 (2019) [cited in page 16].

Glaser, C., Karlewski, F., Kluge, J., Grimmel, J., Kaiser, M., Günther, A., Hattermann, H., Krutzik, M., and Fortágh, J., *"Absolute frequency measurement of Rubidium $5s-6p$ transitions,"* Phys. Rev. A **102**, 012804 (2020) [cited in page 36].

Gottesman, D., Stabilizer Codes and Quantum Error Correction, Ph.D. thesis (1997) [cited in pages 12 and 13].

Gould, T. and Bučko, T., *"C_6 coefficients and dipole polarizabilities for all atoms and many ions in rows 1–6 of the periodic table,"* Journal of Chemical Theory and Computation **12**, 3603–3613 (2016) [cited in page 140].

Graham, T. M., Kwon, M., Grinkemeyer, B., Marra, Z., Jiang, X., Lichtman, M. T., Sun, Y., Ebert, M., and Saffman, M., *"Rydberg-mediated entanglement in a two-dimensional neutral atom qubit array,"* Phys. Rev. Lett. **123**, 230501 (2019) [cited in page 15].

Graham, T. M., Song, Y., Scott, J., Poole, C., Phuttitarn, L., Jooya, K., Eichler, P., Jiang, X., Marra, A., Grinkemeyer, B., Kwon, M., Ebert, M., Cherek, J., Lichtman, M. T., Gillette, M., Gilbert, J., Bowman, D., Ballance, T., Campbell, C., Dahl, E. D., Crawford, O., Noel, T., and Saffman, M., *"Demonstration of multi-qubit entanglement and algorithms on a programmable neutral atom quantum computer,"* (2021), arXiv:2112.14589 [quant-ph] [cited in pages 15, 38, and 133].

Greiner, M., Mandel, O., Esslinger, T., Hänsch, T. W., and Bloch, I., *"Quantum phase transition from a superfluid to a Mott insulator in a gas of ultracold atoms,"* Nature **415**, 39 (2012) [cited in page 14].

Grimm, R., Weidemüller, M., and Ovchinnikov, Y. B., *"Optical dipole traps for neutral atoms,"* (Academic Press, 2000) [cited in pages 22 and 99].

Grünzweig, T., Hilliard, a., McGovern, M., and Andersen, M. F., *"Near-deterministic preparation of a single atom in an optical microtrap,"* Nature Physics **6**, 951 (2010) [cited in page 28].

Guo, Y., Dubessy, R., de Herve, M. d. G., Kumar, A., Badr, T., Perrin, A., Longchambon, L., and Perrin, H., *"Supersonic rotation of a superfluid: A long-lived dynamical ring,"* Phys. Rev. Lett. **124**, 025301 (2020) [cited in page 13].

Haeun, S., Yunheung, S., Andrew, B., J., H., and Jaewook, A., *"Imaging three-dimensional single-atom arrays all at once,"* Opt. Express **29**, 4082 (2021) [cited in page 134].

Hagberg, A., Swart, P., and S Chult, D., *"Exploring network structure, dynamics, and function using networkx,"* Tech. Rep. (Los Alamos National Lab.(LANL), Los Alamos, NM (United States), 2008) [cited in page 57].

Haroche, S., *"Nobel lecture: Controlling photons in a box and exploring the quantum to classical boundary,"* Rev. Mod. Phys. **85**, 1083 (2013) [cited in page 11].

Henriet, L., *"Robustness to spontaneous emission of a variational quantum algorithm,"* Physical Review A **101**, 012335 (2020) [cited in pages 55 and 131].

Henriet, L., Beguin, L., Signoles, A., Lahaye, T., Browaeys, A., Reymond, G.-O., and Jurczak, C., *"Quantum computing with neutral atoms,"* Quantum **4**, 327 (2020) [cited in page 133].

Henry, L.-P., Thabet, S., Dalyac, C., and Henriet, L., *"Quantum evolution kernel: Machine learning on graphs with programmable arrays of qubits,"* Physical Review A **104** (2021), 10.1103/physreva.104.032416 [cited in page 131].

Häffner, H., Hänsel, W., Roos, C., Benhelm, J., Chek-al kar, D., Chwalla, M., Körber, T., Rapol, U., Riebe, M., Schmidt, P., Becher, C., Gühne, O., Dür, W., and Blatt, R., *"Scalable multiparticle entanglement of trapped ions,"* Nature **438**, 643 (2005) [cited in page 16].

Houck, A. A., Türeci, H. E., and Koch, J., *"On-chip quantum simulation with superconducting circuits,"* Nature Phys. **8**, 292 (2012) [cited in page 13].

Hulet, R. G. and Kleppner, D., *"Rydberg atoms in "circular" states,"* Phys. Rev. Lett. **51**, 1430 (1983) [cited in page 19].

Isenhower, L., Urban, E., Zhang, X. L., Gill, A. T., Henage, T., Johnson, T. A., Walker, T. G., and Saffman, M., *"Demonstration of a neutral atom controlled-not quantum gate,"* Phys. Rev. Lett. **104**, 010503 (2010) [cited in pages 14 and 16].

Jaksch, D., Bruder, C., Cirac, J. I., Gardiner, C. W., and Zoller, P., *"Cold bosonic atoms in optical lattices,"* Phys. Rev. Lett. **81**, 3108 (1998) [cited in page 13].

Jenkins, A., Lis, J. W., Senoo, A., McGrew, W. F., and Kaufman, A. M., *"Ytterbium nuclear-spin qubits in an optical tweezer array,"* (2021), arXiv:2112.06732 [physics.atom-ph] [cited in pages 28, 117, 120, and 134].

Jiang, N., Lindemann, U., Giebeler, F., and Thummes, G., *"A ^{3}He pulse tube cooler operating down to 1.3* K*,"* Cryogenics **44**, 809 (2004) [cited in page 74].

Jurcevic, P., Javadi-Abhari, A., Bishop, L. S., Lauer, I., Bogorin, D. F., Brink, M., Capelluto, L., Günlük, O., Itoko, T., Kanazawa, N., Kandala, A., Keefe, G. A., Krsulich, K., Landers, W., Lewandowski, E. P., McClure, D. T., Nannicini, G., Narasgond, A., Nayfeh, H. M., Pritchett, E., Rothwell, M. B., Srinivasan, S., Sundaresan, N., Wang, C., Wei, K. X., Wood, C. J., Yau, J.-B., Zhang, E. J., Dial, O. E., Chow, J. M., and Gambetta, J. M., *"Demonstration of quantum volume 64 on a superconducting quantum computing system,"* Quantum Science and Technology **6**, 025020 (2021) [cited in page 14].

Kim, H., Lee, W., Lee, H., Jo, H., Song, Y., and Ahn, J., *"In situ single-atom array synthesis using dynamic holographic optical tweezers,"* Nature Communications **7**, 13317 (2016) [cited in pages 28 and 41].

Kim, M., Song, Y., Kim, J., and Ahn, J., *"Quantum Ising Hamiltonian programming in trio, quartet, and sextet qubit systems,"* PRX Quantum **1**, 020323 (2020) [cited in pages 15 and 34].

Kitaev, A., *"Quantum computations: algorithms and error correction,"* Russian Math. Surveys **52**, 1191 (1997) [cited in page 12].

Knill, E., *"Quantum computing with realistically noisy devices,"* Nature **434**, 39 (2005) [cited in pages 12 and 13].

Knill, E., Laflamme, R., and Zurek, W. H., *"Resilient quantum computation,"* Science **279**, 342 (1998) [cited in page 12].

Labuhn, H., Rydberg excitation dynamics and correlations in arbitrary 2D arrays of single atoms, Ph.D. thesis, Université Paris-Saclay (2016) [cited in pages 25, 26, and 27].

Labuhn, H., Barredo, D., Ravets, S., de Léséleuc, S., Macrì, T., Lahaye, T., and Browaeys, A., *"Tunable two-dimensional arrays of single Rydberg atoms for realizing quantum Ising models,"* Nature **534**, 667 (2016) [cited in pages 15, 16, and 34].

Lee, W., Kim, H., and Ahn, J., *"Defect-free atomic array formation using the Hungarian matching algorithm,"* Phys. Rev. A **95**, 053424 (2017) [cited in page 54].

Leopold, T., King, S. A., Micke, P., Bautista-Salvador, A., Heip, J. C., Ospelkaus, C., Crespo López-Urrutia, J. R., and Schmidt, P. O., *"A cryogenic radio-frequency ion trap for quantum logic spectroscopy of highly charged ions,"* Review of Scientific Instruments **90**, 073201 (2019) [cited in page 19].

de Léséleuc, S., Quantum simulation of spin models with assembled arrays of Rydberg atoms, Ph.D. thesis (2018) [cited in pages 25, 28, 29, 33, and 36].

de Léséleuc, S., Barredo, D., Lienhard, V., Browaeys, A., and Lahaye, T., *"Analysis of imperfections in the coherent optical excitation of single atoms to Rydberg states,"* Physical Review A **97**, 053803 (2018) [cited in page 35].

de Léséleuc, S., Lienhard, V., Scholl, P., Barredo, D., Weber, S., Lang, N., Büchler, H. P., Lahaye, T., and Browaeys, A., *"Observation of a symmetry-protected topological phase of interacting bosons with Rydberg atoms,"* Science **365**, 775 (2019) [cited in pages 15 and 35].

Lester, B. J., Luick, N., Kaufman, A. M., Reynolds, C. M., and Regal, C. A., *"Rapid production of uniformly filled arrays of neutral atoms,"* Physical Review Letters **115**, 1 (2015) [cited in pages 28 and 134].

Levine, H., Keesling, A., Omran, A., Bernien, H., Schwartz, S., Zibrov, A. S., Endres, M., Greiner, M., Vuletić, V., and Lukin, M. D., *"High-fidelity control and entanglement*

of Rydberg-atom qubits," Physical Review Letters **121**, 123603 (2018) [cited in pages 15 and 35].

Levine, H., Keesling, A., Semeghini, G., Omran, A., Wang, T. T., Ebadi, S., Bernien, H., Greiner, M., Vuletić, V., Pichler, H., and Lukin, M. D., *"Parallel implementation of high-fidelity multiqubit gates with neutral atoms,"* Phys. Rev. Lett. **123**, 170503 (2019) [cited in page 15].

Liao, S., Cai, W., Liu, W., Zhang, L., Li, Y., Ren, J., Yin, J., Shen, Q., Cao, Y., Li, Z., Li, F., Chen, X., Sun, L., Jia, J., Wu, J., Jiang, X., Wang, J., Huang, Y., Wang, Q., Zhou, Y., Denk, L., Xi, T., Ma, L., Hu, T., Zhang, Q., Chen, Y., Liu, N., Wang, X., Zhu, Z., Lu, C., Shu, R., Peng, C., Wang, J., and Pan, J., *"Satellite-to-ground quantum key distribution."* Nature **549**, 43 (2017) [cited in page 12].

Lienhard, V., Experimental quantum many-body physics with arrays of Rydberg atoms. From spin models to topological matter, Ph.D. thesis (2019) [cited in pages 25, 28, and 33].

Lienhard, V., de Léséleuc, S., Barredo, D., Lahaye, T., Browaeys, A., Schuler, M., Henry, L.-P., and Läuchli, A. M., *"Observing the space- and time-dependent growth of correlations in dynamically tuned synthetic Ising models with antiferromagnetic interactions,"* Physical Review X **8**, 021070 (2018) [cited in pages 15, 34, 61, and 66].

Lloyd, S., *"Universal quantum simulators,"* Science **273**, 1073 (1996) [cited in page 12].

Madison, K. W., Chevy, F., Wohlleben, W., and Dalibard, J., *"Vortex formation in a stirred bose-einstein condensate,"* Phys. Rev. Lett. **84**, 806 (2000) [cited in page 13].

Madjarov, I. S., Covey, J. P., Shaw, A. L., Choi, J., Kale, A., Cooper, A., Pichler, H., Schkolnik, V., Williams, J. R., and Endres, M., *"High-fidelity control, detection, and entanglement of alkaline-earth Rydberg atoms,"* (2020), arXiv:2001.04455 [physics.atom-ph] [cited in page 15].

Magnan, E., Spontaneous decoherence in large Rydberg systems, Ph.D. thesis (2018) [cited in page 70].

Martinez-Dorantes, M., Alt, W., Gallego, J., Ghosh, S., Ratschbacher, L., and Meschede, D., *"State-dependent fluorescence of neutral atoms in optical potentials,"* Phys. Rev. A **97**, 023410 (2018) [cited in page 108].

Maze, J., Stanwix, P., Hodges, J., Hong, S., Taylor, J-amd Cappelaro, P., Jiang, L., Gurudev Dutt, M., Zibrov, A., Yacoby, A., Walsworth, R., and Lukin, M. D., *"Nanoscale magnetic sensing with an individual electronic spin in diamond,"* Nature **445**, 644 (2008) [cited in page 11].

McFee, R., *"Optimum input leads for cryogenic apparatus,"* Review of Scientific Instruments **30**, 98 (1959) [cited in pages 83 and 85].

Micke, P., Stark, J., King, S. A., Leopold, T., Pfeifer, T., Schmöger, L., Schwarz, M., Spieß, L. J., Schmidt, P. O., and Crespo López-Urrutia, J. R., *"Closed-cycle, low-vibration 4 K cryostat for ion traps and other applications,"* Review of Scientific Instruments **90**, 065104 (2019) [cited in pages 19 and 70].

Minhyuk, K., Kangheun, K., Jaeyong, H., Eun-Gook, M., and Jaewook, A., *"Rydberg quantum wires for maximum independent set problems with nonplanar and high-degree graphs,"* (2021), arXiv:2109.03517 [quant-ph] [cited in page 131].

Monz, T., Schindler, P., Barreiro, J. T., Chwalla, M., Nigg, D., Coish, W. A., Harlander, M., Hänsel, W., Hennrich, M., and Blatt, R., *"14-qubit entanglement: Creation and coherence,"* Phys. Rev. Lett. **106**, 130506 (2011) [cited in page 16].

Nation, P. D., Blencowe, M. P., Rimberg, A. J., and Buks, E., *"Analogue hawking radiation in a dc-squid array transmission line,"* Phys. Rev. Lett. **103**, 087004 (2009) [cited in page 13].

Nguyen, T. L., Raimond, J. M., Sayrin, C., Cortiñas, R., Cantat-Moltrecht, T., Assemat, F., Dotsenko, I., Gleyzes, S., Haroche, S., Roux, G., Jolicoeur, T., and Brune, M., *"Towards quantum simulation with circular Rydberg atoms,"* Phys. Rev. X **8**, 011032 (2018) [cited in page 19].

Niedermayr, M., Lakhmanskiy, K., Kumph, M., Partel, S., Edlinger, J., Brownnutt, M., and Blatt, R., *"Cryogenic surface ion trap based on intrinsic silicon,"* New Journal of Physics **16**, 113068 (2014) [cited in page 17].

Nirrengarten, T., Qarry, A., Roux, C., Emmert, A., Nogues, G., Brune, M., Raimond, J.-M., and Haroche, S., *"Realization of a superconducting atom chip,"* Phys. Rev. Lett. **97**, 200405 (2006) [cited in page 18].

Nogrette, F., Labuhn, H., Ravets, S., Barredo, D., Béguin, L., Vernier, A., Lahaye, T., and Browaeys, A., *"Single-atom trapping in holographic 2D arrays of microtraps*

with arbitrary geometries," Physical Review X **4**, 021034 (2014) [cited in pages 15, 25, 116, and 117].

Omran, A., Levine, H., Keesling, A., Semeghini, G., Wang, T. T., Ebadi, S., Bernien, H., Zibrov, A. S., Pichler, H., Choi, S., Cui, J., Rossignolo, M., Rembold, P., Montangero, S., Calarco, T., Endres, M., Greiner, M., Vuletić, V., and Lukin, M. D., *"Generation and manipulation of Schrödinger cat states in Rydberg atom arrays,"* Science **365**, 570 (2019) [cited in page 34].

Ott, R., Zache, T. V., Jendrzejewski, F., and Berges, J., *"Scalable cold-atom quantum simulator for two-dimensional QED,"* Phys. Rev. Lett. **127**, 130504 (2021) [cited in page 13].

Pagano, G., Hess, P. W., Kaplan, H. B., Tan, W. L., Richerme, P., Becker, P., Kyprianidis, A., Zhang, J., Birckelbaw, E., Hernandez, M. R., Wu, Y., and Monroe, C., *"Cryogenic trapped-ion system for large scale quantum simulation,"* Quantum Science and Technology **4**, 014004 (2018) [cited in pages 19, 70, and 103].

Pichler, H., Wang, S.-T., Zhou, L., Choi,, and M.D., L., *"Quantum optimization for maximum independent set using Rydberg atom arrays,"* (2018) [cited in pages 55, 131, and 132].

Porras, D. and Cirac, J. I., *"Effective quantum spin systems with trapped ions,"* Phys. Rev. Lett. **92**, 207901 (2004) [cited in page 13].

Preparata, F. and Shamos, M., Computational Geometry: An Introduction (Springer-Verlag, New York, 1985) [cited in pages 56 and 57].

Preskill, J., *"Reliable quantum computers,"* in in: Proc. R. Soc. Lond. A.454385–410 (1998) [cited in page 12].

Preskill, J., *"Quantum Computing in the NISQ era and beyond,"* Quantum **2**, 79 (2018) [cited in page 13].

Ravets, S., Development of tools for quantum engineering using individual atoms : optical nanofibers and controlled Rydberg interactions, Ph.D. thesis, Université Paris-Saclay (2014) [cited in page 37].

Ripka, F., Kübler, H., Löw, R., and Pfau, T., *"A room-temperature single-photon source based on strongly interacting Rydberg atoms,"* Science **362**, 446 (2018) [cited in page 14].

Roux, C., Emmert, A., Lupascu, A., Nirrengarten, T., Nogues, G., Brune, M., Raimond, J.-M., and Haroche, S., *"Bose-Einstein condensation on a superconducting atom chip,"* EPL (Europhysics Letters) **81**, 56004 (2008) [cited in pages 18 and 70].

Ryan-Anderson, C., Bohnet, J. G., Lee, K., Gresh, D., Hankin, A., Gaebler, J. P., Francois, D., Chernoguzov, A., Lucchetti, D., Brown, N. C., Gatterman, T. M., Halit, S. K., Gilmore, K., Gerber, J., Neyenhuis, B., Hayes, D., and Stutz, R. P., *"Realization of real-time fault-tolerant quantum error correction,"* (2021), arXiv:2107.07505 [quant-ph] [cited in page 14].

Sackett, C., Kielpinski, D., King, B., Langer, C., Meyer, V., Myatt, C., Rowe, M., Turchette, A., Itano, W., Wineland, D., and Monroe, C., *"Experimental entanglement of four particles,"* Nature **404**, 256 (2000) [cited in page 16].

Samajdar, R., Ho, W. W., Pichler, H., Lukin, M. D., and Sachdev, S., *"Complex density wave orders and quantum phase transitions in a model of square-lattice Rydberg atom arrays,"* Phys. Rev. Lett. **124**, 103601 (2020) [cited in page 34].

Savard, T. A., O'Hara, K. M., and Thomas, J. E., *"Laser-noise-induced heating in far-off resonance optical traps,"* Phys. Rev. A **56**, R1095 (1997) [cited in page 101].

Schlosser, N., Reymond, G., Protsenko, I., and Grangier, P., *"Sub-poissonian loading of single atoms in a microscopic dipole trap."* Nature **411**, 1024 (2001) [cited in pages 15 and 22].

Schmidt, J., Fiedler, M., Albrecht, R., Djekic, D., Schalberger, P., Baur, H., Löw, R., Fruehauf, N., Pfau, T., Anders, J., Grant, E. R., and Kübler, H., *"Proof of concept for an optogalvanic gas sensor for NO based on Rydberg excitations,"* Applied Physics Letters **113**, 011113 (2018) [cited in page 14].

Scholl, P., Quantum simulation of spin models using large arrays of Rydberg atoms, Ph.D. thesis (2021) [cited in pages 33, 35, 61, and 66].

Scholl, P., Schuler, M., Williams, H., Eberharter, A., Barredo, B., Schymik, K.-N., Lienhard, V., Henry, L.-P., Lang, T., Lahaye, T., Läuchli, A., and Browaeys, A., *"Quantum simulation of 2d antiferromagnets with hundreds of Rydberg atoms,"* Nature **595**, 233 (2021a) [cited in pages 15, 16, 34, 47, 61, 65, and 131].

Scholl, P., Williams, H., Bornet, G., Wallner, F., Barredo, D., Lahaye, T., Browaeys, A., Henriet, L., Signoles, A., Hainaut, C., Franz, T., Geier, S., Tebben, A., Salzinger,

A., Zürn, G., and Weidemüller, M., *"Microwave-engineering of programmable XXZ Hamiltonians in arrays of Rydberg atoms,"* (2021b), arXiv:2107.14459 [physics.atom-ph] [cited in page 15].

Schymik, K.-N., Lienhard, V., Barredo, D., Scholl, P., Williams, H., Browaeys, A., and Lahaye, T., *"Enhanced atom-by-atom assembly of arbitrary tweezer arrays,"* Phys. Rev. A **102**, 063107 (2020) [cited in pages 47 and 131].

Schymik, K.-N., Pancaldi, S., Nogrette, F., Barredo, D., Paris, J., Browaeys, A., and Lahaye, T., *"Single atoms with 6000-second trapping lifetimes in optical-tweezer arrays at cryogenic temperatures,"* Phys. Rev. Applied **16**, 034013 (2021) [cited in pages 95 and 104].

Sesko, D., Walker, T., Monroe, C., Gallagher, A., and Wieman, C., *"Collisional losses from a light-force atom trap,"* Phys. Rev. Lett. **63**, 961 (1989) [cited in page 97].

Shor, P., *"Algorithms for quantum computation: discrete logarithms and factoring,"* in Proceedings 35th Annual Symposium on Foundations of Computer Science (1994) pp. 124–134 [cited in page 12].

Singh, K., Anand, S., Pocklington, A., Kemp, J. T., and Bernien, H., *"A dual-element, two-dimensional atom array with continuous-mode operation,"* (2021), arXiv:2110.05515 [quant-ph] [cited in pages 117 and 120].

Sompet, P., Carpentier, A. V., Fung, Y. H., McGovern, M., and Andersen, M. F., *"Dynamics of two atoms undergoing light-assisted collisions in an optical microtrap,"* Phys. Rev. A **88**, 051401 (2013) [cited in page 134].

Sortais, Y. R. P., Marion, H., Tuchendler, C., Lance, A. M., Lamare, M., Fournet, P., Armellin, C., Mercier, R., Messin, G., Browaeys, A., and Grangier, P., *"Diffraction-limited optics for single-atom manipulation,"* Physical Review A **75**, 8 (2007) [cited in pages 23 and 43].

Steane, A. M., *"Overhead and noise threshold of fault-tolerant quantum error correction,"* Phys. Rev. A **68**, 042322 (2003) [cited in pages 12 and 13].

Steck, D. A., *"Rubidium 87 d line data,"* [cited in page 110].

Stiesdal, N., Busche, H., Kleinbeck, K., Kumlin, J., Hansen, M., Büchler, H., and Hofferberth, S., *"Controlled multi-photon subtraction with cascaded Rydberg superatoms as single-photon absorbers,"* Nature Communication **12**, 4328 (2021) [cited in page 14].

Tabuchi, Y., Tamate, S., and Yorozu, S., *"Superconducting quantum computer: a hint for building architectures,"* (2021), arXiv:2106.10488 [quant-ph] [cited in page 14].

Tuchendler, C., Lance, A. M., Browaeys, A., Sortais, Y. R. P., and Grangier, P., *"Energy distribution and cooling of a single atom in an optical tweezer,"* Phys. Rev. A **78**, 033425 (2008) [cited in page 100].

Turchette, Q. A., Wood, C. S., King, B. E., Myatt, C. J., Leibfried, D., Itano, W. M., Monroe, C., and Wineland, D. J., *"Deterministic entanglement of two trapped ions,"* Phys. Rev. Lett. **81**, 3631 (1998) [cited in page 16].

Vigneron, K., Quantum noise of light control and quantum nondemolition measurement using cold trapped atoms., Ph.D. thesis, Université Paris Sud - Paris XI (1998) [cited in page 23].

Virtanen, P., Gommers, R., Oliphant, T. E., Haberland, M., Reddy, T., Cournapeau, D., Burovski, E., Peterson, P., Weckesser, W., Bright, J., van der Walt, S. J., Brett, M., Wilson, J., Jarrod Millman, K., Mayorov, N., Nelson, A. R. J., Jones, E., Kern, R., Larson, E., Carey, C., Polat, İ., Feng, Y., Moore, E. W., Vand erPlas, J., Laxalde, D., Perktold, J., Cimrman, R., Henriksen, I., Quintero, E. A., Harris, C. R., Archibald, A. M., Ribeiro, A. H., Pedregosa, F., van Mulbregt, P., and Contributors, S. . ., *"SciPy 1.0: Fundamental Algorithms for Scientific Computing in Python,"* Nature Methods **17**, 261 (2020) [cited in pages 49 and 57].

de Waele, A., *"Basic operation of cryocoolers and related thermal machines,"* Journal of Low Temperature Physics **164**, 179 (2011) [cited in pages 72 and 73].

Weimer, H., Müller, M., Lesanovsky, I., Zoller, P., and Büchler, H. P., *"A Rydberg quantum simulator,"* Nature Physics **6**, 382 (2010) [cited in page 14].

Wilk, T., Gaëtan, A., Evellin, C., Wolters, J., Miroshnychenko, Y., Grangier, P., and Browaeys, A., *"Entanglement of two individual neutral atoms using Rydberg blockade,"* Phys. Rev. Lett. **104**, 010502 (2010) [cited in pages 14 and 16].

Willems, P. A. and Libbrecht, K. G., *"Creating long-lived neutral-atom traps in a cryogenic environment,"* Phys. Rev. A **51**, 1403 (1995) [cited in pages 96 and 103].

Wineland, D. J., *"Nobel lecture: Superposition, entanglement, and raising Schrödinger's cat,"* Rev. Mod. Phys. **85**, 1103 (2013) [cited in page 11].

Wineland, D. J., Dalibard, J., and Cohen-Tannoudji, C., *"Sisyphus cooling of a bound atom,"* J. Opt. Soc. Am. B **9**, 32 (1992) [cited in page 100].

Xia, T., Zhang, X. L., and Saffman, M., *"Analysis of a controlled phase gate using circular Rydberg states,"* Phys. Rev. A **88**, 062337 (2013) [cited in page 19].

Zhang, J., Pagano, G., Hess, P. W., Kyprianidis, A., Becker, P., Kaplan, H., Gorshkov, A. V., Gong, Z.-X., and Monroe, C., *"Observation of a many-body dynamical phase transition with a 53-qubit quantum simulator,"* Nature **12551**, 601 (2017) [cited in pages 16 and 17].